ELECTRICAL, MICROWAVE, AND THERMOELECTRIC STUDIES OF EPITAXIAL HEUSLER COMPOUND-BASED THIN FILMS

A THESIS
SUBMITTED TO THE FACULTY OF THE GRADUATE SCHOOL
OF THE UNIVERSITY OF MINNESOTA
BY

Timothy Allen Peterson

IN PARTIAL FULFILLMENT OF THE REQUIREMENTS
FOR THE DEGREE OF
DOCTOR OF PHILOSOPHY

PAUL A. CROWELL

April, 2018

© Timothy Allen Peterson 2018
ALL RIGHTS RESERVED

Acknowledgements

There are many people to whom I owe thanks for their assistance during my time in graduate school, and this list should certainly not be taken as exhaustive. When my time at the Department of Physics and Astronomy began in June of 2012, I had the great fortune to join the Crowell research group. As a bumbling zeroth and first year researcher, I was patiently mentored by Chad Geppert and Kevin Christie, who provided a model of rigor and excellence in research; they were who I aspired to become. I especially owe a great deal to Chad, whose elegant programming structures I have heavily utilized throughout my career. During those initial trying years, the companionship of my fellow incoming classmates (who are too many to name) proved to be a necessary and welcome distraction in the form of good conversation, impromptu Stub & Herb's happy hours, and intramural sports.

As part of the Crowell group, I have been grateful to name (in no particular order) Changjiang Liu, Andrew Galkiewicz, Gordon Stecklein, Justin Watts, Tao Qu, Nick Krueger, Aaron Breidenbach, Bill Peria, and Zhen Jiang as my colleagues, who have all provided unique technical assistance, stimulating research discussions, and have simply made work enjoyable. I am also indebted to Professor Chris Palmstrøm and his students Sahil Patel, Tony McFadden, Tobias Brown-Heft, and Mihir Pendharkar for patiently obliging our at-times hounding requests for samples. In addition, I would like to thank university staff for their time and assistance, in particular Shelley Frankel, Marie Rahne, Bill Voje, and numerous MNC staff members.

The support and companionship of numerous friends, roommates, and family members has been invaluable during my time in graduate school and will continue to be in the future. I would especially like to thank Anna, my parents, and my entire family for their unwavering trust that all these years I have been doing something worthwhile.

Finally, I owe the greatest thanks to my advisor, Professor Paul Crowell, who has tirelessly given his time and advice. I will always think of Paul as the ideal mentor for an experimental physicist.

This work was supported by C-SPIN, one of the six centers of STARnet, a SRC program sponsored by MARCO and DARPA, and supported in part by the National Science Foundation under award DMR-1708287.

Dedication

To my parents, who have stimulated and supported my curiosity for learning from a young age. At the risk of stating the obvious, I would not be where I am today without them.

Abstract

This thesis presents studies of epitaxial thin film structures based on Heusler compound ferromagnets, with particular focus on the static and dynamic properties of these structures relevant for spintronic device applications. In Chapter 1, a brief motivation is followed by an introduction to the spin physics of itinerant electronic materials, providing the framework for understanding the results presented in the following chapters.

In Chapter 2, demonstrations of spin-orbit torques in epitaxial Heusler/Pt bilayers are presented. After characterizing the behavior of the spin-orbit torques through second-harmonic magnetoresistance techniques, the behaviors of the torques as a function of temperature are used to study the influence of the magnetic proximity effect on the dampinglike and fieldlike torque contributions. It is found that the dampinglike torque is due to the platinum spin-Hall effect, and is not influenced by the magnetic proximity effect. Conversely, the fieldlike torque is likely due to the interface Rashba effect, and is suppressed by the presence of the magnetic proximity effect.

In Chapter 3, measurements of ferromagnetic resonance linewidths are presented for Heusler compound thin films, which are used to study the damping mechanisms of magnetization dynamics. Both intrinsic and extrinsic damping mechanisms are found, the former described by Gilbert damping and the latter due to the presence of magnon-magnon scattering processes. The Gilbert damping in these epitaxial Heusler thin films is shown to be very low relative to typical metallic ferromagnets, on the order of $10^{-4} - 10^{-3}$ when expressed as a dimensionless Gilbert damping constant. In addition, evidence of an anisotropic Gilbert damping constant is presented for epitaxial Co_2FeSi thin films. A methodology considering extrinsic magnon-magnon scattering contributions to the resonance linewidth is presented, revealing the characteristic lengthscale of magnetic inhomogeneity in these films.

Finally, in Chapter 4 a method to measure (magneto)thermoelectric coefficients in thin films is outlined, which uses all-lithographic patterning and thermometry. Initial results for the Seebeck and anomalous Nernst coefficients in Heusler compound thin films are presented, along with interpretation.

Contents

List of Tables

List of Figures

Chapter 1

Introduction

1.1 Motivation

In materials characterized by their itinerant electronic states, the spin-orbit interaction provides the means by which spin phenomena may be utilized, but also fundamentally gives rise to spin decoherence and damping processes. Studies of such affects are relevant to the field of *spintronics*, the name of which was coined in analogy to the mainstream field of charge-based *electronics*. Classic spintronic devices seek to merge the capabilities of magnetic recording with those of charge-based electronics (both long-standing areas), to allow novel applications. This thesis is largely concerned with studies of fundamental material physics, with the goal of advancing the general understanding of itinerant spin(-orbit)-related phenomena in materials. The glass through which we will look at material properties is tinted to favor those desirable for potential spintronic device applications.

1.1.1 An example device: The spin valve

To motivate the measurements discussed in this thesis, the archetypal spintronic device is presented, which is the spin valve (SV). The SV device is to spintronics what the transistor has been to semiconductor-based electronics. A cartoon SV device is shown in Fig. 1.1, which consists of two ferromagnetic (F) layers separated by a nonmagnetic (N) spacer layer. The nonmagnetic spacer serves to break the exchange coupling between the two magnetic layers, so that their magnetizations may be engineered to lie in the parallel or antiparallel configurations. The concept underlying the SV action is quite simple:

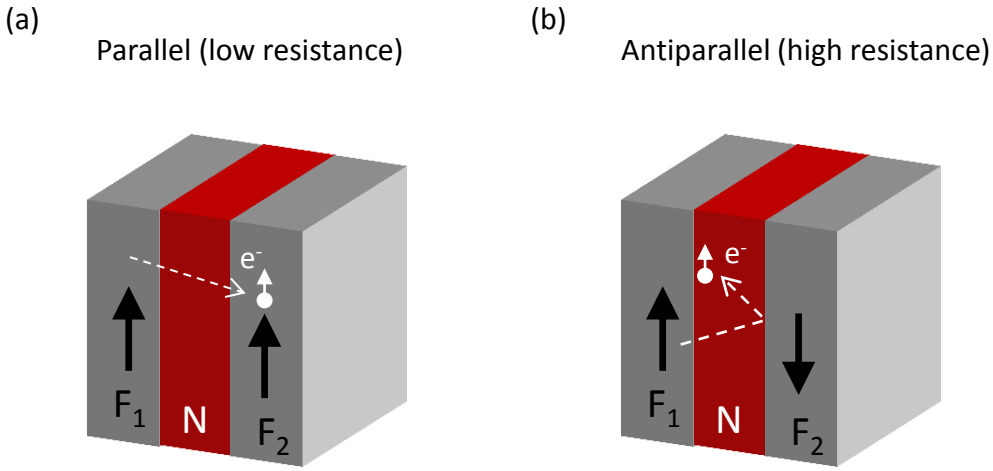

Figure 1.1: Spin valve device cartoon, with two ferromagnetic layers F_1 and F_2 drawn in gray and nonmagnetic spacer layer N drawn in red. In (a) the F_1 and F_2 magnetizations indicated by the black arrows are drawn parallel and in (b) antiparallel, which result in low and high resistance states, respectively. An example electron trajectory is drawn to indicate the higher backscattering probability in the high resistance antiparallel state.

the resistance of the device depends on the relative orientation of the magnetizations[1], through a phenomena known as giant magnetoresistance (GMR). Then, the bit level can be electrically read as a high or low resistance state, and nonvolatile information stored in some form of an integrated array of these devices. The utility of these two states as bit levels (e.g. "1" and "0" respectively) has long provided the technological impetus for spintronics research.

1.1.2 Desirable material properties

The performance of a SV depends critically on the underlying properties of its constituent materials; the devil truly is in the details. The measurements described in this thesis characterize the properties of a class of candidate ferromagnetic materials – Heusler compounds. In the last decade, a growing list of studies have demonstrated the potential of Heusler compounds as magnetic layers in SVs[2, 3]. In fact, the author of this thesis has shown that the utilization of Heusler compounds for n-GaAs-based SVs improved device performance, allowing room temperature electrical spin injection and detection[4] that was challenging to that date. Most of the works studying Heusler compounds for spintronic device applications focus almost entirely on the magnetoresistances that can be achieved in SV geometries. The field of spintronics as it stands today, however, has extended far beyond the SV device itself.

The contents of this thesis represent an effort to characterize additional functionality and properties of Heusler compounds, going beyond SV magnetoresistances. As is often the case in science, the key results that will be presented represent physical and material insights learned along that pathway. Specifically, this thesis contains measurements of spin dynamics, relaxation, and torque processes in several materials systems based on Heusler compound ferromagnets and is organized as follows: Chapter 2 describes measurements of spin-orbit torques generated in Heusler ferromagnet/heavy metal ultrathin bilayers. The mechanism by which the torque is generated is studied by examining the thickness and temperature dependence of the torque efficiencies. In Chapter 3, a study of the ferromagnetic resonance linewidth in epitaxial Heusler thin films is presented. The GHz-timescale magnetization dynamics shed light on various extrinsic and intrinsic viscous damping mechanisms which are critical for high-speed device applications. In addition, in Chapter 4 a methodology to extract (magneto)thermoelectric coefficients

of epitaxial Heusler thin films is outlined along with initial results. The remainder of Chapter 1 provides a brief technical introduction to the field of magnetic materials and spin phenomena in conductors, introducing terminology and material parameters that will be discussed throughout the thesis.

1.2 The properties of magnetic materials

Ferromagnetic materials are condensed matter systems which, by definition, posses a net magnetic dipole moment in equilibrium. The quantum mechanical exchange interaction, which is the preference of overlapping electron wavefunctions to possess parallel spin orientation, gives rise to ferromagnetism. Here, we will outline the key static and dynamic properties of ferromagnets, which give the framework for understanding many of the rich phenomena observed in magnetic materials.

1.2.1 Static properties

Ferromagnetic materials may be characterized by their moment volume density, or saturation magnetization $M_s = V^{-1}\Sigma_i \mu_i$ (where V is volume and μ_i is the magnetic dipole moment at location i) as well as various magnetic anisotropy terms which determine the energetics of the preferred magnetization orientation. The fundamental interaction that gives rise to ferromagnetism is the exchange interaction, which prefers neighboring spins to lie parallel. For an ensemble of spins denoted by S_i, this energy may be described by

$$E_{ex} = -\Sigma_{i,j} J_{ij} S_i \cdot S_j, \tag{1.1}$$

where $J_{ij} > 0$ is the exchange interaction strength of quantum mechanical origin due to the combination of the Coulomb repulsion and the Pauli exclusion principle of spatially overlapping electronic eigenstates, which occur in crystals. All magnetic materials interact with applied magnetic fields through the Zeeman interaction, which in many cases provides the experimenter the method by which he/she may rotate or switch magnetization orientations. The effect of the Zeeman interaction on the energy of the configuration is written as

$$E_Z = -\Sigma_i \mu_i H_i, \tag{1.2}$$

where the magnetic field is given by $\boldsymbol{H}$. Configurations of magnetization in general give rise to magnetic fields that oppose the magnetization and must be self-consistently included in Eq. 1.2, which are referred to as demagnetization fields $\boldsymbol{H}_d$. These fields can be expressed as a gradient of a scalar potential $\boldsymbol{H}_d = -\nabla\Phi_M$, where[5]

$$\Phi_M(\boldsymbol{r}) = -\frac{1}{4\pi}\int_V \frac{\nabla' \cdot \boldsymbol{M}(\boldsymbol{r}')}{|\boldsymbol{r}-\boldsymbol{r}'|}d^3\boldsymbol{r}' + \frac{1}{4\pi}\int_S \frac{\boldsymbol{n}' \cdot \boldsymbol{M}(\boldsymbol{r}')}{|\boldsymbol{r}-\boldsymbol{r}'|}da', \tag{1.3}$$

and $\boldsymbol{n}$ is the surface normal. In the case of an infinite thin film taken as the xy plane with uniform magnetization $|\boldsymbol{M}| = M_s$, as is often the case in this thesis, $\boldsymbol{H}_d = -4\pi M_z\hat{\boldsymbol{z}}$ which in absence of external fields causes the magnetization to preferentially orient parallel to the film plane ($M_z = 0$).

In crystalline materials, the energetics of magnetostatic configurations may also depend on the orientation of the magnetization with regards to the crystal lattice. This is due to the spin-orbit interaction, and is termed magnetocrystalline anisotropy. A common form of magnetocrystalline anisotropy in cubic crystals takes the form[6]

$$E = K_1 V(\alpha^2\beta^2 + \beta^2\gamma^2 + \gamma^2\alpha^2), \tag{1.4}$$

where α, β, γ are direction cosines of the magnetization and K_1 denotes the strength of the cubic anisotropy strength. For thin films where thicknesses may be only several nanometers, as is commonly the case in this thesis, the lowered symmetry of the interfaces can give rise to additional uniaxial magnetic anisotropy terms.

1.2.2 Dynamic properties

If the magnetization vector does not point along the lowest energy configuration determined by Eqs. 1.2, 1.3, and 1.4, magnetization dynamics will occur as dictated by the corresponding Euler-Lagrange equations. As magnetization fundamentally represents angular momentum, magnetization dynamics are governed by a torque equation, which is the Landau-Lifshitz-Gilbert (LLG) equation

$$\frac{d\boldsymbol{M}}{dt} = \gamma\boldsymbol{M} \times \boldsymbol{H}_t + \frac{\alpha\gamma}{M_s}\boldsymbol{M} \times (\boldsymbol{M} \times \boldsymbol{H}_t), \tag{1.5}$$

where $\boldsymbol{M} = M_s\hat{\boldsymbol{m}}$ denotes the magnetization vector, $\boldsymbol{H}_t$ is the total effective magnetic field given by sum of terms from Eq. 1.2, Eq. 1.3, and Eq. 1.4, γ is the gyromagnetic

ratio (28 GHz/Tesla for a free electron), and α is the dimensionless Gilbert damping parameter. In magnetic materials, α may vary broadly from 10^{-1}–10^{-5}. The damping is introduced phenomenologically in the LLG equation to capture magnetization relaxation to the equilibrium orientation in absence of a driving power. It is clear from inspection of Eq. 3.1 that a magnetization perturbed from equilibrium will undergo harmonic precession about $\boldsymbol{H}_t$ with frequency γH_t.

Although ubiquitously observed, the microscopic processes that determine the value of the Gilbert damping α in materials are, in general, poorly understood and remain an active area of research. In Chapter 3 of this thesis, measurements of α in epitaxial Heusler thin films will be presented. The primary focus of Chapter 3 is the separation of intrinsic damping processes from extrinsic dephasing processes. Extrinsic dephasing processes, which are not characterized by α, will be shown to be prevalent in these films due to the presence of spatial inhomogeneity in the magnetic landscape.

1.2.3 Spin torques

Not long after the advent of GMR devices, Slonczewski[7] and Berger[8] independently realized that because the electrical current exiting a F layer necessarily accompanied a spin current that persisted over the lengthscale λ in the N, angular momentum could be transferred from one magnetic system to another. The transfer of angular momentum mediated by driven spin currents manifest as torques, which are called *spin torques*.

LLG-Slonczewski equation phenomenology

Because the LLG Eq. 3.1 describes the equation of motion of the magnetization through torque terms, spin torques are naturally added in through additional terms, giving what is referred to as the Landau-Lifshitz-Gilbert-Slonczewski (LLG-S) equation

$$\frac{d\boldsymbol{M}}{dt} = \gamma \boldsymbol{M} \times \boldsymbol{H} + \frac{\alpha\gamma}{M_s} \boldsymbol{M} \times (\boldsymbol{M} \times \boldsymbol{H}) + \tau_{FL}(\hat{\boldsymbol{m}} \times \hat{\boldsymbol{\sigma}}) + \tau_{DL}(\hat{\boldsymbol{m}} \times (\hat{\boldsymbol{m}} \times \hat{\boldsymbol{\sigma}})), \quad (1.6)$$

where $\hat{\boldsymbol{m}}$ and $\hat{\boldsymbol{\sigma}}$ are unit vectors describing the orientation of the magnetization and spin current, respectively. The prefactor τ_{FL} of the third term on the r.h.s. of Eq. 1.6 describes the strength of the fieldlike (FL) spin torque, so called because of its resemblance to the Larmor precession term. The prefactor τ_{DL} of the fourth term on

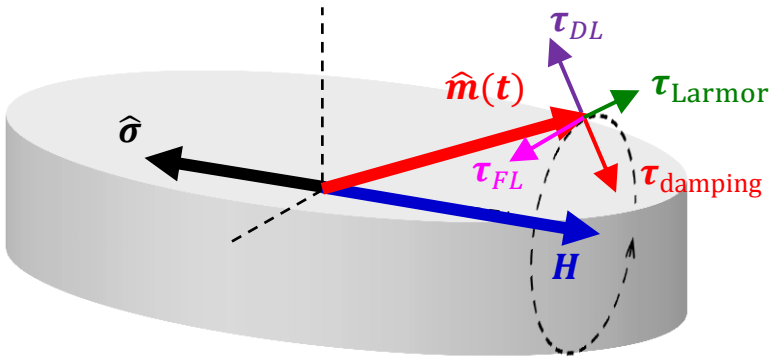

Figure 1.2: Cartoon indicating each term of the LLG-S Eq. 1.6 for an instantaneous orientation of the magnetization (red arrow) under the influence of an applied magnetic field (blue arrow) and spin torques due to spin current along $\hat{\boldsymbol{\sigma}}$ (black arrow). The Larmor, damping, fieldlike, and dampinglike instantaneous torques are indicated which are the four terms on the r.h.s. of Eq. 1.6, respectively. The Larmor torque alone would cause the tip of the magnetization vector to follow the indicated circular trajectory.

the r.h.s. of Eq. 1.6 describes the strength of the dampinglike (DL) spin torque, so called because it can be shown to influence the dynamics identically to the Gilbert damping term. Whether or not the DL torque adds to or opposes the damping depends on the orientation of $\hat{\boldsymbol{\sigma}}$. See Fig. 1.2 for a cartoon example magnetization trajectory under the influence of these torques, which are indicated at an instantaneous moment in time.

Up to this point, the physics that determines τ_{DL} and τ_{FL} has been left intentionally vague. They can be thought of as defining a convenient basis to describe spin torques, which must be confined to the plane perpendicular to the instantaneous magnetization. However, as we will see in Chapter 2 the dampinglike and fieldlike terms can be differentiated by the proper experimental geometry, and in general will originate from different physical origins.

Spin torques have the utility of allowing the experimenter the ability to control the orientation of a magnetization through the application of a spin current, without relying on externally applied magnetic fields. Because of potential magnetic memory applications, a great thrust of recent research has focused on spin torques in diverse geometries. In perhaps the most intuitive geometry of GMR SVs, spin torque has been successfully used to switch the relative orientation of the two F layers from parallel to antiparallel,

and vice versa. See Fig. 1.3 for an example switching trajectory of a magnetization under the influence of a anti-dampinglike spin torque and SV magnetoresistance data where spin torque switching was demonstrated. Both panels in Fig. 1.3 are taken from Ref. [9], which contains a comprehensive introduction to spin torque.

The focus of Chapter 2 of this thesis is the study of spin torques in ferromagnet/metal bilayers. As we will see, these spin torques are not caused by an external magnetic polarizer, as is case in GMR SVs (such those drawn in Fig. 1.1 and summarized in Fig. 1.3). Rather, the spin currents giving rise to the torque on the ferromagnetic layer arise from the spin-orbit interaction in the layer. Which term in the LLG-S Eq. 1.6 describes the spin torque, whether τ_{DL} or τ_{FL}, will allow insight into the respective origins of these torques.

1.3 Spin accumulation and spin current in nonmagnetic materials

A spin accumulation refers to a net spin polarization in a nonmagnetic material. This is a non-equilibrium state, as nonmagnetic materials by definition contain zero net spin polarization (equal spin up and down). The dimensionless vector spin accumulation $\boldsymbol{P}$ may be defined as

$$|\boldsymbol{P}| \equiv \frac{n_\uparrow - n_\downarrow}{n_\uparrow + n_\downarrow} \tag{1.7}$$

where $n_{\uparrow(\downarrow)}$ is the majority (minority) spin-resolved density in the nonmagnetic material. The equation of motion that governs the diffusion of the spin accumulation in the nonmagnetic material may be written as

$$\frac{\partial \boldsymbol{P}}{\partial t} = -\frac{\boldsymbol{P}}{\tau_s} + D\nabla^2 \boldsymbol{P} + \gamma(\boldsymbol{P} \times \boldsymbol{H}) + \hat{\boldsymbol{\alpha}} f(\boldsymbol{r}, t), \tag{1.8}$$

where τ_s is the spin lifetime, D is the spin diffusion constant, e is the electron charge, γ is the gyromagnetic ratio that determines the precession frequency due to the Larmor $\boldsymbol{P} \times \boldsymbol{H}$ term, and the final term on the r.h.s. is the spin generation function along direction $\hat{\boldsymbol{\alpha}}$, which in general may be a function of time and space[10]. The time-independent Green's function solution of Eq. 1.8 at $H = 0$ is an exponential decay of the spin accumulations away from the source, with the spin diffusion lengthscale given

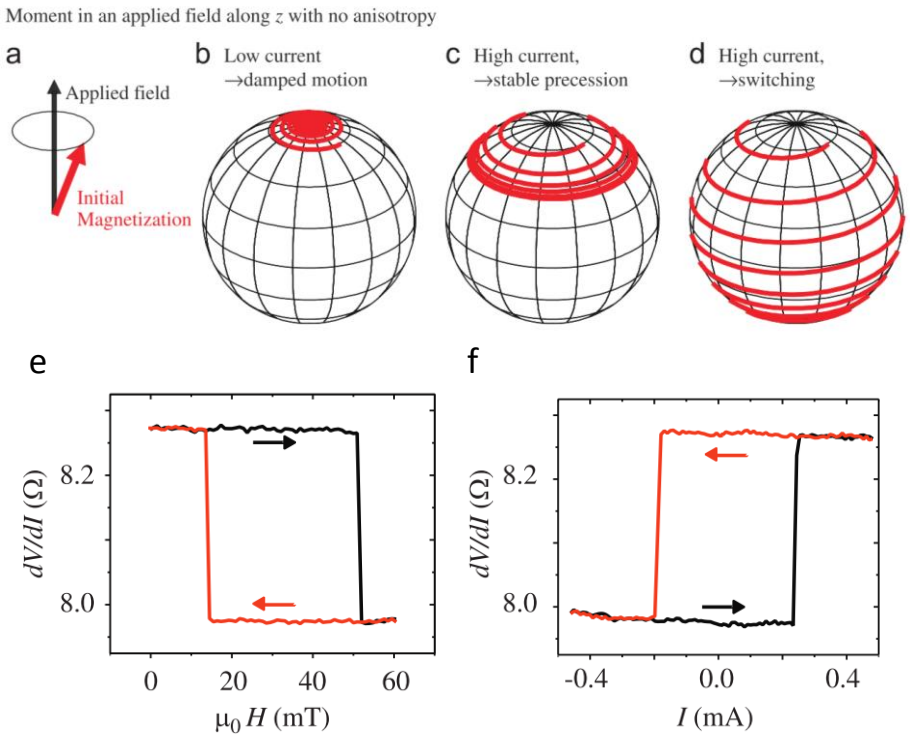

Figure 1.3: These figures are taken from Ref. [9]. In (b-d) the trajectory of the magnetization in a uniaxial free layer under the influence of an antidamping spin torque is shown, with spin torque (current) increasing from (b-d) until in (d) it is large enough to introduce switching (180° reversal). In (e) and (f), minor hysteresis loops of the differential resistance of a Permalloy/Cu/Permalloy nanopillar GMR SV are shown where in (e) magnetic field is used to switch the magnetization and in (f) current is used through the spin torque effect. In both (a) and (b) the high state of the differential resistance corresponds to the antiparallel configuration and the low state to the parallel configuration.

by $\lambda \equiv \sqrt{D\tau_s}$. In nonmagnetic materials, λ can vary widely from the Angstrom-scale in highly spin-orbit coupled heavy metals[11] to several micrometers in graphene[12, 13] or lightly doped semiconductors[14]. The influence of nonzero applied magnetic field $\boldsymbol{H}$ through the third term on the r.h.s. of Eq. 1.8 is to cause transverse dephasing, which is often utilized in so-called Hanle measurements to confirm presence of a spin accumulation. Hanle dephasing measurements may also be used to determine τ_s through study of the magnetic field needed to satisfy $\tau_s^{-1} \simeq \gamma H$[14, 15].

A nonconserved diffusive spin current tensor $J_{ij} = \partial_i P_j$ can be identified from Eq. 1.8, which represents the flow of spin angular momentum aligned along j in direction i. J_{ij} is in general not conserved because of the relaxation term in Eq. 1.8, which prevents the writing of a continuity relation for P ($dP_i/dt \neq -D\partial_j J_{ji}$). It is trivial to see that the spin current exponentially decays over the same lengthscale λ as the spin accumulation away from the source.

The origins of the source function $f(\boldsymbol{r}, t)$ in Eq. 1.8 can be due to a variety of physical mechanisms. First and fundamentally, $f(\boldsymbol{r}, t)$ may represent random statistical fluctuations in $\boldsymbol{P}(\boldsymbol{r}, t)$ which diffuse and decay according to Eq 1.8. This is a statement of the fluctuation-dissipation theorem, and may be considered axiomatic because of the linearity of Eq. 1.8. A second source of spin accumulation is spin-polarized current passed from a F layer into an N layer. In F, electrical current J_e is necessarily accompanied by spin current $\alpha_F J_e$, where α_F is a dimensionless factor describing the degree of current polarization. The boundary condition for spin current at the F/N interface (such as those shown in Fig. 1.1) sets $f(\boldsymbol{r}, t)$. Circularly polarized light may be used to optically "pump" a spin accumulation into direct-gap semiconductors[16, 17]. The spin-Hall effect, which is the conversion of a charge current to a transverse spin current as a result of spin-orbit coupling, may also be used as a source[18–20]. In addition, other more exotic methods such as spin pumping[21] or thermal injection[22] have recently been demonstrated.

1.4 The spin-orbit interaction

For the itinerant electronic materials discussed in this thesis, the magnetizations (in ferromagnetic materials) or spin accumulations (in nonmagnetic materials) are due to

the spin magnetic dipole moment $|\boldsymbol{S}| = e\hbar/2m_e$ per electron, where m_e is the mass of the electron, $\hbar$ is the reduced Planck's constant, and e is the electron charge. If relativistic effects are neglected, $\boldsymbol{S}$ is decoupled from orbital (or spatial) motion of the electron, such as motion about the nucleus or through a crystal lattice. However, in a full relativistic treatment, spin becomes coupled to orbital motion in what is referred to as the spin-orbit interaction (SOI). In atomic physics, the SOI term in the Hamiltonian is written as

$$H_{SO} = -\frac{\hbar^2}{4m_0^2c^2}\boldsymbol{\sigma}\cdot\boldsymbol{k}\times\boldsymbol{\nabla}V, \tag{1.9}$$

where m_0 is the particle mass with spin described by the Pauli spin matrices $\boldsymbol{\sigma}$, $\boldsymbol{k} \equiv \boldsymbol{p}/\hbar$ is the de Broglie wavevector (operator), $\boldsymbol{\nabla}V$ is the electric field (e.g. due to the Coulomb potential of the nucleus), and c is the speed of light. It is convenient to recognize that Eq. 1.9 takes the form of a Zeeman-like interaction in which the magnetic field is replaced by the $\boldsymbol{k}\times\boldsymbol{\nabla}V$ term. In fact, this factor is due to the relativistic transformation of electric fields into magnetic fields in the rest frame of a moving electron. Effects such as spin relaxation in nonmagnetic materials, magnetocrystalline anisotropy, and Gilbert damping all originate due to the SOI. The SOI is ubiquitous in materials, where it can be both a blessing and a curse: both allowing novel effects to be harnessed (e.g. Chapter 2, and at the same time enhancing decoherence and damping effects (e.g. Chapter 3 and Ref. [4]).

1.4.1 The spin-orbit interaction for crystal lattice Bloch states

In electrically conducting materials, that is those characterized by itinerant electronic states described by Bloch wavevector $\boldsymbol{k}$, band index i, and spin $\boldsymbol{\sigma}$, the SOI serves to couple $\boldsymbol{k}$ to $\boldsymbol{\sigma}$, and vice-versa. In crystalline materials electronic wavefunctions are described by Bloch states given by Bloch's theorem[23]

$$\psi(\boldsymbol{r})_{\boldsymbol{k},i} = e^{i\boldsymbol{k}\cdot\boldsymbol{r}}u_{\boldsymbol{k},i}(\boldsymbol{r}), \tag{1.10}$$

where $u_{\boldsymbol{k},i}(\boldsymbol{r})$ has the periodicity of the lattice, that is $u_{\boldsymbol{k},i}(\boldsymbol{r}) = u_{\boldsymbol{k},i}(\boldsymbol{r}+\boldsymbol{T})$ where $\boldsymbol{T}$ is a translation vector of the lattice. If the SOI is set to zero, $\boldsymbol{\sigma}$ serves as a quantum number with arbitrary choice of quantization axis (conventionally taken as $\hat{\boldsymbol{z}}$), so that each Bloch state described by Eq. 1.10 is doubly degenerate with spin up and down states.

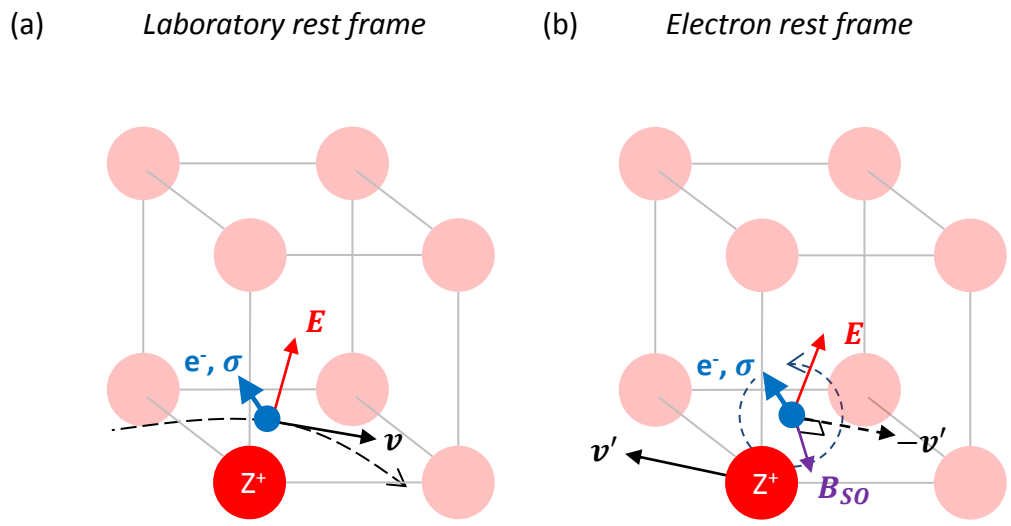

Figure 1.4: Simplified semiclassical picture of the spin-orbit interaction in an crystal lattice. In (a), an electron (blue arrow denoting spin $\boldsymbol{\sigma}$ orientation) is shown transversing the lattice with velocity $\boldsymbol{v}$ and is influenced by the electric field $\boldsymbol{E}$ of a nearby nuclei Z^+. In the electron rest frame shown in (b), the lattice nuclei move relative to the electron which results in a spin-orbit magnetic field $\boldsymbol{B}_{SO}$ which results in a torque on the electron spin.

The inclusion of the SOI given by Eq. 1.9 couples $\boldsymbol{k}$ to $\boldsymbol{\sigma}$, so that individually each no longer serve as appropriate quantum numbers to label eigenfunctions and their energies. Nevertheless, because the SOI strength is much smaller than typical kinetic energies we continue to label Bloch states by $\boldsymbol{k}$ and i and characterize the SOI by inclusion of an effective $\boldsymbol{k}$-dependent magnetic field $\boldsymbol{b}_i(\boldsymbol{k})$ that sets the spin quantization axis for state labelled by $\boldsymbol{k}$ and i. The $\boldsymbol{b}_i(\boldsymbol{k})$ function is referred to as the *Berry curvature* of the band structure. From a tight-binding perspective, the Berry curvature is determined by the spin-orbital characteristics of the microscopic atomic wavefunctions that make up the $u_{\boldsymbol{k},i}(\boldsymbol{r})$ component of the Bloch states.

Perturbation theory for SOI near band extrema in semiconductors

A full theoretical discussion of SOI and resultant Berry curvature of the band structure in materials is far beyond the scope of this thesis, but here we will sketch results for some example cases where analytic tractability is possible. In semiconductors, the relevant electronic Bloch states for transport are near band extrema and may be treated within the effective-mass approximation. Starting with the original bands characterized by their effective mass and atomic orbital characteristics (e.g. $s, p, ..$), the influence of the SOI may be accounted for by performing $\boldsymbol{k} \cdot \boldsymbol{p}$ perturbation theory. For an introduction to SOI and $\boldsymbol{k} \cdot \boldsymbol{p}$ theory in semiconductor systems, see Ref. [24].

A classic result of $\boldsymbol{k} \cdot \boldsymbol{p}$ perturbation theory is the SOI for the conduction band of zinc-blend III-V semiconductors, which was first calculated by Dresselhaus[25] and the lowest order term in $\boldsymbol{k}$ about the Γ-point is

$$H_{SO} = \beta[k_x(k_y^2 - k_z^2)\hat{\boldsymbol{x}} + k_y(k_z^2 - k_x^2)\hat{\boldsymbol{y}} + k_z(k_x^2 - k_y^2)\hat{\boldsymbol{z}}] \cdot \boldsymbol{\sigma}, \tag{1.11}$$

where β parameterizes the strength of the SOI. Equation 1.11, which results in so-called Dresselhaus SOI, can be thought of as a Berry curvature dotted into the vector of Pauli spin matrices $\boldsymbol{\sigma}$.

In semiconductor quantum wells where structural-inversion asymmetry (SIA) is present, the lowered symmetry allows a term linear in $\boldsymbol{k}$ to survive as the lowest order SOI term, resulting in the so-called Rashba SOI[24, 26]

$$H_{SO} = \alpha_R[k_y\hat{\boldsymbol{x}} - k_x\hat{\boldsymbol{y}}] \cdot \boldsymbol{\sigma}, \tag{1.12}$$

where the direction of SIA is taken as $\hat{\boldsymbol{z}}$ and α_R parameterizes the strength of the Rashba SOI.

We include Eq. 1.11 and Eq. 1.12 to illustrate the correspondence to the microscopic atomic expression of Eq. 1.9: in systems exhibiting time-reversal symmetry, the Berry curvature must appear in the Hamiltonian as an odd function of k,[1] and allowed terms are determined by symmetries of the lattice, which breaks translational symmetry. Note that in ferromagnetic conductors, time-reversal symmetry is explicitly broken so that these conditions are relaxed. We will see in Chapter 4 that the Berry curvature in ferromagnets can lead to detectable electrical transport phenomena.

Implications of the spin-orbit interaction for itinerant electronic systems

The details of the SOI may vary from one material system to another, but several generic effects originating due to the SOI (and relevant for this thesis) should be appreciated. The first important realization is that *any process that scatters electrons from state k to k' necessarily alters the spin orientation.* In nonmagnetic materials with itinerant electrons, the rate at which spin information is scrambled is fundamentally determined by momentum scattering processes. For example, for metals and semiconductors the τ_s relaxation time factor that appears in Eq. 1.8 is governed by the so-called Elliot-Yafet[27, 28] and D'yakonov-Perel[29] mechanisms, in which quasiparticle scattering (i.e. resistivity) is the controlling factor.

Second, and complementary to the statement above, *any process that alters the spin orientation necessarily is accompanied by shifts in the Fermi sea.* As we will see in Chapter 3, the α damping factor in Eq. 3.1 is determined by resistivity as well through Berry-curvature-mediated Fermi sea oscillations.

Third, and finally, *the influences of the SOI becomes more pronounced in materials made up of heavy elements, and/or in structures or materials in which the spatial symmetry is lowered.* The crystalline electric fields that give rise to the SOI are ultimately due to those of the nuclei, and increase roughly proportional to Z^4, where Z is the atomic number. Lowered spatial symmetry necessarily manifests as additional SOI terms in the Hamiltonian. For example, zinc-blende III-V semiconductors lack an

[1] For further reading on this subject, see Kramers degeneracy.

inversion center, and hence possess additional SOI terms not found in group IV semiconductors, such as Dresselhaus SOI (Eq. 1.11). Interfaces or asymmetric confinement may also lead to novel SOI due to the additional symmetry breaking, such as the Rashba SOI (Eq. 1.12).

Chapter 2

Spin-orbit torques in ferromagnet/platinum bilayers

The measurements and discussion that comprise the following chapter in this thesis were published on Jan. 10, 2018 as Physical Review B **97**, 020403(R) (2018). For convenience, this article as it appears in the journal along with a corresponding supplemental information document is included in Appendix E.2. Many of the figures presented below are modified versions of those that appeared in these manuscripts. In this chapter, measurements of spin-orbit torque efficiencies are presented for Heusler/platinum epitaxial bilayers. The key result we identify is the influence of the magnetic proximity effect on spin-orbit torque efficiencies in Heusler/platinum bilayers. We will show that the fieldlike efficiency shows a suppression at low temperatures, which we attribute to the influence of the magnetic proximity effect.

2.1 Introduction to SOTs in ferromagnet/nonmagnet bilayers

Characterization of the influence of the spin-orbit interaction (SOI) for spin transport and dynamics is one of the primary goals of this thesis. In Chapter 1, the SOI was discussed as giving rise to spin relaxation and damping mechanisms. In spin valve geometries, the SOI is often the enemy as its presence leads to non-conservation of

spin accumulations and currents. For example, see Ref. [4] (authored by T.A.P., and included for convenience in Appendix E.1 of this thesis) for a description of how spin relaxation processes in n-GaAs governed by the Dresselhaus SOI[25] influence and limit the temperature-dependent performance of the SV devices.

In contrast to the structures studied in Ref. [4], for the effects that will be discussed in this chapter, the SOI *enhances* rather than hinders the device action. These effects can be generically understood as the logical inversion of the SOI principle, which couples spin degrees of freedom to orbital motion, and leads to spin relaxation and damping in condensed matter systems possessing itinerant spin and charge carriers. If instead the orbital degrees of freedom are driven away from equilibrium (e.g. by application of a current bias), the accompanying spin degrees of freedom must also respond by deviating from their equilibrium properties. For a pictorial illustration of the spin-orbital interplay and some corresponding physical effects see Fig. 2.1. Because the degree to which the spin degrees of freedom respond to the orbital effects is determined by the strength of the SOI, material systems with large SOIs are desired.

In metallic structures, study of the SOI as a method of generating spin currents and spin torques began with the (inverse) spin-Hall effect (SHE)[20, 29, 30]. The SHE began as a topic of interest in semiconductors[29], where it was first studied through optical orientation experiments[19] and later through all-electrical experiments[31]. The Rashba interaction[26, 32], through which current at an interface may result in a spin accumulation, also became a well-known paradigm in semiconductor quantum-well literature[33]. Semiconductors were the initial focus of SOI phenomena because 1) a broad knowledge base existed due to their optical and electronic use, 2) tunability of (spin) transport parameters could be achieved by doping and alloying, and 3) mesoscopic carrier spin and momentum coherence times and lengths are achievable in lightly-doped semiconductor systems.

Although semiconducting systems have served as the test-bed for SOI phenomena, the *magnitude* of the SOI in such systems to-date has limited experimental work[19, 31, 34, 35] to study of novel effects at cryogenic temperatures. On the other hand, metals, while lacking tunability, do not require the painstaking material synthesis of semiconductors and can permit current densities larger by a factor of 10^4 or more. The large current densities achievable in metallic structures brought the SHE and Rashba

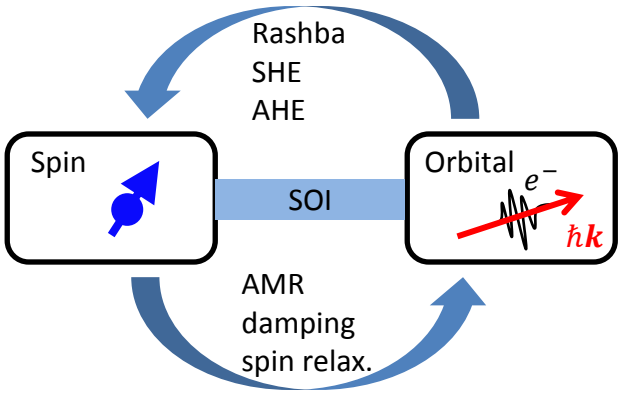

Figure 2.1: Diagram meant to illustrate the class of effects which couple orbital effects to spin (upper half), as well as effects which couple spin to orbital effects (lower half). Note that the direction of the arrows are not determined by any physics (via time-reversal symmetry), but are schematic and respective to the quantity studied by the experimentalist.

effects from low temperature semiconductor transport novelties to effects able to create spin currents large enough to apply relevant torques to F magnetizations[21, 36–38]. In particular, the heavy 5d transition metals (Ta, W, Pt, and Au) with large SOI became established as candidate Rashba and SHE materials in F/N bilayer structures. The torques which originate from the SOI-generated spin accumulation and current are known broadly as spin-orbit torques(SOTs), to distinguish them within the more general field of spin-transfer torques(STTs)[7, 8, 39] introduced in Chapter 1. Below, the SHE and Rashba effects will be briefly introduced in the context of SOTs in F/N bilayers.

2.1.1 The spin-Hall effect

The spin-Hall effect[20, 29, 30], which bears its name in analogy to the ordinary Hall effect(OHE), refers to a transverse deflection of charge carriers in which the sign of the transverse deflection is determined by the spin orientation of the carrier. Figure 2.2 compares the OHE, which involves a magnetic field and results in a transverse *charge* current J_{xy}, to the SHE, which involves no magnetic field and results in a transverse

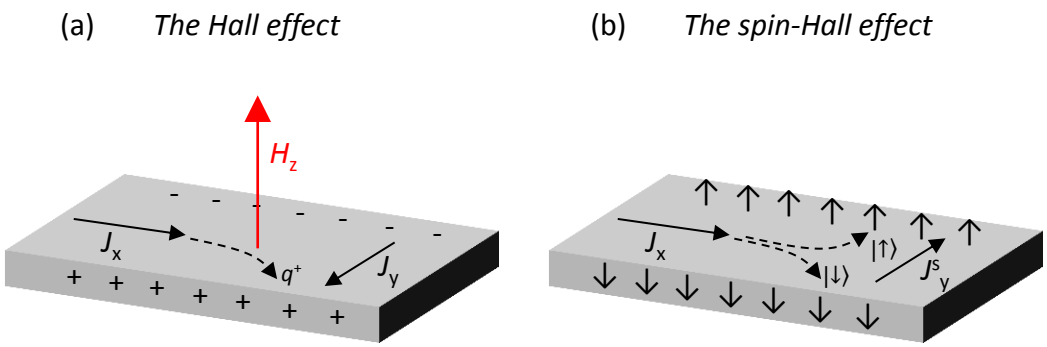

Figure 2.2: (a) Cartoon illustrating the mechanism of the OHE, by which the Lorentz force due to the out-of-plane magnetic field H_z results in a transverse deflection of the charge carriers, leading to a charge buildup on the edges of the sample. (b) Cartoon illustrating the SHE, in which in charge carriers of opposite spin polarization experience opposite transverse deflection, leading to a transverse spin current J_s in absence of a transverse charge current.

spin current J_s. For a sample of finite size, the OHE and SHE result in a charge and spin buildup at the edges of the sample, respectively. The SHE may be expressed phenomenologically through the expression

$$J^s_y = \theta_{SH} J^c_x, \tag{2.1}$$

where J^s_y (the transverse spin current) and J^c_x (the longitudinal charge current) are conveniently expressed in the same units, and θ_{SH} is the dimensionless spin-Hall ratio (sometimes referred to as spin-Hall angle) which parameterizes the magnitude and sign of the spin-dependent deflection. While it is intuitively useful to write scalar relations such as Eq. 2.1, in general, spin current is a tensor quantity (3 spatial and 3 spin indices) and so with full generality Eq. 2.1 should be replaced with [40]

$$J^s_{ij} = -\theta_{SH} \epsilon_{ijk} J^c_k, \tag{2.2}$$

where ϵ_{ijk} is the unit antisymmetric Levi-Civita tensor.

Microscopically, the SHE may originate from any of several distinct processes. The language used to describe the spin-dependent processes involved is borrowed from the

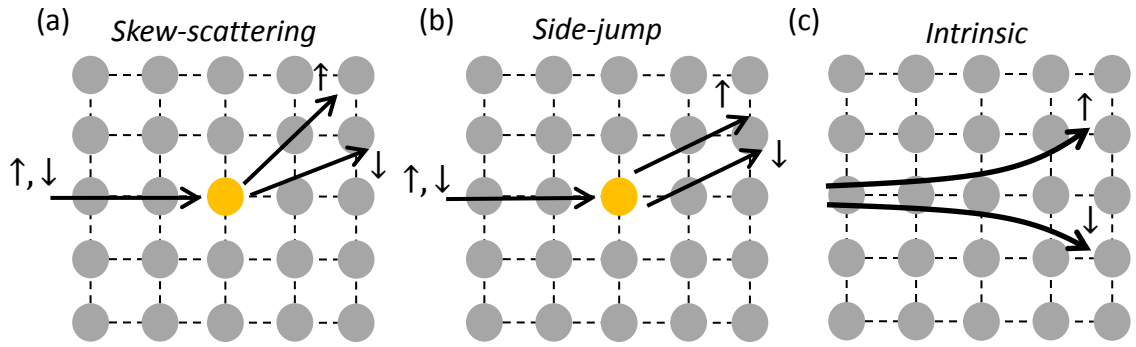

Figure 2.3: Semiclassical cartoon illustrations of three mechanisms which may give rise to the SHE in materials. The black arrows pointed from left to right indicate the imposed charge current through a crystal lattice (an example square lattice of atomic nuclei is shown by the gray circles), and the spin-dependent trajectories indicated by the ↑ and ↓ labels. For the skew-scattering (a) and side-jump (b) mechanisms, the scattering defect is indicated by the gold lattice site.

closely related anomalous Hall effect (AHE) literature (see Ref. [41], for instance). The three commonly-discussed microscopic mechanisms for the SHE are described schematically in Fig. 2.3, which are the skew-scattering, side-jump, and intrinsic mechanisms[18]. The first two of these mechanisms, illustrated in Fig. 2.3(a) and Fig. 2.3(b), involve defect scattering, while the intrinsic mechanism shown in Fig. 2.3(c) is a property of the Berry curvature and hence does not invoke defect scattering. In studies of the AHE, the preceding three mechanisms are typically distinguished by the dependence of the AHE conductivity $\sigma_{AHE} \equiv \rho_{AHE}^{-1}$ on the longitudinal conductivity σ_{xx}: for the skew-scattering mechanism $\sigma_{AHE} \propto \sigma_{xx}$, while for the side-jump and intrinsic mechanisms σ_{AHE} is independent of conductivity. It is believed that an identical scaling of σ_{SHE} occurs with σ_{xx} for these mechanisms, however unlike σ_{AHE} (which manifests in a transverse charge current) σ_{SHE} cannot be simply measured in charge transport. Distinguishing these processes is not the main focus of this thesis, and a good reviews of experiments and theory may be found in Sinova et al.[18] for the SHE and Nagaosa et al.[41] for the AHE. Through a straightforward application of Ohm's Law in combination with Eq. 2.1, one may show that the oft-reported SHE figure-of-merit $\theta_{SHE} = \sigma_{SHE}\rho_{xx}$. For Pt, which is the SHE metal that will be discussed in this thesis,

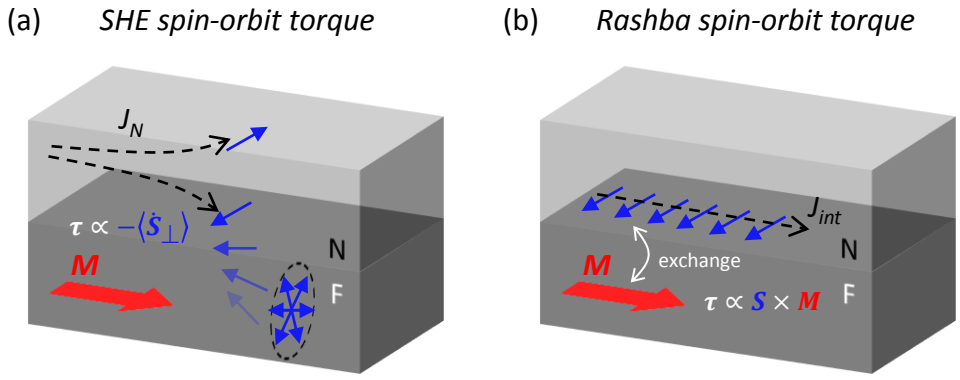

Figure 2.4: Illustration of the SHE SOT mechanism (a) and the Rashba SOT mechanism (b). The blue arrows denote the itinerant carrier spin polarization, and the red arrow the F magnetization. In (a) J_N is the current in N which gives rise to the SHE, and in (b) J_{int} is the interface current which gives rise to the Rashba interface spin accumulation.

several recent experiments[11, 42] have shown $\theta_{SHE} \propto \rho_{xx}$, implying the intrinsic SHE mechanism is dominant. This result is supported by theoretical calculations of the 5d element intrinsic SHE[43]. In the results section of this chapter, we will show that our SOT measurements are consistent with the $\theta_{SHE} \propto \rho_{xx}$ relation.

It was soon realized that if the spin current generated in the SHE could be directed at (and absorbed by) an adjoining ferromagnetic (F) layer, a torque on the F magnetization must result. Originally, the inverse process was detected: ferromagnetic resonance (FMR) driven in the F layer sourced a spin current into the nonmagnetic (N) layer via the spin pumping effect[21], which was detected through the inverse SHE (ISHE)[44]. Shortly after, it was demonstrated that a dc applied current could enhance or suppress the FMR damping, depending on the sign of the current (and corresponding spin current)[45]. The group at Cornell then showed that FMR could be *driven* by the torque created by the SHE[46], and finally, in a seminal experiment demonstrated dc switching of a M layer through the SHE in an adjoining tantalum layer[38].

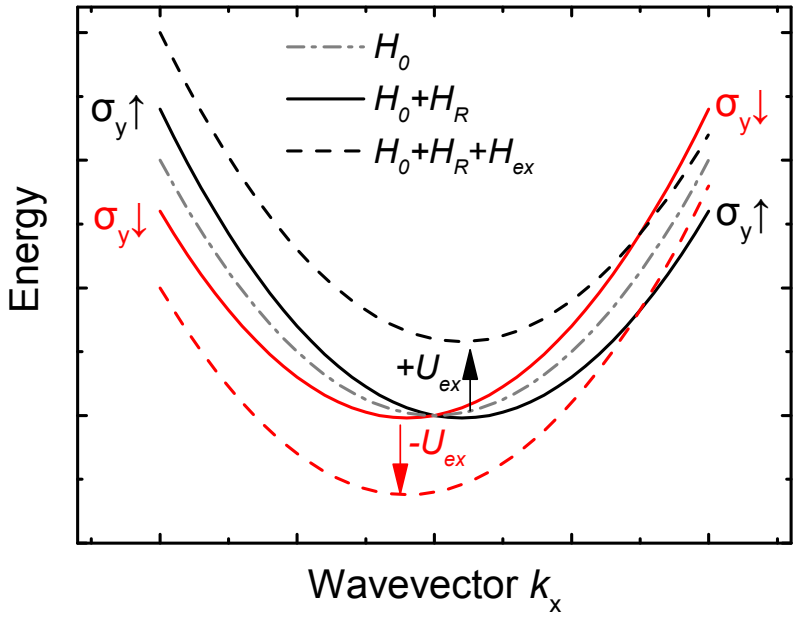

Figure 2.5: Energy-wavevector band dispersions for the Rashba interaction Hamiltonian (Eq. 2.3). The SIA direction is taken along z, and a k_x cut is shown where the spin along y, σ_y, is the appropriate spin quantum number. As indicated, the black bands are σ_y up and the red bands are σ_y down, while the gray-dash-dot line is for $\alpha_R = U_{ex} = 0$. The dashed lines illustrate the effect of a finite exchange interaction with magnetization along y, which further splits up and down bands.

2.1.2 The Rashba effect

Whereas for the SHE an applied current results fundamentally in a transverse *spin current*, for the Rashba effect an applied current results in a *spin polarization*. The Rashba effect was first discussed by Rashba[47] and Dresselhaus[25] as an allowable term in the Hamiltonian of semiconductor systems possessing structural inversion asymmetry (SIA), lifting the spin degeneracy to leading order linear in $\boldsymbol{k}$. The Hamiltonian for a carrier with effective mass m^* in the presence of Rashba SOI and the exchange interaction may be expressed as[26]

$$H = H_0 + H_R + H_{ex} = \frac{\hbar^2 \boldsymbol{k}^2}{2m^*} + \alpha_R(\hat{\boldsymbol{z}} \times \boldsymbol{k}) \cdot \boldsymbol{\sigma} + U_{ex}(\boldsymbol{m} \times \boldsymbol{\sigma}), \tag{2.3}$$

where α_R parameterizes the strength of the Rashba interaction, $\boldsymbol{k}$ is carrier wavevector, $\boldsymbol{\sigma}$ is the vector of the carrier Pauli spin matrices, $\hat{\boldsymbol{z}}$ specifies the direction of SIA, and U_{ex} is an exchange splitting giving rise to magnetization $\boldsymbol{m}$. In Figure 2.5, the energy bands given by Eq. 2.3 are shown for cases of nonzero α_R ($U_{ex} = 0$) and for nonzero α_R and U_{ex}. Note that because the bands in Fig. 2.5 are shown in one dimension k_x, they may be labelled by σ_y, but in general the spin quantization axis of $\boldsymbol{k}$-states is along $\hat{\boldsymbol{z}} \times \boldsymbol{k}$.

For the case of $U_{ex} = 0$ at equilibrium (zero current, so $\Sigma_k f_{\boldsymbol{k}} \nabla_k E_{\boldsymbol{k}} = 0$ where $f_{\boldsymbol{k}}$ is the occupation function equal to the Fermi-Dirac distribution in equilibrium), it can be seen that while the Rashba interaction introduces a spin texture to the Fermi circle, the net polarization remains zero. However, by applying a current $J_x = \Sigma_k f_{\boldsymbol{k}} \nabla_k E_{\boldsymbol{k}}$ the Fermi circle is shifted so that a net polarization results proportional to $\alpha_R J_x \hat{\boldsymbol{y}}$, which we will refer to as the Rashba spin accumulation.

In the presence of a magnetization with $U_{ex} \neq 0$, a spin polarization exists in equilibrium, but similar to the case above the application of a current J_x induces a change in the polarization along the $\hat{\boldsymbol{y}}$ direction[48]. As we will see, if not collinear with the equilibrium magnetization, the current-induced change in the polarization is equivalent to a torque exerted on the magnetization.

2.1.3 SHE and Rashba effect spin-orbit torques

The SHE and Rashba effects discussed in Section 2.1.1 and Section 2.1.2, respectively, may be used to apply spin transfer torques to the magnetization of an adjacent F

layer. As mentioned previously, these classes of spin transfer torques are collectively referred to as spin-orbit torques (SOTs) because they originate due to the SOI. In fact, in nearly the entirety of SOT literature the presence of the underlying SHE or Rashba mechanisms is *inferred* indirectly through study of the torques on a magnetization. As discussed in Sec. 2.1.1, the SHE drives a transverse spin current, while the Rashba effect discussed in Sec. 2.1.2 results in an interface spin accumulation. The influence of SOTs on the F magnetization may be described by Eq. 1.6, which is written again below for convenience:

$$\frac{d\boldsymbol{M}}{dt} = \gamma \boldsymbol{M} \times \boldsymbol{H} + \frac{\alpha\gamma}{M_s} \boldsymbol{M} \times (\boldsymbol{M} \times \boldsymbol{H}) + \tau_{FL}(\hat{\boldsymbol{m}} \times \hat{\boldsymbol{\sigma}}) + \tau_{DL}(\hat{\boldsymbol{m}} \times (\hat{\boldsymbol{m}} \times \hat{\boldsymbol{\sigma}})). \quad (2.4)$$

In the following sections, the means by which the SHE and the Rashba effects lead to dampinglike (DL) τ_{DL} and fieldlike (FL) τ_{FL} torques will be discussed.

SHE spin-orbit torques

In the geometry of a F/N bilayer defining the xy plane, by Eq. 2.2 if $\boldsymbol{J}^c = J_x^c \hat{\boldsymbol{x}}$ the surviving spin current tensor elements are $J_{zy}^s = -J_{yz}^s = \theta_{SH} J_x^c$. (We remind the reader that J_{ij}^s denotes the flow in coordinate i of spin polarized along j.) J_{zy}^s is the only relevant tensor element for SOT on the F layer, because it corresponds to the z flow of angular momentum (oriented along y). We can therefore omit the tensor notation and recognize that $\sigma = \hat{\boldsymbol{y}}$ in Eq. 2.4.

Haney et al.[49] have solved for τ_{DL} and τ_{FL} by enforcing the proper boundary conditions at the F/N interface with SHE spin current $J_{zy}^s = \theta_{SH} J_x^c$, and find that through the parametrization of a complex interface spin-mixing conductance $G_{\uparrow\downarrow}$ the torques may be written as

$$\tau_{DL} = \theta_{SH} J_x^c Re[G_{\uparrow\downarrow}] F(\lambda, \rho) \quad (2.5)$$

and

$$\tau_{FL} = \theta_{SH} J_x^c Im[G_{\uparrow\downarrow}] F(\lambda, \rho) \quad (2.6)$$

where $F(\lambda, \rho)$ is a dimensionless geometric suppression factor due to spin diffusion and relaxation in N determined, and is determined by the spin diffusion length and resistivity.

(Expressions for $F(\lambda, \rho)$ will be shown in Sec. 2.3.2.) Microscopically, the complex spin-mixing conductance is given by[49, 50]

$$G_{\uparrow\downarrow} = \frac{e^2}{h} \int_{FS} \frac{d^2k}{(2\pi)^2} (1 - r_\downarrow r_\uparrow^*), \tag{2.7}$$

where the integral is over the N Fermi surface and the r values are F/N interface spin-resolved reflection coefficients. The real component $Re[G_{\uparrow\downarrow}]$ of Eq. 2.7 corresponds to spin-resolved reflection and transmission across the F/N interface, while the imaginary component $Im[G_{\uparrow\downarrow}]$ corresponds to precession through finite phase upon reflection. It is helpful to think of Eq. 2.7 in the case of a majority-polarized half-metallic F layer for which $r_\uparrow = 0$, and $G_{\uparrow\downarrow}$ is purely real and given by the N DOS at the Fermi level. Conversely, for the case of a nonmagnetic interface Eq. 2.7 trivially gives zero. Calculations of Eq. 2.7 in metallic F/N bilayers have shown that the ratio $Re[G_{\uparrow\downarrow}]/Re[G_{\uparrow\downarrow}] \gtrapprox 10$[36, 49], which results in predominantly DL SOTs via Eq. 2.5 and much smaller FL SOTs via Eq. 2.6.

To gain intuitive understanding of Eq. 2.5, it is useful to consider Fig. 2.4(a). The SOT that can be applied on an adjoining M layer through the SHE in the N layer is a consequence of angular momentum conservation. The predominantly DL SOT is due to the component of the incident SHE spin current transverse to the magnetization, which undergoes efficient precessional dephasing at the F/N interface due to the F exchange field. By conservation of angular momentum, the absorption of the transverse spin current $\boldsymbol{S}_\perp$ into F must result in a back-torque on the F magnetization equal to the transverse incident SHE spin current $\langle \dot{\boldsymbol{S}}_\perp \rangle$, where the angle brackets denote the average over all carriers.

2.1.4 Rashba effect spin-orbit torques

In contrast to the SHE SOT described in the previous section, the Rashba SOT does not originate from a spin current drawn by the magnetization, but rather originates due to the exchange interaction between the Rashba spin accumulation and the F magnetization. The Rashba spin accumulation that exists at the F/N interface can be defined as $\boldsymbol{S}_R \equiv \alpha_R(\hat{\boldsymbol{z}} \times \boldsymbol{J}^c)\delta(z)$, so that the Rashba SOT $\boldsymbol{\tau}_R$ is given by[48]

$$\boldsymbol{\tau}_R = \int U_{ex}(\boldsymbol{M} \times \boldsymbol{S}_R) dz, \tag{2.8}$$

where U_{ex} is the exchange interaction strength. For an F/N bilayer defining the xy plane with $\boldsymbol{J}^c = J_x^c \hat{\boldsymbol{x}}$, it is clear that $\boldsymbol{S}_R \parallel \hat{\boldsymbol{y}}$, so that Rashba SOTs given by Eq. 2.8 are accounted for by the τ_{FL} term in Eq. 2.4. See Fig. 2.4(b) for a cartoon illustration of the Rashba SOT in an F/N bilayer.

2.2 SOT measurement technique

To characterize the strength of the SOT in F/N bilayers, two approaches may be used. The first approach is to measure the critical current J_c at which the magnetization is reversed, or switched. The critical current is all-important in technological spintronic device applications, where magnetic switching is the primary goal. For expressions for J_c in several geometries for SHE and Rashba SOT mechanisms, see Refs. [48, 51]. However, the J_c expressions involve magnetostatic and dynamic parameters, and are not directly determined by the SOI mechanisms themselves. Furthermore, detection of switching itself is challenging for some magnetic films. The anomalous Hall effect (AHE) or magneto-optical Kerr effect (MOKE) are typically used to detect magnetic switching in films with perpendicular magnetic anisotropy, but may not be used for in-plane magnetized films.

Because of these considerations, we have characterized the SOI in our bilayers with a magnetoresistive harmonic response (MR-HR) measurement. Rather than reverse the magnetization orientation, in this technique a current applied to the bilayer at frequency ω rocks the magnetization small angles about the equilibrium orientation at ω through the SOT. The influence of the SOTs on the static orientation of $\boldsymbol{M}$ can be determined by setting the l.h.s. of Eq. 2.4 to zero. Magnetoresistances (MRs), which are resistances that depend on the orientation of the magnetization, result in detectable harmonic 2ω voltages due to the product of the MR and current, both of which vary at ω. In addition, this measurement allows distinguishable characterization of the DL and FL components of the SOT. Below, we will describe the measurement details and geometry.

2.2.1 Heusler/platinum bilayer stack and growth

The F/N bilayers used in this study were grown on MgO(001) substrates by molecular-beam epitaxy (MBE) by Anthony McFadden in the group of Chris Palmstrøm at the

University of California Santa Barbara. Prior to F growth, an *in-situ* MgO buffer was grown by e-beam evaporation on prepared MgO substrates in order to bury residual carbon and improve surface morphology. The F layer is the Heusler compound Co_2FeAl (CFA) with thickness $t_F = 1.2$ nm, grown by MBE at a substrate temperature of 200° C by codeposition of individual elemental sources in ultrahigh vacuum (UHV). Reflection high energy electron diffraction (RHEED) monitored during CFA growth confirmed a 45° rotated orientation CFA<110> || MgO<100>. X-ray diffraction (XRD) measurements conducted on thicker 4 and 30 nm MgO/CFA samples confirm a single phase of (001) oriented CFA while the presence and relative peak area of the (002) reflection confirms at least B2 ordering. The samples were cooled to room temperature before capping with Pt, which was grown using e-beam evaporation in UHV. The Pt grew epitaxially and was (001) oriented with Pt<100> || CFA<110>, as confirmed by RHEED and XRD. After Pt capping, samples were removed from UHV and exposed to atmosphere for subsequent processing. Vibrating sample magnetometry was used to measure the CFA(1.2 nm) saturation magnetization $M_s = 800 \pm 100$ emu/cm^3 at room temperature. The saturation magnetic field of the anomalous Hall effect (AHE) at 300 K matched $4\pi M_s$ within uncertainty. Therefore, the AHE saturation field was used to infer the temperature dependence of M_s, which increased from 850 emu/cm^3 at 300 K to 1050 emu/cm^3 at 10 K. Ferromagnetic resonance (FMR) measurements were performed at room temperature on a companion MgO/CFA(1.2 nm)/Pt(7 nm) bilayer (TMC183), for which Kittel formula[52] fits of the FMR field for rf excitation frequencies from 4-20 GHz revealed a cubic in-plane anisotropy $K_1 = -6 \times 10^3$ J/m^3 with magnetic easy axes along CFA<110>(MgO<100>).

2.2.2 MR-HR measurement geometry and derivation of response

The technique described below follows closely from the original MR-HR characterization techniques of SOTs developed in References [53–55] for perpendicularly magnetized films, and the adaptation to in-plane magnetized films by Ref. [56]. Later, Ref. [57] discussed magnetothermoelectric (MTE) effects which must be accounted for in harmonic MR measurements of SOTs in the in-plane geometry. Our expressions are similar to Ref. [57], however we arrive at a more compact expression in a simplified geometry to account for MTE effects.

Geometry and hardware setup

The bilayers were patterned into Hall bar devices with optical lithography and Ar^+ ion milling, and Ti/Au bonding vias deposited with electron beam evaporation. For further details of the fabrication process, see Appendix D.0.3. The MR-HR measurements presented in this thesis were performed on samples TMC223 and TMC224. To achieve multiple Pt thicknesses per growth, a shadowmask technique was used in which four Pt thicknesses could be grown on a given MgO/CFA(1.2 nm) underlayer. Growth TMC224 resulted in Pt thicknesses of 1, 2, 3, and 4 nm, and growth TMC223 resulted in Pt thicknesses of 5, 6, 7, and 8 nm. A square shadowmask was translated 3 times during growth to achieve the four different Pt thicknesses, each in a 3 mm×3 mm quadrant of a 2×2 grid. See Fig. 2.6 for a diagram illustrating the shadowmask translation scheme. For the lithography, a corresponding photomask was used that matched the pitch of the 3 mm×3 mm grid.

The MR-HR measurements were performed in a Quantum Design PPMS cryostat capable of achieving 1.8-400 K temperature and magnetic fields up to 9 Tesla. Through chip mounting on a rotator platform probe, the magnetic field could be applied with arbitrary orientation ϕ and rotated 360° in a chosen plane. The geometry[1] chosen for the MR-HR measurement is shown in Fig. 2.7(a), and the hardware setup is summarized in Fig. 2.7(b).

A low-frequency ($\omega/2\pi \simeq 10$ Hz) ac excitation current $\sim \sin\omega t$ with root-mean-square (RMS) amplitude I was applied to a Hall bar, and the second harmonic Hall resistance $R_H^{2\omega} \equiv \langle V_H^+ - V_H^- \rangle^{2\omega}/I$ measured with phase and harmonic sensitive lock-in detection, where the brackets denote the RMS amplitude of the 2ω Y-quadrature Hall voltage. The orientation ϕ of the static applied magnetic field H was rotated 360° in the bilayer plane while recording $R_H^{2\omega}$, for varied magnetic field strengths. Below, we discuss the model that was used to fit the data and extract the DL and FL SOT efficiencies from these data.

[1] The unorthodox definition of ϕ (taken with respect to the negative y axis) is historical in origin, reflecting the sample mounting convention used in initial MR-HR measurements. The ϕ angle could be trivially shifted by 90° to coincide with the usual polar coordinate definition, however for transparency this was not performed.

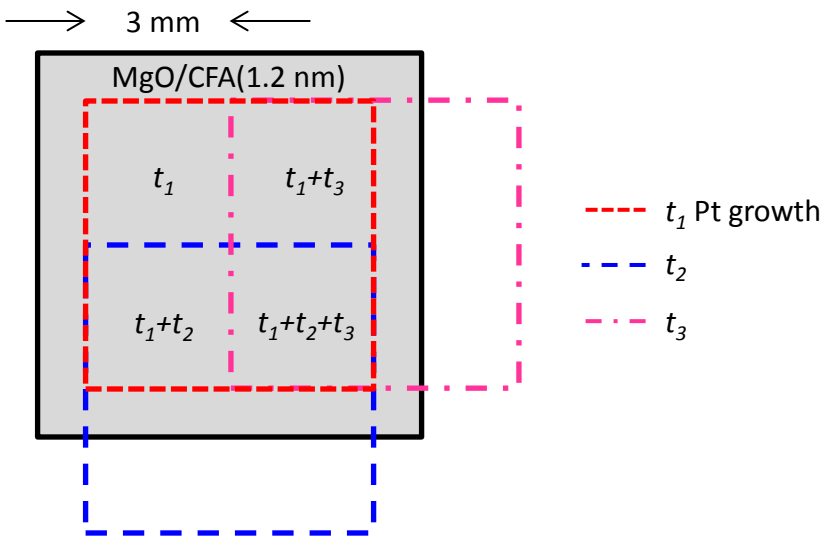

Figure 2.6: Diagram illustrating the shadowmask translation scheme used to grow 4 Pt thicknesses on a given MgO/CFA underlayer for samples TMC223 and TMC224. The dashed squares illustrate the position of the shadowmask window for Pt growths of thickness t_1, t_2, and t_3, and the total Pt thickness is indicated on each quadrant. The grid spacing was 3 mm. For TMC223 $t_1 = 5$ nm, $t_2 = 2$ nm, and $t_3 = 1$ nm resulting in Pt thicknesses of 5, 6, 7, and 8 nm, while for TMC224 $t_1 = 1$ nm, $t_2 = 2$ nm, and $t_3 = 1$ nm resulting in Pt thicknesses of 1, 2, 3, and 4 nm.

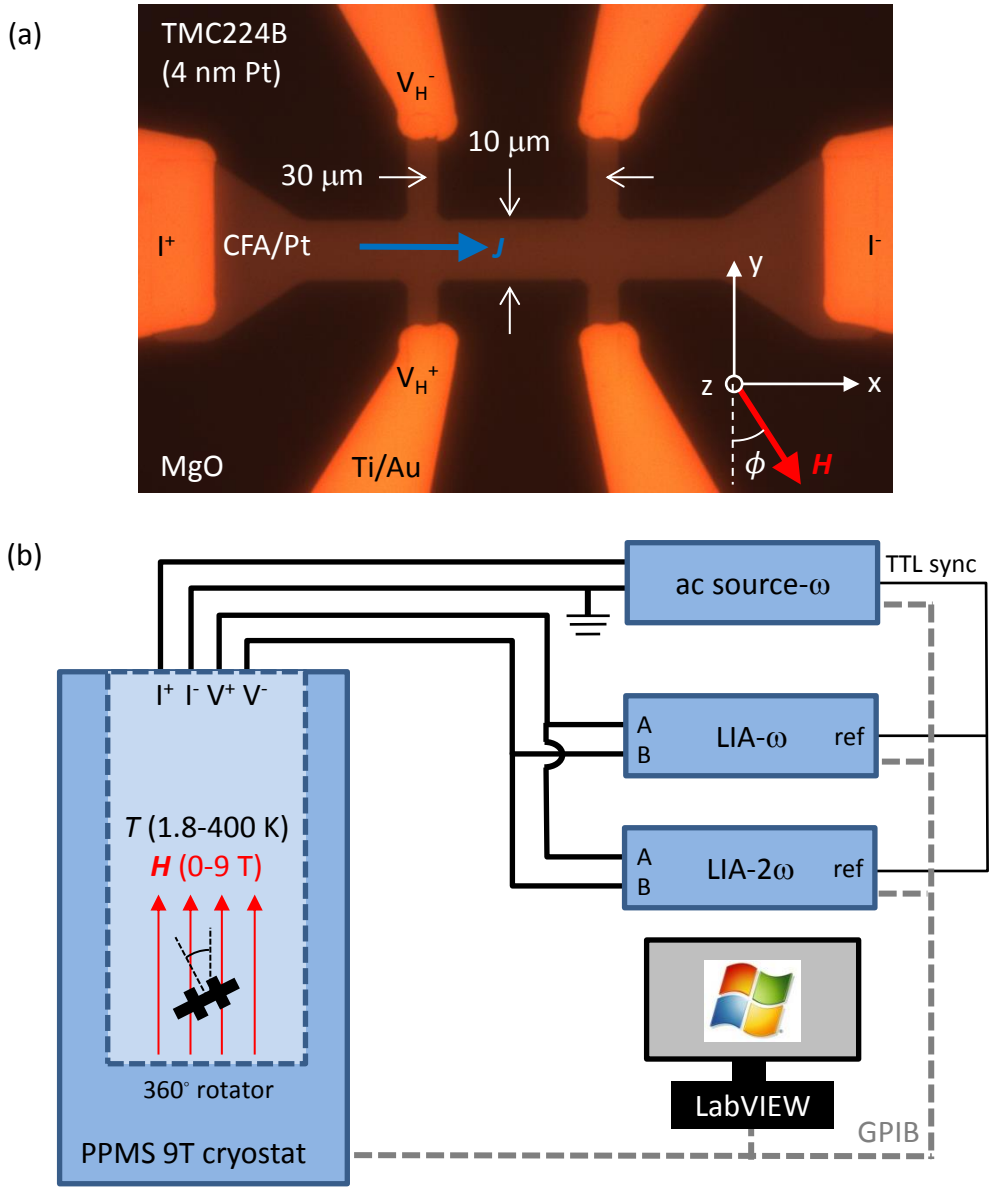

Figure 2.7: (a) Optical micrograph of a Hall bar used in the MR-HR measurement, with the coordinate system indicated on the lower right. This micrograph was taken on TMC224B, for which the Pt thickness is 4 nm. The conventions for current and voltage terminals are indicated on the appropriate Hall arms. (b) Hardware diagram for the MR-HR measurement. All measurements were performed in a Quantum Design PPMS 9T cryostat equipped with a rotator probe. A Keithley 6221 ac current source was used with either SR830 or EG&G 7260 LIAs, and experiment control was facilitated by LabVIEW.

Fieldlike SOT harmonic response derivation

First, we derive an expression which expresses the contribution to $R_H^{2\omega}$ due to the FL SOT, which is the SOT that may be parameterized as an effective field $H_{FL}\hat{y}$, where the y coordinate is perpendicular to the current as shown in Fig. 2.7(a). The magnetization $\hat{\boldsymbol{m}}$ orientation in the xy-plane is given by angle γ, defined in the same way as ϕ (i.e. if $\hat{\boldsymbol{m}}$ is saturated parallel to H $\gamma = \phi$). The total magnetic field is given by

$$\boldsymbol{H}_t = H\sin\phi\hat{x} - H\cos\phi\hat{y} + \tilde{H}_y\hat{y}, \tag{2.9}$$

where $\tilde{H}_y = \tilde{H}_{FL} + \tilde{H}_{Oe}$ is the sum of the ac FL SOT effective field and the ac Oersted field created by the current in N. Any in-plane magnetocrystalline anisotropy field H_k is ignored in Eq. 2.9, which is valid for $H \gg H_k$. As all frequencies are low, the instantaneous orientation of the magnetization is given by the magnetostatic condition $\hat{\boldsymbol{m}} \parallel \boldsymbol{H}_t$. Then, solving for α we have

$$\alpha = \arctan\Big(\frac{\sin\phi}{\cos\phi - \tilde{\zeta}}\Big), \tag{2.10}$$

where we have introduced the dimensionless parameter $\tilde{\zeta} \equiv \tilde{H}_y/H$. The Hall resistance R_H is sensitive to the orientation of the magnetization in the xy plane through the planar Hall effect (PHE)[58], which may be expressed as

$$R_H = R_{PHE}\sin 2\alpha, \tag{2.11}$$

where R_{PHE} (e.g. in Ohms) accounts for the magnitude and sign of the PHE resistance. Substituting Eq. 2.10 into Eq. 2.11, and Taylor expanding in powers of $\tilde{\zeta}$ we get

$$R_H = R_{PHE}\Big\{\sin 2\alpha + (\sin 3\alpha - \sin\alpha)\tilde{\zeta} + O[\tilde{\zeta}^2] + ...\Big\}. \tag{2.12}$$

In the first term within the brackets in Eq. 2.12 we have recovered the ordinary PHE, and the following terms represent higher order nonlinear Hall resistances present for nonzero $\tilde{\zeta}$. All but the $\tilde{\zeta}$-linear term may be dropped for $\tilde{H}_y \ll H$. Finally, we express the Hall voltage $V_H = R_H I\sin\omega t$ as a function of time explicitly by substituting $\tilde{H}_y = H_y\sin\omega t$ into Eq. 2.12, which gives

$$V_H(t) = I\sin\omega t R_{PHE}\Big\{\sin 2\alpha + (\sin 3\alpha - \sin\alpha)\frac{H_y\sin\omega t}{H}\Big\}. \tag{2.13}$$

The lockin amplifier referenced shown in Fig. 2.7(b) recovers the root-mean-square (RMS) amplitude of $V_H(t)$ at the reference frequency 2ω. Carrying out some algebra we get

$$R_H^{2\omega} = \frac{\langle V_H^{2\omega,Y} \rangle_{RMS}}{\langle I \rangle_{RMS}} = -\frac{1}{2} R_{PHE} \frac{H_{FL} + H_{Oe}}{H} (\sin 3\phi - \sin \phi), \tag{2.14}$$

where we have substituted $\alpha = \phi$ which is appropriate for $H \gg H_{FL} + H_{Oe}$, and the brackets denote the RMS amplitude of the time-varying voltage or current. The factor of $-1/2$ in Eq. 2.14 arise from the trigonometric identity $\sin^2 \omega t = (1/2)(1 - \cos 2\omega t)$, as the 2ω lockin Y-quadrature signal is proportional to $\cos 2\omega t$. Figure 2.8 shows example plots of Eq. 2.14 vs ϕ. Equation 2.14 represents the main result of this section.

DL SOT harmonic response derivation

Next, we derive an expression expressing the contribution to $R_H^{2\omega}$ due to the DL SOT, which is the SOT that may be parameterized as an effective field $H_{DL} \sin \phi \hat{z}$, where the z coordinate is perpendicular to the current and normal to the bilayer plane as shown in Fig. 2.7(a). The DL SOT rotates the magnetization out of the bilayer plane, which for in-plane magnetized films is opposed by the out-of-plane anisotropy field $H_d \sin \theta \hat{z}$, where θ parameterizes the out-of-plane canting of the magnetization (e.g. $\theta = 0^\circ$ for $\hat{\boldsymbol{m}}$ in the xy plane, $\theta = 90^\circ$ for $\hat{\boldsymbol{m}} \parallel \hat{z}$). In the case of a magnetic thin film with negligible perpendicular magnetic anisotropy, H_d is simply the demagnetization field given by $4\pi M_s$ ($\simeq 1.5T$ for these films). The total magnetic field is

$$\boldsymbol{H}_t = H \sin \phi \hat{x} - H \cos \phi \hat{y} + (\tilde{H}_{DL} \sin \phi - H_d \sin \theta) \hat{z}. \tag{2.15}$$

The condition for θ satisfying the magnetostatic condition $\hat{\boldsymbol{m}} \parallel \boldsymbol{H}_t$ for small θ is

$$\tan \theta \simeq \sin \theta \simeq \theta = \frac{\tilde{H}_{DL} - H_z \theta}{H}. \tag{2.16}$$

The Hall resistance sensitive to the z component of the magnetization is the anomalous Hall effect (AHE), which is given by

$$R_H = R_{AHE} \frac{M_z}{M_s} = R_{AHE} \sin \theta, \tag{2.17}$$

where R_{AHE} parameterizes the magnitude and sign of the AHE. Substituting Eq. 2.16 into Eq. 2.17 for $\tilde{H}_{DL} \ll H_d$ we have

$$R_H = R_{AHE} \frac{\tilde{H}_{DL}}{H + H_d}. \tag{2.18}$$

Substituting the time-dependence $\tilde{H}_{DL} = H_{DL} \sin \omega t$, and solving for the 2ω Hall resistance in identical fashion to Section 2.2.2 one finds

$$R_H^{2\omega} = \frac{\langle V_H^{2\omega,Y} \rangle_{RMS}}{\langle I \rangle_{RMS}} = -\frac{1}{2} R_{AHE} \frac{H_{DL}}{H + H_d} \sin \phi. \tag{2.19}$$

Figure 2.8 shows example plots of Eq. 2.19 vs ϕ, in which the angular dependence is distinct from that given by the FL SOT (Eq. 2.9). Equation 2.19 represents the main result of this section.

Magnetothermoelectric voltages

Because $R_H^{2\omega}$ is in essence a voltage that depends on the square of the current, care must be taken to account for magnetothermoelectric (MTE) voltages, which can arise from Joule heating effects. MTE voltages originate due to a class of thermoelectric emfs that are present for nonzero temperature gradient ∇T. In the geometry used for the MR-HR measurement, the Joule heat created in the bilayer predominantly dissipates into the substrate, creating a $\nabla T \parallel \hat{\boldsymbol{z}}$. The MR-HR measurement is then susceptible to MTE emfs proportional to $\nabla T \times \hat{\boldsymbol{m}}$, which may be caused by the anomalous Nernst effect (ANE) and/or logitudinal spin-Seebeck effect (LSSE)[59–61] and result in 2ω Hall resistances given by

$$R_H^{2\omega} = R_{MTE} \sin \phi, \tag{2.20}$$

where R_{MTE} parameterizes the magnitude of the MTE effect. While the angular dependence of these signals are identical to those due to the DL SOT given by Eq. 2.19, the magnetic field dependence of $R_H^{2\omega}$ allows differentiation. MTE signals are independent of the magnitude of H so long as the magnetization is saturated, while the DL contribution decreases as H increases. In all of our measurements, no contribution proportional to $H \sin \phi$ was detected, implying that the contribution of the ordinary Nernst effect to $R_H^{2\omega}$ was negligible. See Chapter 4 for a detailed study of the ANE and thermoelectric coefficients in thin Heusler films.

MR-HR angular rotations and fitting

As derived in the proceeding sections, the FL and DL SOTs applied at ω give rise to $R_H^{2\omega}$ angular dependencies originating from the PHE and AHE, respectively. In general,

both FL SOTs, DL SOTs, and MTE effects may be present, so that the sum of Eq. 2.14, Eq. 2.19, and Eq. 2.20 is the total 2ω Hall resistance is given by

$$\begin{aligned} R_H^{2\omega}(\phi, H) = & \\ & -\frac{1}{2} R_{AHE} \frac{H_{DL}}{H + H_d} \sin\phi \\ & -\frac{1}{2} R_{PHE} \frac{H_{FL} + H_{Oe}}{H} (\sin 3\phi - \sin\phi) \\ & + R_{MTE} \sin\phi + R_0^{2\omega}, \end{aligned} \tag{2.21}$$

where $R_0^{2\omega}$ is an overall offset, likely due to the Seebeck effect. H_{Oe} is calculated from Ampere's law. Equation 2.21 is valid for $H \gg H_{DL}, H_{FL}$. The applied magnetic field is much larger than the in-plane magnetic anisotropy field ($\sim$ 150 Oe at room temperature) so that the static magnetization may be considered saturated along the applied field direction at all ϕ angles for fields larger than a few kOe. The AHE and PHE resistances were measured on the same Hall bar with low excitation current using conventional transport techniques for each Pt thickness and temperature. The sign of the SOT efficiency corresponds to the sign of the effective field (in a right-handed Cartesian coordinate system) produced by a charge current applied in the $+\hat{x}$ direction shown in Fig. 2.7(a). For example, the positive ξ_{DL} values reflect $\boldsymbol{H}_{DL} \parallel +\hat{z}$ for $\hat{\boldsymbol{m}} \parallel +\hat{x}$, and the negative ξ_{FL} values reflect $\boldsymbol{H}_{FL} \parallel -\hat{y}$ direction, both for current applied in $+\hat{x}$ direction.

Figure 2.8 shows example cases of Eq. 2.21 with ϕ varying over 360°, for different contributions of the DL and FL terms. The FL contribution gives a characteristic curve with 3 minima and maxima, while the DL contribution gives a simple $\sin\phi$ curve with one peak and one minima. All other things being equal, in the bilayers studied in this thesis the FL contribution to $R_H^{2\omega}$ was much smaller than the DL contribution because R_{PHE} was typically a factor of 10 or more less than R_{AHE}. Thus, the combination of the first term of Eq. 2.21 with a smaller second term resulted in either a triangular or square angular-dependence of $R_H^{2\omega}$, depending on the relative signs of the two terms in Eq. 2.21. Both cases are illustrated in Fig. 2.8.

Figure 2.9 shows example MR-HR 360° ϕ-rotations taken on the 8 nm Pt sample, at fixed magnetic field of 1.2 T, for different applied current magnitudes I. The inset illustrates the linear dependence of $R_H^{2\omega}$ on I. (Current dependencies were not performed

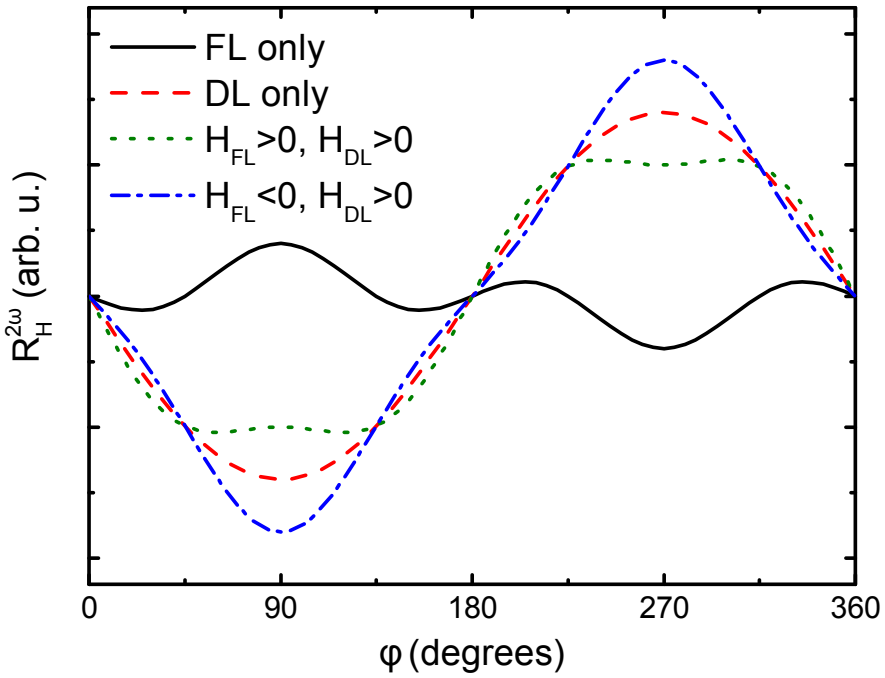

Figure 2.8: Example plots of the second harmonic Hall resistance for 360° ϕ rotations, given by Eq. 2.21. The black solid curve is with H_{DL} set to zero, and the red dashed curve with H_{FL} set to zero. The green dashed curve and blue dash-dot curve are for H_{FL} and H_{DL} of same and opposite sign, respectively. In all the dashed curves, the DL $\sin\phi$ contribution has been set larger than the FL $\sin 3\phi - \sin\phi$ contribution to replicate the experimental conditions for which the DL contribution is dominant.

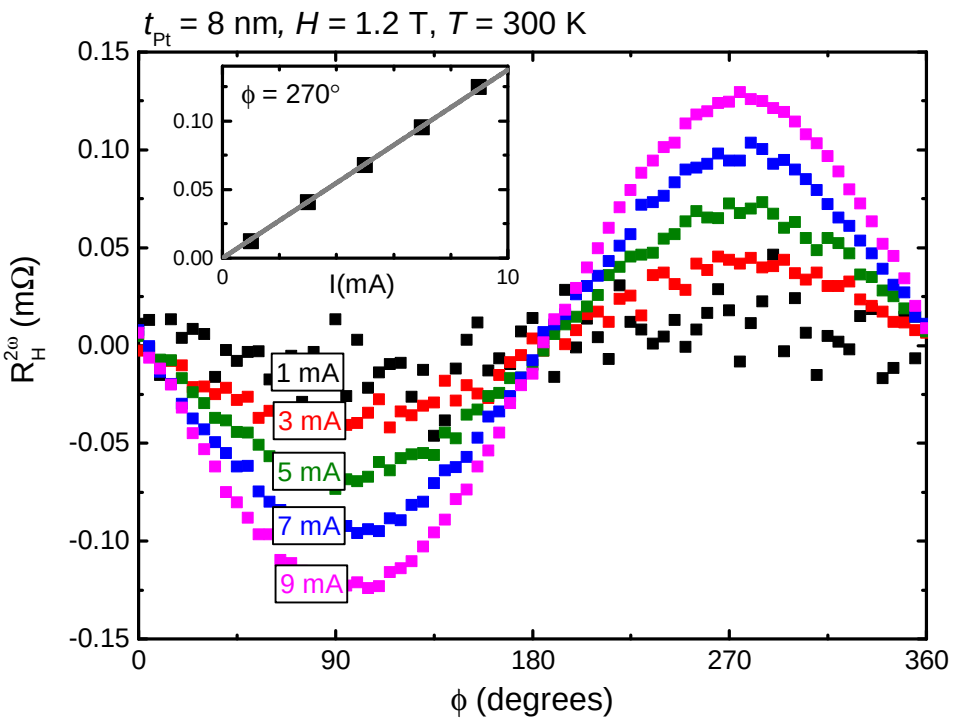

Figure 2.9: Example MR-HR 360° ϕ-rotations, for a fixed magnetic field of 1.2 T and different current amplitudes (indicated on figure). The inset shows the $\phi = 270°$ $R_H^{2\omega}$ value vs current, and the gray solid line is a linear fit with zero intercept.

exhaustively as the 2ω referenced lockin detection method itself guarantees that $R^{2\omega} \propto I$, i.e. voltages that go as the square of the current.) It was found that the use of taut and radial (non-crossing) wire-bonds to twisted pairs for voltage and current leads greatly minimized spurious artifacts in the $R_H^{2\omega}$ data, which likely originated from a coupling between of mechanical movement of wirebonds with Faraday's law voltage pickup, exacerbated by crossed or loose wirebond loops.

Anomalous and planar Hall effect measurements

The AHE and PHE magnitudes defined by Equations 2.17 and 2.11 where obtained at each temperature for each Pt thickness with dedicated measurements. As such, the size, sign, and microscopic origins of the R_{AHE} and R_{PHE} do not systematically influence the values of H_{DL} and H_{FL} extracted by fitting to Eq. 2.21.

The AHE measurement was performed by measuring the Hall resistance R_H using conventional transport techniques (i.e. first harmonic detection) while sweeping an applied out-of-plane magnetic field along z. In this geometry, the Hall resistance is given by

$$R_{xy} = R_{AHE}\left(\frac{M_z}{M_s}\right) + A_{OHE}H_z, \tag{2.22}$$

where A_{OHE} is the ordinary Hall effect slope which is related to the Hall coefficient R_H by $A_{OHE} = R_H/t$, t being the film thickness. For in-plane magnetized films, M_z is proportional to to H_z for fields less than the saturation field ($H_z < H_{sat}$), while for $H_z \geq H_{sat}$ the magnetetization is field-independent and saturated, i.e. $M_z = M_s$. Example AHE data is shown in Fig. 2.10(a), with the fit to Eq. 2.22 showing good agreement. To extract A_{OHE} in these bilayers, the full magnetic field range of the PPMS ($\pm$9 T) was utilized, however for most of the bilayer Hall measurements in this thesis the AHE contribution to R_{xy} was much larger than the OHE contribution, and a field range of $\pm$3 T was adequate to extract R_{AHE}. The PHE measurement was performed by rotating the orientation of an applied magnetic field in the sample plane 360° while recording the Hall resistance R_{xy}, as indicated in the diagram included in Fig. 2.10(b). A sufficiently large magnetic field ($H \simeq 1$ T) was used so that the magnetization was saturated along the applied field at all angles. For these angle rotations, the Hall

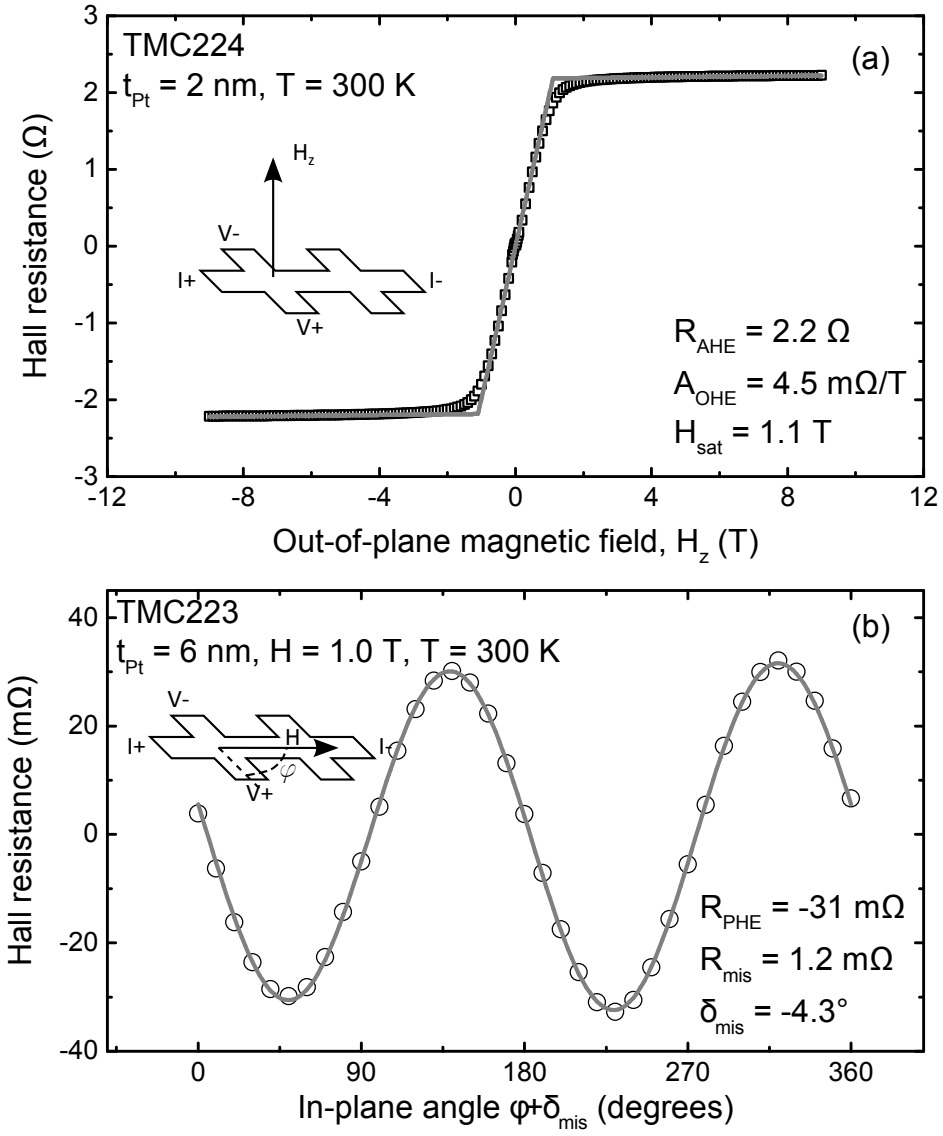

Figure 2.10: (a) Example AHE field sweep data (black squares) with the fit to Eq. 2.22 shown as the gray solid curve. The fit parameters are included in the lower right of the panel. (b) Example PHE angle rotation data (open circles) with the fit to Eq. 2.23 shown as the gray solid curve. The fit parameters are shown in the lower right. In both (a) and (b), a constant offset resistance has been subtracted, which originates due to Hall bar misalignment.

resistance is given by

$$R_{xy} = R_{PHE}\sin[2(\phi + \delta_{mis})] + R_{mis}\cos(\phi + \beta), \tag{2.23}$$

where δ_{mis} allows for small mounting misalignments ($\pm$ few degrees) causing the nominal PPMS rotator angle to differ from ϕ, and the second term accounts for any small component of the field in the out-of-plane direction due to imperfect chip mounting, giving rise to a cosine term with general phase β due to the AHE. Example data taken at 300 K on the 6 nm Pt bilayer and corresponding fit to Eq. 2.23 are shown in Fig. 2.10(b).

2.2.3 SOT efficiencies

The HR-MR measurements, such as the data shown in Fig. 2.8, were fit to Eq. 2.21 to give H_{DL} and H_{FL}, which are the SOT effective magnetic fields resultant from applied current I through the bilayer. To compare SOTs across differing Pt thicknesses and temperatures, a metric must be defined to characterize the strength of the torque exerted on the magnetization by application of current. To this end, we define dimensionless SOT efficiencies as the ratio of the torque to Pt current density,

$$\xi_{DL(FL)} \equiv \frac{M_s t_F H_{DL(FL)}}{(\hbar/2e) j_N^e}, \tag{2.24}$$

where the numerator is the torque per area (areal moment density times field) and the denominator is the Pt current density (e.g. in $\mathrm{A/m^2}$) scaled by $\hbar/2e$ to make the efficiency dimensionless. The efficiency defined by Eq. 2.24 is convenient for analysis discussing the SHE mechanism, as it may be directly compared (or in much literature incorrectly equated) to the N spin-Hall ratio $\theta_{SH} \equiv j^s/j^e$. It should be noted that for SOTs originating from the interface Rashba mechanism, the SOT *field* is fundamental rather than the *torque*, and in addition it is the current "at the interface" rather than the N bulk current density that is the proper normalization factor. However, because the latter current is challenging to define in all-metallic structures, SOTs originating from the Rashba effect have also been characterized by the efficiency defined in Eq. 2.24.

Current shunting considerations

To calculate the factor of j_N^e that appears in the denominator of Eq. 2.24, a parallel-resistor model was assumed for the F/N bilayer. That is, the (directly measurable) square resistance R_{xx} is given by

$$R_{xx}^{-1} = R_F^{-1} + R_F^{-1}, \tag{2.25}$$

where $R_{F(N)} \equiv \rho_{F(N)}/t_{F(N)}$. The current density in N may then be calculated according to the standard current-divider expression

$$j_N^e = \frac{\sqrt{2}I}{t_N}\frac{R_F}{R_F + R_N}, \tag{2.26}$$

where the $\sqrt{2}$ in the numerator converts I from an RMS to a sinusoidal amplitude. To evaluate Eq. 2.26, ρ_F and ρ_N must be known. In the following results section, we will explain how the N and F resistivities are extracted from analyzing the dependence of R_{xx} on N thickness.

In the results section we will wish to consider the influence of bilayer shunting on magnetoresistances (MRs) originating from F alone. To understand show the shorting effect of the N Pt layer influences the measured net MR, we first express the resistance tensors in both N and F as

$$R_F = \begin{bmatrix} R_{xx,F} & R_{xy,F} \\ -R_{xy,F} & R_{xx,F} \end{bmatrix}, R_N = \begin{bmatrix} R_{xx,N} & R_{xy,N} \\ -R_{xy,N} & R_{xx,N} \end{bmatrix}, \tag{2.27}$$

where we have enforced time-reversal symmetry ($R_{xy} = -R_{yx}$) and isotropic transport ($R_{xx} = R_{yy}$). The total resistance tensor R_T is given by adding R_F and R_N in parallel, i.e. $R_T^{-1} = R_F^{-1} + R_N^{-1}$. To simplify we note that $R_{xx} \gg R_{xy}$ for both N and F, and for purpose of this exercise we take $R_{xy,N} = 0$. Carrying out the algebra and simplifying for the transverse (i.e. Hall) total resistance we have

$$R_{xy,T} = \frac{R_{xx,N}^2 R_{xy,F}}{(R_{xx,F} + R_{xx,N})^2}. \tag{2.28}$$

To compare to data, it is most helpful to rearrange Eq. 2.28 by substituting $R_{xx,N}^{-1} = R_{xx,T}^{-1} - R_{xx,F}^{-1}$. We then have

$$R_{xy,T} = \frac{R_{xx,T}^2 R_{xy,F}}{R_{xx,F}^2}. \tag{2.29}$$

It is also straightforward to show for longitudinal MR (e.g. AMR) N shunting also gives rise to $R_{AMR,T} \propto R_{xx,T}^2$.

2.3 Results and interpretation

To study the underlying mechanisms which give rise to the DL and FL SOT, the MR-HR SOT efficiency measurement was performed on Hall bars patterned from TMC223 (1.2 nm CFA/5, 6, 7, and 8 nm Pt) and TMC224 (1.2 nm CFA/1, 2, 3, and 4 nm Pt) heterostructures from 20 K to 300 K. Because the different Pt thicknesses where grown with the shadowmask technique on the same 1.2 nm CFA underlayer, dependencies of the SOT efficiencies on the Pt thickness could be explored while keeping identical ferromagnet and interface properties.

Figure 2.11 summarizes the Pt thickness dependence of various quantities at 300 K and low temperature (20 K). The bilayer square resistance R_{xx} is shown in Fig. 2.11(a), and the DL and FL SOT efficiencies are shown in Fig. 2.11(b). It is clear from Fig. 2.11(a) that R_{xx} is a stronger function of Pt thickness than a thickness-independent Pt resistivity can account for. This is commonly observed in ultrathin metal films, where diffuse surface scattering[62] and/or grain-boundary scattering[63] give rise to increased scattering rates that contribute to the resistivity with a t_N^{-1} scaling. The R_{xx} data in Fig. 2.11(a) has been fit to a model in which the CFA resistance is constant, and the Pt resistivity is given by $\rho_N = \rho^b + At_N^{-1}$, where ρ^b is the bulk Pt resistivity. The fit is shown in the inset of Fig. 2.11(a), in which the Pt resistivity is plotted vs t_N^{-1} for clarity.

Turning to the SOT efficiencies shown in Fig. 2.11(b), it is observed that both ξ_{DL} and ξ_{FL} monotonically decrease in magnitude as the Pt thickness is increased. When interpreting the SOT efficiency data shown in Fig. 2.11(b), the dependence of the Pt resistivity on thickness should be kept in mind. ξ_{DL} is larger in magnitude than ξ_{FL}, and decreases more gradually and steadily than ξ_{FL} as t_N is increased. In contrast, ξ_{FL} drops sharply as t_N is increased above 1 nm, and appears to saturate for t_N greater than 4 nm. The SOT efficiencies were characterized as a function of temperature as well as Pt thickness. See Fig. 2.11(b) for FL and DL efficiency data at 300 K and 20 K, and Fig. 2.14 for ξ_{DL} and ξ_{DL} values as function of temperature for selected Pt thicknesses. Both DL and FL efficiencies decrease in magnitude as temperature is decreased for

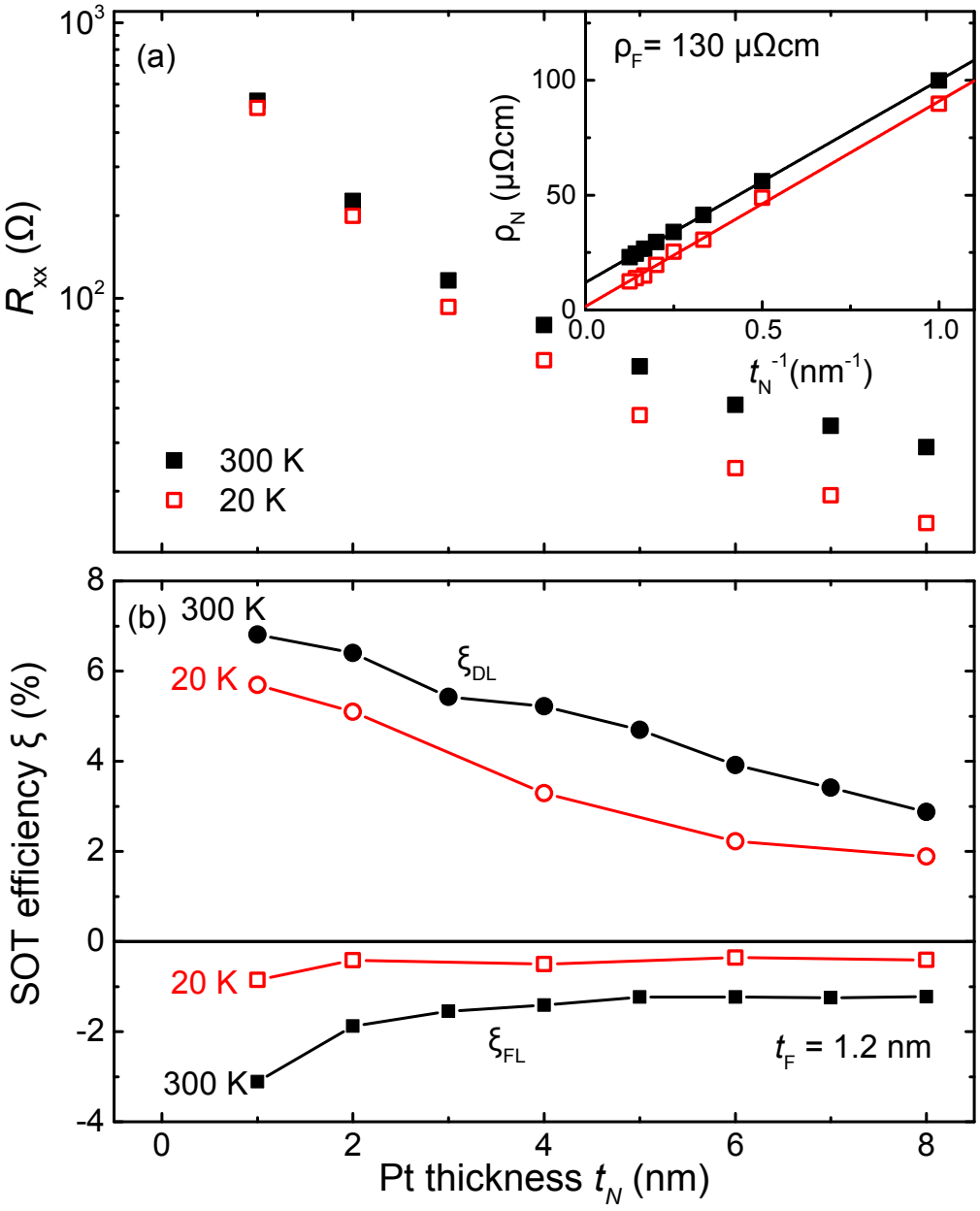

Figure 2.11: (a) The bilayer square resistance for all Pt thicknesses. The solid black squares are 300 K data and open red squares are 20 K data. In the inset, the Pt resistivity is plotted vs the inverse of the Pt thickness. The intercepts of the solid lines correspond to the bulk resistivity of Pt. In (b), the SOT efficiencies ξ_{DL} (circles) and ξ_{FL} (squares) are shown for different Pt thicknesses at 300 K (black solid symbols) and 20 K (red open symbols). The lines connect data points. For all data the CFA thickness is 1.2 nm.

all Pt thicknesses. In the case of ξ_{DL}, the temperature dependence becomes stronger as Pt thickness is increased, and is nearly temperature-independent for the lowest Pt thickness ($t_N = 1$ nm). In comparison, ξ_{FL} decreases by a factor of 3-4 as temperature is decreased from 300 K to 20 K for all Pt thicknesses.

2.3.1 Observation of the magnetic proximity effect through magnetoresistance measurements

In these bilayers, the anomalous Hall effect and the anisotropic magnetoresistance (AMR) were measured from 10 K to 300 K for all Pt thicknesses. See Fig. 2.10(a) for an example R_{AHE} measurement, and Fig. 2.12(a) for an example R_{AMR} measurement, which are described in Sec. 2.2.2. Note that the geometry used in Fig. 2.12(a) used to extract R_{AMR} was chosen so that magnetoresistances (MRs) due to recently reported spin-Hall MR (SMR)[64–67] could be differentiated and did not influence the R_{AMR} values extracted. That is, R_{AMR} represents the traditional AMR effect discussed in the classic review article by McGuire and Potter[58].

The MR behaviors we identify are best summarized by plotting the MR vs R_{xx}, in which temperature is the implicit variable. The dependence of R_{AHE} and R_{AMR} on R_{xx} is summarized in Fig. 2.12(b) for the different Pt thicknesses, in which temperature was varied between 10 K (low R_{xx}) and 300 K (high R_{xx}). To understand the data in Fig. 2.12(b), we must first discuss the simplest means by which extraordinary or anomalous[2] MR can appear in F/N bilayers. For all-metallic F/N bilayers, nonzero MR is typically measured because of the fraction of the current shunted through the F layer. The F and N layer may be thought of as parallel resistances through Eq. 2.29.[3]

In measurements of stand-alone thicker CFA films (growths TMC249-252), we have found that the resistivity $\rho_F \simeq 100$ $\mu\Omega$cm, and is nearly temperature independent with residual-resistivity ratios (RRRs) $\simeq$ 1.1. Then, for thinner 1.2 nm CFA films we can approximate $R^F_{xx} = \rho_F/t_F$ in Eq. 2.29 as as a temperature-independent quantity and expect MRs that originate due to F shunting to scale as R^{-2}_{xx}. (Note that the preceding statement is valid if and only if R^F_{MR} is independent of temperature.) In the case of the

[2] Historically, these adjectives have been used to describe MRs which depend on the magnetization rather than the applied magnetic field.

[3] Although, where mean-free paths are comparable to the layer thicknesses the parallel resistor model is no longer strictly valid.

AHE, we have verified for the TMC249-252 CFA films $R_{AHE} \propto (R_{xx}^F)^2$, as is commonly reported for the intrinsic or side-jump AHE mechanisms. The temperature variation of R_{xx}^F ($\mathrm{RRR}_F \leq 1.1$ for the 1.2 nm CFA) would then lead to a cancellation in the numerator and denominator of Eq. 2.29 and R_{AHE} would still scale as R_{xx}^2.

In Fig. 2.12(b), we have indicated the trends that would be expected *if the MR originated from F shunting alone* with the dashed trendline, which is predicted by Eq. 2.29. However, upon inspection it is clear that both the R_{AHE} and R_{AMR} data trend above Eq. 2.29; in fact, the R_{AMR} data even *increase* as R_{xx} decreases at low temperature for all Pt thicknesses. Thus, we conclude that significant fractions of the AHE and AMR resistances measured in these bilayers do not originate due to F shunting, and the excess fraction *increases* as temperature is decreased. Surely, a significant fraction of the MRs shown in Fig. 2.12(b) do originate from F shunting. (However, we note that for 5 nm CFA films R_{AMR} is opposite in sign to these R_{AMR} measurements in the CFA/Pt bilayers.) Because independent characterization of the AHE and AMR MRs in an ultrathin 1.2 nm CFA film is challenging, it is difficult to make more quantitative statements than these.

We attribute the excess MR fraction that increases as temperature is decreased (and hence cannot be attributed to F shunting) to a proximity magnetized Pt layer. The band structure of Pt, a 5d transition metal, is close to satisfying the Stoner criterion for bulk ferromagnetism. Reports of magnetic proximity effects (MPE) have been ubiquitous in studies of F/Pt bilayers[68–71], and the MPE in ferromagnet insulator(i.e. Yttrium iron garnet)/Pt bilayers has been shown to give rise to proximity-induced extraordinary MRs[69, 72–74]. The enhancement in the *sd* exchange interaction at the F/Pt interface mediated by the F layer can induce a magnetic moment in Pt near the interface. (In fact, nanoparticles and ultrathin films of Pt can possess static moments due to changes in the DOS from finite size effects, even in the absence of an adjoining F layer[75–77].) X-ray magnetocircular dichroism (XMCD) studies have shown that a nonzero moment density (some tenths of a μ_B per Pt atom) is induced in the first few Angstroms of Pt adjoining the F layer[78]. Also, several studies of the MPE in F/Pt bilayers have shown a temperature dependence[69, 70, 73, 79] with stronger MPEs at low temperature. Our AHE and AMR measurements support an MPE that increases significantly at low temperature. In the following section, where the SOT efficiency data is discussed, we

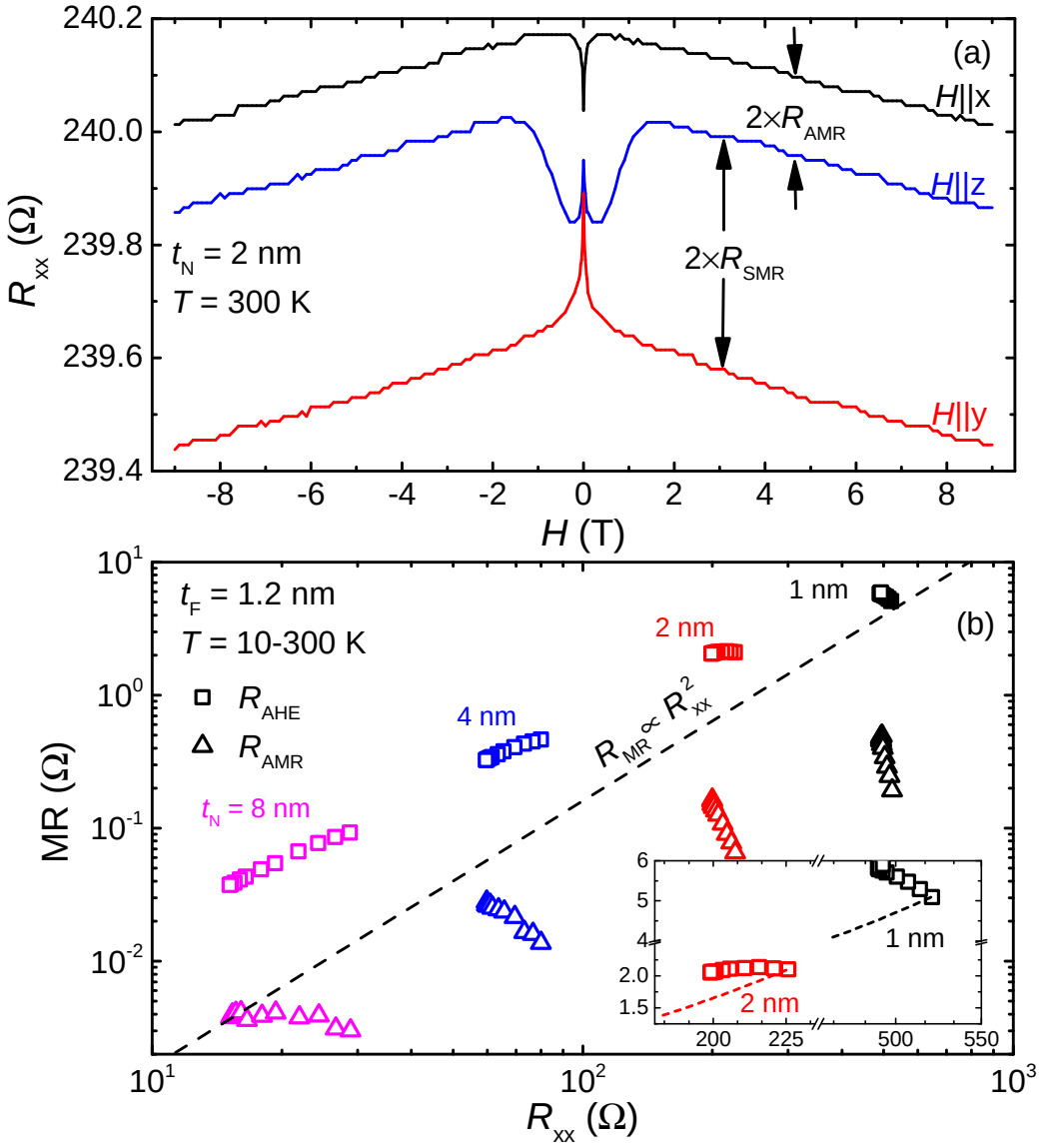

Figure 2.12: (a) Example magnetic field sweeps used to extract R_{AMR}, which is indicated on the figure as the difference in R_{xx} with magnetization saturated along x and z axes. Also indicated is the SMR magnitude R_{SMR}. The conditions for the data in (a) are indicated in the upper left (taken on the TMC224 heterostructure). (b) Summary plot of the dependence of MR magnitudes R_{AHE} (squares) and R_{AMR} (triangles) vs R_{xx} for different Pt thicknesses, in which temperature is the implicit variable and was varied over the range 10-300 K. In all cases low temperature corresponded to low R_{xx} and high temperature high R_{xx}, except for the 1 nm Pt bilayer for which R_{xx} exhibited a slight upturn below 20 K. The dashed line indicates a power law $R_{MR} \propto R_{xx}^2$. The inset magnifies the $t_N = 1, 2$ nm AHE data for clarity.

will consider the influence of the MPE on the SOTs present in the system.

2.3.2 Platinum thickness dependence of the dampinglike and fieldlike SOT efficiencies

We now turn to discussing the DL and FL SOT efficiency data on the epitaxial Pt/CFA/MgO structures (growths TMC223, TMC224) summarized in Fig. 2.11(b) and Fig. 2.14. The magnitudes we observe, which for the different Pt thicknesses and temperatures are in the few percent range, are typical of values reported for F/Pt bilayers[11, 55, 80]. However, because of differences in bilayer materials, growth techniques, and measurement techniques, rather than making detailed comparison to literature ξ values we will focus on implications of the measured Pt thickness and temperature trends for the underlying SOT mechanisms.

First, we discuss the DL SOT efficiency ξ_{DL}. In F/N bilayer SOT literature, N thickness dependencies of ξ_{DL} have been widely used to interpret magnitudes through perpendicular-to-plane spin diffusion models[11, 81, 82], which invoke the N bulk SHE as the spin current source. These diffusion models predict SOT efficiencies are determined by the N θ_{SH} through the expressions[49, 83]

$$\begin{aligned}\xi_{DL} &= \theta_{SH} Re\left[\frac{2G_{\uparrow\downarrow}\tanh(t_N/2\lambda)}{(\rho_N\lambda)^{-1}+2G_{\uparrow\downarrow}\coth(t_N/\lambda)}\right],\\ \xi_{FL} &= \theta_{SH} Im\left[\frac{2G_{\uparrow\downarrow}\tanh(t_N/2\lambda)}{(\rho_N\lambda)^{-1}+2G_{\uparrow\downarrow}\coth(t_N/\lambda)}\right],\end{aligned} \tag{2.30}$$

where $G_{\uparrow\downarrow}$ is the complex F/N interface spin mixing conductance, which parameterizes the spin-dependent reflection and transmission coefficients for carriers incident on the F/N interface. Eq. 2.30 stipulate that SOT efficiencies are determined by the N bulk θ_{SH} value, and monotonically increase with increasing t_N and saturating at a thickness set by the N spin diffusion length λ. Physically, Re($G_{\uparrow\downarrow}$), which sets ξ_{DL}, accounts for carrier spin-flipping upon transmission across or reflection from the F/N interface, while Im($G_{\uparrow\downarrow}$), which sets ξ_{FL}, accounts for a precession of finite phase of carriers' spin orientation upon reflection from the F/N interface.

At first glance, the data shown in Fig. 2.11(b) show the opposite Pt thickness trend to that predicted by Eq. 2.30. Both ξ_{DL} and ξ_{FL} monotonically *decrease* as t_N increases.

The Cornell group[11] measured a similar behavior, but emphasized that all the parameters of Eq. 2.30 are not fixed when the N resistivity is a strong function of thickness. They observed a similar steady decrease in ξ_{DL} upon increasing Pt thickness above 2-3 nm, which they showed could be attributed to dependence of θ_{SH} on Pt resistivity for the intrinsic SHE mechanism. For the intrinsic SHE, $\theta_{SH} = \sigma_{SH}\rho$ where σ_{SH}, the SH conductivity, is the fundamental (resistivity-independent) material parameter rather than the oft-reported θ_{SH}. Thus, for Pt films where ρ is a strongly decreasing function of Pt thickness (which is the case in our films as shown by the inset of Fig. 2.11(a)), the ξ_{DL} and ξ_{FL} behaviors predicted by Eq. 2.30 will decrease as Pt thickness increases even though the tanh and coth functions are saturated to unity. Furthermore, Nguyen et al.[11] have advocated for a relation where $\lambda = A\rho^{-1}$, as would be appropriate for the Elliot-Yafet (EY) mechanism of spin relaxation[27, 28] with EY material constant A. If the EY relation holds, λ may continue to decrease as ρ increases for thinner films, which effectively prevent the observation of a downturn in ξ predicted by Eq. 2.30 for $t_N < \lambda$. While a growing body of evidence implies the intrinsic SHE is dominant in Pt [11, 42, 84](and the relation $\theta_{SH} = \sigma_{SH}\rho$ is appropriate), one should recognize that the factor of ρ alone in the denomenator of Eq. 2.30 would cause a decrease in ξ as ρ decreases with increasing t_N.

To highlight the challenges with fitting ξ vs t_N data to models like Eq. 2.30, we have fit the 300 K ξ_{DL} data to three models for the parameters θ_{SH} and λ. The first model, hereafter referred to as model 1, is that advanced by Nguyen et al.[11] in which $\theta_{SH} = \sigma_{SH}\rho$ and $\lambda = A\rho^{-1}$. Model 2 also assumes the intrinsic SHE relation $\theta_{SH} = \sigma_{SH}\rho$, but has a fixed ($\rho$-independent) spin diffusion length. Finally, in model 3 both θ_{SH} and λ are taken as fixed quantities. The model 1-3 best-fits to the 300 K ξ_{DL} data are shown in Fig. 2.13, and the corresponding fit parameters listed in Table 2.1. For all fits we have taken $\mathrm{Re}(G_{\uparrow\downarrow}) = 10^{15}\ \Omega^{-1}m^{-2}$, which is typical for metallic F/N bilayers[85]. While the fit parameter results in Table 2.1 are dependent on the exact value of $G_{\uparrow\downarrow}$, the qualitative results we draw are unchanged so long as $\mathrm{Re}(G_{\uparrow\downarrow})$ is within a factor of two of $10^{15}\ \Omega^{-1}m^{-2}$. Also, t_N was allowed to deviate from the as-grown thickness by δ, to account for the few-Angstrom thickness of the MPE Pt layer.

The fits to models 1-3 shown in Fig. 2.13 can be seen to all describe the measurement results reasonably well. The "degeneracy of models" in their ability to describe the data

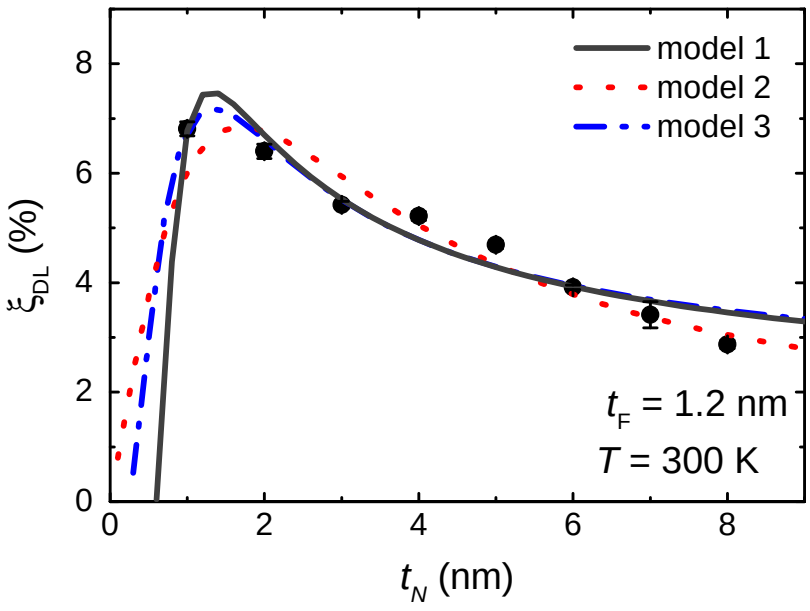

Figure 2.13: The 300 K ξ_{DL} data with best fit curve shown for models 1, 2, and 3 as the solid black, dashed red, and dash-dot blue curves respectively. The corresponding parameters are listed in Table 2.1.

model	θ_{SH}	λ	δ(nm)
1	0.21	0.4 nm	0.2
2	$\sigma_{SH} = 3.4 \times 10^{-3}$	1.4 nm	0.0
3	$\sigma_{SH} = 3.6 \times 10^{-3}$	$A = 0.36$	0.6

Table 2.1: Best-fit parameters for models 1, 2, and 3. The spin-Hall conductivities σ_{SH} are in units of $\mu\Omega^{-1}\text{cm}^{-1}$ and Elliot-Yafet constant A in units of $10^2\mu\Omega$cm nm.

makes deciphering which model, if any, appropriately describes the underlying physics of the DL SOT impossible within the context of our data. In the case of data such as that shown in Ref. [11] or Ref. [81], an increase in the SHE metric is observed as Pt thickness is increased, lending some credence to a fit of a diffusion length. In the case of our bilayers, it appears that any relevant spin diffusion length is less than 1.0 nm, if the SHE diffusion model does reflect the underlying physics. We should emphasize that the fit parameters shown in Table 2.1 may not be physically meaningful, but rather are presented as a cautionary tale to highlight that nearly *any* conceivable N thickness dependence of SOTs can be fit to the model, with certain assumptions. This type of fitting has been performed rampantly in recent years of SOT literature, and the over-interpretation of perhaps meaningless fit parameters may be hampering the progress of the field. In addition, in metallic F/N bilayers systematic errors in calculating SOT efficiencies (which are sometimes reported as effective θ_{SH} values) at single-nm Pt thicknesses become large, because the fraction of current shunting through F must be accurately known to calculate the j_N^e in the denominator of Eq. 2.24. In some cases, thickness independent[81] or witness film[11] F and N resistivities have been used to calculate current shunting, which may be a grossly inaccurate approach in ultrathin films, where interface scattering is dominant.

In the discussion above, we have focussed on interpretation of the DL SOT efficiency with SHE diffusion models because DL SOTs have been widely attributed to N bulk SHE[11, 38, 80, 86], while the FL contribution is attributed to the F/N interfacial SOI[37, 86] (i.e. the Rashba interaction). Because the ξ_{FL} data shown in Fig. 2.11(b) show a qualitatively different Pt thickness dependence and temperature dependence when compared to ξ_{DL}, we believe it is likely their origins are distinct. In the following section, where the temperature dependence of the SOT efficiencies are discussed, we will discuss the ξ_{FL} at greater length.

2.3.3 Temperature dependence of the dampinglike and fieldlike SOT efficiencies

Now, we turn to discuss the temperature dependence of the SOT efficiencies, which are summarized at 300 K and 20 K in Fig. 2.11(b) and shown explicitly as functions of temperature in Fig. 2.14. In particular, we will discuss the implications of the MPE

discussed in Section 2.3.1 for the temperature-dependent SOT efficiency results.

First, we discuss the DL SOT efficiency. In the previous section, we described how, if attributed to the N bulk SHE, the t_N dependence of ξ_{DL} could be adequately described through Eq. 2.30 by several phenomenologies that all crudely result in ξ_{DL} scaling with the Pt resistivity ρ_N. When examining Fig. 2.14, it can be seen that ξ_{DL} follows ρ_N for a given thickness quite closely over the entire temperature range. For the thinnest $t_N = 1$ nm film, T-independent interface scattering dominates the value of ρ_N, and the RRR is near unity. Correspondingly, a weak temperature dependence of ξ_{DL} is observed. In contrast, for a thicker (e.g. $t_N = 6$ nm) film, where the interface scattering contribution to the ρ_N is less dominant, both ρ_N and ξ_{DL} decrease by nearly a factor of two from 300 K to low temperature. This behavior fits with the prediction of any of models 1-3 discussed in Section 2.3.2. So, the T-dependence of ξ_{DL} is consistent with, but agnostic between, the models 1-3 SHE parameter phenomenologies.

In contrast to ξ_{DL}, the FL SOT efficiency ξ_{FL} shows a steady decrease as temperature is decreased, with a relative suppression by a factor between 3 and 4 for all Pt thicknesses from 300 K to 20 K. For instance, in Fig. 2.14 for the $t_N = 1$ nm bilayer ξ_{FL} varies from above 3% at 300 K to below 1% at 20 K, while both ξ_{DL} and ρ_N are relatively T-independent. We note that a similar behavior of ξ_{FL} was reported in a study of SOTs in annealed CoFe/Pt[83] bilayers, for which the authors offered no explanation.

We believe that the T-dependence of ξ_{FL} is intimately related with the increase of the MPE at low temperatures. In the discussion that follows below, we will explain why the FL SOT only is influenced by the MPE, and not the DL SOT. As we have stated, we attribute the FL SOT primarily to the F/N interface Rashba effect rather than the Pt bulk SHE (through nonzero $\mathrm{Im}(G_{\uparrow\downarrow})$ in Eq. 2.30). Numerous other literature reports have also concluded that the FL SOT cannot be attributed to the N SHE alone[11, 82, 87–89]. Later in this section, we will discuss how the presence of the MPE could modify $\mathrm{Im}(G_{\uparrow\downarrow})$ to explain our data in the picture where the Pt bulk SHE gives rise to the FL SOT. Of course, it is certainly possible that ξ_{FL} we measure is the combined effect of an interface Rashba SOI contribution and the Pt SHE contribution. Unfortunately, any quantitative analysis that assumes a sum of two contributions is intractable and poorly constrained, so we will focus on describing qualitative explanations of the influence of the MPE on each mechanism.

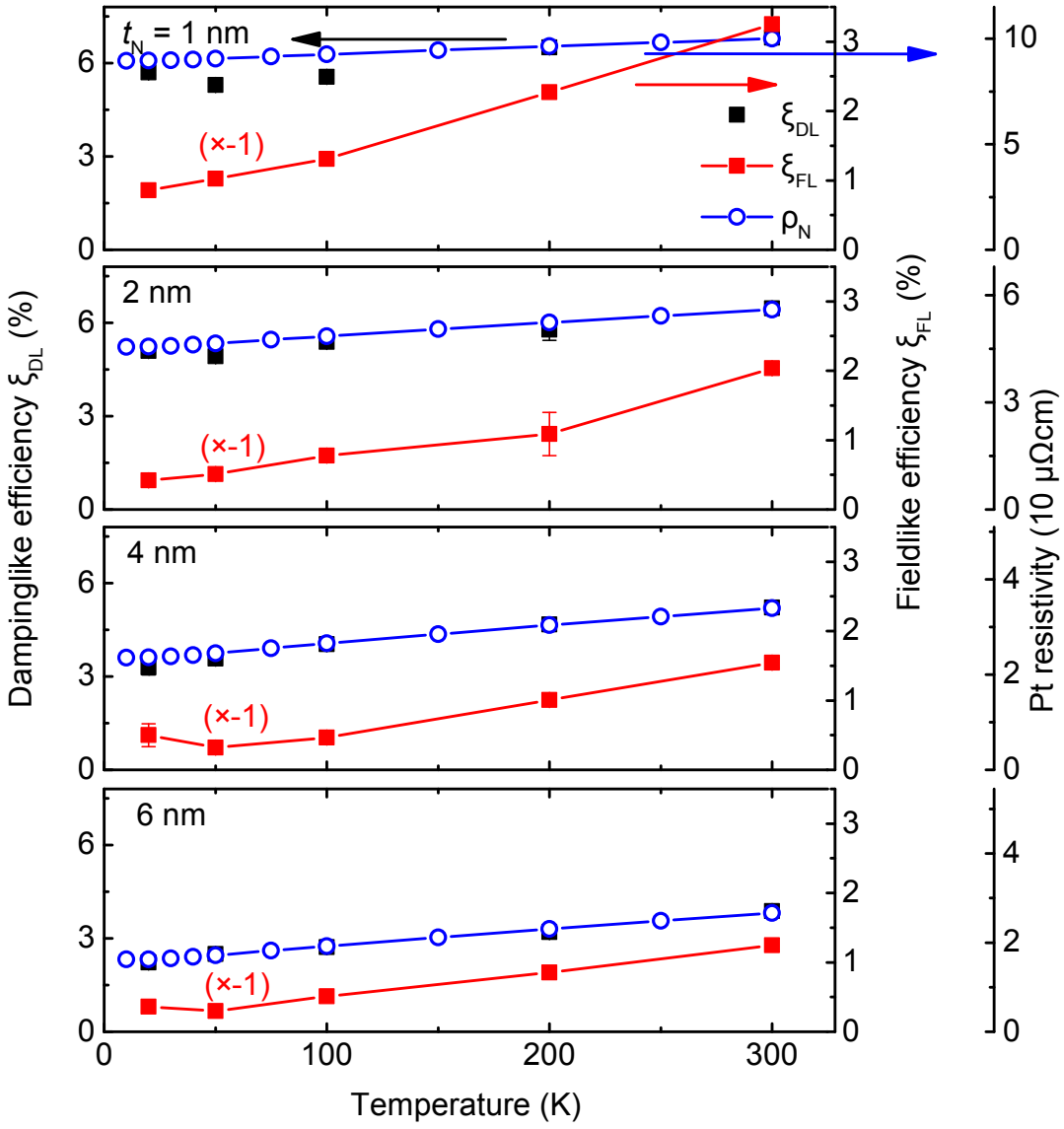

Figure 2.14: Temperature dependence of the DL (black squares, left ordinate) and FL (red squares, right ordinate 1) SOT efficiencies and Pt resistivity (blue circles, right ordinate 2) for the different Pt thicknesses indicated on the figure. The ξ_{FL} data have been scales by -1 for clarity. The lines (where drawn) connect data points.

Here, we propose a simple explanation of MPE-related suppression of the Rashba SOT to explain the temperature-dependent ξ_{FL} data. The FL component of the SOT originates from the exchange interaction between a Rashba-induced spin accumulation in N and the F magnetization[87, 88], that is

$$\boldsymbol{\tau}_{FL} = U_{ex}(\hat{\boldsymbol{m}} \times \boldsymbol{S}_R) \tag{2.31}$$

where U_{ex} is the exchange interaction between the F/N interface Rashba spin polarization $\boldsymbol{S}_R$. Via Eq. 2.31 it is clear that the maximal torque configuration in absence of the MPE is when the F magnetization $\hat{\boldsymbol{m}}$ and $\boldsymbol{S}_R$ are perpendicular, as drawn in Fig. 2.15(a). We propose that in the presence of the MPE, $\boldsymbol{S}_R$ undergoes efficient transverse dephasing when $\hat{\boldsymbol{m}}$ and $\boldsymbol{S}_R$ are perpendicular, due to the presence of the MPE exchange field parallel to $\hat{\boldsymbol{m}}$. This is illustrated in Fig. 2.15(b). Perhaps counter-intuitively, at low temperatures where moments in N and F are strongly coupled, ξ_{FL} decreases because the exchange interaction extends into N and destroys the spin accumulation responsible for the FL SOT. The physics of the MPE suppression of the FL SOT may not be captured by existing models, which assume an interface delta function exchange coupling between the F and N moments[49, 90] rather than a spatially nonuniform MPE exchange interaction extending a finite thickness into N. It may be that a more appropriate model for the effect we propose considers a T_2-like spin relaxation induced by the nonuniform MPE exchange field, similar to what has been developed for nuclear hyperfine interactions in GaAs[91]. We note that in several other studies[92–94] the FL SOT has been observed to increase with temperature in bilayers with Ta and W as the N metal, which are not believed to support MPEs. It is not clear if the FL SOTs presented in Refs. [92–94], and their temperature-dependencies, are due to the same mechanisms as those presented in this chapter.

To motivate the possibility of a MPE-induced transverse dephasing of Rashba spin accumulation, we must discuss the history of the Rashba effect, which was first introduced as a novelty of broken inversion symmetry semiconductor quantum wells for which the itinerant electronic transport is confined to two dimensions[26, 32]. In purely 2D Rashba systems, current j and S_R are one-to-one related. That is, no spin relaxation rate enters the expression determining S_R for a given j. Mathematically, introducing the Rashba effect as a current-driven source in a diffusion-relaxation equation is *not*

appropriate; rather we should write $S_R = U_R j$[48, 95]. Notice that because neither an electron or spin relaxation time enters the expression for S_R, considering the influence of an MPE-induced transverse dephasing time is problematic. The quandary can be reconciled, however, in metallic F/N bilayers by realizing carriers are not confined *to the interface* but rather scatter *off the interface*. The Rashba interaction, which exists only at the F/N interface, is better thought of in metallic (unconfined) systems as a current-driven pump of spin current into the bulk system. Then, in metallic F/N bilayers spin relaxation rates must enter into the expression for Rashba spin accumulations (and torques). The influence of N spin relaxation on the Rashba FL SOT is demonstrated in calculations by Amin and Stiles[96], who show a decrease for N thicknesses larger than a spin diffusion length.[4]

We note that, in principle, the anisotropic nature of the proposed dephasing process may modify the angular dependence of the FL SOT contribution harmonic response measurement described in Section 2.2.2. This modification is discussed at length in the Supplemental Material of Ref. [97], which is included in Appendix E.2 of this thesis for convenience. The end result is that within the fitting uncertainty of our measurement we cannot resolve if the anisotropic transverse dephasing modifications are reflected in our data. In any case, the small modifications to the angular dependence of the FL SOT harmonic response would not alter our critical observation, which is the suppression of the FL SOT at low temperatures.

In the discussion above, we have attributed the ξ_{FL} to the F/N Rashba interaction. Here, we briefly discuss the alternative picture of the FL SOT which invokes the N SHE through $\mathrm{Im}(G_{\uparrow\downarrow})$. Physically, a nonzero $\mathrm{Im}(G_{\uparrow\downarrow})$ refers to incomplete absorption of SHE-generated spin current incident on M. The component of the reflected spin current orthogonal to the incident spin current then corresponds the FL SOT contribution, by conservation of angular momentum. When interpreting the ξ_{FL} data shown in Fig. 2.14 within this picture, the implication would be that $\mathrm{Im}(G_{\uparrow\downarrow})$ grows pseudo-linearly with increasing temperature, and is nearly negligible at low temperatures of 20 K. In fact, this phenomenology may also be argued to originate due to the influence of the MPE. The presence of the MPE at low temperatures may effectively increase the thickness of the F layer, which increases the likelihood of complete dephasing upon reflection

[4] Discussed in private communication with V. P. Amin.

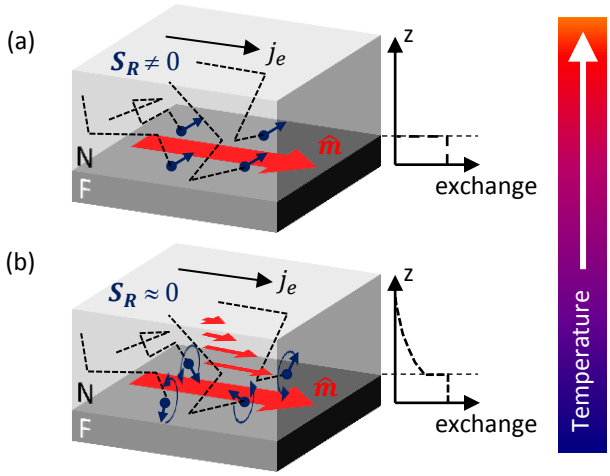

Figure 2.15: Cartoon illustrations of the influence of the MPE on the Rashba spin accumulation, shown with the blue arrows. The magnetization is shown as the red arrow. In (a), meant to illustrate high temperatures in absence of the MPE, the exchange interaction quickly drops to zero upon entering the N metal. In (b), meant to illustrate the MPE at low temperatures, the exchange interaction is finite in the N layer, which causes precessional dephasing of the Rashba spin accumulation.

(decreasing Im($G_{\uparrow\downarrow}$)). However, if ξ_{DL} and ξ_{FL} were solely determined by the N SHE through Re($G_{\uparrow\downarrow}$ and Im($G_{\uparrow\downarrow}$), respectively, one would not expect the qualitatively different trends observed in ξ_{DL} and ξ_{FL} in Fig. 2.11(b) when Pt thickness is varied.

2.4 Conclusions

In conclusion, in this chapter we have shown measurements of spin-orbit torques in epitaxial Co_2FeAl/Pt bilayers. The measurements were carried out through magnetoresistive harmonic response techniques, which allow differentiation between the dampinglike and fieldlike spin-orbit torque contributions. We have shown that the dampinglike torque efficiency is proportional to the Pt resistivity, and unlike the fieldlike torque is not influenced by the magnetic proximity effect. We attribute the dampinglike torque to the Pt spin-Hall effect, but have emphasized that the Pt resistivity-dependence of the torque efficiency may not be sufficient to determine the resistivity dependence of the Pt spin-Hall ratio and/or spin diffusion length. In addition, the striking temperature-dependence of the fieldlike contribution has been identified as due to to the influence of the magnetic proximity effect in these bilayers. The temperature-dependent magnetic proximity effect has been identified through the anomalous temperature-dependence of the bilayer anisotropic magnetoresistance and anomalous Hall effect. Identification of the influence of the magnetic proximity effect, which has been ubiquitous in ferromagnet/platinum bilayers, represents a critical contribution to the understanding of spin-orbit torques. The data and interpretation described in this chapter may be found in published article form as Physical Review B **97**, 020403(R) (2018), which is included in full form at the end of this thesis in Appendix E.2 for convenience.

Chapter 3

Damping processes and resonance linewidths in Heusler ferromagnet thin films

Engineering the damping properties of magnetic materials is critical for device applications. Metallic ferromagnets with ultralow damping are desired for efficiency of magnetic switching mechanisms[9]. In addition, understanding the microscopic material properties that determine their intrinsic damping is of fundamental scientific interest. Due to their potential half-metallicity, Heusler compounds have recently attracted much interest as candidate low damping metallic ferromagnets. Understanding the mechanisms by which extrinsic and intrinsic damping contributions arise is crucial for achieving ultralow damping materials. In this chapter, ferromagnetic resonance (FMR) measurements will be presented in which the FMR linewidth is used to extract information regarding the extrinsic and intrinsic damping properties of epitaxial Heusler compound thin films. Linewidth measurements are presented for all principal orientations of the magnetization, allowing a consistent characterization of the intrinsic Gilbert linewidth and extrinsic inhomogeneous and two-magnon linewidth contributions. By characterizing these linewidths, we extract the characteristic disorder lengthscale responsible for two-magnon scattering, which limits the lifetime of the $q = 0$ FMR magnonic state. In addition, the separation of extrinsic and intrinsic contributions has allowed us to observe

the predicted anisotropy of the intrinsic damping constant, which to our knowledge up to this work has never been demonstrated. Finally, for Co_2FeAl films we measure intrinsic damping constants of the order 10^{-4}, which rank near the lowest ever measured for metallic ferromagnets. Complete characterization of all contributions to the FMR linewidth represents significant progress towards the optimization of Heusler compounds as ultralow damping ferromagnetic metals.

3.1 Introduction to ferromagnetic resonance

FMR is a condition in which the magnetization of a ferromagnetic material is driven to precess at its natural resonance frequency. To understand FMR, we remind the reader of the equation of motion governing magnetization dynamics introduced in Sec. 1.2.2, a torque equation known as the Landau-Lifshitz-Gilbert equation

$$\frac{d\boldsymbol{M}}{dt} = \gamma \boldsymbol{M} \times \boldsymbol{H}_t + \frac{\alpha}{M_s} \boldsymbol{M} \times \frac{\partial \boldsymbol{M}}{\partial t}, \tag{3.1}$$

where $\boldsymbol{M} = M_s \hat{\boldsymbol{m}}$ denotes the magnetization vector, $\boldsymbol{H}_t$ is the sum of anisotropy and applied magnetic fields, γ is the gyromagnetic ratio (28 GHz/Tesla for a free electron), and α is the dimensionless Gilbert damping parameter. For typical ferromagnetic systems, α may range from $10^{-1} - 10^{-5}$. We will devote the next section to discussing the material properties that are thought to determine α, but at the moment it can simply be thought of as a phenomenological damping constant. If an ac magnetic field is applied, then on the r.h.s. of Eq. 3.1 $H_t \rightarrow H_t^s + h_{rf} e^{i\omega t}$, where H_t^s is static and h_{rf} denotes the amplitude of an ac magnetic field varying at frequency $\omega \equiv 2\pi f$. The ac magnetic field will result in an oscillatory torque on the magnetization and drive precession about H_t^s. The amplitude of precession is characterized by the dynamic susceptibility $\chi_{ac} \equiv \partial \boldsymbol{M} / \partial h_{rf}$, which is in general a tensor quantity possessing both real and imaginary components. For external magnetic field $H_z \hat{z}$, by guessing harmonic solutions ($M_{x,y} \sim e^{i\omega t}$) to Eq. 3.1 and linearizing for small precession angles, it can be shown that $\chi_{ac}(\omega)$ has a *resonance* condition. That is, χ_{ac} is sharply peaked at a specific ω which we will refer to as the FMR frequency $f_{FMR} = 2\pi\omega_{FMR}$, which is given by the Kittel equation[52]

$$f_{FMR} = \gamma \sqrt{(H_z + (N_x - N_z)M_s)(H_z + (N_y - N_z)M_s)}, \tag{3.2}$$

where the two terms whose product appears inside the square-root are the stiffnesses to perturbation in the $\hat{x}$ and $\hat{y}$ directions, involving the applied field H_z and generalized demagnetization tensor components $N_{x,y,z}$ which account for the presence of shape and/or magnetocrystalline anisotropy discussed in Sec. 1.2.1. Figure 3.1(a) illustrates several example solutions of Eq. 3.2 for typical conditions and geometries achieved in thin-film FMR experiments.

As with any resonant system, finite damping in the equation of motion broadens the peak in χ_{ac} from a δ-function at f_{FMR} to a Lorentzian function of finite width Δf, centered at f_{FMR}. If the drive frequency is varied and $\chi_{ac}(f)$ recorded, Δf contains valuable information regarding the damping of the system. In FMR experiments, more commonly the applied magnetic field H_z is varied for fixed f, rather than vice versa.[1]

Therefore, in this thesis the full-width-half-maximum (FWHM) field width ΔH of the resonance will be discussed more often than the corresponding frequency width Δf. (If desired, Eq. 3.2 can be used with the expression $\Delta f = (df_{FMR}/dH_z)\Delta H$ to convert between field-swept and frequency-swept linewidths.) It can be shown that solving Eq. 3.1 with nonzero α and driving field $h_{rf}e^{i\omega t}$ give solutions for $\chi_{ac} = \chi' + i\chi''$ taking the form of antisymmetric (symmetric) Lorentzian functions for the dispersive real component χ' (absorptive imaginary component χ''), that is,

$$\chi' = A\frac{(\Delta H/2)(H_z - H_{FMR})}{(\Delta H/2)^2 + (H_z - H_{FMR})^2}, \tag{3.3}$$

and

$$\chi'' = A\frac{(\Delta H/2)^2}{(\Delta H/2)^2 + (H_z - H_{FMR})^2}, \tag{3.4}$$

where H_{FMR} is the resonant field satisfying Eq. 3.2 and A is a prefactor.[2] The resonance peaks given by Eqs. 3.3 and 3.4 are plotted in Fig. 3.1(b). The linewidth is determined by the Gilbert damping constant through the relation

$$\Delta H = \frac{2\alpha f_{FMR}}{\gamma}, \tag{3.5}$$

[1] Responses of rf systems are notoriously frequency-dependent due to reflections and standing waves, and so varying the magnetic field is the surest way of enforcing the lineshape measured is due to FMR and not contaminated by a frequency-dependent background.

[2] For the low precession amplitude (linear regime) FMR measurements discussed in this thesis we will only be concerned with the FMR dispersion and linewidth, and the prefactor A is not important (or measured). See Ref. [98], for instance, for a discussion of the quantities that determine the prefactor.

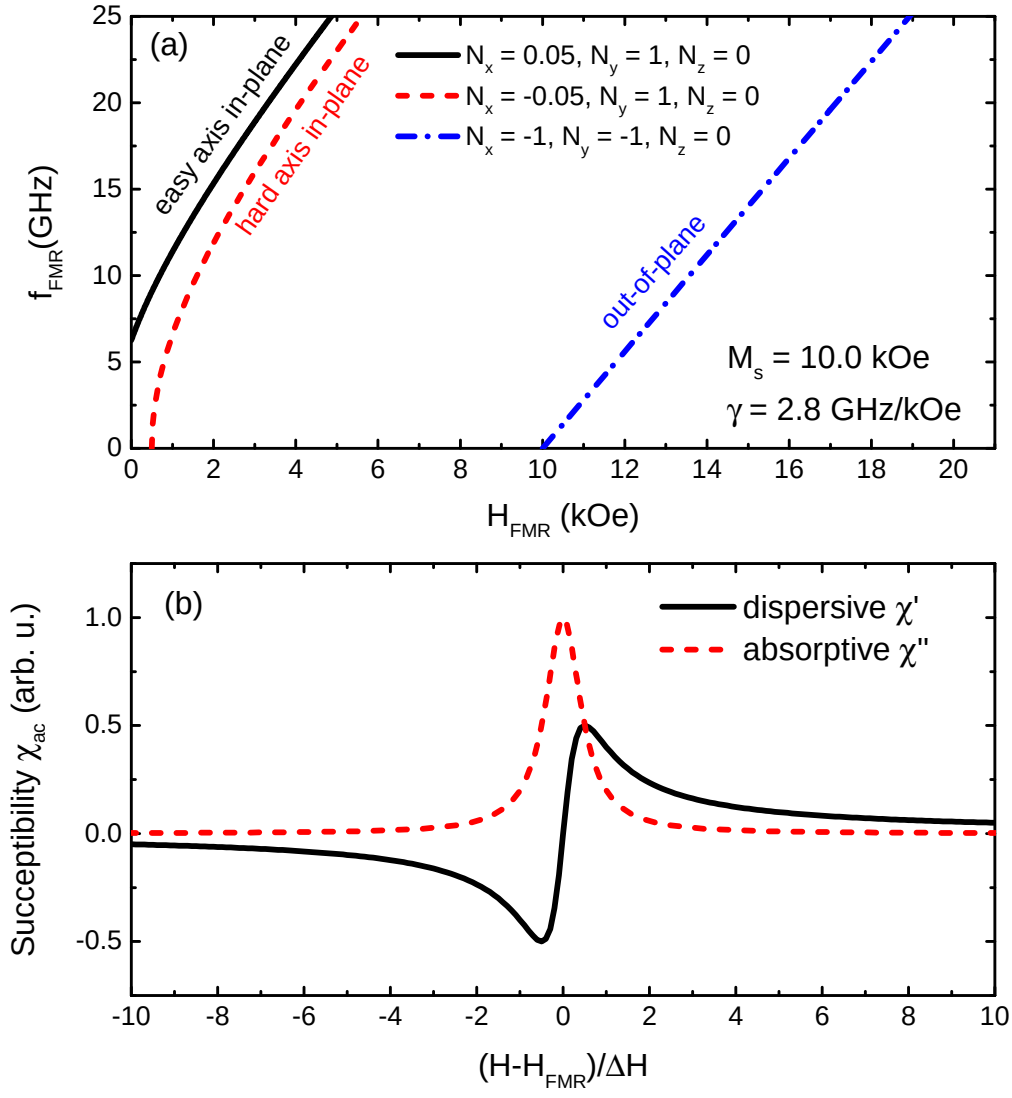

Figure 3.1: (a) Example FMR dispersions given by the Kittel equation (Eq. 3.2) for different choices of demagnetization tensor components as indicated in the legend, to reflect typical in-plane easy axis, in-plane hard axis, and out-of-plane behaviors for thin films with a hard axis out-of-plane due to shape anisotropy, and in plane magnetocrystalline anisotropy. (b) AC susceptibility around the FMR condition ($H - H_{FMR} = 0$) for the dispersive real component χ' (Eq. 3.3) and the absorptive imaginary component χ'' (Eq. 3.4). The abscissa units in (b) have been normalized to the FWHM linewidth ΔH.

which, as the expression is commonly used, may be rearranged algebraically to solve for α given measured ΔH values. Note that Eq. 3.5 is sometimes written with a factor $\sqrt{3}$ in the denomenator, appropriate in the convention where ΔH is the peak-to-peak width of the derivative spectrum, and/or omitting the factor of 2 in the numerator for cases where ΔH is taken as the half-width half-maximum (HWHM).

It should be emphasized that, as written in Eq. 3.5, it is the *field-swept* linewidth that is proportional to f_{FMR} for a given α, rather than the *frequency-swept* linewidth Δf. It is trivial to see that given Eq. 3.5, for nonlinear solutions of Eq. 3.2 (e.g. the in-plane Kittel dispersions shown in Fig. 3.1(a)) Δf cannot be linear with f_{FMR}. In resonance systems, the quality factor $Q \equiv f/\Delta f$ is often used to describe the degree of dissipation present in the system. Given the preceding discussion, it is clear that α is not equivalent to Q^{-1} (as defined previously) in certain FMR configurations. See Heinrich[99] for a detailed description of the solution to the LLG Equation 3.1 deriving the Kittel Equation 3.2, as well as inclusion of damping to prove Eq. 3.5 and discussion of Δf.

3.1.1 Ferromagnetic resonance experimental technique

A hardware diagram of the FMR experimental measurement technique used for the data discussed in this chapter is shown in Fig. 3.2(a). The measurements presented in this thesis were done in the transmission configuration,[3] in which the driving of FMR in the sample influences the microwave power transmitted through a coplanar waveguide (CPW) through inductive coupling. A cartoon of the sample lying face-down over the centerline of the CPW is shown in Fig. 3.2(b). A typical sample size was a cleaved shard of $\sim$ 1 mm^2, which was held fixed on the CPW with a small amount of thermal grease. The CPW board was connected to input and output coaxial transmission lines at each end by nonmagnetic Southwest launchers, which completed the probe head. As indicated in Fig. 3.2(a), the probe head was hung cantilevered between the electromagnet, without making mechanical contact, and input and output radiofreqequency (RF) lines were rigid Cu SMA cables. The RF power was supplied by a 0-20 GHz Agilent (now Keysight) N5183A MXG microwave source, which could be

[3] In two-port network terminology this is described as S_{21}. Reflection configured (i.e. S_{11}) measurements are common as well.

frequency doubled, if desired, for measurements up to 40 GHz using a Marki D-0250 passive microwave doubler.[4] Inner/outer dc blocks (Pasternack PE8227) could be used to prevent Faraday pickup voltages and mitigate ground loops. The transmitted RF signal was converted to low frequency voltage with a rectifying Agilent 8474B diode, the video output of which was connected to the input of a lock-in amplifier (SR830 or EG&G7260). The magnetic field H was produced with an electromagnet configured with Fe cores; with tapered cores the maximum H was 2.4 T, without tapered cores the maximum H was 0.7 T. The field homogeneity was verified to be better than $1 : 10^3$ over a 1" region in the center of the Fe cores. In addition to the magnetic field produced by the electromagnet, Helmholtz coils were used to produce a small (0.1-1 Oe) field modulation ac magnetic field $H_{FM}e^{i\omega_{FM}t}$ (($\omega_{FM} \sim 330$ Hz typical). The ac field modulation technique was used to enhance the signal-to-noise ratio by enabling lock-in detection of the Fourier component of the diode voltage that depended on magnetic field, and therefore removing the large off-resonant transmitted power background voltage.

The transmitted power through the sample/CPW system is modified at FMR due to the influence of χ_{ac} on the complex impedance $\boldsymbol{Z} = Z' + iZ''$ of the CPW. It is most straightforward to consider the influence of χ_{ac} on the local inductance of the CPW. Inductive reactance is given by $Z'' = \omega L = \omega\Phi/I$, where Φ is the magnetic flux due to current I in a transmission line. Because $\chi_{ac} = \partial\boldsymbol{M}/\partial h_{rf}$ where $h_{rf} \propto I$ and $\partial\boldsymbol{M} \propto \Phi$, it is clear that the component of the inductive reactance locally due to the magnetic sample is $Z''_m \propto \omega\chi_{ac}$. That is, the sharp feature in χ_{ac} at FMR will result in a sharp feature in $\boldsymbol{Z}$, imprinting a detectable feature in the transmitted or reflected power. For a more detailed description of CPW FMR, see Ref. [98] or Ref. [100]. In general, $\boldsymbol{Z}_m$ is much smaller than $Z_0 = 50\ \Omega$, giving a change in transmitted power at FMR less than 1%. In the case of the field modulation technique, only the temporal Fourier component of the transmitted power that depends on the applied field is detected. The lock-in voltage is therefore proportional to $(d\chi_{ac}/dH) \times H_{FM}$ for H_{FM} values sufficiently smaller than the field scale of the contours in χ_{ac}. Because the actual voltage depends on the RF power, the value of H_{FM}, the diode sensitivity, and the sample volume and exact mounting geometry, we will customarily label the lock-in voltage signal as

[4] Note that the doubler necessarily creates sidebands at $1f$ and $3f$. For measurements in which sideband FMR peaks encroached on the sweep range, an appropriate bandpass filter was used.

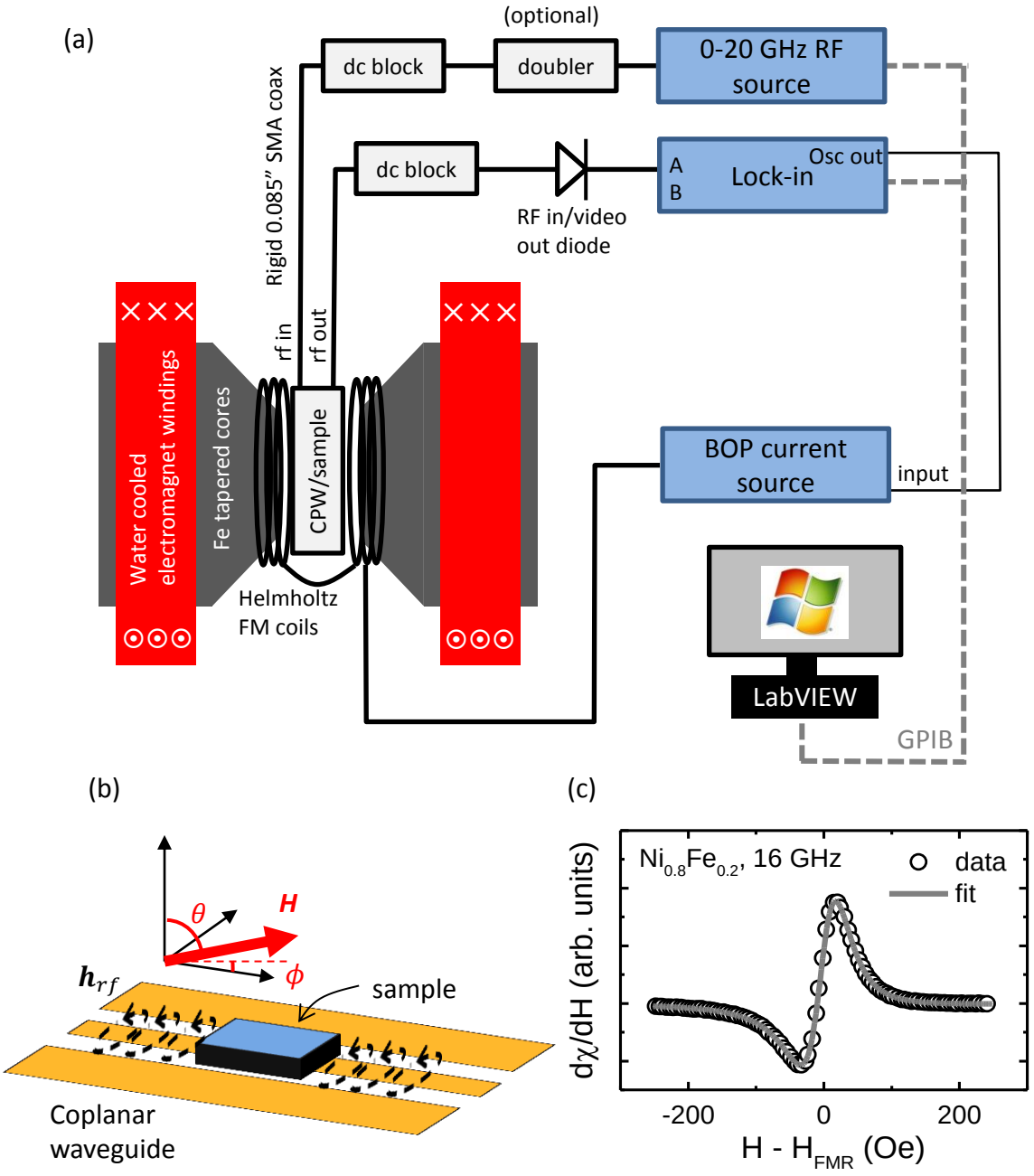

Figure 3.2: (a) Hardware diagram for the transmission FMR experimental setup. The rf detection diode was an Agilent 8474B, the inner/outer dc blocks were Pasternack PE8227s. Southwest nonmagnetic launchers were used to connect to a custom Cu CPW with nonmagnetic organic solderability preservative coating. (b) Cartoon of sample geometry face-down over CPW centerline. (c) Example FMR field sweep on 50 nm Permalloy ($Fe_{0.8}Ni_{0.2}$) film. The vertical scale is equivalent to the Fourier component of the diode video output at the FM frequency.

$d\chi/dH$ (arbitrary units), as shown in Fig. 3.2(c) for an example Permalloy FMR sweep. Typically, the dc diode voltage was in the 10-100 mV range, and the change in diode voltage at FMR was 1-100 μV.

Because of unavoidable reflections, standing waves, and imperfect impedance matching, in a power transmission measurement one does not measure χ' and χ'' separately but rather a rotated projection involving an angle ρ that is determined by the properties of the entire rf transmission line. Explicitly, we may write[98]

$$\begin{pmatrix} \chi'_{mix} \\ \chi''_{mix} \end{pmatrix} = \begin{pmatrix} \cos\rho & \sin\rho \\ -\sin\rho & \cos\rho \end{pmatrix} \begin{pmatrix} \chi' \\ \chi'' \end{pmatrix}, \tag{3.6}$$

and recognize the field modulated power transmission measurement is proportional to $d|\boldsymbol{\chi}_{mix}|/dH = d\chi/dH$, we fit the FMR sweep data to a function of the form

$$\begin{aligned} \frac{d\chi}{dH} = A_1 &\frac{(H_z - H_{FMR})\Delta H^3}{2\Big((\Delta H/2)^2 + (H_z - H_0)^2\Big)^2} \\ &- A_2 \frac{(H_z - H_{FMR})^2 \Delta H^2}{\Big((\Delta H/2)^2 + (H_z - H_0)^2\Big)^2} \\ + A_2 &\frac{\Delta H^2}{2\Big((\Delta H/2)^2 + (H_z - H_0)^2\Big)} + A_3, \end{aligned} \tag{3.7}$$

where the terms represent a sum of the H-derivatives of Eq. 3.3 and Eq. 3.4 with arbitrary weight given by A_1 and A_2 real constants. (A_1 and A_2 could be used to determine the rf rotation phase ρ, if desired, but typically are simply left as fit prefactors). A 0^{th} order background A_3 is included as a fitting constant to account for any spurious off-resonant background (typically small). For some data in this thesis where the signal was very low, a 1^{st} order background was included in the fitting function as well. An example of a raw FMR data and corresponding fit to Eq. 3.7 is shown in Fig. 3.2(c), which was taken on a 50 nm sputtered Permalloy film (i.e. $Ni_{0.8}Fe_{0.2}$ alloy) at excitation frequency of 16 GHz. The parameters extracted from the fit are the FMR peak position H_{FMR} and the FMR field-swept linewidth ΔH.

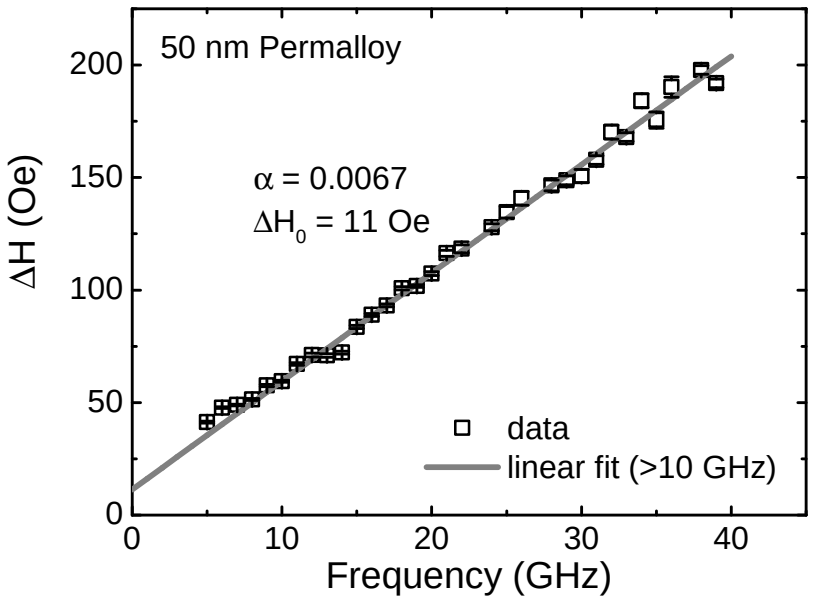

Figure 3.3: FMR linewidth vs excitation frequency for 50 nm sputtered Permalloy film with the magnetization saturated in the out-of-plane configuration. The gray line is a linear fit to the data above 10 GHz (below 10 GHz slight misalignment begins to strongly influence results), the fit results interpreted with Eq. 3.5 are indicated on the figure.

3.1.2 Linewidth broadening mechanisms

Using the measured FMR linewidth to extract dynamic damping properties of the material under study is the main focus of this chapter. Before presenting linewidth data for Heusler thin films, the primary mechanisms that influence the FMR linewidth are discussed in the sections below. First we will discuss the Gilbert damping, which is the most commonly discussed metric of damping and is characterized by α in Eq. 3.1. Then, we will introduce two mechanisms by which spatial inhomogeneity of the magnetic properties of a film can influence the FMR linewidth, which are the inhomogeneous broadening of the linewidth and the two-magnon scattering mechanism.

Intrinsic Gilbert damping and the Kamberský mechanism

Gilbert damping is characterized by nonzero α in Eq. 3.1. While α is often referred to as an *intrinsic* parameter, it should not be thought of as intrinsic in the proper sense (e.g. it is the property of a perfect crystal of a given material), but rather should be thought of as intrinsic in the sense that α accounts for the longitudinal (spin-lattice) relaxation rate, or unrecoverable loss of angular momentum from the magnetic subsystem, in contrast to the inhomogeneous and transverse dephasing mechanisms to be discussed in the following sections. In fact, Gilbert phenomenologically introduced damping[101] in the equation of motion through α, and its best definition may remain exactly that: Gilbert damping is that which mirrors the dynamics described by Eq. 3.1. The phenomenon symptomatic of Gilbert damping is that ΔH is proportional to excitation frequency by Eq. 3.5. Data exemplifying this behavior are shown in Fig. 3.3, in which the slope of the linear fit may be used with Eq. 3.5 to give $\alpha = 6.7 \times 10^{-3}$ for Permalloy. (The finite zero-frequency intercept ΔH_0 of the linear fit shown in Fig. 3.3 will be discussed in the following section.)

A comprehensive discussion of the microscopic origins of the Gilbert α is beyond the scope of this thesis, but we will briefly discuss what is believed to be the governing mechanism for metallic ferromagnets, for which α is typically found in the $10^{-1} - 10^{-3}$ range. In metallic ferromagnets, α is believed to be determined by quasiparticle scattering processes and the spin-orbit interaction, as originally described by Kamberský[102], and developed further in recent years[103–105].

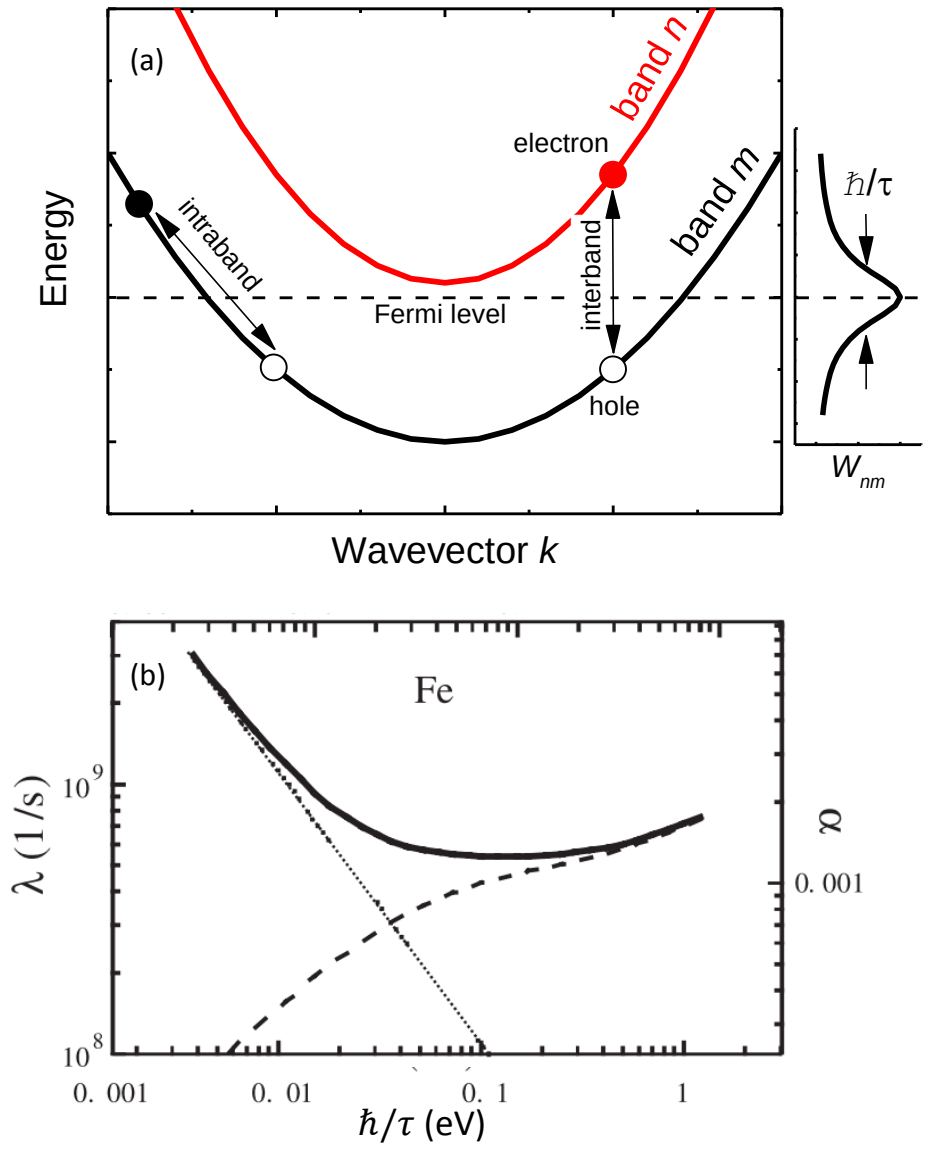

Figure 3.4: (a) Cartoon band structure with bands n, m illustrating the intraband and interband scattering processes which give rise to damping in the Kamberský mechanism. The spectral overlap function W_{nm} is shown on the right, with width determined by scattering rate $\hbar/\tau$. The Fermi level is drawn as the dashed horizontal line. (b) Figure copied from Gilmore et al.[104], showing the calculated damping for Fe as function of scattering rate using the Kamberský torque-correlation model, with the dotted and dashed curves giving the intraband and interband contributions, respectively. The left ordinate is the Landau-Lifshitz damping parameter $\lambda = \alpha\gamma M_s$.

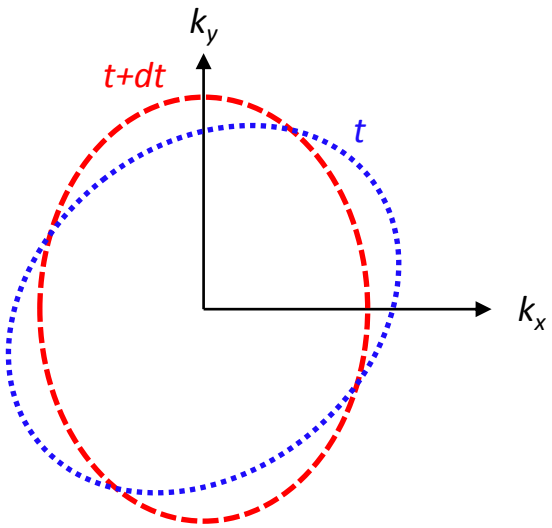

Figure 3.5: Cartoon equilibrium Fermi surfaces drawn in two dimensions k_x, k_y at time t (blue dots) and time $t+dt$ (red dashes). As the magnetization precesses the equilibrium Fermi surface oscillates, or breathes, due to the SOI but the actual occupation of states lags behind due to the finite momentum relaxation time τ. The lag manifests as electron-hole pairs created (see Fig. 3.4(a)), the relaxation of which transfers energy and angular momentum to the lattice. Larger lag (longer τ) results in a higher population of electron-hole pairs, which causes the intraband contribution to α to scale proportionally to the conductivity.

The Kamberský mechanism gives rise to two distinct contributions to the damping, termed the *conductivitylike* and *resistivitylike* contributions. The conductivitylike (resistivitylike) contribution, which is due to intraband (interband) scattering, causes the damping to decrease (increase) as the quasiparticle scattering rate $\hbar/\tau$ increases. Because of the two contributions, calculations of the Kamberský α vs $\hbar/\tau$ give a characteristic "v" or "u" shape, with a minimum at intermediate $\hbar/\tau$. Results of such a calculation done for Fe are shown in Fig. 3.4(b), which was taken from Ref. [104].

The conductivitylike intraband scattering contribution may be understood qualitatively within the *Fermi surface breathing* model. As described in Sec. 1.4, the Bloch

states which make up the bands of metals are described not only by wavevector $\boldsymbol{k}$ quantum numbers but also spin orientation $\boldsymbol{\sigma}$. That is, the SOI *mixes* spin and wavevector labelling of states, so that each individually no longer completely describes quantum states. In FMR, the spin orientation (i.e. magnetization) is driven to precess at the microwave frequency. As the magnetization precesses, the equilibrium Fermi surface (determined by the instantaneous orientation of the magnetization) oscillates, or breathes, as drawn in Fig. 3.5. However, for finite momentum relaxation time τ the instantaneous occupation of states is not equivalent to the equilibrium Fermi surface, but lags behind by a degree determined by τ. The lag of the instantaneous Fermi surface with regard to the equilibrium Fermi surface can be thought of as creating electron-hole pairs, because some states that would be occupied in equilibrium (i.e. are below the Fermi level) are not, and other states that would not be occupied in equilibrium (i.e. are above the Fermi level) are occupied. See Fig. 3.4(a). It is the equilibration of these spin-polarized electron-hole pairs through scattering with the lattice that gives rise to damping, and it is clear that for larger lag (longer τ) the damping is larger because of the larger population density of electon-hole pairs.

If only considering the conductivitylike mechanism described above, the damping of metallic ferromagnets could be tuned arbitrarily low by decreasing the conductivity (e.g., by intentionally introducing defects). On intuitive grounds, the latter approach might strike the reader as dubious in its limiting case. Indeed, a resistivitylike interband contribution to the damping arises from the widening of the bands due to nonzero $\hbar/\tau$ to the point that interband transitions become likely. These interband transitions, which are drawn in Fig. 3.4(a), are unlikely to conserve spin as they occur between bands of differing character and lead to damping. The band overlaps and corresponding scattering probabilities scale with the bandwidth $\hbar/\tau$, causing the interband contribution to the damping to grow proportionally to the resistivity. As an interesting side-note, the intraband and interband damping mechanisms are reminiscent of the D'yakonov-Perel[29] and Elliot-Yafet[27, 28] mechanisms, respectively, which describe the analogous spin-lattice relaxation rates in nonmagnetic conductors.

Both the intraband and interband contributions to α are captured by the so-called torque-correlation model of Kamberský damping[103, 104], in which α may be expressed

as[5]

$$\alpha = \frac{\gamma\hbar}{M_s}\Sigma_{n,m}\int \frac{dk^3}{(2\pi)^3}|\mathbf{\Gamma}^{-}_{\boldsymbol{nm}}(k)|^2 W_{nm}(k), \tag{3.8}$$

where $W_{nm}(k)$ describes the spectral overlap (determined by $\hbar/\tau$) between states in bands n and m near the Fermi level at wavevector k, and $\mathbf{\Gamma}^{-}_{nm}(k) = \langle n,k|\left[\sigma^{-}, H_{SO}\right]|m,k\rangle$ is the matrix element describing spin-flip transitions between states in bands n and m due to the spin-orbit field H_{SO}, which is equivalent to the Berry curvature of the band structure. While the intraband and interband contributions have been discussed qualitatively for decades, only recently have Gilmore and Stiles et al.[104, 105] calculated Eq. 3.8 for realistic band structures corresponding to transition metals Fe, Co, and Ni, giving quantitatively meaningful predictions.

Experimental tests of the torque-correlation model of Kambersky̆ damping have been few and far between, largely because of complications in utilizing the FMR linewidth to extract the intrinsic Gilbert damping. Varying temperature is the best experimental way to tune $\hbar/\tau$. Complications arise, however, as thick polycrystalline samples with strong temperature dependence of $\hbar/\tau$ suffer from eddy-current damping contributions, while for epitaxial thin films spin pumping and two-magnon contributions to the FMR linewidth become significant. In addition, in thin films $\hbar/\tau$ is typically dominated by surface and grain-boundary scattering[62, 63] and not strongly temperature dependent. In Ni, the crossover from conductivitylike to resistivitylike damping has been observed[106]. Also, in bulk Ni disks a strong conductivitylike temperature dependence has been reported in Ref. [107], but it is not clear if eddy current damping (which also scales with the conductivity) was taken into account in this study. A more recent experiment has demonstrated that the resistivitylike contribution to damping dominates in Permalloy thin films, in which the thickness was varied to tune the resistivity[108]. Shoen et al.[109] have demonstrated that α is minimized in the Co_xFe_{1-x} alloy at the composition x for which the DOS at the Fermi level is minimized, in qualitative agreement with Eq. 3.8. It is believed that the very low damping constants observed in Heusler compounds[110–112] are due to influence of their spin-resolved band structure on the efficiency of Kamberský damping. Specifically, half-metallicity has been proposed as the ideal attribute to minimize Kamberský damping in metallic ferromagnets[113].

[5] Many calculations of Kamberský damping report $\lambda = \alpha\gamma M_s$, which is an alternative metric describing damping in the so-called Landau-Lifshitz form of the LLG equation.

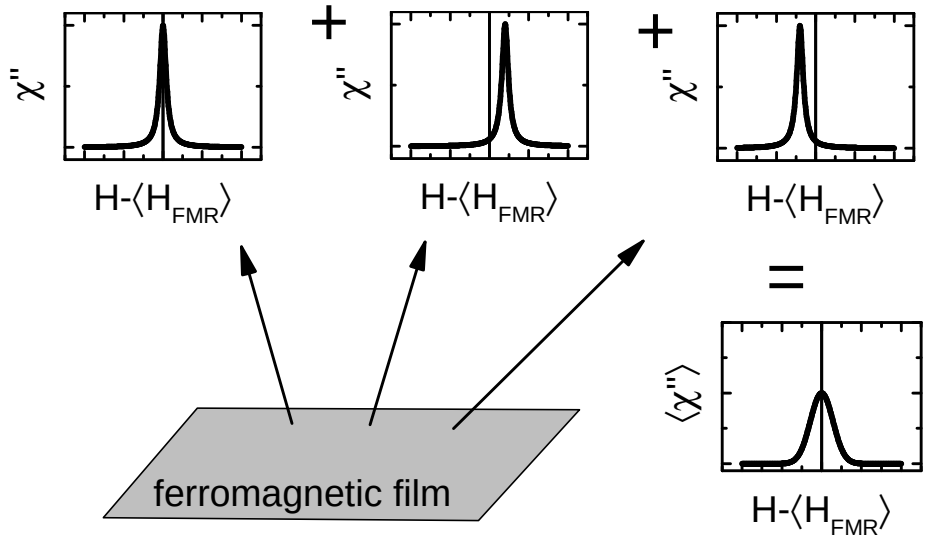

Figure 3.6: Schematic diagram of inhomogeneous broadening of the measured FMR linewidth. At different spatial locations on the film, the position of the local resonance peak in χ_{ac} varies, as indicated by the top three plots. On the lower right, an example of the experimentally measured spatially averaged $\langle\chi\rangle$ is plotted for a Gaussian distribution of local resonance peak positions.

Inhomogeneous broadening

Spatial inhomogeneity of any term in Eq. 3.2 leads to a spatial variation in H_{FMR}, broadening the χ_{ac} feature as measured for the entire sample. See Fig. 3.6 for a schematic illustration of inhomogeneous linewidth broadening. Local narrow Lorentzian peaks with varying resonance fields add to give a broadened total χ_{ac} peak, which has a Gaussian shape for δ-function local resonances with a Gaussian distribution of resonance fields. Kupriyanova and Orlava[114] have discussed how the shape of the resonance feature is influenced by the type of magnetic inhomogeneity present in the system. In the time domain, dephasing processes (whether due to inhomogeneous dephasing or damping) cause a decay in the transverse precession amplitude of the form $e^{-(t/\tau)^{\kappa}}$, where the value of the exponent κ determines the frequency (magnetic field) domain

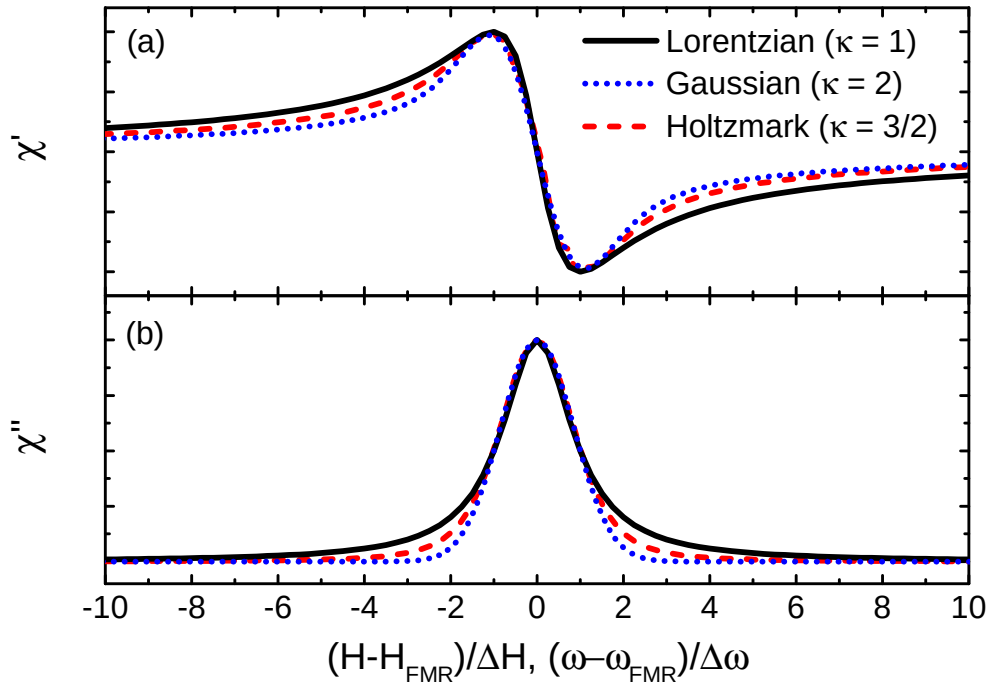

Figure 3.7: (a) Real dispersive χ' and (b) imaginary absorptive χ'' for Lorentzian (black solid line), Gaussian (blue dotted line), and Holtzmark (red dashed line) functions which correspond to the broadened lineshapes for dissipative damping, random Gaussian inhomogeneity, and point defect inhomogeneity, respectively. The abscissa scale has been normalized to the FWHM of χ'' for each curve.

lineshape $\boldsymbol{\chi}(\omega)$ ($\boldsymbol{\chi}(H)$) by the Fourier transform of $e^{-(t/\tau)^{\kappa}}$. For dissipative damping (e.g. of the Gilbert form), $\kappa = 1$ and $\boldsymbol{\chi}$ is a Lorentzian function as discussed in Section 3.1.2. For Gaussian inhomogeneity $\kappa = 2$, resulting in a Gaussian $\boldsymbol{\chi}$ feature, while for point-like inhomogeneities $\kappa = 3/2$, resulting in a Holtzmark function for $\boldsymbol{\chi}$. The Lorentzian, Gaussian, and Holtzmark lineshapes for χ' and χ'' are shown in Fig. 3.7. (The Holtzmark function may only be expressed in terms of hypergeometric functions. The dispersive components of the Gaussian and Holtzmark susceptibilities were evaluated by integrating the Kramers-Kronig relations[5] numerically.)

By inspection of Fig. 3.7, it is clear that while the Lorentzian lineshape has longer "tails" than the Gaussian or Lorentzian lineshapes, excellent experimental data would

be needed to distinguish between these lineshapes. In addition, the combination of multiple broadening mechanisms results in a convoluted lineshape[114] and separately identifying individual broadening mechanisms becomes nearly impossible. Because of these considerations, the standard method to distinguish between Gaussian or Holtzmark inhomogeneous FMR linewidths and Gilbert damping Lorentzian linewidths is to record the FWHM ΔH of the resonance feature at multiple frequencies. Unlike the intrinsic linewidth ΔH_i, the inhomogeneous contribution to the linewidth ΔH_0 may be shown to be frequency-independent. Then, for data such as that shown in Fig. 3.3, a linear fit may be performed and the zero-frequency offset ascribed to ΔH_0, while the slope is used to extract α by Eq. 3.5.

Inhomogeneous broadening of the linewidth may be quantitatively described by the following intuitive expression [115]

$$\Delta H_0 = \left(\frac{df}{dH}\right)^{-1} \Sigma_i \left|\frac{\partial f}{\partial x_i}\right| \Delta x_i, \tag{3.9}$$

where x_i is any parameter of Eq. 3.2 with corresponding Gaussian widths Δx_i (which are zero for an ideal homogeneous film). All derivatives in Eq. 3.9 are evaluated at the FMR condition. McMichael and Twisselman[115] have noted that ΔH_0 is constant (independent of frequency) if the relevant inhomogeneities behave as random additions or subtractions to the applied field. In analysis of experimental FMR linewidth data it is typically assumed that this assumption holds, and ΔH_0 may be treated as an isotropic constant. This approach is used in this thesis, largely because one must make simplifying assumptions to render analysis on anisotropic and nonlinear two-magnon scattering linewidths tractable. It should be recognized, however, that both anisotropic and frequency-dependent ΔH_0 are possible given Eq. 3.9 for certain realizations of inhomogeneity. Reference [116] contains a qualitative discussion in which the possibility of anisotropic ΔH_0 is raised.

The two-magnon scattering mechanism

The final linewidth broadening mechanism we will discuss is the two-magnon scattering (TMS) mechanism. Similar to inhomogeneous broadening, this mechanism originates due to spatial inhomogeneity of the magnetic system. Unlike inhomogeneous broadening, however, which treats local FMR dynamics as decoupled from those elsewhere

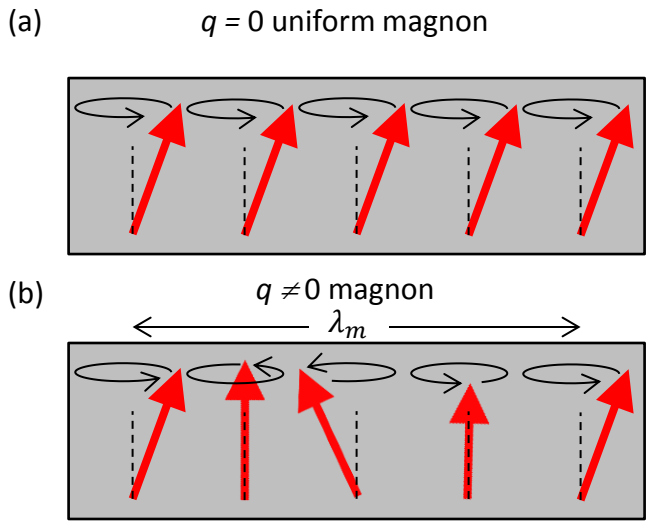

Figure 3.8: Illustration of magnons, or spin waves. The red arrows denote the orientation of magnetization excited to precess around the equilibrium orientation which is the dashed black line. The $q = 0$ uniform, or infinite wavelength FMR magnon is shown in (a), while a finite-q magnon is shown in (b) with the wavelength λ_m indicated.

in the system, the TMS mechanism considers the dipole and exchange-mediated interactions between magnetic excitations. Up until this point, we have avoided discussing non-zero-wavevector magnetic excitations, or magnons, and have assumed that the dynamics can be described in terms of a spatially-uniform macrospin. TMS considers the coupling between local FMR conditions in an inhomogeneous system as mediated by spatially-dependent dipole and exchange interactions, which are naturally expressed in terms of magnons specified by their wavenumber $q \equiv 2\pi/\lambda_m$, where λ_m is the corresponding real-space wavelength of the magnetic wave.[6] See Fig. 3.8 for a cartoon illustration of magnons, which are also be referred to as spin waves. In fact, the system's macroscopic susceptibility $\boldsymbol{\chi}$ discussed at in Sec. 3.1.1 corresponds to the $q = 0$ (or infinite wavelength) magnon shown in Fig. 3.8(a).

As with any elementary excitation in condensed matter systems, the properties of magnons are governed by their dispersion relation $\omega(\boldsymbol{q})$. The magnon dispersion relation

[6] We will use q to denote magnon wavenumber and distinguish from k, the electronic state wavenumber.

can be thought of as a generalization of the Kittel equation (Eq. 3.2) in which the two transverse stiffness fields may be $\boldsymbol{q}$-dependent. In addition to the Zeeman energy due to external, demagnetization, or magnetocrystalline effective magnetic fields[52], finite $\boldsymbol{q}$ magnon frequencies (or equivalent energies) contain terms due to the exchange stiffness D_{ex} and magnetostatic dipolar interactions[117, 118]. The magnon dispersion relation for magnetization lying in the plane of a ferromagnet thin film of thickness d may be written as

$$\omega(\boldsymbol{q}) = \gamma\left[\left(H + H_k + D_{ex}q^2 + H_s(1 - N(q))\sin^2\psi_q\right)\left(H - H_k + D_{ex}q^2 + H_s N(q)\right)\right]^{1/2} \tag{3.10}$$

where $N(q) \equiv (1 - e^{-kd})/kd$ is the q-dependent demagnetization tensor component, and ψ_q is the angle between $\boldsymbol{q}$ and $\boldsymbol{M}$ lying in the film plane. Example dispersion curves are shown in Fig. 3.9(a) for various ψ_q, where it can be seen that the lowest energy magnon branch is for $\psi_q = 0$ while the highest energy branch is for $\psi_q = \pi/2$. At high q the exchange interaction causes $\omega(\boldsymbol{q})$ to increase $\propto q^2$ for all $\boldsymbol{q}$, however for the curves near $\psi_q = 0$ it can be seen that the dispersion is initially negative, and a degeneracy with the $\boldsymbol{q} = 0$ FMR magnon exists at finite $\boldsymbol{q}$. This degeneracy allows a zero-energy scattering process to scatter angular momentum from the FMR magnon to finite $\boldsymbol{q}$, and is referred to as two-magnon scattering in reference to the initial $q = 0$ magnon and the final finite $\boldsymbol{q}$ magnon. In the inset of Fig. 3.9(a) line contours of $\omega(\boldsymbol{q}) = \omega_{FMR}$ are shown in $\boldsymbol{q}$-space, for different FMR conditions.

TMS broadens the FMR linewidth because the scattering mechanism imposes a lifetime on the $\boldsymbol{q} = 0$ magnon.[7] The zero-energy scattering process from the $\boldsymbol{q} = 0$ FMR magnon to the degenerate finite-$\boldsymbol{q}$ magnon must involve a defect to break translational invariance, because $\boldsymbol{q}$ is not conserved. The influence of defects, or magnetic inhomogeneities, on the linewidth (inversely related to the lifetime) of the unperturbed magnon states described by Eq. 3.10 has been developed through perturbation theory in Refs. [119, 120], in which it is shown that the TMS linewidth may be cast into the form

$$\Delta H_{TMS} = \frac{\gamma^2\xi^2 H'^2}{df_{FMR}/dH|_{f_{FMR}}}\int \Gamma_{0\boldsymbol{q}} C_{\boldsymbol{q}}(\xi)\delta_\alpha(\omega - \omega_{\boldsymbol{q}})d^2q, \tag{3.11}$$

[7] In contrast to Gilbert damping, which is a T_1-type longitudinal relaxation process, TMS is a T_2-type transverse dephasing process, because angular momentum is contained within the magnon system for the TMS process. It does, however, reflect dissipation of angular momentum in the sense that it is irreversible (could not be cancelled by a spin-echo experiment).

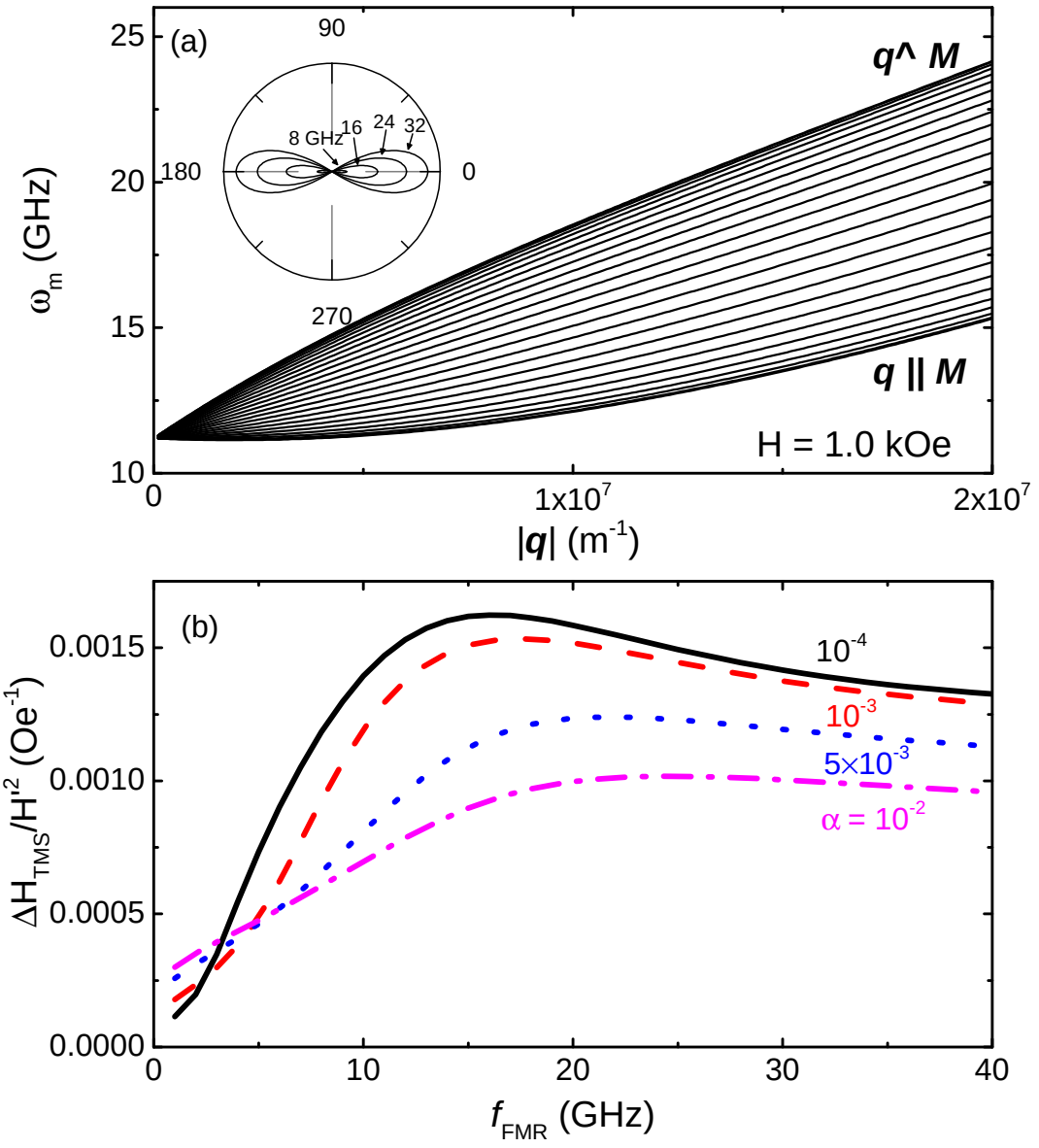

Figure 3.9: (a) Example $\omega(\boldsymbol{q})$ magnon dispersions given by Eq. 3.10 for the case of an in-plane magnetized thin film. The dispersions plotted span from $\psi_q = 0$ ($\boldsymbol{q} \parallel \boldsymbol{M}$, lowest curve) to $\psi_q = \pi/2$ ($\boldsymbol{q} \perp \boldsymbol{M}$, upper curve) and evenly spaced ψ_q values in between. The applied magnetic field used to generate the dispersions is indicated on the figure, which corresponds to a $\boldsymbol{q} = 0$ FMR magnon frequency of 11.2 GHz. The inset shows contours of constant frequency in 2D q-space for FMR conditions of $\omega(0) = 8, 16, 24$ and 32 GHz, where the polar angle is ψ_q and the scale of the radial coordinate is 1.6×10^7 m^{-1}. (b) The normalized TMS linewidth given by Eq. 3.11 vs FMR frequency for various intrinsic α values, as indicated on the figure. In (a) and (b), the in-plane anisotropy was set to zero, $H_s = 1.5$ T, $D = 500$ meV A^2, $\gamma = 28$ GHz/T, $\xi = 10^{-7}$ m, and $d = 25$ nm.

where $\Gamma_{0\boldsymbol{q}}$ is the defect-mediated interaction term between magnons at wavevector 0 and $\boldsymbol{q}$, $C_{\boldsymbol{q}}(\xi) = 1/[1 + (q\xi)^2]^{3/2}$ is the correlation function of the inhomogeneity with correlation length ξ, and H' is the magnitude of the inhomogeneity (units of magnetic field). The $\delta_\alpha(\omega - \omega_{\boldsymbol{q}})$ function in Eq. 3.11 selects out magnon scattering channels which conserve energy: in limit of zero intrinsic damping it is identical to the Dirac delta function, and to account for finite α is taken as a Lorentzian function of width $\delta\omega = (2\alpha f/\gamma)d\omega_{FMR}/dH$. (The Lorentzian function is normalized such that in the limit $\alpha \to 0$ it is equivalent to the Dirac δ-function.) In Fig. 3.9(b), Eq. 3.11 was used to generate ΔH_{TMS} vs f_{FMR} curves for various intrinsic α values. Note that for $\alpha = 0$ the properties of the δ-function in Eq. 3.11 can be used to convert the area integral to a line integral along the contours shown in the inset of Fig. 3.9(a). For the finite α curves shown in Fig. 3.9(b), the integral in Eq. 3.11 must be evaluated numerically.

The first striking feature of the curves shown in Fig. 3.9(b) is the "knee" frequency above which ΔH_{TMS} saturates or even downturns, which for the parameters chosen occurs near 15 GHz. The knee frequency occurs because of the large-q cuttoff in the integrand of Eq. 3.11 enforced by the correlation function $C_{\boldsymbol{q}}(\xi)$, and is determined by D_{ex} and ξ. For magnon states with $q > \xi^{-1}$ ($\lambda_m < \xi$), no TMS process is allowed because the system is homogeneous for lengthscales smaller than ξ. The second striking feature of Fig. 3.9(b) is the *increase* of ΔH_{TMS} as the intrinsic α *decreases*. While perhaps counterintuitive, a generic feature of degenerate perturbatively coupled modes is the tendency of coupling effects to grow stronger as the dissipation of the underlying states is decreased. McMichael and Krivosik[119] have shown identical results to Fig. 3.9(b), and the influence of the intrinsic α on TMS linewidths will become important in our discussion of Heusler compound thin film FMR results.

At this stage, because both inhomogeneous broadening and TMS have been attributed to underlying spatial inhomogeneity, it may not be clear in which limit each mechanism is appropriate. McMichael et al.[115] have addressed this confusion, and have stated that the local resonance model of inhomogeneous broadening is appropriate if the condition $H'\xi \geq M_s d$ is satisfied.

Finally, a crucial experimental quality of TMS is that it is inoperable, or said to be "turned off", for the geometry in which the magnetization is saturated out-of-plane (OOP). It can be shown that there are no degenerate magnon states at finite q in this

case[121], leading to zero TMS linewidth.[8] Therefore, an FMR measurement with the magnetization saturated in the OOP geometry may be performed as a check for the presence of TMS linewidths in the IP geometry.

3.2 FMR linewidth results for epitaxial Heusler compound thin films

The FMR data presented in this section were collected on epitaxially grown full-Heusler compound thin films, grown by Sahil Patel and Anthony McFadden of the Palmstrøm group at UCSB. The pervasive feature observed in these films that attracted our study was the strong anisotropy of the FMR linewidth: ΔH was highly anisotropic when the direction of the saturated magnetization was varied, both when rotated in the film plane and in the out-of-plane geometry. In Fig. 3.10, anisotropic results on both (a) Co_2FeAl/MgO films (CFA)[9] and (b) Co_2FeSi/GaAs (CFS) films are shown, in which the orientation of the applied magnetic field was rotated in the sample plane. In both instances, the extrema of ΔH coincide with those of H_{FMR}, which strongly suggests the two are linked. Note that field-dragging or mosaicity effects[122], which give a maximum in ΔH where $|dH_{FMR}/d\phi|$ is largest (where ϕ is the angle of the applied field), cannot be invoked to to explain the data in Fig. 3.10.

For the CFA films, the magnetocrystalline anisotropy is cubic, leading to the four-fold symmetry of H_{FMR} vs angle as shown in Fig. 3.10(a). The easy axes of the cubic magnetocrystalline anisotropy are along the MgO(001) substrate principal cubic directions $\langle 100 \rangle$, and hard axes along $\langle 110 \rangle$. The CFA grows in the [001] direction oriented at 45° with respect to the MgO substrate, that is $\langle 100 \rangle_{CFA}$ is parallel to $\langle 110 \rangle_{MgO}$. As shown in 3.10(a), ΔH is largest along the hard axis and smallest along the easy axis. For the CFS films, the dominant magnetocrystalline anisotropy is uniaxial, leading to the two-fold symmetry of H_{FMR} vs angle shown in Fig. 3.10(b). In this case, the CFS grows cube-on-cube on the GaAs(001) substrate. The uniaxial anisotropy in the CFS/GaAs sample is due to the $c(4 \times 4)$ surface reconstruction of the GaAs, which breaks four-fold symmetry[123, 124]. In the case of the CFS, it can be seen in Fig. 3.10(b) that ΔH is

[8] However, the presence of magnetic inhomogeneity will still manifest as inhomogeneous broadening.
[9] The CFA films were annealed at 500° C, see Appendix A for details.

a minimum along the hard axis, and a maximum along the easy axis.

Anisotropic FMR linewidths in epitaxial thin films have been reported elsewhere, where it was originally attributed to anisotropic inhomogeneous linewidths or anisotropic Gilbert damping[125]. After further development of TMS theory in the late 1990s[121], it was realized that anistropic linewidths were due to anisotropic defects in highly textured epitaxial films that preferentially scattered magnons along certain crystallographic directions[116, 126]. For the CFA films, we have demonstrated that the primary source of the anisotropic linewiths is TMS by performing the FMR measurement in the OOP geometry. The results are shown in Fig. 3.11(a), where it may be seen that all linewidths in the OOP geometry fall well below the IP linewidths, and are nearly frequency-independent. However, in the case of the CFS linewidth data shown in Fig. 3.11(b), the OOP linewidths are comparable to the IP hard axis linewidth, which is clearly a nonlinear function of frequency (indicating a TMS-dominated linewidth). The fits of the OOP CFA(24 nm)/MgO and CFS(5 nm)/GaAs linewidth data shown in Fig. 3.11 to the linear function $\Delta H(f) = 2\alpha f/\gamma + \Delta H_0$ give $\alpha \leq 2 \times 10^{-4}$ and $\alpha = 1.7 \times 10^{-3}$, and $\Delta H_0 = 31$ Oe and 9 Oe, respectively. Notably, the slope for the CFA(24 nm)/MgO OOP linewidth data shown in Fig. 3.11(a) is so small that only an upper bound on α may be given. The bound for CFA/MgO of $\alpha_{[001]} \leq 2 \times 10^{-4}$ to our knowledge represents the lowest reported intrinsic damping constant for a metallic ferromagnet, but the $\alpha \sim 10^{-4}$ range is not unexpected from Kamberský model calculations performed for similar full-Heusler compounds[113]. It should be noted that Shoen et al. [109] have recently reported $\alpha = 5 \times 10^{-4}$ for $Co_{25}Fe_{75}$ thin films, and in quoting that value interface and radiative damping contributions were subtracted from the value extracted from the slope of the measured linewidth, which was a factor of 4 higher. We have not subtracted either of these contributions to arrive at our quoted α values. We expect interface (i.e. spin pumping) contributions to the intrinsic damping are not significant in our films, as no heavy-metal seed layers have been used. For the radiative damping contribution[100] in the geometry of our CPW and sample, we calculate contributions $\alpha_{rad} \simeq 10^{-4}$, near or below the uncertainty in our fit α values. Recently, perovskite LSMO films have also been shown to give 7×10^{-4} intrinsic damping values[127].

Woltersdorf and Heinrich[116] showed similar measurements of pronounced IP FMR linewidth anisotropy for epitaxial Fe/GaAs films in which a lattice mismatched Pd

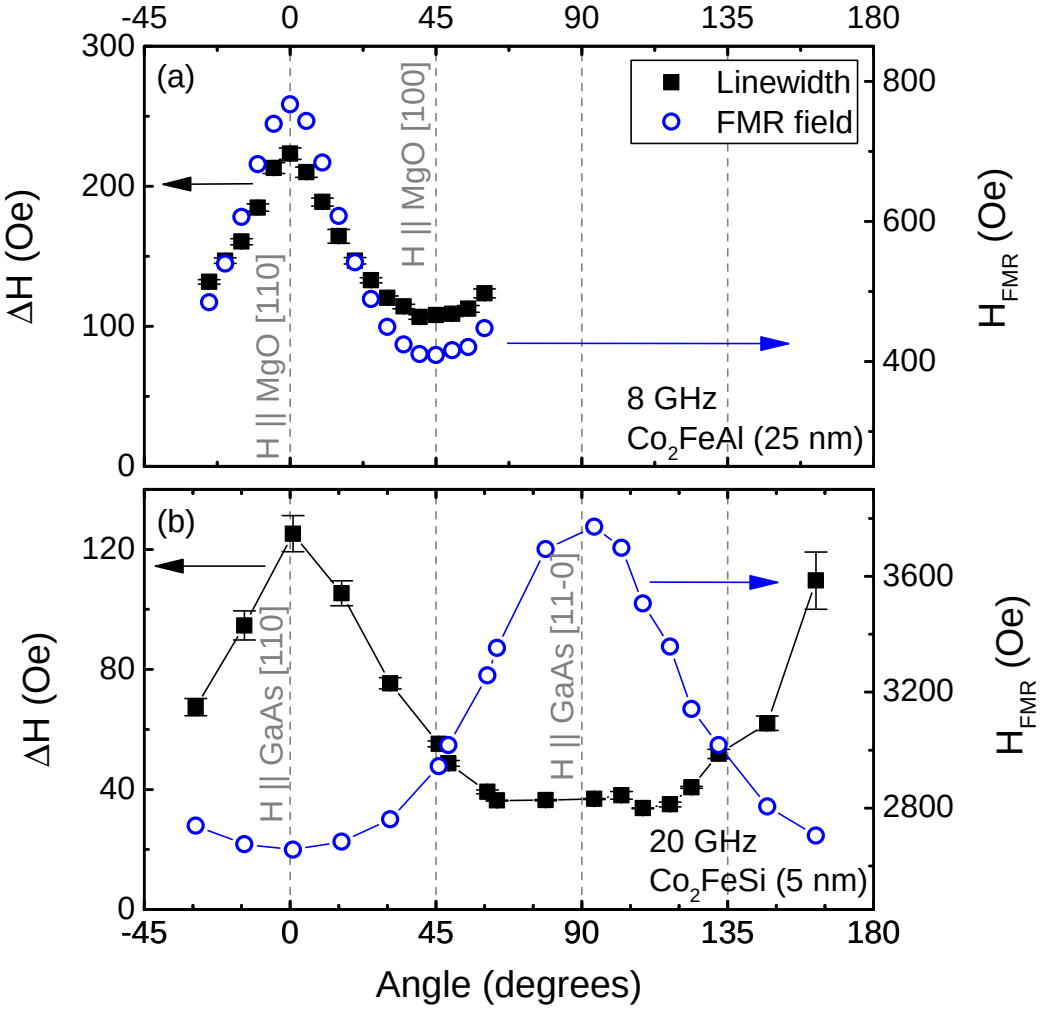

Figure 3.10: Summary of the FMR linewidth ΔH (black squares, left ordinate) and FMR field H_{FMR} (blue open circles, right ordinate) vs the in-plane field orientation angle, where the principal directions are indicated on the figure with respect to the substrate crystalline axes. Data taken on TMC250-500C, which is 25 nm of Co_2FeAl grown epitaxially on MgO(001), at a frequency of 8 GHz are shown in (a), and shown in (b) are data taken on UMN055, which is 5 nm of Co_2FeSi grown epitaxially on GaAs(001) at frequency of 20 GHz. In (b), the lines connect the data points.

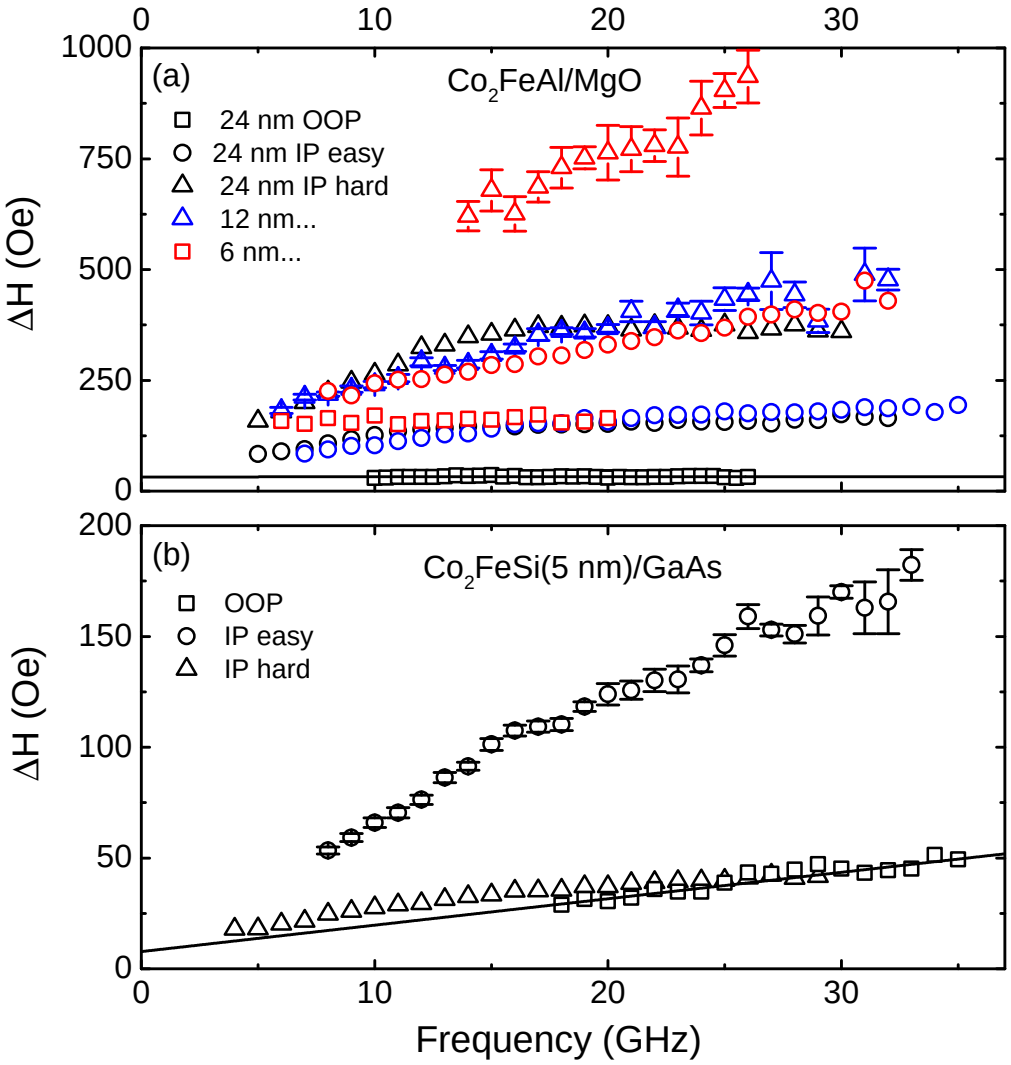

Figure 3.11: FMR linewidth ΔH vs frequency for the epitaxial Heusler films studied, as measured in the OOP (squares), in-plane easy axis (circles), and in-plane hard axis (triangles) geometries for (a) the Co_2FeAl/MgO TMC249-252 growth series (annealed *ex situ* at 500° C) and (b) the $Co_2FeSi/GaAs$ UMN055 growth. The error bars represent standard errors and are smaller than symbol size if not visible. The 12 nm OOP data is not shown in (a) because of the distorted FMR lineshape present. Linear fits to the 24 nm CFA and 5 nm CFS OOP data are shown as the black solid lines; the slopes give $\alpha \leq 2 \times 10^{-4}$ and $\alpha = 1.7 \times 10^{-3}$, and $\Delta H_0 = 31$ Oe and 9 Oe, respectively.

overlayer was grown to intentionally to create misfit dislocations. The resultant network of misfit dislocations formed a rectangular pattern, and the 4-fold symmetry of ΔH was attributed due to the resultant TMS. Interestingly, in their Fe/GaAs system the magnetocrystalline anisotropy was uniaxial and the H_{FMR} and ΔH were incommensurate, unlike for our films (shown in Fig. 3.10). More recently, He et al.[128] have shown similar large TMS anisotropy in Heusler $Fe_2Cr_{1-x}Co_xS$ thin films. Following these interpretations, Fig. 3.10 suggests that our CFA/MgO films possess a rectangular array of misfit dislocations oriented along $\langle 110 \rangle_{MgO}$ while our CFS/GaAs films possess misfit dislocations that predominantly form stripes along $[110]_{GaAs}$. See Fig. 3.12 for schematic illustrations of the proposed array of misfit dislocations giving rise to the anisotropic TMS linewidths in CFA/MgO (Fig. 3.12(a)) and CFS/GaAs (Fig. 3.12(b)). Note that the defects drawn schematically in Fig. 3.12 are meant to indicate the defects in the magnetic system that accompany the structural (e.g. topographical) defects due to misfit dislocations. Further microscopy studies such as plan-view TEM are needed to visualize and confirm the defects in these structures, and it remains to be seen whether or not the structural defects follow the same symmetry as the magnetic defects. It may be that the magnetic defects possess a lower degree of symmetry than the structural defects to which they owe their origin, due to edge magnetocrystalline anisotropy or pinning at the defects.

Aside from drawing attention to the influence of misfit dislocations on magnetization dynamics through TMS in epitaxial Heusler films, there are two important observations that deserve further analysis. The first is the pronounced nonlinearity of the IP ΔH vs frequency curve for the 24 nm CFA/MgO shown in Fig. 3.11(a). In fact, along the IP hard axis ΔH *decreases* at high frequency, which is reminiscent of the ΔH_{TMS} calculation shown in Fig. 3.9(b) for α of 10^{-3} and 10^{-4}. To our knowledge, FMR measurements on Heusler films (see Refs. [111, 112, 128], and this work) have produced some of the starkest nonlinearities in TMS ΔH vs frequency curves. The calculated curves shown in Fig. 3.9(b) illustrate the degree to which the value of α alters the ΔH_{TMS} vs frequency curve, enhancing the nonlinearity and increasing the magnitude of ΔH for *lower* α. This behavior was noticed and emphasized by McMichael and Krivosik[119], but it has not been appreciated in experimental literature the degree to which the intrinsic α alters the TMS ΔH vs frequency curve. In fact, in Refs.

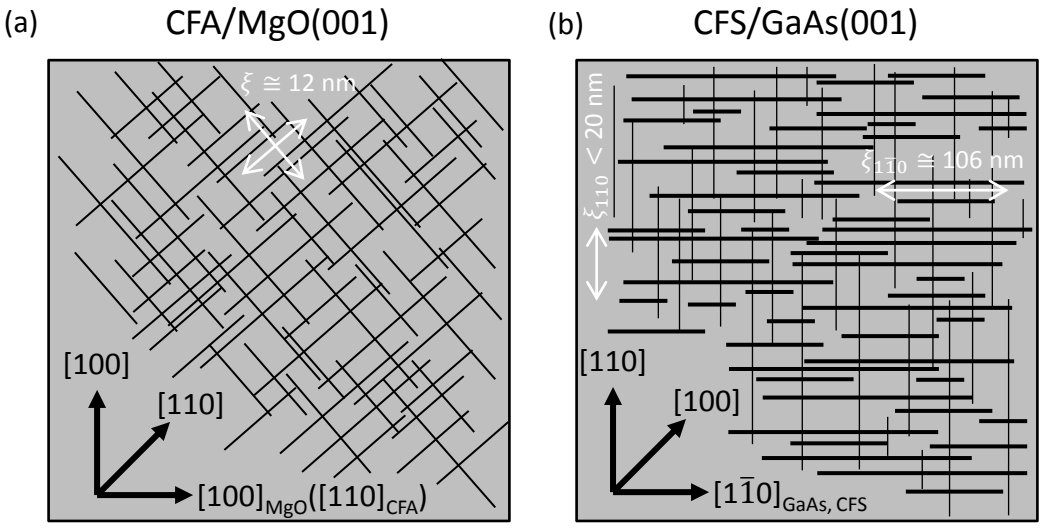

Figure 3.12: Cartoon drawings of the array of misfit dislocations which generate the TMS linewidth for (a) CFA/MgO and (b) CFS/GaAs systems. The magnitude of the magnetic defect is indicated by the weight of the line. The random defect array is four-fold symmetric for CFA/MgO in (a) and two-fold symmetric for CFS/GAs in (b) to reflect the symmetries of the measured TMS linewidth. The magnetic correlation length ξ is schematically indicated on the figure as the white bar. Note that the weight of the lines do not necessarily reflect the topography of structural defects due to misfit dislocations, but rather the accompanying magnetic defects.

[111, 112, 128] the fitting of the measured ΔH with TMS expressions similar to Eq. 3.11 were done in the limit of zero intrinsic damping, which considering Fig. 3.9(b) may lead to significant error in the quoted α values. The inversely-correlated behavior of the TMS linewidth with α may explain to some degree why Heusler compounds are prone to distinct TMS linewidths, because of their ultralow α values.

3.2.1 In-plane linewidth fitting to extrinsic and intrinsic contributions

To quantify these considerations, the CFA and CFS frequency-dependent IP linewidth data has been fit with a combined expression including intrinsic Gilbert damping, inhomogeneous broadening, and TMS. That is,

$$\Delta H = \Delta H_i + \Delta H_{TMS} + \Delta H_0, \tag{3.12}$$

where ΔH_i is due to the Gilbert damping by Eq. 3.5 and is proportional to the product of frequency and α, ΔH_{TMS} is the TMS linewidth given by Eq. 3.11 and a function of frequency, α, ξ, and H', and ΔH_0 is the inhomogeneous linewidth, which is independent of frequency. The fitting of a set of ΔH and frequency points could be performed in the 2D phase space of α and ξ, wherein a curve given by Eq. 3.12 was generated at each $\{\alpha, \xi\}$ pair (with H' chosen to minimize χ^2, the sum of the residuals). The $\{\alpha, \xi\}$ pair that minimized χ^2 was the best fit to the data. ΔH_0 was not a fitting parameter, but was fixed to the value consistent with the OOP measurement for which ΔH_{TMS} is zero (see the end of Section 3.1.2 for a discussion of the validity of this assumption). For both CFA and CFS, we have used an exchange stiffness constant $D_{ex} = 600$ meV A^2, which is typical for ternary full Heusler compounds with Curie temperatures near 1000 K[129, 130].

The results of fitting to the measured IP linewidth to Eq. 3.12 as described above for the CFA(24 nm)/MgO film are summarized in Fig. 3.13. Panels (b) and (d) of Fig. 3.14 show the curves that correspond to the α and ξ values which minimized χ^2. It can be seen that the sharp "knee" feature in the linewidth data as function of frequency reveal an inhomogeneity correlation length ξ of about 12 nm. Notably, the value is similar for magnetization along the IP easy axis $[100]_{MgO}$ ($[110]_{CFA}$) and the IP hard axis $[110]_{MgO}$ ($[100]_{CFA}$). The χ^2 contours are quite vertical and do not precisely constrain α because the TMS linewidths are so large (100s of Oe), but recall the slope of the OOP linewidth measurement shown in Fig. 3.11(a) which gave $\alpha \leq 2 \times 10^{-4}$. These results imply that a defect array of four-fold symmetry forms in these CFA/MgO films.

The results of the same fitting procedure for the CFS/GaAs film are summarized in Fig. 3.14. The best-fit parameters are listed in the caption. The most interesting feature to emphasize involves the striking data for magnetization aligned along the hard axis $[1\bar{1}0]_{GaAs}$ shown in Fig. 3.14(b). Because the linewidth was narrow ($\sim$ 10s of Oe)

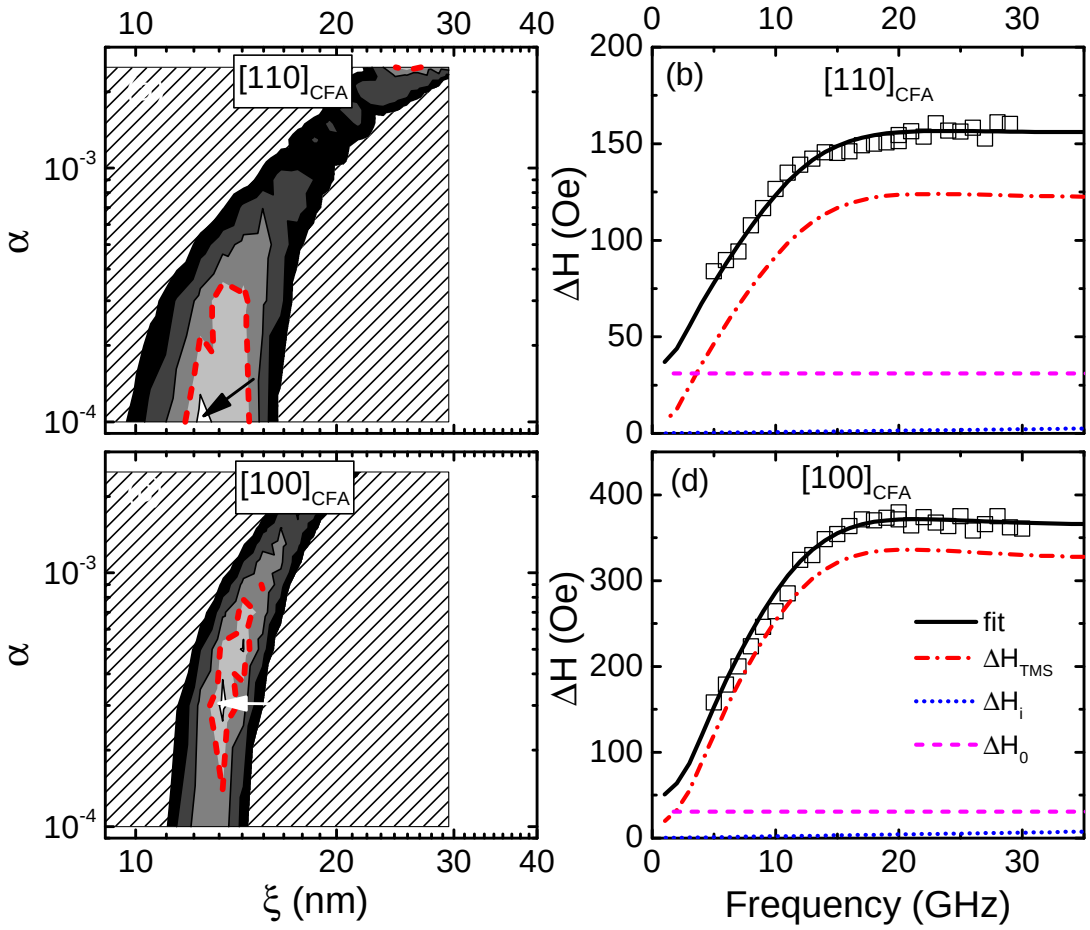

Figure 3.13: Summary figure for TMS fitting of Co_2FeAl(24 nm)/MgO (TMC250-500C) IP linewidth data. Panels (a) and (c) show the reduced sum of residual squared χ_r^2 surfaces for magnetic field applied along the IP easy axis $[100]_{MgO}$ ($[110]_{CFA}$) and the IP hard axis $[110]_{MgO}$ ($[100]_{CFA}$), respectively, in $\{\alpha, \xi\}$ space. The red dashed lines encircle the best fit points in parameter space and are the 2σ contours based on the reduced scaled χ^2. The grayscale increments represent 1, 2, 3, 4, and 5σ confidence intervals; the hashed area is outside of the 5σ region. The arrows in (a,c) point to the choice of parameters used to generate the lines in (b,d), respectively, which represent the contributions (see legend in (d)) to the linewidth given by Eq. 3.12. The parameters used to generate the lines in (b) are $\alpha = 10^{-4}$, $\xi = 12$ nm, and $H' = 640$ Oe, and for (d) are $\alpha = 3 \times 10^{-4}$, $\xi = 13$ nm, and $H' = 1.0$ kOe.

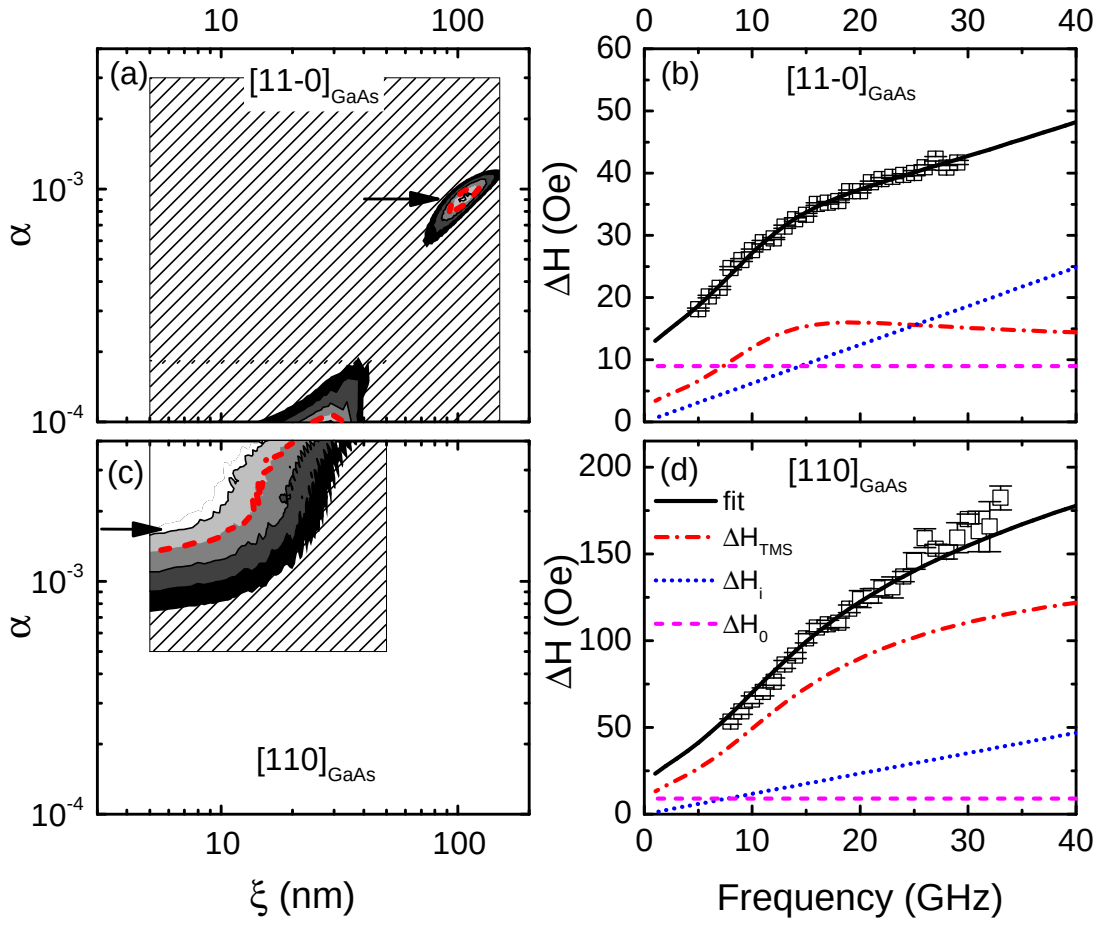

Figure 3.14: Summary figure for TMS fitting of Co_2FeSi(5 nm)/GaAs (UMN055) IP linewidth data. Panels (a) and (c) show the reduced sum of residual squared χ_r^2 surfaces for magnetic field applied along the IP hard axis $[1\bar{1}0]_{GaAs}$ and the IP easy axis $[110]_{GaAs}$, respectively, in $\{\alpha, \xi\}$ space. The red dashed lines encircle the best fit points in parameter space and are the 2σ contours based on the reduced scaled χ^2. The grayscale increments represent 1, 2, 3, 4, and 5σ confidence intervals; the hashed area is outside of the 5σ region.The arrows in (a,c) point to the choice of parameters used to generate the lines in (b,d), respectively, which represent the contributions (see legend in (d)) to the linewidth given by Eq. 3.12. The parameters used to generate the lines in (b) are $\alpha = 9 \times 10^{-4}$, $\xi = 110$ nm, and $H' = 33$ Oe, and for (d) are $\alpha = 1.7 \times 10^{-3}$, $\xi = 5$ nm, and $H' = 1.2$ kOe.

the SNR was excellent, the results of the fitting constrain α and ξ with good precision. The extracted parameters for magnetization along $[1\bar{1}0]_{GaAs}$ are $\alpha = 9 \times 10^{-4}$ and $\xi = 106$ nm. By inspecting the 2, 3, and 4σ contours shown in Fig. 3.14(a) it can be seen that there is some uncertainty in the best-fit, but α certainly cannot be much larger than 10^{-3}. Recall that in Fig. 3.11(b), the linear fit to the OOP linewidth data for which $\Delta H_{TMS} = 0$ gave $\alpha = 1.7 \times 10^{-3}$, which is nearly a factor of two larger. So, in these CFS/GaAs films it appears α is not isotropic, but varies depending on the orientation of the saturated magnetization about which FMR is excited. A peculiarity of Fig. 3.14(a) is that an area with $\alpha \leq 10^{-4}$ equivalently gives a low χ^2. We have disregarded this χ^2 minimum because the OOP α value is 1.7×10^{-3}, and do not believe it is warranted to believe α is anisotropic by a factor of 10 or larger.

It must be emphasized that the fitting used here to identify the anisotropy of α in CFS does not depend sensitively on the nuances of the $C_{\boldsymbol{q}}(\xi)$ and $\Gamma_{0\boldsymbol{q}}$ used within Eq. 3.11, for which we have used the most generic expressions based on Gaussian disorder. The linewidths at 28 GHz for CFS OOP and CFS IP $[1\bar{1}0]_{GaAs}$ are nearly identical, while the latter shows a distinct TMS "knee" behavior. Therefore, the only way to reconcile the linewidth measurements along the two orientations is to invoke anisotropy in the Gilbert α contribution.

In fact, Gilmore et al. [105] and later Qu and Victora[131] have performed Kamberský damping calculations for realistic transition metal band structures and shown that it is not appropriate to treat α as an isotropic scalar, but rather damping is characterized by an anisotropic tensor quantity. Because FMR involves small cone-angle precession around the direction of the saturated magnetization, a scalar quantity in Eq. 3.1 is still appropriate to describe the dynamics along a given direction but α can vary depending on the orientation of the time-averaged magnetization[10] and the ellipticity of the orbit. Our results as described above show that for the CFS/GaAs(001) system, $\alpha_{[001]} > \alpha_{[1\bar{1}0]}$ (the growth is cube-on-cube, so for the OOP orientation the magnetization is saturated along [001]). While we are not aware of any calculations for the anisotropy of α for Heusler compounds, we note that the scale of the anisotropy we measure, nearly a factor of two, is similar to the scale of the calculated anisotropy for Fe, Ni, and Co[105, 131] where the intraband scattering (conductivitylike) mechanism of

[10] In the language of Ref. [105], here we are referring to *rotational anisotropy* of α.

Kamberský damping is dominant. To our knowledge, the only other report of anisotropy of the intrinsic damping constant was Rudd et al.[107], for bulk single-crystal Ni disks in the 1980s. (However it is not clear if eddy-current damping was accounted for by Rudd et al., as the Ni disks were larger than the microwave skin depth ~ 50 μm.)

Briefly, we note the results of the linewidth fitting for CFS magnetization IP along $[110]_{GaAs}$ summarized in Fig. 3.14(c) and (d) should be taken with a high degree of uncertainty, because the linewidth data had poorer SNR and did not possess a well-defined "knee" like the $[1\bar{1}0]_{GaAs}$ linewidth data. Because the χ^2 contours do not yield a unique point in α and ξ space, for the calculated lines shown in Fig. 3.14(d) we have shown a ξ best-fit with fixed intrinsic damping of $\alpha = 1.7 \times 10^{-3}$ fixed to the OOP value. In fact, due to the nearly linear nature of the data in Fig. 3.14(d) if α and ξ are left freely to vary with no constraints the best fit is near $\alpha = 6 \times 10^{-3}$ with negligible TMS contributions. While it is possible that α is anisotropic to this degree, we believe it is highly unlikely and in any case the fitting procedure cannot differentiate between the large TMS with short ξ possibility and large intrinsic α possibility, unlike the $[1\bar{1}0]_{GaAs}$ data in Fig. 3.14(b).

3.2.2 Future work to identify magnon-scattering defects

As we have shown in the CFA and CFS linewidth fitting contained in Fig. 3.13 and Fig. 3.14, we constrain the characteristic correlation length ξ responsible for the TMS mechanism to be of order 10-100 nm. In Ref. [116], the defects that result in inhomogeneity of the magnetic system were attributed to misfit dislocations. Motivated by the misfit dislocation interpretation of the defects, we have sketched Fig. 3.12 for the expected realization of defects given our fits to Eq. 3.12 for the CFA and CFS IP linewidth data. It should also be noted that in Ref. [112], good agreement was reported between the characteristic grain size ($\sim$ 30 nm) measured through Jade analysis of XRD and the TMS mechanism correlation length inferred from fitting FMR linewidth data.

It is likely that up until now, characterization techniques such as routine XRD and cross-sectional HAADF-STEM have failed to highlight the prevalence of these 10s-of-nm lengthscale defects in epitaxial thin films. For example, see HAADF-STEM images in Ref. [4] on similar Heusler growths, and Fig. 3.15 for X-ray characterization of the TMC250 CFA(24 nm)/MgO sample. In essence, both XRD and HAADF-STEM are

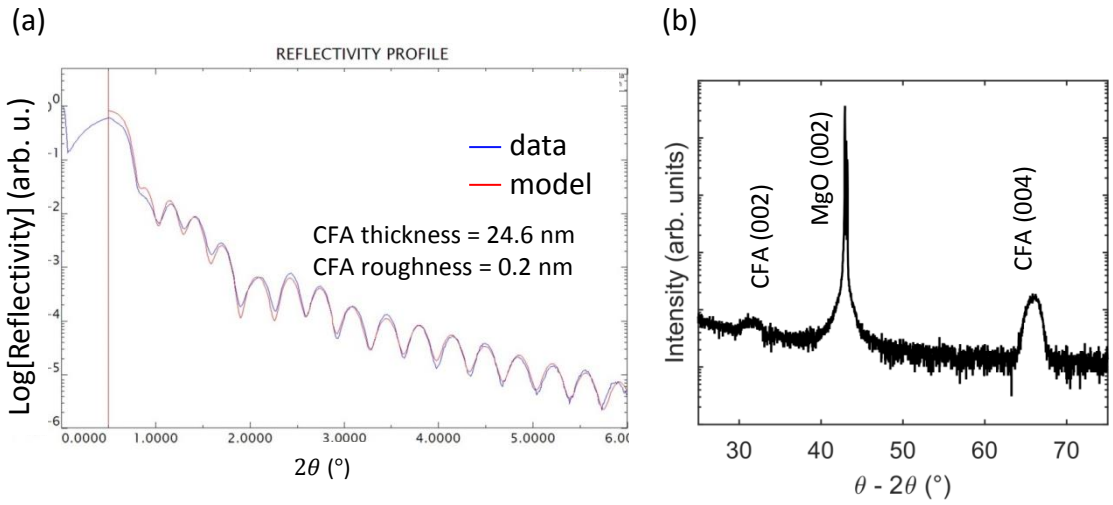

Figure 3.15: X-ray characterization of TMC250 growth. (a) Grazing-incidence X-ray reflectivity (GIXR) data (blue line) with model fits (red line). The corresponding parameters from the model fits are shown in the figure. (b) XRD data showing presence of 002 and 004 CFA peaks, indicating good crystalline texture and $B2$ or $L2_1$ order by presence of 002 peak. The data collection and analysis contained in this figure were performed by Anthony McFadden and Tobias Brown-Heft at UCSB.

based on interference and as such probe the presence of crystalline order but *by construct* wash out evidence of point-like defect structures. In the case of cross-sectional HAADF-STEM, the beautiful atomic "checkerboard" pattern can be misconstrued to imply that no defects exist in the field of view, but recall each apparent "atom" represents the Z-contrast averaged over a column of atoms the thickness of the slice imaged, which may be 50-100 nm thick.

To visualize the defects leading to the inhomogeneity of the magnetic system, the most powerful technique is likely plan-view TEM. In order to utilize plan-view TEM, however, the substrate must be removed to allow electron transmission. Another possibility is *in situ* scanning-tunnelling microscopy (STM). STM has been used effectively to visualize the epitaxial growth nucleation processes of ferromagnets on GaAs in Ref. [132], but the insulating nature of the MgO substrates presents a technical challenge for STM.

3.2.3 Conclusion

In conclusion, complete characterization of the FMR linewidth in epitaxial Heusler compound thin films has been performed, from which three critical results emerge. First, in all cases we observe large and anisotropic TMS linewidth contributions, implying inhomogeneity correlation lengthscales of order tens-to-hundreds of nanometers. The microscopic origin of these inhomogeneities is the subject of ongoing work, but are likely caused by arrays of misfit dislocations[116]. The lengthscales of these defects may cause them to be easily overlooked in epitaxial film characterization techniques such as XRD and HAADF-STEM, but give profound influence on magnetization dynamics. It is likely that, until this work, these defects and the associated TMS influence on the FMR linewidth have obscured confirmation of Kamberský's model for anisotropic and (in the case of Heusler compounds) ultralow intrinsic damping in metallic ferromagnets. Second, for epitaxial CFA thin films in which FMR was excited in the configuration with magnetization saturated out of the film plane, we have constrained $\alpha \leq 2 \times 10^{-4}$. To our knowledge, this is the lowest reported constraint for metallic ferromagnets, but is consistent in order-of-magnitude with Kamberský mechanism calculations performed for highly spin-polarized Heusler compounds[113]. Third and finally, for epitaxial CFS thin films we have observed an anisotropic Gilbert α, measuring $\alpha_{[001]}/\alpha_{[1\bar{1}0]} = 1.9$ and

qualitatively confirming the torque-correlation model predictions of Gilmore et al.[105] and Qu and Victora[131]. We have shown that by careful fitting of the in-plane linewidth including all contributions, constraints on the intrinsic damping may be reached notwithstanding the presence of the two-magnon linewidth. Heusler compounds, in particular, have been shown to give highly nonlinear and large two-magnon linewidths *because* the intrinsic damping value is low. Because of the ubiquity of TMS in thin-films, accounting for extrinsic TMS linewidths self-consistently with the underlying intrinsic damping of the material may prove valuable for the understanding of intrinsic damping processes in ferromagnets.

Chapter 4

Magnetothermoelectric coefficients in epitaxial Heusler compound thin films

In this chapter, a technique developed to measure (magneto)thermoelectric coefficients in thin films will be presented along with preliminary results for epitaxial Heusler compound thin films. This experiment was designed and carried out in close collaboration with Aaron Breidenbach, who performed most of the fabrication, measurement, and analysis presented here.

4.1 Introduction to thermoelectric coefficients

4.1.1 Phenomenology

Application of an electric field $E_\alpha \equiv \partial_\alpha V$ to a conductor eponymously results in flow of charge J_α, leading to the definition of the conductivity tensor $\sigma \equiv \rho^{-1}$ through Ohm's Law $J_\alpha = \sigma_{\alpha\beta} E_\beta$. Experimentally, σ is widely measured as a means to study the microscopic electronic properties in a given material through linear response. In Ohm's Law, the electrical current is a response to the perturbation from electrochemical equilibrium due to the application of a potential gradient. Alternatively, electrochemical equilibrium may be perturbed by application of a temperature gradient $\partial_\alpha T$ to a conductor,

which also causes an electrical current to flow. Ohm's Law may then be generalized to include temperature gradients and electrical gradients as

$$J_\alpha = \sigma_{\alpha\beta}(\partial_\beta V - S_{\beta\gamma}\partial_\gamma T), \tag{4.1}$$

which defines the thermoelectric tensor coefficients $S_{\alpha\gamma}$. (The minus sign is due to convention, and the sum over repeated indices is implied as is typical in Einstein notation.) Note than in Eq. 4.1, if steady-state current is prevented from flowing ($J_x = J_y = J_z = 0$) we have $\partial_\alpha V = S_{\alpha\beta}T_\beta$. Then, it is trivial to show through integration that if an infinite-impedance voltmeter is used to measure the voltage difference between hot and cold end of a conductor ΔV with temperature difference ΔT, the Seebeck coefficient $S \equiv S_{xx}$, which may be interchangeably referred to as the *thermopower*, is given by

$$S = -\frac{\Delta V}{\Delta T}. \tag{4.2}$$

An intuitive grasp of the Seebeck voltage ΔV can be gained by considering the energy-dependence of σ in a conductor. Itinerant charge carriers are distributed according to Fermi-Dirac statistics and, in general, there may be dependence on energy of the density-of-states (DOS), group velocities, or scattering times, all of which figure directly in σ. In Fig. 4.1, the carrier diffusion currents that results from the presence of a thermal gradient are indicated; "hot" carriers with excess energy diffuse from hot to cold, while an equal but opposite "cold" carrier current diffuses from cold to hot (if experimentally $J = 0$ is enforced by the open circuit configuration). However, if σ is a function of chemical potential, one may think that the Ohm's law voltages due to individual hot and cold diffusion currents do not exactly cancel, and the difference is the Seebeck voltage.

While the previous explanation motivated by Fig. 4.1 is commonly given at the introductory level, it is subtly deceiving as it seems to equate thermoelectric voltages to *electric* potential differences. Thermodynamically, it is more rigorous to consider the behavior of the *chemical* potential of a metal with varied temperature, and recall a voltmeter measures the *electrochemical* potential difference. Thus, if the two ends of a metal bar are held at different temperatures, a voltage will be measured. See Ref. [133] for a complete discussion of this oft-misunderstood subtlety of thermoelectric voltages.

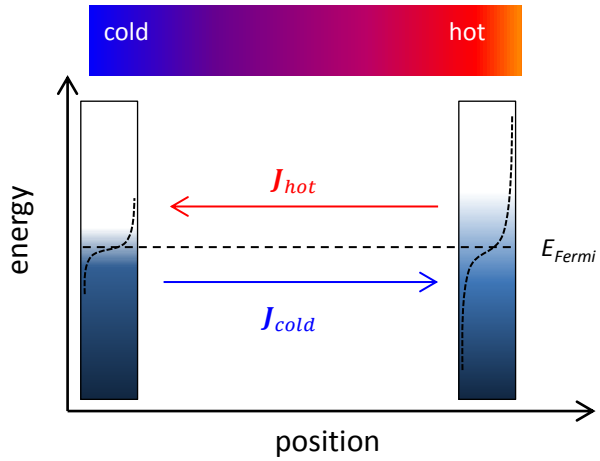

Figure 4.1: Schematic illustration of the mechanism that gives rise to the Seebeck effect. The left side is cold, the right side is hot. The shaded bars are meant to illustrate the Fermi occupation functions of a metal; the right side is more smeared due to the hot temperature. Carriers with excess energy (with respect to the Fermi level) diffuse towards the unfilled states to the left as shown by current J_{hot}, while lower energy carriers diffuse to the right. If total current is fixed at zero, a voltage can occur due to the differing conductivities experienced by high and low energy carriers.

4.1.2 Mott expressions for thermoelectric coefficients

Mott showed that when considering carrier diffusion processes in a single band metal or semiconductor, the thermoelectric coefficient tensor components may be expressed by[134]

$$S_{\alpha\beta} = -\frac{\frac{k_B}{e}\int \frac{E-\mu}{k_B T} c_{\alpha\beta}(E)(-df(E)/dE)dE}{\sigma}, \tag{4.3}$$

where it is understood that $\sigma \equiv \sigma_{xx} \equiv \rho_{xx}^{-1}$, and where $c_{\alpha\beta}(E)$ is a component of the energy-dependent conductivity tensor subject to the normalizing constraint

$$\sigma_{\alpha\beta} = \int c_{\alpha\beta}(E)(-df(E)/dE)dE, \tag{4.4}$$

μ is the chemical potential (or Fermi level), and $f(E)$ is the Fermi-Dirac occupation function. In metals where $c(E)$ is not a strong function of energy near μ, the Sommerfeld expansion can be used to give

$$S_{\alpha\beta} = -\frac{\pi^2 k_B^2 T}{3e}\frac{dc_{\alpha\beta}(\mu)/dE}{c(\mu)} + O[T^3]. \tag{4.5}$$

It should be emphasized at this stage that $c_{\alpha\beta}(E)$ is not an experimentally measurable quantity, only integral quantities such as Eq. 4.3 or Eq. 4.4 are measurable. Nonetheless, $c_{xx}(E)$ can be thought of in a Drude-like sense as the product of the energy-resolved DOS $D(E)$ and a relaxation time. The utility of Eq. 4.5 is that it emphasizes the role of DOS and temperature in thermoelectric coefficients: nonzero T is necessary to broaden the Fermi-Dirac occupation function and allow a distribution of carrier energies, and generally coefficients are larger for materials where μ lies near the top or bottom of bands, because of the strong energy-dependence of the DOS near band extrema.

It is understood through Boltzmann transport theory that when time-reversal symmetry is broken through application of a magnetic field or presence of a magnetization, off-diagonal components of the conductivity tensor (e.g. σ_{xy}) may be nonzero provided $\sigma_{\alpha\beta} = -\sigma_{\beta\alpha}$. These off-diagonal conductivity tensor components give rise to the familiar family of Hall effects, such as the ordinary, planar, and anomalous Hall effects. In analogy to these, ordinary, planar, and anomalous off-diagonal thermoelectric coefficients arise naturally from Eq. 4.3. Collectively, these are termed Nernst effects. Equation 4.5 expresses these coefficients in terms of energy dependent conductivity tensor components, containing an energy derivative of the corresponding conductivity

tensor component and factor of $k_B T$. These low energy linear expansion relations are known collectively as *Mott relations*, which have proven widely applicable in relating electrical transport coefficients $\sigma_{\alpha\beta}$ to thermoelectric coefficients $S_{\alpha\beta}$.

4.1.3 Dragging effects on thermoelectric coefficients

The Mott relation (Eq. 4.5) is a result of solving the diffusion equation for charge carriers out of thermal equilibrium. Charge carriers such as electrons or holes are not the only excitations, however, that flow in the direction of a thermal gradient. In particular, phonons or magnons, which are the respective elementary excitations of the lattice and magnetization, also flow in the presence of a thermal gradient ∇T. Clearly, phonon or magnon flow is not directly measurable with a voltmeter because they carry no charge, and moreover their number is not conserved. (Note that phonon and magnon thermal currents can be inferred with bolometers and spin current detectors, respectively.)

However, while they do not carry electrical charge, phonon or magnon thermal currents can indirectly influence thermoelectric coefficients through *dragging* effects. Phenomenologically, this can be understood in a coupled two-fluid model describing the electron drift velocity v^e and the phonon (magnon) drift velocity $v^{p(m)}$. For the case of electrons and phonons, the phenomenological equations are[135]

$$\frac{dv_\alpha^e}{dt} = \frac{e}{m}\left(E_i - S_{\alpha\beta}\partial_\beta T - \frac{v_\alpha^e}{\tau_e}\right) - \frac{v_\alpha^e - v_\alpha^p}{\tau_{pe}}, \tag{4.6}$$

and

$$\frac{dv_\alpha^p}{dt} = \frac{c_p}{n_p}\partial_\alpha T - \frac{v_\alpha^p}{\tau_p} - \frac{v_\alpha^p - v_\alpha^e}{\tau_{ep}}, \tag{4.7}$$

where τ_e and τ_p are transport scattering times for electrons and phonons, respectively, c_p is the phonon specific heat capacity, n_p is the phonon density, and the final two terms in both equations describe the coupling drag effect through the electron-phonon scattering time τ_{pe} and the phonon-electron scattering time τ_{ep}.

It is easily shown that the influence of Eq. 4.7 on the thermoelectric transport is equivalent to adding an additional term to the $S_{\alpha\beta}$ Mott term in Eq. 4.6, that is $S_{\alpha\beta} \to S_{\alpha\beta} + S_{pd}$. S_{pd} is the *phonon drag* contribution to the thermoelectric coefficient. An analogous S_{md} may occur due to *magnon drag* in ferromagnetic metals. Blatt et

al.[136] have shown that

$$S_{pd} = \frac{c_p}{3ne}\left(\frac{\tau_p'}{\tau_p' + \tau_{pe}}\right) \tag{4.8}$$

and

$$S_{md} = \frac{c_m}{3ne}\left(\frac{\tau_m'}{\tau_m' + \tau_{me}}\right) \tag{4.9}$$

where n is the electron density, c_p and c_m are the phonon and magnon contributions to the specific heat capacity, and the primes denote the phonon and magnon scattering times due to all other scattering processes. (Note that Eq. 4.8 and Eq. B.1 describe longitudinal Seebeck coefficients, and the subscripts are for labelling clarity and do not represent tensor indices such as those in Eq. 4.3. A more rigorous approach using Boltzmann transport gives the same result as the simple fluid model[137].) Equations 4.8 and B.1 are convenient because they allow simple predictions for the behavior of the dragging contributions based on the specific heat. First and foremost, it can be seen that in order to maximize drag contributions the scattering rate of the dragging excitation should be dominated by electron scattering, e.g. $\tau_{pe} \ll \tau_p'$. If other scattering processes dominate the scattering time, only a small fraction of the excitation scattering events will contribute to drag on the electrons. Second, if the latter condition is maximized such that the scattering time ratio in Eq. 4.8 and Eq. B.1 is near unity, the drag contribution to the Seebeck coefficient will scale with the relevant excitations specific heat capacity. For ferromagnetic magnons $c_m \propto T^{3/2}$, while for phonons below the Debye temperature $c_p \propto T^3$[23].

In principle, phonon drag contributions to the Seebeck coefficient may be very large due to the large value of c_p (the phonon contribution to the specific heat is typically dominant). However, the condition $\tau_{pe} \ll \tau_p'$ is only satisfied for low temperatures, typically much less than 200 K, where Umklapp phonon-phonon scattering processes are not dominant. Because of this, contributions to the Seebeck coefficient from phonon drag are significant only for highly crystalline materials at low temperatures[136, 138], and are considered negligible at room temperature and above.

Magnon drag contributions to the Seebeck coefficient are typically considered to be very small with respect to the phonon drag (Eq. 4.8) and diffusion (Eq. 4.5) contributions, because c_m is very small, typically a factor of $10^2 - 10^3$ smaller than c_p[136]. For example, Blatt et al.[136] have estimated $S_{md} \simeq 10^{-2}$ μV/K for Ni and Fe at 50 K.

Notwithstanding these considerations, magnon drag has a controversial history and has been invoked to explain the strange Seebeck coefficient of Fe[138]. More recently, Watzman et al.[135] have again attributed the low-temperature Fe and Co Seebeck coefficients to magnon drag, and claim to reach good agreement with a magnon drag calculation with no free fitting parameters. However, it should be noted that Watzman's Seebeck coefficient data certainly does not show the clear $T^{3/2}$ behavior expected for magnon drag, and in order to reach quantitative agreement only the *sp* electron density was used as n in the denominator of Eq. B.1 (which is two orders of magnitude lower than the total *sp* and *d* electron density).

In the sections below, we will focus on the diffusive contributions for the thermoelectric coefficients given by Eq. 4.5. As we will show in the results section, only at low temperature do we see small contributions due to phonon drag.

4.2 Motivation for (magneto)thermoelectric measurements in Heusler compounds

Full Heusler compounds with chemical formula Co_2YZ are of interest because of their tendency to have nearly half-metallic, or half-metallic band structures[139]. Seebeck coefficient measurements have been performed by Balke et al.[140], who showed relatively large and negative Seebeck coefficients ($|S| = 5 - 55\ \mu V/K$ at 300 K) for a variety of Co_2-based Heusler compounds. Similarly, Hayashi et al.[141] have reported negative Seebeck coefficients in Co_2YZ ternary full-Heusler compounds, which in the case of Co_2MnSi was used to argue that the highly spin-polarized *d*-bands contributed negligibly to transport.

References [139, 141] measured bulk crystals prepared by arc-melting and sintering or annealing. However, in spintronic devices Heusler compounds are typically found in thin film form, deposited by a variety of techniques. In this chapter, we focus on epitaxial thin films of Heusler compounds, which may be readily grown on lattice-matched insulating substrates. It should be emphasized that resistivity values in Heusler thin films typically range from several tens to $\sim 100\ \mu\Omega$cm, due to the abundance of disorder realizations in the large multi-element unit cells from nonequilibrium thin film growth techniques. Critically, the advantage of thermoelectric coefficients over

electrical transport coefficients (e.g. resistivity) is that the scattering rate cancels out of expressions such as Eq. 4.5(to first approximation), so that the measured coefficients may be directly equated to the band structure of the material and do not depend strongly on disorder. Characterization of thin film thermoelectric coefficients and comparison to bulk values provides a sensitive method to compare thin film band structure to that of the bulk. Furthermore, a logical extension of the Seebeck thermoelectric measurements is to anomalous Nernst coefficients, because the anomalous Nernst coefficients contain information about the *spin-resolved* band structure near the Fermi level.

4.2.1 Boltzmann transport expressions for $c_{\alpha\beta}$

Equation 4.3 specifies $S_{\alpha\beta}$ thermoelectric coefficients in terms of temperature and energy-resolved conductivities $c_{\alpha\beta}$, and results in the useful Mott relations. However, to connect measured thermoelectric coefficients to realistic band structure a framework for expressing $c_{\alpha\beta}$ is needed. This is achieved through Boltzmann transport theory, which begins with the Boltzmann equation

$$\frac{df_{\boldsymbol{k}}}{dt} = \left(\frac{df_{\boldsymbol{k}}}{dt}\right)_{field} + \left(\frac{df_{\boldsymbol{k}}}{dt}\right)_{diff} + \left(\frac{df_{\boldsymbol{k}}}{dt}\right)_{scatt}, \tag{4.10}$$

which governs the distribution function of carriers $f_{\boldsymbol{k}}$ in response to influence of an external field, diffusion, or scattering. In the absence of perturbations, $f_{\boldsymbol{k}}$ is equivalent to the Fermi-Dirac distribution. A pedagogical introduction to Boltzmann transport theory can be found in Yu and Cardona[142] or Ziman[137]. Because our measurements will give the Seebeck and anomalous Nernst coefficients, we briefly introduce Boltzmann transport expressions for the respective energy-dependent conductivities.

Seebeck coefficient

In the case of the Seebeck coefficient, the on-diagonal components c_{xx} are relevant. They may be calculated within the relaxation time-approximation to Eq. 4.10, by introduction of a momentum relaxation time $\tau(E)$ of $f_{\boldsymbol{k}}$ that is, in general, a function of energy. One can show[137, 142] that within this approximation, $c_{xx}(E)$ can be related to the band dispersion relations $E_i(k)$ by

$$c_{\alpha\beta}(E,T) = \frac{1}{(2\pi)^3}\Sigma_i \int (d^3\boldsymbol{k}) \frac{e^2\tau_i(T)}{\hbar^2} \frac{\partial E_i(k)}{\partial k_\alpha} \frac{\partial E_i(k)}{\partial k_\beta} \delta(E - E_i(k)), \tag{4.11}$$

where α, β run over x, y, z, i denotes the band index, and $\tau_i(T)$ is the ith band relaxation time. Note that because $\int (d^3\boldsymbol{k})\delta(E - E_{\boldsymbol{k}}) \equiv D(E)$ (the DOS at energy E), Eq. 4.11 for the case of an isotropic band dispersion is simply the product of the relaxation time, the DOS, and the band group velocity at energy E. Density-functional theory (DFT) calculations have been performed for ternary full-Heusler compounds[139, 143], such as those with dispersion relations shown in Fig. 4.2. Given these band dispersions, if one assumes a band and energy independent $\tau_i(E) \to \tau$, Eq. 4.11 may be combined with Eq. 4.3 to generate predicted Seebeck coefficients that may be compared to measurements.

To give some intuition for magnitudes and signs, we evaluate Eq. 4.5 for the case of free-electron like isotropic parabolic band dispersions given by $E(\boldsymbol{k}) = E^0 + \hbar^2 k^2/2m$. It can be shown that the result for the longitudinal diffusive thermopower S for a single band metal dominated by impurity scattering is[136]

$$S = \frac{\pi^2 k_B^2 T}{3eE_F}, \tag{4.12}$$

where E_F is the Fermi level taken with respect to the bottom of the contributing band, and the electron charge e is taken to be negative for upward dispersing electron-like bands (if hole-like bands, E_F is taken with respect to the top of the band and e is positive). From Eq. 4.11, Eq. 4.12 can be generalized to include multiple bands labelled by i, so we have

$$S = \frac{\pi^2 k_B^2 T}{2} \frac{\Sigma_i \tau_i m_i^{1/2} E_i^{1/2}}{\Sigma_i e\tau_i m_i^{1/2} E_i^{3/2}}, \tag{4.13}$$

where τ_i and m_i are respectively the scattering time and effective mass of the ith band. The band Fermi level E_i in Eq. 4.13 is taken with regard to the bottom of band i.

An example evaluation of Eq. 4.13 is shown in Fig. 4.3 for the case of a light band crossed by a heavier band, which is meant to resemble the band dispersions shown in Fig. 4.2, which consist of upward dispersing *sp* bands (bandwidth ~ 5 eV) with flatter *d* bands (bandwidth ~ 0.5 eV) near the Fermi level. The results shown in Fig. 4.3 are typical for metals; for Fermi level $\sim 5 - 10$ eV the expected thermopower is only a few μV/K at 300 K. If the Fermi level lies nearer a band extrema the thermopower may be significantly larger, perhaps tens of μV/K. Where multiple bands are present, the total thermopower via Eq. 4.13 is a weighted average of single band thermopower with weighting factor $\tau_i m_i^{1/2}$.

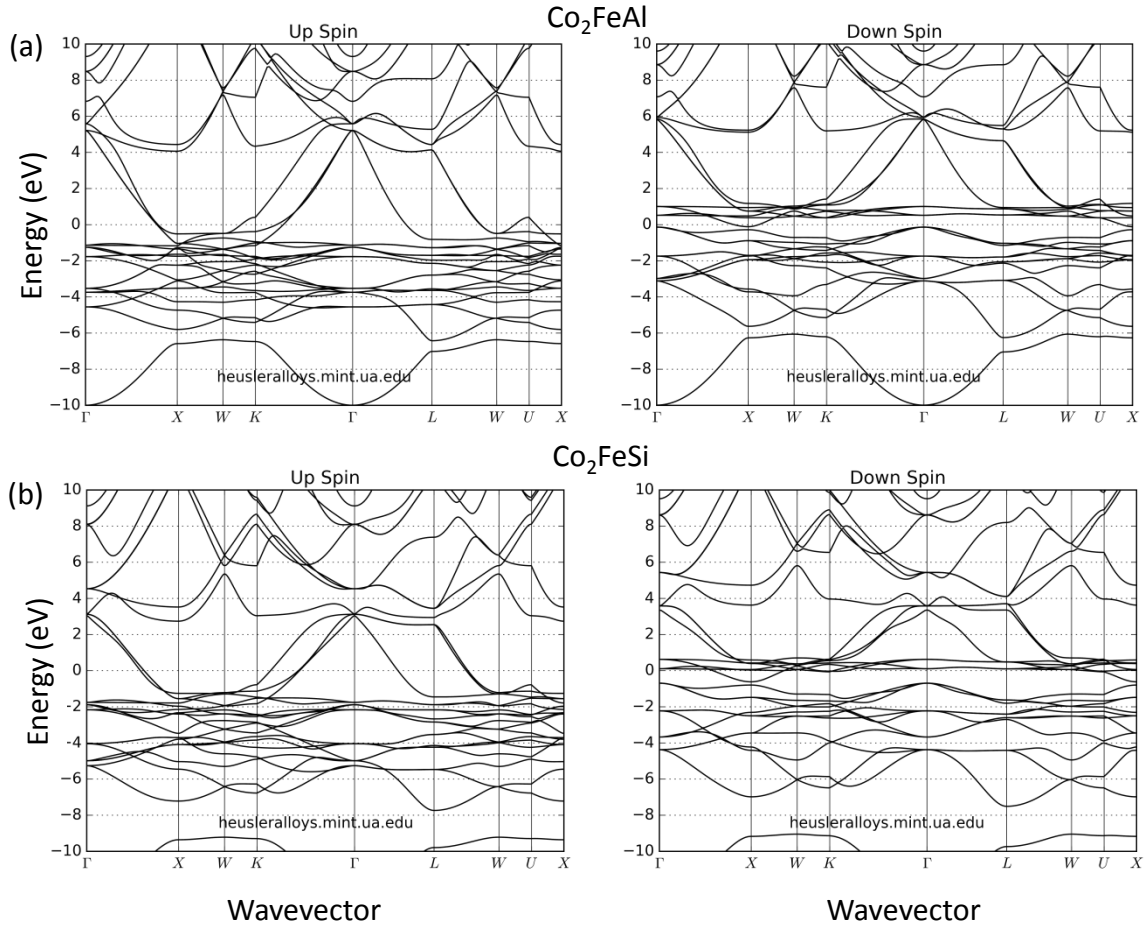

Figure 4.2: Spin-resolved density-functional theory calculated dispersion relations for majority (up spin, left column) and minority (down spin, right column) states in full-Heusler compounds. Majority corresponds to the direction of the magnetization. Row 1 (a) is for $L2_1$ ordered Co_2FeAl, and row 2 (b) is for $L2_1$ ordered Co_2FeSi. Zero energy is the chemical potential, at which the integrated density-of-states for Co_2FeAl is 75% majority polarized and for Co_2FeSi is 72% minority polarized. These plots were taken from `http://heusleralloys.mint.ua.edu/`, and were calculated using the Vienna Ab-Initio Simulation Package (VASP)[144].

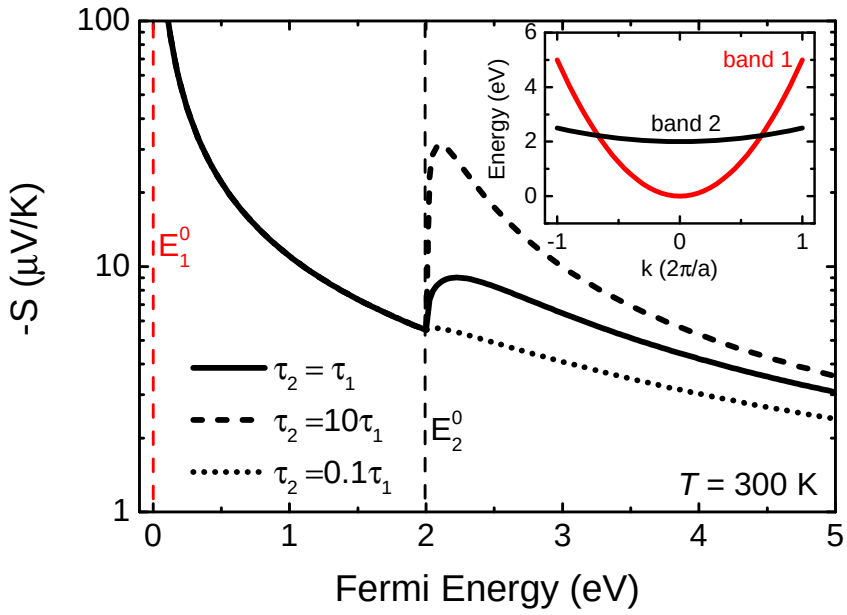

Figure 4.3: Inverse-thermopower ($-S$) vs Fermi level for the toy band dispersions shown in the inset. For unit cell size $a = 6$ Angstroms, the band 1 dispersion corresponds to effective mass $m_1/m_0 = 0.83$ (bandwidth 5 eV) and band 2 dispersion to $m_1/m_0 = 8.3$ (bandwidth 0.5 eV), where $m_0 = 9.11 \times 10^{-31}$ kg is the free-electron mass. Band 2 is offset +2 eV with respect to band 1 to crudely simulate the flat d bands shown in Fig. 4.2. The solid, dashed, and dotted lines illustrate the case for different choices of band scattering times as indicated in the legend. The temperature is set at 300 K.

Anomalous Nernst coefficient

For the case of the anomalous Nernst coefficient, an expression for the off-diagonal components c_{xy}^A is needed. The superscript A will be used to differentiate anomalous Nernst effects, which depend on the magnetization and persist in zero field, from ordinary Nernst effects that depend only the magnetic field.

The anomalous Nernst effect S_{xy}^A is not captured by Eq. 4.11 because at the level of Eq. 4.11 off-diagonal terms are clearly zero. Physically, this is due to time-reversal symmetry.[1] However, in the presence of an external magnetic field or a magnetization that explicitly break time-reversal symmetry c_{xy} is not in general zero, which may be thought of in a semiclassical picture as due to Lorentz-like transverse forces. In the equations of motion of a Bloch wavepacket at real-space coordinate $\boldsymbol{r}$ with wavevector $\boldsymbol{k}$ in electric field $\boldsymbol{E}$, these effects are formally described by the inclusion of the momentum-space Berry curvature[41, 145],

$$\hbar\dot{\boldsymbol{k}} = -e\boldsymbol{E}, \tag{4.14}$$

$$\dot{\boldsymbol{r}} = \frac{\partial E(\boldsymbol{k})}{\partial \boldsymbol{k}} - \hbar\dot{\boldsymbol{k}} \times \boldsymbol{b}(\boldsymbol{k}), \tag{4.15}$$

where $\boldsymbol{b}(\boldsymbol{k}) = \nabla \times \boldsymbol{a}$ is the Berry curvature of state $\boldsymbol{k}$ and $\boldsymbol{a}$ is the Berry phase or connection. For physical intuition, note that for externally applied magnetic fields $\boldsymbol{b}(\boldsymbol{k})$ is simply given by the magnetic field, where $\boldsymbol{a}$ is the vector potential, and Eqs. 4.14 and 4.15 would give rise to the ordinary Hall effect if included in the Boltzmann Equation 4.10.

In the case of the intrinsic anomalous Hall effect, $\boldsymbol{b}(\boldsymbol{k})$ is predominantly determined by the $\boldsymbol{k}$-dependent spin-orbit field introduced in Chapter 1.[2] It can be shown[41, 146–148] that the Berry curvature integrated over all filled bands determines the intrinsic AHE through

$$\sigma_{xy}^A = -\frac{e^2}{\hbar}\int \frac{d^3\boldsymbol{k}}{(2\pi)^3} b_z(\boldsymbol{k}) f_{\boldsymbol{k}}. \tag{4.16}$$

[1] As is usual, here we mean *local* time-reversal symmetry (i.e. magnetization or magnetic field do not invert upon applying the $T : t \to -t$ operator) *Global* T-symmetry is believed to apply, which enforces $\sigma_{xy} = -\sigma_{yx}$.

[2] Note that demagnetization fields should *not* be thought of as determining $\boldsymbol{b}(\boldsymbol{k})$ and hence the AHE/ANE. This geometric explanation for the AHE was ruled out in the early days of the AHE.

whence

$$c_{xy}^{A}(E) = \frac{e^2}{\hbar}\frac{1}{(2\pi)^3}\Sigma_i \int (d^3\boldsymbol{k}) b_z \delta(E - E_i(k)). \tag{4.17}$$

Because the anomalous Nernst effect can be described by the dependence of Eq. 4.16 on electrochemical potential through the Mott relation (Eq. 4.5), a Sommerfeld expansion expected to hold for low temperatures gives[147]

$$\alpha_{xy}^{A} \equiv S_{xy}^{A}\sigma = \frac{\pi^2 k_B^2 T}{3e}\frac{d\sigma_{xy}^{A}(\mu)}{dE}. \tag{4.18}$$

To our knowledge, calculations of Eq. 4.18 have not been performed for realistic transition-metal ferromagnet band structures. However, a straightforward extension of the intrinsic AHE conductivity calculations (e.g. those described for bcc Fe performed by Yao et al.[146]) should allow prediction of ANE coefficients, which may be compared to experimental data. For example, reasonable agreement between experiment and theory has been reached for ANE coefficients in $CuCr_2Se_{4-x}Br_x$[147, 149]. We expect that valuable information regarding the spin-resolved DOS at the chemical potential is encoded in the anomalous Nernst coefficient.

At the level of Eq. 4.16 and the ANE corresponding Eq. 4.18, the behaviors of σ_{xy}^{A} and α_{xy}^{A} may be rather opaque because factors determining $\boldsymbol{b}(\boldsymbol{k})$ for realistic band structures have not been discussed. As pointed out in Refs.[41, 146], the Berry curvature b_z is always strongly enhanced near avoided level crossings in the band structure, and opposite in sign for upper and lower bands. The strong enhancement near avoided level crossings is intuitive when we recall $\boldsymbol{b}(\boldsymbol{k})$ is determined by the SOI, which from a perturbation theory perspective is always largest when bands of differing orbital character are nearly degenerate. With this intuition in mind, it should be expected that the largest σ_{xy}^{A} and α_{xy}^{A} should be found in materials where an avoided level crossing occurs near the chemical potential, so that upper and lower band contributions do not cancel.

4.3 Ac thermoelectric measurement technique

4.3.1 Device design and hardware

We have devised a unique (to our knowledge) all-electrical device to measure magnetothermoelectric (MTE) coefficients of metallic thin films on insulating substrates, which

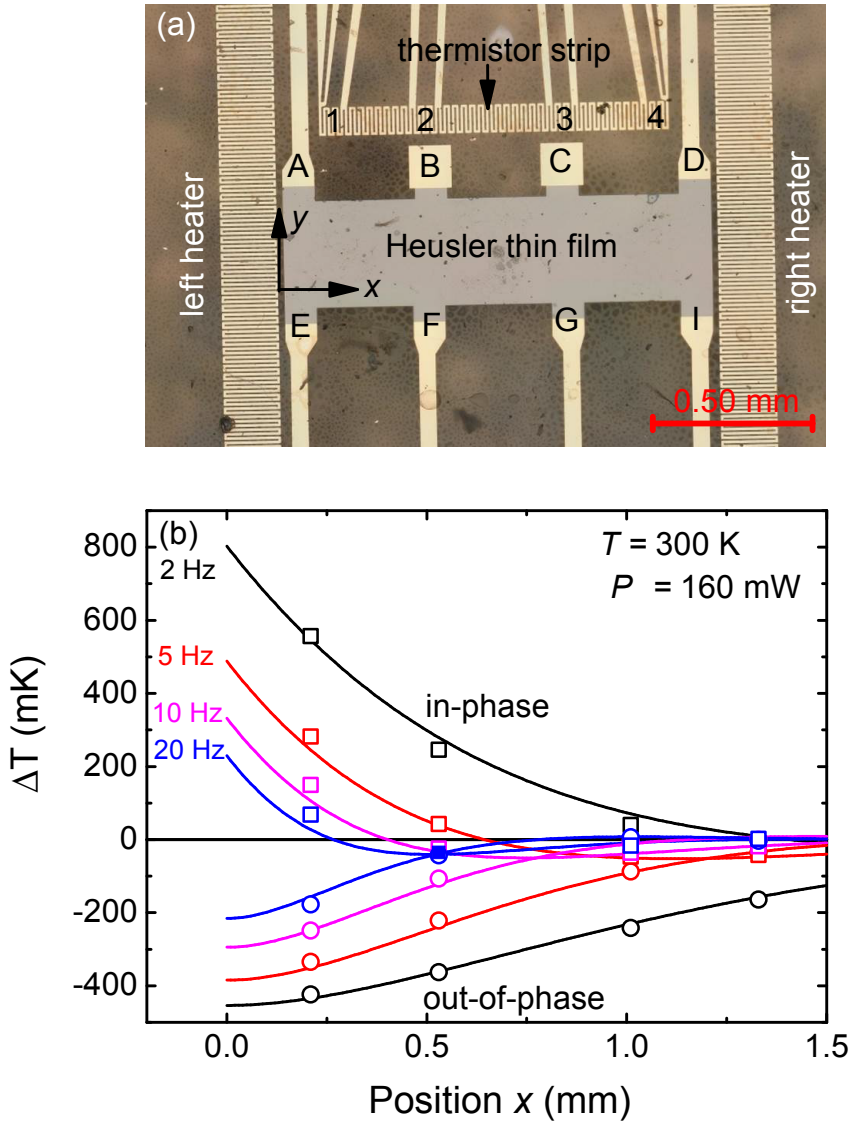

Figure 4.4: (a) Optical plan-view micrograph of the device design used to measure magnetothermoelectric coefficients. All heaters, thermistors, and bonding pads are 5 nm Ti/50 nm Au. (b) Complex ΔT values for thermistors 1-4 as function of coordinate x taken from edge of the left heater. The squares are the in-phase with heater power quadrature while the circles are the out-of-phase quadrature, and data for several drive frequencies ω are shown as indicated. The data shown in (b) are taken on TMC249 at 9 mA RMS heater excitation, which corresponds to 160 mW.

may be fabricated through straightforward top-down photolithography techniques (i.e. ion milling, e-beam evaporation of metals and liftoff). Critically, our design does not rely on careful sample mounting, macroscopic (m̃m) bulk material volume, or thermocouple use. An example MTE device is shown in Fig. 4.4(a). A Hall bar is patterned from the Heusler film through Ar^+ ion milling, and subsequently a Ti(5 nm)/Au(50 nm) layer defined by e-beam evaporation at $\sim 10^{-6}$ Torr. The Ti/Au layer defines the bonding pads and vias, heaters, and thermistor strip which are electrically isolated through the insulating substrate. See Appendix D.0.3 for further fabrication details. The serpentine resistive heater elements shown on the left and right of the Hall bar in Fig. 4.4(a) may be used to create a thermal gradient $\partial_x T$ along the Hall bar, with $\partial_x T \gg \partial_y T$ ensured by the device aspect ratio. The thermistor strip indicated in Fig. 4.4(a) allows for 4-wire resistance measurements of the sections labelled 1-4. The residual resistivity ratio of the Ti/Au was typically $2-3$ (giving adequate thermistor action from 20-400 K), and the typical 2-wire resistances of the heaters R_h ∼1-2 kΩ, and 4-wire resistance of the thermistors $\sim 100\ \Omega$.

A phase-sensitive harmonic lock-in technique was used to measure both the thermistor local temperature changes and thermoelectric voltages on the Hall bar upon application of Joule heating power to the heater elements. An ac excitation current $I = \sqrt{2} I_h \sin \omega t$ was driven through the heater at frequency ω, which resulted in a local power dissipation $P = I^2 R_h$. Then, with ac excitation at ω we have

$$P(t) = I_h^2 R_h (1 - \cos 2\omega t), \tag{4.19}$$

in which it is clear that the power dissipated in the heater element has an ac component at 2ω. Phase-sensitive lock-in detection was used to monitor all thermoelectric voltages and thermistor resistance changes at 2ω, ensuring that the effects measured were due to the applied ac heater power. The thermistor elements were used to measure the ac thermal profile created in the device upon application of a heater power. A dc probe current ($I_p = 1$ mA typical) was passed through the thermistor strip, and 4-wire resistance measurements recorded over elements 1-4 shown in Fig. 4.4(a). The 4-wire resistances of elements 1-4 were measured previously as a calibration to give dR/dT as a function of temperature for each element, so that the local ac temperature profile ΔT_i

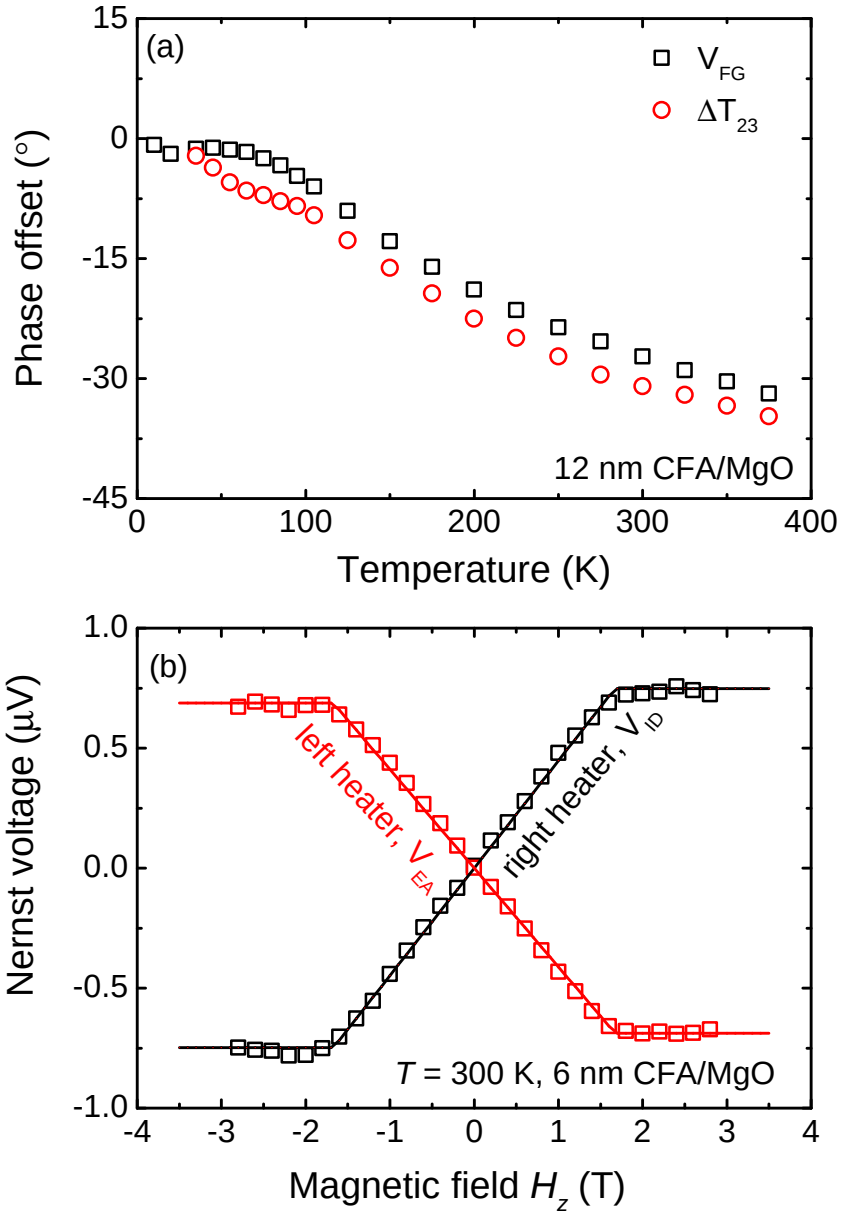

Figure 4.5: (a) Comparison of phase offset with respect to heater power for Seebeck voltage (black squares) and thermistor ΔT readings at $\omega = 10$ Hz excitation. (b) Nernst voltage (in-phase 2ω component with $\omega = 2$ Hz heater drive) field sweeps for left heater and right heater configurations, illustrating the inversion of sign with inverted ∇T orientation. The solid lines are fits. A constant background has been removed from the raw data. The power used was 130 mW. The data shown in (a) are for the TMC249 structure (12 nm CFA), and the data in (b) are taken on TMC252 (6 nm CFA).

of the ith thermistor element could be determined through

$$\Delta T_i = \frac{V_i^{2\omega}}{I_p}\left(\frac{dR_i}{dT}\right)^{-1}, \tag{4.20}$$

where $V_i^{2\omega}$ is the second harmonic voltage measured over a thermistor element i through lock-in detection, and contains both in-phase and out-of-phase quadrature components with respect to the heater excitation.[3] Although in principal $V_i^{2\omega}$ may include Seebeck voltages built up along the Au element, it was verified that $V_i^{2\omega}$ inverted sign with inverting I_p, implying these contributions were negligible for the I_p values used.

Example spatial ΔT profiles measured from Eq. 4.20 on the device shown in Fig. 4.4(a) are shown in Fig. 4.4(b) for several choices of drive frequency ω, which are plotted for thermistors 1-4 as a function of their distance x from the heater element. In general, we observed a spatial dependence of the magnitude and phase of ΔT along the thermistor strip that was nontrivial, motivating the model fits shown in Fig. 4.4(b). The spatial model of the ac temperature profile to which the fits correspond will be discussed in the following section.

4.3.2 Spatial and temporal model of temperature profile

To understand the spatial and temporal temperature profile in our device, such as that shown Fig. 4.4(b), we derived an analytic time-varying model of heat diffusion in our device. The model not only sheds light on the physical parameters that determine the thermal profile, but in addition when fit to the thermometry data allows extrapolation of the thermal profile to arbitrary position coordinate x.

We begin by writing the inhomogeneous heat diffusion equation, which follows directly from Fourier's law $Q = -\kappa\nabla T$ and conservation of energy $C\dot{T} = -\nabla Q$ (where κ is the thermal conductivity and C the specific heat capacity)

$$\frac{dT(\boldsymbol{r},t)}{dt} = D\nabla^2 T + f(\boldsymbol{r},t), \tag{4.21}$$

where $D \equiv \kappa/C$ is the thermal diffusivity and $f(\boldsymbol{r},t)$ is the inhomogeneous source term, which is in general a function of position and time. In the geometry of our experiment,

[3] Because of the $-\cos 2\omega t$ factor in Eq. 4.19, care must be taken to transform the as-recorded lock-in Y quadrature to $-X$, and the as-recorded X quadrature to Y.

we may simplify to one dimension x, but account for heat flow in the z direction (into the substrate and underlying copper block) by adding a relaxation term $-rT$, so that the homogeneous part of Eq. 4.21 may be simplified as

$$\frac{dT(x,t)}{dt} = D\partial_x^2 T - rT. \tag{4.22}$$

The simplification of three-dimensional heat diffusion to one dimension with an added term $-rT$ is appropriate for the aspect ratio of our experiment, which is elongated in the y-direction shown, because the substrate thickness is smaller than the thermal diffusion length, and the large heat capacity and thermal conductivity of the copper block below the substrate (the chip is held to the copper block with a thin layer of thermal grease).

To solve Eq. 4.22, we look for harmonic separable solutions of the form $T(x,t) = \mathrm{T}(x)\tau(t) = \mathrm{T}(x)e^{i\omega' t}$. Inserting into Eq. 4.22 and manipulating we have

$$0 = \partial_x^2 T + k^2 T, k = i\left(\frac{r + i\omega'}{D}\right)^{1/2}, \tag{4.23}$$

which is the well-known Helmholtz equation. The Green's function solution (l.h.s. equals $-\delta(x)$) of Eq. 4.23 is $G(x) = ie^{ik|x|}/2k$, so that we may write

$$T(x,t) = A\frac{e^{\left(\frac{r+i\omega'}{D}\right)^{1/2}|x|}}{2\left(\frac{r+i\omega'}{D}\right)^{1/2}}e^{i\omega' t}, \tag{4.24}$$

where A is a constant of proportionality related to the applied heater power and the heat capacity of the system. Note that the prefactor before the $e^{i\omega' t}$ is in general complex, leading to a spatial dependence of the magnitude and phase of $T(x,t)$. The fits to Eq. 4.24 with A, r, and D as fitting parameters, and $\omega' = 2\omega$ are shown in Fig. 4.4(b), where it can be seen that the spatial and frequency-dependence of the thermistor magnitudes and phases are well-described by Eq. 4.24. While several frequencies are shown in Fig. 4.4(b), after verification of the validity of the model typically only one frequency was used for temperature-dependent data. Note that because each ΔT_i thermistor recording specified magnitude and phase, effectively 8 (rather than 4) data points are fitted to. In addition, it was verified that the fitted D values agree well with literature MgO thermal diffusivity data. For example, the TMC249 device fit gave $D = 15$ mm^{2}s^{-1} at 300 K, which is in good agreement with the MgO value reported by Hofmeister[150].

4.4 Results and discussion

With the spatial and temporal profile of the temperature created by application of heater power characterized by the thermistor data fits to Eq. 4.24, Seebeck and Nernst voltages measured on the Heusler Hall bar could be used to calculate the corresponding Seebeck and anomalous Nernst coefficients.

4.4.1 Seebeck coefficient results in Heusler thin films

First, we describe the Seebeck coefficient measurement. The Seebeck voltage could be measured using pairs of Hall arm leads shown in Fig. 4.4(a), for example V_{EF} or V_{FG}. While pairs closest to the heater used gave the largest Seebeck voltages, typically the middle pair (i.e. V_{FG}) were used to mitigate Seebeck contributions from the Au vias, which build up if ∇T is not entirely in the x-direction. ($\partial_y T$ would be largest near at the end regions of the heater elements, which are not shown in Fig. 4.4(a). It is for this reason the Au vias run perpendicular to the x-direction.) In any case, because the Seebeck coefficient of Au is less than a few $\mu V/K$ over the entire temperature range we have measured[151], any spurious contamination from these Au contributions will only slightly modify the extracted Heusler film Seebeck coefficients, which are larger by a factor of 10 or more. The phase of the Seebeck voltage with respect to heater power is nearly identical to that predicted by the fits to Eq. 4.24 over a broad temperature range, for an example plot see Fig. 4.5(a). Then, the Seebeck coefficient may be calculated as $S = -\mathrm{sgn}(V_{FG}^{2\omega})|V_{FG}^{2\omega}|/|T_F - T_G|$, where the vertical bars represent the modulus of a complex number and $\mathrm{sgn}(V_{FG}^{2\omega})$ is taken with respect to $T_F - T_G$.

Seebeck coefficient results for a 12 nm Co_2FeAl(CFA) film grown on MgO(001) (TMC249) and a 5 nm Co_2FeSi(CFS) film grown on GaAs(001) are summarized in Fig. 4.6(a) as function of temperature. Notably, for both CFA and CFS films at temperatures around room temperature we observe a quasi-T-linear S, which in both cases is negative[4] and relatively large in magnitude (tens of $\mu V/K$ at 300 K) with respect to simple metals[151], implying a low, upward dispersing DOS at the Fermi level. Our results are in good agreement with Seebeck measurements reported in Refs.[140, 141] for CFS

[4] Negative Seebeck coefficients, if interpreted in a simple single-band picture of a monovalent metal through Eq. 4.5, correspond to electron-like (less than half-filled, positive dispersion) states at the Fermi level.

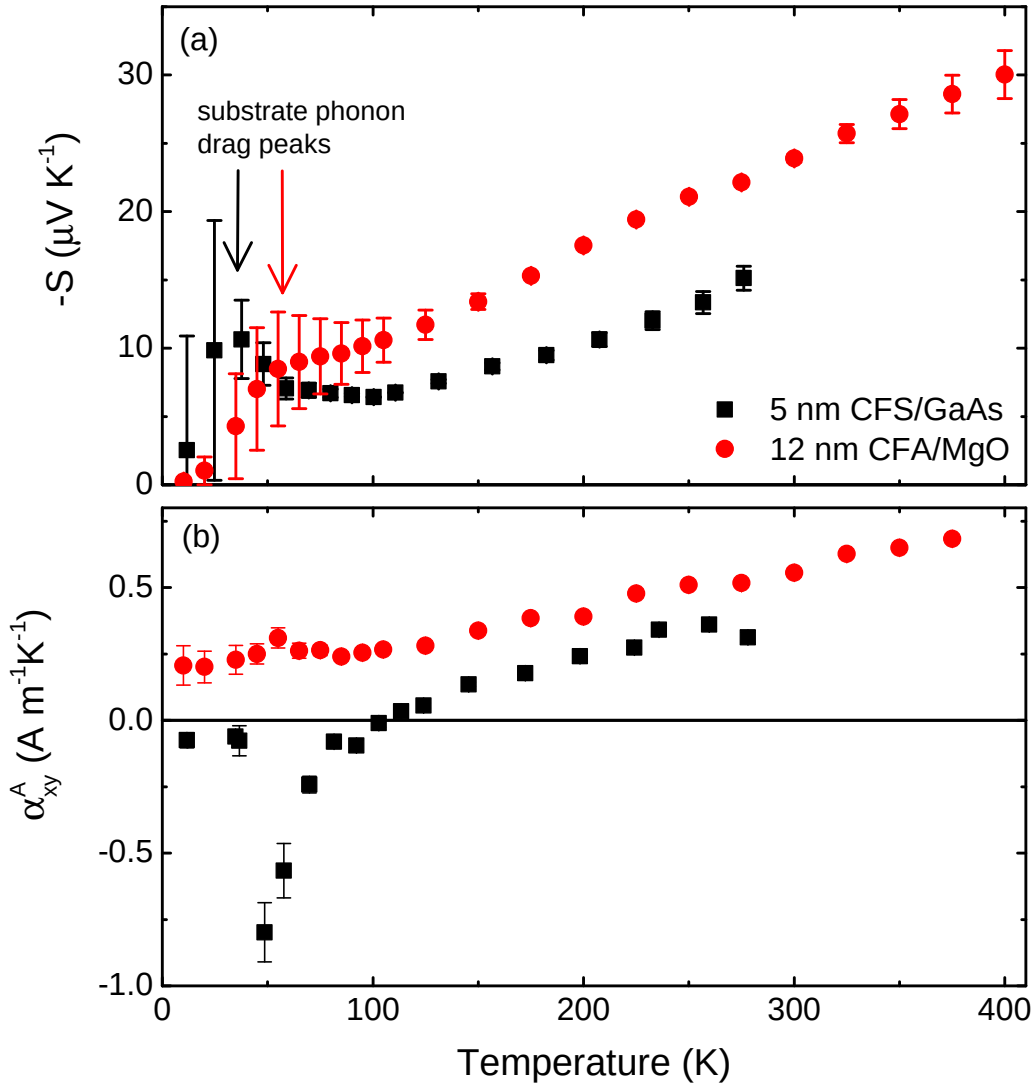

Figure 4.6: Summary of temperature dependence of Seebeck (a) and anomalous Nernst coefficients (b) for CFS (black squares) and CFA (red circles) Heusler thin films, which are TMC249 and UMN055 structures, respectively. Note that the Seebeck coefficients in (a) are negative. The CFS data only goes to 275 K due to issues from increasing substrate conductivity at high temperature.

and and CFA. Note the peaks in $|S|$ for both CFA and CFS at low temperature in Fig. 4.6(a), indicated by the arrows. These peaks are likely due to the phonon drag contribution to S[138], which quickly dies out at high temperature due to Umklapp phonon-phonon scattering processes. The relevant "dragging" phonons are likely from the substrate[152]. In Fig. 4.2, we have shown the spin-resolved band structure for CFA and CFS in the $L2_1$ phase, as calculated by density-functional theory (DFT). It can be seen that just above the chemical potential in both CFA and CFS there exist a multitude of relatively flat d down spin bands, while sp-like bands (both up and down spin) exist with a negative dispersion characteristic. With these band dispersions in mind, the sign of the measured Seebeck coefficients (negative) suggest that the transport which determines the coefficients is dominated by the character of the highly spin-polarized down-spin d bands present at or just above the chemical potential in both materials. Note that Hayashi et al.[141] attempted to reconcile their negative measured Seebeck coefficients with Co_2MnSi band structure calculations (from which a positive S would be naively expected) by claiming the flatter d bands are not relevant for S due to their low group velocity. However, for the case of the CFA and CFS band structure shown in Fig. 4.2, the DOS increases above the Fermi level and hence the sign we measure is in agreement with the naive expectation upon inspection of the band structure.

A note on potential magnon drag contributions

It should be noted that some authors[135, 138] have proposed that the magnon drag contributions to the Seebeck coefficients are significant, or dominant, in 3d transition metal ferromagnets. See Sec. 4.1.3 for a theoretical sketch outlining phonon and magnon drag contributions to the thermopower. The claims in Refs. [135, 138] have been controversial because the low value of the magnon specific heat capacity is generally considered to lead to small or negligible Seebeck coefficient contributions (via Eq. B.1). Certainly, these works do not convincingly demonstrate the $S \propto T^{3/2}$ relation expected for magnon drag thermopower.

An application of a large external magnetic field suppresses the magnonic specific heat capacity, and hence should lead to a measurable field-dependence of S. In Appendix B of this thesis, we have derived a negative field-linear correction to the magnon drag

contribution to Seebeck coefficient

$$S_{md} = \frac{k_B}{12\pi^2 neD^{3/2}}\left((3.35)(k_BT)^{3/2} - (5.86)\hbar\gamma H(k_BT)^{1/2}\right)\left(\frac{\tau'_m}{\tau'_m + \tau_{me}}\right) \tag{4.25}$$

where H is the applied magnetic field and is much larger than demagnetization or anisotropy fields, and D is the exchange stiffness. Eq. 4.25 can be used to test for (or rule out) magnon drag contributions to the Seebeck coefficient in future measurements. For $\gamma = 28$ GHz/T, and $T = 300$ K, Eq. 4.25 gives $\Delta S_{md}/S_{md}(H = 0)$ of $\sim -7\%$ at $H = 9$ T. Note that this is much larger than negative field-linear magnetoresistances ($< 1\%$) reported for transition metal ferromagnets due to the suppression of magnon-electron scattering[153, 154], which may influence the diffusive contributions to the Seebeck coefficient. (However, because the scattering rate cancels to first approximation in Eq. 4.5, it is not clear that the field-linear MR would introduce a field-linear contribution to the diffusive Seebeck coefficient.)

In Fig. 4.7, we have shown the magnetic field dependence of the thermopower for CFA at 300 K and CFS at 200 K. (A temperature of 200 K was used for the CFS data because spurious effects correlated with increasing GaAs substrate conductivity contaminate the thermoelectric measurements at and above 300 K.) In both cases, the $|H|$-linear behavior predicted by Eq. 4.25 is not observed, which we can constrain to better than 0.1% at $H = 9$ T. The small dependence on magnetic field shown in Fig. 4.7 can be attributed to Nernst contributions to the longitudinal voltage, which may arise due to misalignments of ∇T with the Hall bar. Because we constrain less than 0.1% decrease in the thermopower out to 9 T, while the magnon-drag calculation from Eq. 4.25 predicts $\sim 7\%$, we believe magnon drag thermopower is insignificant for these samples.

4.4.2 Anomalous Nernst coefficient results in Heusler thin films

Finally, we discuss the anomalous Nernst effect (ANE) measurements. The anomalous Nernst coefficient α^A_{xy} is defined from Eq. 4.1 by the expression

$$\frac{\alpha_{xy}}{\sigma} = -\frac{\partial_y V}{\partial_x T}, \tag{4.26}$$

where the anomalous contribution is the value of α_{xy} with the magnetization saturated along z. In the geometry shown in Fig. 4.4(a), for instance with the left heater on and the

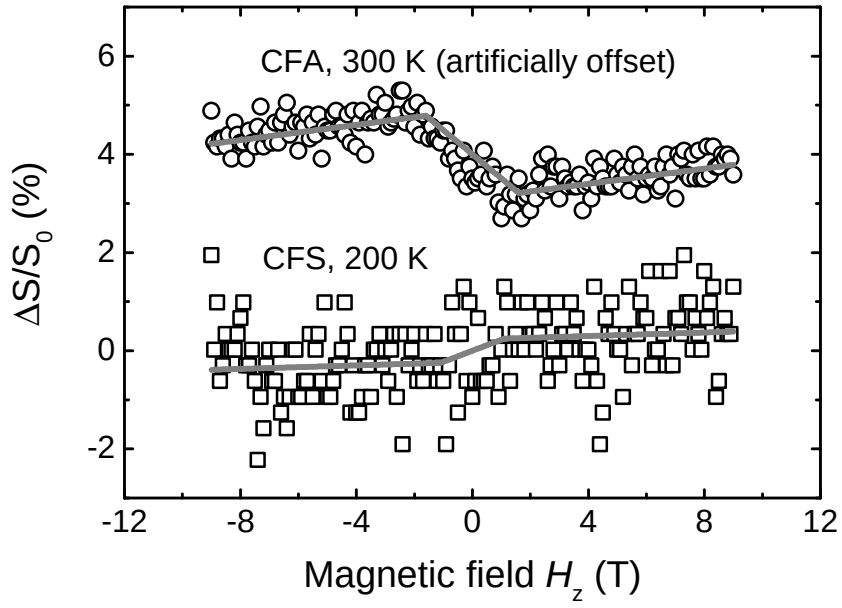

Figure 4.7: Magnetic field dependence of Seebeck coefficient, here indicated as a percentage relative to the zero-field value S_0. The squares are CFS at 200 K, the circles are for CFA at 300 K (which are artificially offset for clarity). The gray solid lines are fits to ordinary and anomalous Nernst contributions, which arise due to slight misalignment. The absence of the magnon drag field dependence predicted by Eq. 4.25 is confirmed to better than 0.1% at 9 T.

voltage measured across Hall bar contacts A and E, the anomalous Nernst coefficient may be determined by the relation $S^A_{xy} = -V^{2\omega}_{EA}/(l\partial_x T^{2\omega})$, where l is the width of the Hall bar. (Note that it is common to see anomalous Nernst coefficients reported divided by H_s, the out-of-plane saturation field of the magnetization, so they have the same units as ordinary Nernst coefficients.) As in the Seebeck measurement, $V^{2\omega}_{EA}$ is measured using the 2ω harmonic detection lock-in technique. In order to distinguish the ANE voltage from the ordinary Nernst effect and background Seebeck contributions, a magnetic field H_z is swept in the out-of-plane orientation, and the Nernst voltage $V^{2\omega}_{EA}$ recorded. Sample Nernst magnetic field sweeps with corresponding fits to a hard-axis saturation characteristic are shown in Fig. 4.5(b), where it is demonstrated that the Nernst signal inverts sign when ∇T is inverted by using left or right heaters.

In Fig. 4.6(b), α^A_{xy} is plotted as function of temperature for the 12 nm CFA/MgO film (TMC249). Similar to the Seebeck coefficient, the magnitude of α^A_{xy} increases at high temperatures as predicted by the Mott relation 4.5. Literature reports of ANE coefficients for ferromagnets are rare, but Ramos et al.[155] have reported $S^A_{xy}/H_s = 0.2\ \mu V/KT$ for crystalline magnetite (Fe_3O_4), and Watzman et al.[135] report $S^A_{xy}/H_s = 0.4\ \mu V/KT$ for bulk polycrystalline Fe, where both quoted values at 300 K. The values shown in Fig. 4.5 for CFA and CFS are comparable in magnitude to S^A_{xy}/H_s reported in Refs.[135, 155], which to our knowledge represent the only comparable data for ANE coefficients in metallic ferromagnets.

At this stage, a subtlety of presenting ANE coefficients must be emphasized. Experimentally, S^A_{xy}/H_s is usually presented (as is done in Ref. [135]). However, if the ANE is governed by the material intrinsic Berry curvature as described by Eq. 4.18, it is $\alpha^A_{xy} = S^A_{xy}\sigma$ that is fundamental, and should follow a Mott relation, rather than the experimentally presented S^A_{xy}/H_s. In fact, the polycrstalline bulk Fe used by Watzman et al.[135] had $\rho(300\ K) \simeq 10\mu\Omega$cm, implying in Watzman's Fe for comparable S^A_{xy}/H_s values, $\alpha^A_{xy} = 8\ AK^{-1}m^{-1}$, which is nearly a factor of 10 higher than that of our CFA(which has $\rho(300\ K) \simeq 100\mu\Omega$cm).

To further explore the comparison of α^A_{xy}, we have measured the AHE magnitudes of CFS and CFA samples. In Fig. 4.8, a summary plot of ρ^A_{xy} vs ρ_{xx} is shown, along with fits to the power law $\rho^A_{xy} = \sigma^A_{xy}\rho^2_{xx}$ that is appropriate for the intrinsic AHE. Reasonable agreement with the power law of 2 is observed, implying the intrinsic AHE

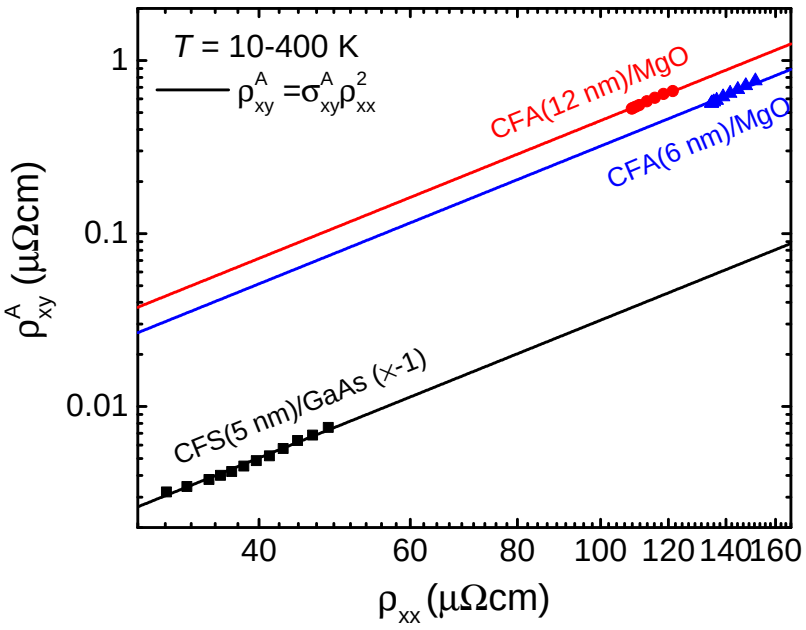

Figure 4.8: Summary of AHE magnitude vs resistivity for CFS (black squares) and CFA (12 nm red circles, 6 nm blue triangles), where temperature is the implicit variable and spans 10-400 K. The solid lines are fits to the power law $\rho^A_{xy} = \sigma^A_{xy}\rho^2_{xx}$, which gave σ^A_{xy} (units $(\mu\Omega\text{cm})^{-1}$) of -3.2×10^{-6}, 4.5×10^{-5}, and 3.2×10^{-5} for CFS, CFA(12 nm), and CFA(6 nm), respectively.

(and ANE) mechanism is dominant. The fit values of σ^A_{xy} are included in the Fig. 4.8 caption. For the CFA films, $\sigma^A_{xy} = 3 - 4\times10^{-5}$ $(\mu\Omega\text{cm})^{-1}$. The intrinsic AHE in Fe $\sigma^A_{xy} \simeq 10^{-3}$ $(\mu\Omega\text{cm})^{-1}$[156] is larger by a factor of more than 10 compared to our CFA films, which is likely due to its on-average higher atomic number constituents. This reconciles our $\alpha^A_{xy}(\text{Fe})/\alpha^A_{xy}(\text{CFA})\simeq$ 10 observation with the ANE Mott relation (Eq. 4.18), without needing to invoke grossly differing relative band derivatives of $d\sigma^A_{xy}/dE$ between Fe and CFA.

It should be noted that while a high-field linear slope in the Nernst geometry can be readily measured, with the device design shown in Fig. 4.4(a) *ordinary* Nernst coefficients cannot be reliably extracted because of the geometry of the Au vias used to connect to the Hall bar. Unlike anomalous Nernst voltages, which only build up along

the ferromagnetic Heusler Hall bar, ordinary Nernst voltages build up along the Hall bar and Au vias. Thus, the measured high-field slope is an addition of ordinary Nernst voltages from the Heusler hall bar and the Au vias, which cannot be reliably separated in our measurement scheme.

4.5 Conclusions and future work

In this chapter, a methodology for measuring Seebeck and anomalous Nernst coefficients in ferromagnetic thin films has been described. The contents of this chapter were very recent at the time of the writing of this thesis and represent prototype working examples of the thermoelectric measurement technique described. The primary advantage of the technique described is its convenience for use on thin film samples. The thin films may be micropatterned to give fast (∼Hz) thermal relaxation rates over the probed volume, which in turn enables lock-in detection to mitigate ubiquitous $1/f$ drift noise in thermoelectric voltages. It should be emphasized that the experiment and results presented in this chapter are due to the excellent work by Aaron Breidenbach, who designed and fabricated these devices as well as collected and analyzed the measurement data.

Several interesting avenues exist to utilize this technique for future study. First, elemental ratios in quaternary full Heusler alloys such as $Co_2Fe_xMn_{1-x}Si$ or $Co_2Fe(Ga_xGe_{1-x})$ have been varied to optimize damping properties[157] and spin injection properties[4, 158, 159]. Because of the sensitivity of Seebeck and anomalous Nernst coefficients to the density-of-states and spin-resolved density-of-states near the Fermi level, respectively, measurements of these coefficients for different quaternary alloy ratios may allow testing of theoretical band structure calculations and optimization of their half-metallicity. In principle, given calculated band dispersions such as those shown in Fig. 4.2, it should be straightforward to calculate S with Eq. 4.3 and Eq. 4.11, and compare to the measurements. Note that a corresponding calculation of S_{xy}^A (or α_{xy}^A) would require knowledge of the Berry curvature in addition to the band structure, analogous to the intrinsic AHE calculations performed by Yao et al.[146].

A second interesting avenue involves Heusler/heavy metal heterostructures, which can be used for spin pumping or spin-torque measurements. In these measurements,

more exotic effects such as the longitudinal spin-Seebeck effect(LSSE)[22] or the inverse spin-Hall effect due to spin pumping(ISHE)[21, 44] can give signals that follow the same phenomenology as the ANE. If the film ANE coefficient was known *a priori* through the techniques we have described, the degree to which ANE signals contribute to (or contaminate) the claimed LSSE or ISHE signals could be quantified.

Chapter 5

Summary and outlook

In this thesis, the properties of epitaxial thin film structures based on Heusler compounds have been characterized with regards to their potential for spintronic device applications. While we have focused on Heusler compound-based structures, many (if not all) of the key results presented are generic and applicable to other material systems.

With the potential for Heusler compound integration in spin valve application having been established (see Ref. [4] authored by the writer of this thesis, e.g.), the first two sections of this thesis focus on magnetization dynamics. In Chapter 2, we have demonstrated the ability to exert spin-orbit torques on Heusler ultrathin films by application of a charge current through an adjoining Pt layer. The demonstration of spin-orbit torques in similar epitaxial thin films to those that have been used in spin valve geometries represents significant progress towards Heusler spintronic device integration. Spin-orbit torque writing may provide significant gains in energy efficiency compared to the traditional spin-transfer torque writing scheme used for magnetic tunnel junctions (MRAM technologies consisting of which are already at the verge of commercialization). While spin-orbit torques are readily measurable in heavy-metal ultrathin bilayers, we have attempted to highlight the ambiguity that remains in attributing these torques to specific theoretical models, after almost a decade of study. Moreover, we have demonstrated the influence of the magnetic proximity effect on spin-orbit torques. The results described in Chapter 2 may also be found published in Ref. [97].

In Chapter 3 of this thesis, measurements probing GHz-timescale magnetization dynamics in epitaxial Heusler thin films are presented. Elucidation of the mechanisms

governing the damping of magnetization dynamics has been at the forefront of both fundamental and applied magnetics research. The emphasis of Chapter 3 is twofold: First, we stress that extrinsic resonance linewidth contributions due to defects are pervasive in epitaxial thin films, and may commonly dwarf the intrinsic linewidth contributions due to damping. The implicated defects may be commonly overlooked in routine epitaxial film characterization techniques. Perhaps counterintuitively, the lower the damping the more prevalent extrinsic linewidths may be. Notwithstanding the extrinsic linewidth contributions, we have used broadband measurements to constrain the damping constant. This methodology is the second emphasis of Chapter 3, which we have used to measure the anisotropy of the damping constant in a fully textured crystal and is, to our knowledge, the first report of its kind. Such measurements of anisotropic damping open the door to rigorous testing of existing theories governing metallic ferromagnet damping processes.

The final section of this thesis, Chapter 4, we break from the torque-induced dynamics studies of Chapters 2 and 3 to describe thermopower measurements on the same Heusler compound epitaxial thin films. Longitudinal and transverse thermopower measurements are of great utility, as they may be compared to predictions computed from first-principles electronic structure calculations, or used to compare ultrathin film electronic properties to those of bulk crystals. The thermopower measurements have been performed in a novel all-on-chip patterned thin film device, in contrast to the traditional hot-cold island with bridging sample geometry utilizing thermocouples. At the time of the writing of this thesis, the thermoelectric coefficient results for Heusler thin films may be considered preliminary, but the initial results show promise for testing theories such as the intrinsic anomalous Nernst effect and magnon drag thermopower effects.

References

[1] T. Valet and A. Fert, Phys. Rev. B **48**, 7100 (1993).

[2] Y. K. Takahashi, S. Kasai, S. Hirayama, S. Mitani, and K. Hono, Appl. Phys. Lett. **100**, 052405 (2012).

[3] T. M. Nakatani, N. Hase, H. S. Goripati, Y. K. Takahashi, T. Furubayashi, and K. Hono, IEEE Trans. Magn. **48**, 1751 (2012).

[4] T. A. Peterson, S. J. Patel, C. C. Geppert, K. D. Christie, A. Rath, D. Pennachio, M. E. Flatté, P. M. Voyles, C. J. Palmstrøm, and P. A. Crowell, Phys. Rev. B **94**, 235309 (2016).

[5] J. D. Jackson, *Classical Electrodynamics* (Wiley, Hoboken, NJ, 1999), 3rd ed.

[6] R. C. O'Handley, *Modern Magnetic Materials* (Wiley, New York, NY, 2000).

[7] J. Slonczewski, J. Magn. Magn. Mater. **159**, L1 (1996).

[8] L. Berger, Phys. Rev. B **54**, 9353 (1996).

[9] D. Ralph and M. Stiles, J. Magn. Magn. Mater. **320**, 1190 (2008).

[10] Z. G. Yu and M. E. Flatté, Phys. Rev. B **66**, 201202 (2002).

[11] M.-H. Nguyen, D. C. Ralph, and R. A. Buhrman, Phys. Rev. Lett. **116**, 126601 (2016).

[12] N. Tombros, C. Jozsa, M. Popinciuc, H. T. Jonkman, and B. J. van Wees, Nature **448**, 571 (2007).

[13] W. Han, K. Pi, K. M. McCreary, Y. Li, J. J. I. Wong, A. G. Swartz, and R. K. Kawakami, Phys. Rev. Lett. **105**, 167202 (2010).

[14] X. Lou, C. Adelmann, S. A. Crooker, E. S. Garlid, J. Zhang, K. S. M. Reddy, S. D. Flexner, C. J. Palmstrøm, and P. A. Crowell, Nat. Phys. **3**, 197 (2007).

[15] F. J. Jedema, H. B. Heersche, A. T. Filip, J. J. A. Baselmans, and B. J. van Wees, Nature **416**, 713 (2002).

[16] J. M. Kikkawa and D. D. Awschalom, Phys. Rev. Lett. **80**, 4313 (1998).

[17] L. Xie and X. Cui, Proc. Natl. Acad. Sci. **113**, 3746 (2016).

[18] J. Sinova, S. O. Valenzuela, J. Wunderlich, C. H. Back, and T. Jungwirth, Rev. Mod. Phys. **87**, 1213 (2015).

[19] Y. K. Kato, R. C. Myers, A. C. Gossard, and D. D. Awschalom, Science (80-.). **306**, 1910 (2004).

[20] S. O. Valenzuela and M. Tinkham, Nature **442**, 176 (2006).

[21] Y. Tserkovnyak, A. Brataas, and G. E. W. Bauer, Phys. Rev. Lett. **88**, 117601 (2002).

[22] G. Bauer, E. Saitoh, and B. J. Van Wees, Nat. Mater. **11**, 391 (2012).

[23] C. Kittel, *Introduction to Solid State Physics* (John Wiley and Sons, Inc, Hoboken, NJ, 2005), 8th ed., ISBN 978-0-471-41526-8.

[24] R. Winkler, *Spin Orbit Coupling Effects in Two-Dimensional Electron and Hole Systems* (2003), ISBN 3540011870.

[25] G. Dresselhaus, Phys. Rev. **100**, 580 (1955).

[26] Y. A. Bychkov and E. I. Rashba, J. Phys. C Solid State Phys. **17**, 6039 (1984).

[27] R. J. Elliott, Phys. Rev. **96**, 266 (1954).

[28] Y. Yafet, Solid State Phys. **14**, 1 (1963).

[29] M. Dyakonov and V. Perel, Phys. Lett. A **35**, 459 (1971).

[30] J. E. Hirsch, Phys. Rev. Lett. **83**, 1834 (1999).

[31] E. S. Garlid, Q. O. Hu, M. K. Chan, C. J. Palmstrøm, and P. A. Crowell, Phys. Rev. Lett. **105**, 156602 (2010).

[32] V. Edelstein, Solid State Commun. **73**, 233 (1990).

[33] S. Datta and B. Das, Appl. Phys. Lett. **56**, 665 (1990).

[34] K. Ando, S. Takahashi, J. Ieda, H. Kurebayashi, T. Trypiniotis, C. H. W. Barnes, S. Maekawa, and E. Saitoh, Nat. Mater. **10**, 655 (2011).

[35] H. C. Koo, J. H. Kwon, J. Eom, J. Chang, S. H. Han, and M. Johnson, Science (80-.). **325**, 1515 (2009).

[36] K. Xia, P. J. Kelly, G. E. W. Bauer, A. Brataas, and I. Turek, Phys. Rev. B **65**, 220401 (2002).

[37] I. M. Miron, K. Garello, G. Gaudin, P.-J. Zermatten, M. V. Costache, S. Auffret, S. Bandiera, B. Rodmacq, A. Schuhl, and P. Gambardella, Nature **476**, 189 (2011).

[38] L. Liu, C.-F. Pai, Y. Li, H. W. Tseng, D. C. Ralph, and R. A. Buhrman, Science (80-.). **336**, 555 (2012).

[39] A. Brataas, Y. V. Nazarov, and G. E. W. Bauer, Eur. Phys. J. B **22**, 99 (2000).

[40] M. Dyakonov and A. V. Khaetskii, *Spin Physics in Semiconductors*, vol. 157 of *Springer Series in Solid-State Sciences* (Springer Berlin Heidelberg, Berlin, Heidelberg, 2008), ISBN 978-3-540-78819-5.

[41] N. Nagaosa, J. Sinova, S. Onoda, A. H. MacDonald, and N. P. Ong, Rev. Mod. Phys. **82**, 1539 (2010).

[42] E. Sagasta, Y. Omori, M. Isasa, M. Gradhand, L. E. Hueso, Y. Niimi, Y. Otani, and F. Casanova, Phys. Rev. B **94**, 060412 (2016).

[43] T. Tanaka, H. Kontani, M. Naito, T. Naito, D. S. Hirashima, K. Yamada, and J. Inoue, Phys. Rev. B **77**, 165117 (2008).

[44] E. Saitoh, M. Ueda, H. Miyajima, and G. Tatara, Appl. Phys. Lett. **88**, 182509 (2006).

[45] K. Ando, S. Takahashi, K. Harii, K. Sasage, J. Ieda, S. Maekawa, and E. Saitoh, Phys. Rev. Lett. **101**, 036601 (2008).

[46] L. Liu, T. Moriyama, D. C. Ralph, and R. a. Buhrman, Phys. Rev. Lett. **106**, 036601 (2011).

[47] E. I. Rashba, Sov. Phys. Solid State **2**, 1109 (1960).

[48] A. Manchon and S. Zhang, Phys. Rev. B **78**, 212405 (2008).

[49] P. M. Haney, H.-W. Lee, K.-J. Lee, A. Manchon, and M. D. Stiles, Phys. Rev. B **87**, 174411 (2013).

[50] A. Brataas, Y. V. Nazarov, and G. E. W. Bauer, Phys. Rev. Lett. **84**, 2481 (2000).

[51] K.-S. Lee, S.-W. Lee, B.-C. Min, and K.-J. Lee, Appl. Phys. Lett. **102**, 112410 (2013).

[52] C. Kittel, Phys. Rev. **73**, 155 (1948).

[53] U. H. Pi, K. Won Kim, J. Y. Bae, S. C. Lee, Y. J. Cho, K. S. Kim, and S. Seo, Appl. Phys. Lett. **97**, 162507 (2010).

[54] J. Kim, J. Sinha, M. Hayashi, M. Yamanouchi, S. Fukami, T. Suzuki, S. Mitani, and H. Ohno, Nat. Mater. **12**, 240 (2012).

[55] S. Emori, U. Bauer, S.-M. Ahn, E. Martinez, and G. S. D. Beach, Nat. Mater. **12**, 611 (2013).

[56] M. Kawaguchi, K. Shimamura, S. Fukami, F. Matsukura, H. Ohno, T. Moriyama, D. Chiba, and T. Ono, Appl. Phys. Express **6**, 113002 (2013).

[57] C. O. Avci, K. Garello, M. Gabureac, A. Ghosh, A. Fuhrer, S. F. Alvarado, and P. Gambardella, Phys. Rev. B **90**, 224427 (2014).

[58] T. R. Mcguire and R. I. Potter, IEEE Trans. Magn. **11**, 1018 (1975).

[59] S. Y. Huang, W. G. Wang, S. F. Lee, J. Kwo, and C. L. Chien, Phys. Rev. Lett. **107**, 216604 (2011).

[60] K. Uchida, M. Ishida, T. Kikkawa, A. Kirihara, T. Murakami, and E. Saitoh, J. Phys. Condens. Matter **26**, 343202 (2014).

[61] S. H. Wang, L. K. Zou, J. W. Cai, B. G. Shen, and J. R. Sun, Phys. Rev. B **88**, 214304 (2013).

[62] E. Sondheimer, Adv. Phys. **1**, 1 (1952).

[63] A. F. Mayadas and M. Shatzkes, Phys. Rev. B **1**, 1382 (1970).

[64] H. Nakayama, M. Althammer, Y.-T. Chen, K. Uchida, Y. Kajiwara, D. Kikuchi, T. Ohtani, S. Geprägs, M. Opel, S. Takahashi, et al., Phys. Rev. Lett. **110**, 206601 (2013).

[65] M. Althammer, S. Meyer, H. Nakayama, M. Schreier, S. Altmannshofer, M. Weiler, H. Huebl, S. Geprägs, M. Opel, R. Gross, et al., Phys. Rev. B **87**, 224401 (2013).

[66] S. Meyer, M. Althammer, S. Geprägs, M. Opel, R. Gross, and S. T. B. Goennenwein, Appl. Phys. Lett. **104**, 242411 (2014).

[67] J. Kim, P. Sheng, S. Takahashi, S. Mitani, and M. Hayashi, Phys. Rev. Lett. **116**, 097201 (2016).

[68] L. Cheng, Z. Altounian, D. H. Ryan, J. O. Ström-Olsen, M. Sutton, and Z. Tun, Phys. Rev. B **69**, 144403 (2004).

[69] S. Y. Huang, X. Fan, D. Qu, Y. P. Chen, W. G. Wang, J. Wu, T. Y. Chen, J. Q. Xiao, and C. L. Chien, Phys. Rev. Lett. **109**, 107204 (2012).

[70] W. Zhang, M. B. Jungfleisch, W. Jiang, Y. Liu, J. E. Pearson, S. G. E. T. Velthuis, A. Hoffmann, F. Freimuth, and Y. Mokrousov, Phys. Rev. B **91**, 115316 (2015).

[71] Y. Yang, B. Wu, K. Yao, S. Shannigrahi, B. Zong, and Y. Wu, J. Appl. Phys. **115**, 17C509 (2014).

[72] Y. M. Lu, Y. Choi, C. M. Ortega, X. M. Cheng, J. W. Cai, S. Y. Huang, L. Sun, and C. L. Chien, Phys. Rev. Lett. **110**, 147207 (2013).

[73] B. F. Miao, S. Y. Huang, D. Qu, and C. L. Chien, Phys. Rev. Lett. **112**, 236601 (2014).

[74] B. F. Miao, L. Sun, D. Wu, C. L. Chien, and H. F. Ding, Appl. Phys. Lett. **110**, 222402 (2017).

[75] A. M. N. Niklasson, S. Mirbt, H. L. Skriver, and B. Johansson, Phys. Rev. B **56**, 3276 (1997).

[76] X. Liu, M. Bauer, H. Bertagnolli, E. Roduner, J. van Slageren, and F. Phillipp, Phys. Rev. Lett. **97**, 253401 (2006).

[77] Y. Sakamoto, Y. Oba, H. Maki, M. Suda, Y. Einaga, T. Sato, M. Mizumaki, N. Kawamura, and M. Suzuki, Phys. Rev. B **83**, 104420 (2011).

[78] C. Klewe, T. Kuschel, J.-M. Schmalhorst, F. Bertram, O. Kuschel, J. Wollschläger, J. Strempfer, M. Meinert, and G. Reiss, Phys. Rev. B **93**, 214440 (2016).

[79] W. L. Lim, N. Ebrahim-Zadeh, J. C. Owens, H. G. E. Hentschel, and S. Urazhdin, Appl. Phys. Lett. **102**, 162404 (2013).

[80] L. Liu, O. J. Lee, T. J. Gudmundsen, D. C. Ralph, and R. A. Buhrman, Phys. Rev. Lett. **109**, 096602 (2012).

[81] A. Ganguly, K. Kondou, H. Sukegawa, S. Mitani, S. Kasai, Y. Niimi, Y. Otani, and A. Barman, Appl. Phys. Lett. **104**, 072405 (2014).

[82] G. Allen, S. Manipatruni, D. E. Nikonov, M. Doczy, and I. A. Young, Phys. Rev. B **91**, 144412 (2015).

[83] C.-F. Pai, Y. Ou, L. H. Vilela-Leão, D. C. Ralph, and R. A. Buhrman, Phys. Rev. B **92**, 064426 (2015).

[84] H. Nguyen, W. Pratt, and J. Bass, J. Magn. Magn. Mater. **361**, 30 (2014).

[85] F. D. Czeschka, L. Dreher, M. S. Brandt, M. Weiler, M. Althammer, I.-M. Imort, G. Reiss, A. Thomas, W. Schoch, W. Limmer, et al., Phys. Rev. Lett. **107**, 046601 (2011).

[86] X. Fan, J. Wu, Y. Chen, M. J. Jerry, H. Zhang, and J. Q. Xiao, Nat. Commun. **4**, 1799 (2013).

[87] A. Manchon and S. Zhang, Phys. Rev. B **79**, 094422 (2009).

[88] I. Mihai Miron, G. Gaudin, S. Auffret, B. Rodmacq, A. Schuhl, S. Pizzini, J. Vogel, and P. Gambardella, Nat. Mater. **9**, 230 (2010).

[89] X. Fan, H. Celik, J. Wu, C. Ni, K.-j. Lee, V. O. Lorenz, and J. Q. Xiao, Nat. Commun. **5**, 3042 (2014).

[90] V. P. Amin and M. D. Stiles, Phys. Rev. B **94**, 104419 (2016).

[91] N. J. Harmon, T. A. Peterson, C. C. Geppert, S. J. Patel, C. J. Palmstrøm, P. A. Crowell, and M. E. Flatté, Phys. Rev. B **92**, 140201 (2015).

[92] X. Qiu, P. Deorani, K. Narayanapillai, K.-S. Lee, K.-J. Lee, H.-W. Lee, and H. Yang, Sci. Rep. **4**, 4491 (2015).

[93] J. Kim, J. Sinha, S. Mitani, M. Hayashi, S. Takahashi, S. Maekawa, M. Yamanouchi, and H. Ohno, Phys. Rev. B **89**, 174424 (2014).

[94] Y. Ou, C.-F. Pai, S. Shi, D. C. Ralph, and R. A. Buhrman, Phys. Rev. B **94**, 140414 (2016).

[95] J.-i. Inoue, G. E. W. Bauer, and L. W. Molenkamp, Phys. Rev. B **67**, 033104 (2003).

[96] V. P. Amin and M. D. Stiles, Phys. Rev. B **94**, 104420 (2016).

[97] T. A. Peterson, A. P. McFadden, C. J. Palmstrøm, and P. A. Crowell, Phys. Rev. B **97**, 020403 (2018).

[98] E. Montoya, T. McKinnon, A. Zamani, E. Girt, and B. Heinrich, J. Magn. Magn. Mater. **356**, 12 (2014).

[99] B. Heinrich, in *Ultrathin Magn. Struct. II*, edited by B. Heinrich and A. C. Bland (Springer-Verlag, Berlin Heidelberg, 1994), chap. 3, pp. 195–296.

[100] M. A. W. Schoen, J. M. Shaw, H. T. Nembach, M. Weiler, and T. J. Silva, Phys. Rev. B **92**, 184417 (2015).

[101] T. Gilbert, IEEE Trans. Magn. **40**, 3443 (2004).

[102] V. Kamberský, Czechoslov. J. Phys. **26**, 1366 (1976).

[103] V. Kamberský, Phys. Rev. B **76**, 134416 (2007).

[104] K. Gilmore, Y. U. Idzerda, and M. D. Stiles, Phys. Rev. Lett. **99**, 027204 (2007).

[105] K. Gilmore, M. D. Stiles, J. Seib, D. Steiauf, and M. Fähnle, Phys. Rev. B **81**, 174414 (2010).

[106] B. Heinrich, D. J. Meredith, and J. F. Cochran, J. Appl. Phys. **50**, 7726 (1979).

[107] J. M. Rudd, K. Myrtle, J. F. Cochran, and B. Heinrich, J. Appl. Phys. **57**, 3693 (1985).

[108] S. Ingvarsson, L. Ritchie, X. Y. Liu, G. Xiao, J. C. Slonczewski, P. L. Trouilloud, and R. H. Koch, Phys. Rev. B **66**, 214416 (2002).

[109] M. A. W. Schoen, D. Thonig, M. L. Schneider, T. J. Silva, H. T. Nembach, O. Eriksson, O. Karis, and J. M. Shaw, Nat. Phys. **12**, 839 (2016).

[110] B. Heinrich, G. Woltersdorf, R. Urban, O. Mosendz, G. Schmidt, P. Bach, L. Molenkamp, and E. Rozenberg, J. Appl. Phys. **95**, 7462 (2004).

[111] S. Mizukami, D. Watanabe, M. Oogane, Y. Ando, Y. Miura, M. Shirai, and T. Miyazaki, J. Appl. Phys. **105**, 07D306 (2009).

[112] S.-Z. Qiao, Q.-N. Ren, R.-R. Hao, H. Zhong, Y. Kang, S.-S. Kang, Y.-F. Qin, S.-Y. Yu, G.-B. Han, S.-S. Yan, et al., Chinese Phys. Lett. **33**, 047601 (2016).

[113] C. Liu, C. K. A. Mewes, M. Chshiev, T. Mewes, and W. H. Butler, Appl. Phys. Lett. **95**, 022509 (2009).

[114] G. Kupriyanova and A. Orlova, Phys. Procedia **82**, 32 (2016).

[115] R. D. McMichael, D. J. Twisselmann, and A. Kunz, Phys. Rev. Lett. **90**, 227601 (2003).

[116] G. Woltersdorf and B. Heinrich, Phys. Rev. B **69**, 184417 (2004).

[117] J. R. Eshbach and R. W. Damon, Phys. Rev. **118**, 1208 (1960).

[118] R. Damon and J. Eshbach, J. Phys. Chem. Solids **19**, 308 (1961).

[119] R. McMichael and P. Krivosik, IEEE Trans. Magn. **40**, 2 (2004).

[120] P. Krivosik, N. Mo, S. Kalarickal, and C. E. Patton, J. Appl. Phys. **101**, 083901 (2007).

[121] R. Arias and D. L. Mills, Phys. Rev. B **60**, 7395 (1999).

[122] Y. V. Goryunov, N. N. Garif'yanov, G. G. Khaliullin, I. A. Garifullin, L. R. Tagirov, F. Schreiber, T. Mühge, and H. Zabel, Phys. Rev. B **52**, 13450 (1995).

[123] M. Hashimoto, J. Herfort, H.-P. Schonherr, and K. H. Ploog, Appl. Phys. Lett. **87**, 102506 (2005).

[124] C. Liu, Y. Boyko, C. C. Geppert, K. D. Christie, G. Stecklein, S. J. Patel, C. J. Palmstrøm, and P. A. Crowell, Appl. Phys. Lett. **105**, 212401 (2014).

[125] Z. Celinski and B. Heinrich, J. Appl. Phys. **70**, 5935 (1991).

[126] K. Lenz, H. Wende, W. Kuch, K. Baberschke, K. Nagy, and A. Jánossy, Phys. Rev. B **73**, 144424 (2006).

[127] Q. Qin, S. He, W. Song, P. Yang, Q. Wu, Y. P. Feng, and J. Chen, Appl. Phys. Lett. **110**, 112401 (2017).

[128] S. He, Y. Liu, Y. Zheng, Q. Qin, Z. Wen, Q. Wu, Y. Yang, Y. Wang, Y. Feng, K. L. Teo, et al., Phys. Rev. Mater. **1**, 064401 (2017).

[129] O. Gaier, J. Hamrle, S. Trudel, B. Hillebrands, H. Schneider, and G. Jakob, J. Phys. D. Appl. Phys. **42**, 232001 (2009).

[130] M. Belmeguenai, M. S. Gabor, F. Zighem, Y. Roussigné, D. Faurie, and C. Tiusan, Phys. Rev. B **94**, 104424 (2016).

[131] T. Qu and R. H. Victora, J. Appl. Phys. **115**, 17C506 (2014).

[132] S. J. Patel, Ph.D. thesis, University of California Santa Barbara (2015).

[133] Y. Apertet, H. Ouerdane, C. Goupil, and P. Lecoeur, Eur. Phys. J. Plus **131**, 76 (2016).

[134] M. Cutler and N. F. Mott, Phys. Rev. **181**, 1336 (1969).

[135] S. J. Watzman, R. A. Duine, Y. Tserkovnyak, S. R. Boona, H. Jin, A. Prakash, Y. Zheng, and J. P. Heremans, Phys. Rev. B **94**, 144407 (2016).

[136] F. J. Blatt, P. A. Schroeder, C. L. Foiles, and D. Greig, *Thermoelectric Power of Metals* (Plenum Press, New York, London, 1976).

[137] J. M. Ziman, *Electrons and Phonons* (Oxford University Press, Oxford, New York, 1960).

[138] F. J. Blatt, D. J. Flood, V. Rowe, P. A. Schroeder, and J. E. Cox, Phys. Rev. Lett. **18**, 395 (1967).

[139] B. Balke, G. H. Fecher, H. C. Kandpal, C. Felser, K. Kobayashi, E. Ikenaga, J.-J. Kim, and S. Ueda, Phys. Rev. B **74**, 104405 (2006).

[140] B. Balke, S. Ouardi, T. Graf, J. Barth, C. G. Blum, G. H. Fecher, A. Shkabko, A. Weidenkaff, and C. Felser, Solid State Commun. **150**, 529 (2010).

[141] K. Hayashi, M. Eguchi, and Y. Miyazaki, J. Electron. Mater. **46**, 2710 (2017).

[142] P. Y. Yu and M. Cardona, *Fundamentals of Semiconductors* (Springer-Verlag, Berlin; Heidelberg; New York, 1996).

[143] S. Wurmehl, G. H. Fecher, H. C. Kandpal, V. Ksenofontov, C. Felser, H.-J. Lin, and J. Morais, Phys. Rev. B **72**, 184434 (2005).

[144] G. Kresse and J. Hafner, Phys. Rev. B **47**, 558 (1993).

[145] M. V. Berry, Proc. R. Soc. A Math. Phys. Eng. Sci. **392**, 45 (1984).

[146] Y. Yao, L. Kleinman, A. H. MacDonald, J. Sinova, T. Jungwirth, D.-s. Wang, E. Wang, and Q. Niu, Phys. Rev. Lett. **92**, 037204 (2004).

[147] D. Xiao, Y. Yao, Z. Fang, and Q. Niu, Phys. Rev. Lett. **97**, 026603 (2006).

[148] S. Saha and S. Tewari, Eur. Phys. J. B **91**, 4 (2018).

[149] W.-L. Lee, S. Watauchi, V. L. Miller, R. J. Cava, and N. P. Ong, Phys. Rev. Lett. **93**, 226601 (2004).

[150] A. M. Hofmeister, Phys. Chem. Miner. **41**, 361 (2014).

[151] N. Cusack and P. Kendall, Proc. Phys. Soc. **72**, 898 (1958).

[152] G. Wang, L. Endicott, H. Chi, P. Lošt'ák, and C. Uher, Phys. Rev. Lett. **111**, 046803 (2013).

[153] B. Raquet, M. Viret, E. Sondergard, O. Cespedes, and R. Mamy, Phys. Rev. B **66**, 024433 (2002).

[154] C. Liu, Ph.D. thesis, University of Minnesota (2016).

[155] R. Ramos, M. H. Aguirre, A. Anadón, J. Blasco, I. Lucas, K. Uchida, P. A. Algarabel, L. Morellón, E. Saitoh, and M. R. Ibarra, Phys. Rev. B **90**, 054422 (2014).

[156] T. Miyasato, N. Abe, T. Fujii, A. Asamitsu, S. Onoda, Y. Onose, N. Nagaosa, and Y. Tokura, Phys. Rev. Lett. **99**, 086602 (2007).

[157] B. Varaprasad, A. Srinivasan, Y. Takahashi, M. Hayashi, A. Rajanikanth, and K. Hono, Acta Mater. **60**, 6257 (2012).

[158] T. Kubota, S. Tsunegi, M. Oogane, S. Mizukami, T. Miyazaki, H. Naganuma, and Y. Ando, Appl. Phys. Lett. **94**, 122504 (2009).

[159] K. D. Christie, Ph.D. thesis, University of Minnesota (2014).

[160] K. Williams and R. Muller, J. Microelectromechanical Syst. **5**, 256 (1996).

[161] K. Williams, K. Gupta, and M. Wasilik, J. Microelectromechanical Syst. **12**, 761 (2003).

[162] C. C. Geppert, Ph.D. thesis, University of Minnesota (2014).

[163] K. D. Christie, C. C. Geppert, S. J. Patel, Q. O. Hu, C. J. Palmstrøm, and P. A. Crowell, Phys. Rev. B **92**, 155204 (2015).

Appendix A

CFA annealing effect on FMR in-plane linewidth

In Fig. A.1 of this appendix the effect of a 500° C 1 hr vacuum anneal on the in-plane FMR linewidth is summarized for the TMC250 growth. It can be seen that annealing decreased the linewidth, especially along the in-plane hard axis. Presumably, annealing altered the defect structure leading to a decrease in two-magnon scattering. The annealing effect on the linewidth was much more pronounced than the annealing effect on the FMR dispersion (i.e. the magnetostatic parameters). Annealing above 500° C was not pursued.

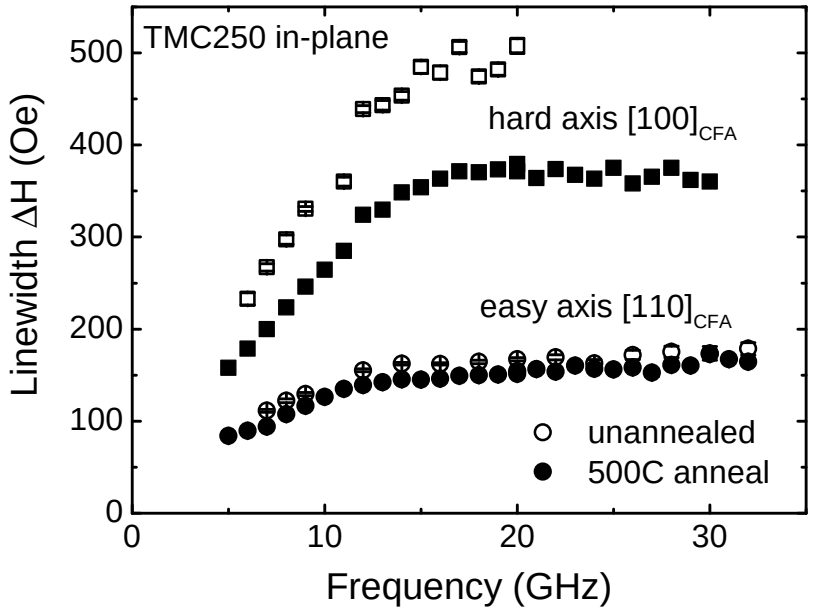

Figure A.1: Summary of the effect of vacuum annealing on the in-plane FMR linewidth for sample TMC250. The open symbols are as-grown unannealed film, closed symbols are film annealed at 500° C for 1 hr in Leighton vacuum annealer.

Appendix B

Magnon drag thermopower dependence on magnetic field

Here, the dependence of the magnon drag Seebeck coefficient (or thermopower) S_{md} on applied magnetic field H is derived beginning with Eq. B.1, reproduced below for convenience,

$$S_{md} = \frac{c_m}{3ne}\left(\frac{\tau'_m}{\tau'_m + \tau_{me}}\right), \tag{B.1}$$

where n is the electron density, c_m is the magnon contribution to the specific heat capacity, and the primes denote the magnon scattering times due to all other scattering processes. To account for the presence of a magnetic field, we solve for c_p at large H such that the magnon dispersion relation may be approximated as $\omega(\boldsymbol{q}) = \gamma H + Dq^2$, where γ is the gyromagnetic ratio, D is the exchange stiffness, and q is the magnon wavevector.

We begin by defining the magnonic specific heat capacity

$$c_m \equiv \frac{U_m}{dT}, \tag{B.2}$$

where

$$U_m = L^{-3}\int_0^\infty \epsilon D(\epsilon) f_{BE}(\epsilon, T) d\epsilon \tag{B.3}$$

is the magnonic energy density of system with density-of-states $D(\epsilon)$ and $f_{BE}(\epsilon, T) = (e^{\hbar\omega/k_B T} - 1)^{-1}$ is the Bose-Einstein distribution function at temperature T appropriate for bosonic harmonic oscillator modes (the chemical potential must be set to zero

because magnon number is not conserved). Taking $\epsilon = 0$ as the bottom of the magnon dispersion it is easy to show for a three-dimensional system of size L

$$D(\epsilon) = \frac{L^3}{4\pi^2}\frac{\epsilon^{1/2}}{D^{3/2}}. \tag{B.4}$$

Substituting Eq. B.4 into Eq. B.3 we get

$$U_m = \frac{1}{4\pi^2 D^{3/2}}\int_0^\infty (k_B T)^{5/2}(\xi-\delta)^{3/2}\frac{1}{e^\xi - 1}d\xi, \tag{B.5}$$

which has been expressed by conveniently changing variables in the integrand to $\xi \equiv (\epsilon + \hbar\gamma H)/k_B T$ and $\delta \equiv \hbar\gamma H/k_B T$. The change of variables is convenient because for typical ($\sim$Tesla) magnetic fields $\delta \ll 1$, such that we may expand $(\xi-\delta)^{3/2} = \xi^{3/2} - (3/2)\xi^{1/2}\delta + O[\delta^2]$ and neglecting all but the zeroth and linear terms in δ arrive at

$$U_m = \frac{(k_B T)^{5/2}}{4\pi^2 D^{3/2}}\int_0^\infty (\xi^{3/2} - (3/2)\xi^{1/2}\delta)\frac{1}{e^\xi - 1}d\xi. \tag{B.6}$$

Now, the integral may be evaluated as tabulated Riemann Zeta function values so we get

$$U_m = \frac{(k_B T)^{5/2}}{4\pi^2 D^{3/2}}\left(1.34 - (2.61)\frac{3}{2}\frac{\hbar\gamma H}{k_B T}\right), \tag{B.7}$$

which upon differentiating with respect to temperature gives

$$c_m = \frac{k_B}{4\pi^2 D^{3/2}}\left((3.35)(k_B T)^{3/2} - (5.86)\hbar\gamma H (k_B T)^{1/2}\right). \tag{B.8}$$

Note that at $H = 0$ Eq. B.8 gives the classic $c_m \propto T^{3/2}$ result[23]. Combining Eq. B.1 with Eq. B.8, it is clear that at large field S_{md} should exhibit a negative field-linear behavior.

Appendix C

Acronyms, symbols, and sample labels

C.1 Acronyms

Care has been taken in this thesis to minimize the use of jargon and acronyms, but this cannot always be achieved. This appendix contains a table of acronyms and their meaning.

Table C.1: Acronyms

Acronym	Meaning
F	ferromagnet (material or volume understood)
N	nonmagnet (material or volume understood)
SIA	structural inversion asymmetry
AHE	anomalous Hall effect
PHE	planar Hall effect
MR	magnetoresistance
AMR	anisotropic magnetoresistance
SHE	spin Hall effect
SOT	spin orbit torque

Continued on next page

Table C.1 – continued from previous page

Acronym	Meaning
SHA	spin Hall angle
NLSV	nonlocal spin valve
BDSV	biased-detector spin valve
UHV	ultrahigh vacuum
MBE	molecular-beam epitaxy
RHEED	reflection high-energy electron diffraction
XRD	X-ray diffraction
GIXR	grazing-incidence X-ray reflectivity
STM	scanning-tunnelling microscopy
HAADF-STEM	high-angle annular dark field scanning transmission electron microscopy
MTE	magnetothermoelectric
FMR	ferromagnetic resonance
TMS	two-magnon scattering
IP	in-plane
OOP	out-of-plane
DOS	density of states

C.2 Symbol definitions

Below a list of symbols and the physical quantities they denote. Note that certain symbols, such as the Greek letter α, have been re-used and the appropriate meaning must be understood from the context.

Table C.2: Symbol defnitions

Symbol	Meaning
τ_s	spin lifetime

Continued on next page

Table C.2 – continued from previous page

Symbol	Meaning
D	diffusion constant
ΔV_{NL}	spin valve signal size
η	dimensionless detection efficiency
α	dimensionless injection efficiency or Gilbert damping constant
$\boldsymbol{M}$	vector magnetization orientation
M_s	saturation magnetization
ω	angular frequency
f	frequency
γ	gyromagnetic ratio
H	external magnetic field
$\xi_{DL(FL)}$	dampinglike (fieldlike) torque/current efficiency
β	Dresselhaus SOI strength
α_R	Rashba SOI strength
$\boldsymbol{b}(\boldsymbol{k})$	Berry curvature at wavevector $\boldsymbol{k}$
N_i	dimensionless ith demagnetization tensor component
ξ	TMS defect correlation length
H'	TMS defect characteristic strength
$\boldsymbol{k}, k$	vector or scalar electronic wavevector
$\boldsymbol{q}, q$	vector or scalar magnon wavevector
ΔH_i	intrinsic FMR linewidth
ΔH_0	inhomogeneous broadening FMR linewidth
ΔH_{TMS}	TMS FMR linewidth
S	Seebeck coefficient
S_{xy}^A	anomalous Nernst coefficient
ρ	resistivity
σ	conductivity
μ	electrochemical potential
k_B	Boltzmann constant $\equiv 1.38 \times 10^{-23}$ J/K
$\hbar$	reduced Planck constant $\equiv 1.05 \times 10^{-34}$ Js

Continued on next page

Table C.2 – continued from previous page

Symbol	Meaning
$f(E)$	Fermi-Dirac distribution function
T	temperature
∇T	temperature gradient
ΔT	temperature difference
τ_p	quasiparticle momentum relaxation time
$\langle hkl \rangle$	family of equivalent crystallographic directions
$[hkl]$	crystallographic direction
(hkl)	crystallographic plane described by normal [hkl]

C.3 Sample names

For posterity, a list of the samples to which the important data presented in this thesis corresponds is included. They are by convention identified by their as-grown names (e.g. UMNXXX) and an informative dash-suffix if additional identification is necessary to describe annealing conditions, fabrication number, or device type. See `http://groups.physics.umn.edu/fastspin/samplebook/samples_list.php` for further growth details. Note that spin injection samples grown by Sahil Patel at UCSB begin with the prefix UMN, while growths by Anthony McFadden or Mihir Pendharkar at UCSB are denoted by their initials (e.g., TMCXXX, MPXXX).

Table C.3: Sample structure names

Name	Description
UMN043-05[1]	Co_2FeSi/n-GaAs SV array used for BDSV measurements
UMN032-03	Co_2MnSi/n-GaAs SV array used for BDSV measurements
TMC183	MgO/Co_2FeAl(1.2 nm)/Pt(7 nm) bilayer used for FMR characterization of ultrathin CFA

Continued on next page

[1] Suffix -05 denotes the 5th fabrication run of the UMN043 heterostructure.

Table C.3 – continued from previous page

Symbol	Meaning
TMC223	$MgO/Co_2FeAl(1.2\ nm)/Pt(t_N = 5, 6, 7, 8\ nm)$ bilayer used for SOT measurements
TMC224	$MgO/Co_2FeAl(1.2\ nm)/Pt(t_N = 1, 2, 3, 4\ nm)$ bilayer used for SOT measurements
UMN055	$AlOx/Co_2FeSi(5\ nm)/GaAs$ film for CFS FMR linewidth measurements
TMC249-500C[2]	$AlOx/Co_2FeAl(12\ nm)/MgO$ film for CFA FMR linewidth measurements
TMC250-500C	$AlOx/Co_2FeAl(24\ nm)/MgO$ film for CFA FMR linewidth measurements
TMC252-500C	$AlOx/Co_2FeAl(6\ nm)/MgO$ film for CFA FMR linewidth measurements
TMC249-MTE	$AlOx/Co_2FeAl(12\ nm)/MgO$ CFA magnetothermoelectric device
TMC252-MTE	$AlOx/Co_2FeAl(6\ nm)/MgO$ CFA magnetothermoelectric device
UMN055-MTE	$AlOx/Co_2FeSi(5\ nm)/GaAs$ CFS magnetothermolectric device
Py	$Ni_{0.8}Fe_{0.2}(50\ nm)/SiNx$ permalloy film used for FMR characterization grown in Dahlberg lab

[2] Annealed post-growth for 1 hr at 500°C in Leighton vacuum annealer.

Appendix D

Device fabrication and lithographic processing

In this appendix, the details of the processing steps used to fabricate the devices discussed in this thesis will be outlined. All fabrication was performed in the Minnesota Nano Center (MNC) cleanrooms located in Keller Hall and the Physics and Nanotechnology (PAN) building at the University of Minnesota.

D.0.1 Concepts in lithographic processing

In Figure D.1, a standard lithographic processing step flow diagram is illustrated. In step (a), a polymer resist is spun and baked to the chip. The resist is initially dissolved in a solvent so that it may be spun into a thin (hundreds of nm or single μm typical) layer, which is then baked to evaporate the solvent and set the resist. In step (b), the resist is selectively exposed to ionizing radiation. In the case of photolithography, ultraviolet light is used with the areas of exposure defined by a glass/chromium stencil mask. In the case of electron-beam (e-beam) lithography, keV electrons are focused into a beam which is rastered across the extents of the desired exposure. In a standard "positive" resist, exposure to ionizing radiation weakens the polymer chains, so that the exposed resist is selectively removed by the developing chemical. Note that "negative" resists can also be used, which are specifically designed such that the exposure step hardens the resist towards the developer chemical, so that the resultant resist pattern is

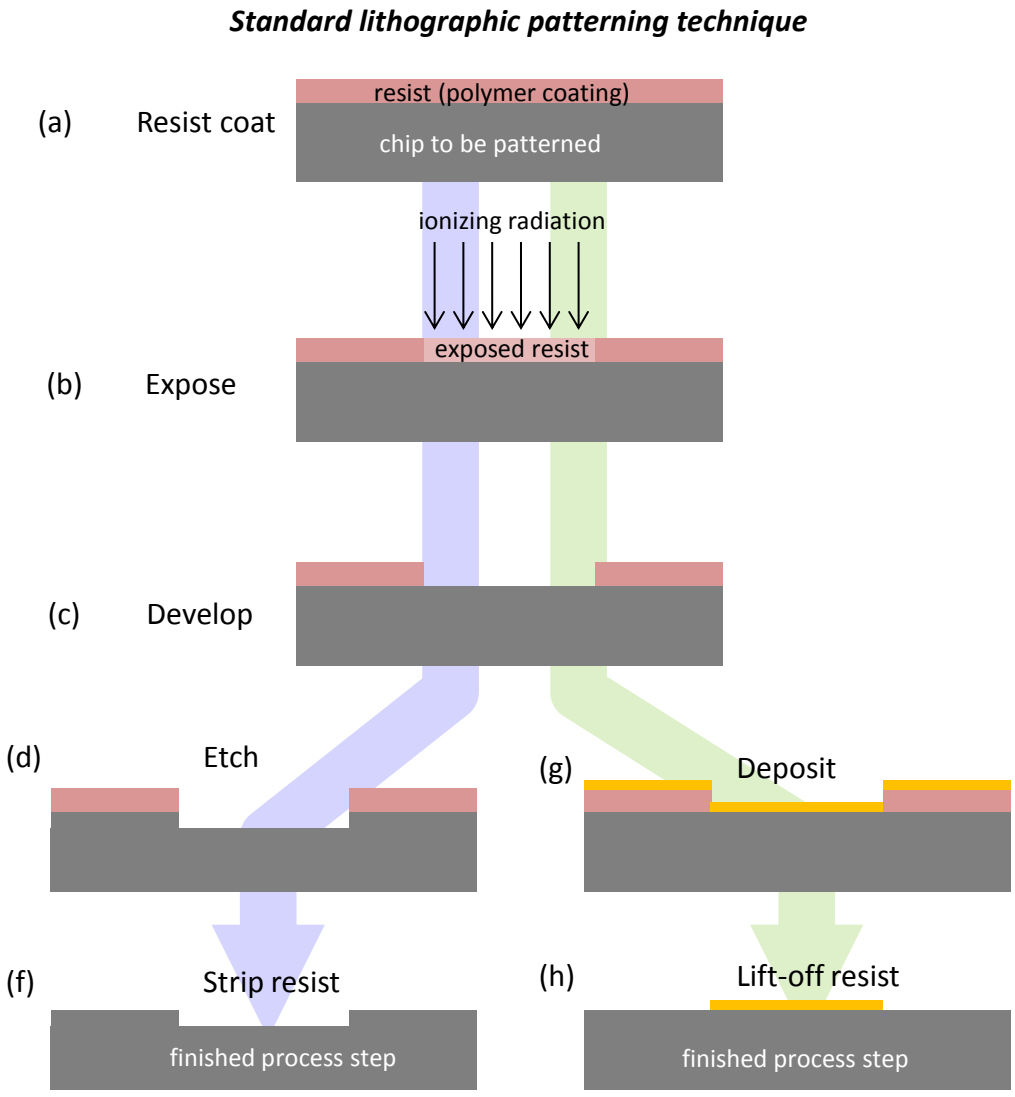

Figure D.1: Flow diagram illustrating the standard steps of a subtractive processing step (blue arrow) and an additive step (green arrow). The subtractive process final two steps (d,f) differ from the additive process final two steps (g,h). Typically, a combination of several additive and substractive processing steps are performed to achieve the desired final device structure.

inverted with regards to a positive resist process. The resist pattern left after a positive exposure and development process is shown in Fig. D.1 step (c).

After steps (a-c) have been completed, the patterned resist may be used to either protect a portion of the chip from a subtractive etching step, or from additional deposited material in an additive step, depending on the desires of the fabricator. In Fig. D.1 steps (d) and (f), the results of a subtractive step is shown, while steps (g) and (h) show the results of a deposition step. A variety of solvents may be used to remove the resist at the end of the processing step, which in the case of a deposition is referred to as "lift-off" (step (h)) because the deposited film of material is lifted off with the underlying resist everywhere except for the lithographically defined areas.

For tabulated etch rates of common materials in a variety of solutions, see Williams et al.[160, 161].

D.0.2 Heusler/*n*GaAs e-beam spin valve fabrication

A combination of photolithography and e-beam lithography was used for fabrication of the Heusler/nGaAs spin valve devices discussed in Ref. [4]. The fabrication procedure is closely descended from that used by Chad Geppert and Kevin Christie[162, 163], however e-beam lithography replaced photolithography in the process steps defining and depositing contacts to the ferromagnetic spin valve contacts. The miniaturization allowed by e-beam lithography allowed fabrication of spin valves with injector-detector edge-to-edge separations as small as 250 nm. For the AutoCAD drawings of the e-beam and photo masks used, see `.dxf` files found at `//files.umn.edu/SPA/groups/fastspin/Research/SpinTransport/Masks/2014/e-beammasks/12-19-14sizearray`. The photomask used for the mesa etch and SiN_x step is labelled "E_BEAM MESA/NITRIDE 1". The following is a list of processing details used for each step in fabrication of the Heusler/nGaAs e-beam spin valve devices, such as the UMN043-05 and UMN032-02 devices that were used for the measurements discussed in Ref. [4].

Cleave piece Place heterostructure face-down on clean weighing paper. Use razor blade to carefully scrape off excess indium, so that no high points exist. Apply constant downward pressure to avoid any sliding motion of the piece. To cleave into desired size (5-6 mm square typical), lightly nick topside of piece in desired

location, turn over, and press downwards with cylindrical object over nick. The GaAs(001) should fracture cleanly along [110] and [1$\bar{1}$0] directions.

Mount on Si piece To enable easy handling of the brittle and small GaAs piece, mount on larger ($\sim$ 2 cm) Si piece with mounting wax. Melt morsel of wax on Si piece on a hotplate set to 110°C, and place GaAs piece on top taking care to note [110] (ferromagnetic easy axis) direction, which is parallel to the marker lines on the backside of the heterostructure. Slide piece around and press lightly but firmly on the corners with wooden swab ends to ensure piece is lying flat and not "rockered" by wax or indium.

Pattern alignment marks The alignment marks used for subsequent process steps are (20 μm)^2 Ti/Au squares. Solvent clean (acetone, methanol, isopropanol). Pre-bake 60 sec at 90°C. Spin PMGI 30 sec 3 kRPM, bake at 150°C for 30 min[1] . Spin PMMA A4 30 sec 3 kRPM, bake at 150°C for 15 min. Expose in Vistec e-beam writer, optimal doses for fine features (5 nA beam) is close to 700 μC cm^{-2} while for course features (100 nA beam) 1200 μC cm^{-2} typical. Perform dose array periodically to optimize process window and achievable resolution. Develop PMMA 5 seconds 3:1 IPA:MIBK, stop develop in IPA. Develop PMGI 30 seconds in CD-26 developer, stop develop in IPA. Check under microscope to verify PMGI fully developed, will see visible Vistec raster marks in "oil-slick" coloration pattern if not. Continue PMGI develop in 10 second intervals if not complete. 30 second descum step in O_2 plasma. 5 nm Ti, greater than 40 nm Au in e-beam evaporator. Lift-off in NMP-based solvent heated to 80°C, sonicate if stubborn.

Pattern ferromagnetic contacts Pre-bake 60 sec at 90°C. Spin PMMA A4 30 sec 3 kRPM, bake at 150°C for 15 min, expose in Vistec. Develop PMMA 5 seconds 3:1 IPA:MIBK, stop develop in IPA. Descum for 30 seconds. Ar^+ on mill through metals and n^+ doping region (12 min at optimal angle, 3 min at oblique angle in Intl. Vac ion mill "slow" recipe). 30 min O_2 clean to remove ion mill crosslinked PMMA.

[1] While bake temperatures near 180°C are desired for e-beam resists, bake temperatures greater than 150°C were found to degrade Fe/nGaAs heterostructures

Etch mesa Pre-bake. Spin Shipley 1813 photoresist, 30 sec 3 kRPM. Bake 2 min 115°C. Expose 5 sec on Karl Suss MA-6 photoaligner "soft contact" mode. Use dummy wafer in photoaligner, with piece held by water bead. Develop 30 sec 1:1 Microdev:H_2O,[2] stop develop in running water. Measure resist height with KLA Tencor profilometer. Wet etch in 5:5:500 H_2O_2:NH_4OH:H_2O solution, with magnetic stirrer at room temperature. Etch through 2.5 μm nGaAs epilayer, etch rate $\sim$ 100 nm/min. Check progress with profilometer. Strip resist with solvent clean. Note– remove piece from Si carrier during this step, as Si oxidation will exhaust H_2O_2 from solution and stall etch.

Deposit isolation layer Pre-bake. Spin Shipley 1813 photoresist, 30 sec 3 kRPM. Bake 5 min 115°C. Spin and bake second layer of 1813 for 5 min (improves subsequent lift-off). Expose 10 sec on Karl Suss MA-6 photoaligner "soft contact" mode. Develop 30 sec 1:1 Microdev:H_2O. Deposit 100 nm of SiN_x insulator with PECVD 100°C process. Lift-off in NMP solution heated to 80°C, sonicate for 5 min, solvent clean, inspect. Repeat NMP bath and sonication if necessary. Note that piece will likely become un-waxed to holder during this process.

Deposit Ti/Au bonding pads and vias Same steps as previous step, except deposit Ti(5 nm)/Au(120 nm) in e-beam evaporator at $\sim 10^{-6}$ Torr. Lift-off for the Ti/Au should not require sonication.

Document Capture representative optical micrographs of completed devices, noting defects or open vias. Device is finished and ready for mounting, wire bonding, and electrical characterization.

D.0.3 Metallic thin-film Hall bar fabrication

The thin-film Hall bars used for the measurements described in Ref. [97] and the magnetothermoelectric devices were fabricated with a two-step photolithography process. First, the metal film was ion milled to define the Hall bar structure. Next,

[2] Microdev does not etch Al cap. Should not use MICROPOSIT 351 standard developer with Al-capped heterostructures.

a lift-off process was used to define Ti/Au bonding pads and vias (as well as thermistors and heaters for the magnetothermoelectric device). For the AutoCAD drawings of the bilayer Hall bar 3×3 mm pitch shadowmask photomask, see `SHMR_2.dxf` file found at `//files.umn.edu/SPA/groups/fastspin/Research/SpinPumping/Masks/MRhallbarswithshadowmaskcompatibility`. The resultant photomask is labelled "TP_SMR_2 2x2 3MM". The magnetothermoelectric photomask is labelled "A.BREIDENBACH MTE_2". Below the details of each lithography step are described.

Cleave and mount sample Cleave and mount on glass slide, similar to description in Sec. D.0.2. Note that MgO(001) cleaves along [100] directions, and being much less brittle than GaAs and requires a larger nick and firmer pressure to fracture.

Define Hall bar Solvent clean, pre-bake. Spin Shipley 1813 30 sec 3 kRPM, bake 2 min 115°C. Expose 5 sec in photoaligner. Develop 30 sec in 1:1 Microdev:H_2O, stop develop in running water. Ar^+ ion mill at optimal angle for required time to punch through to insulating substrate (10s of minutes typical), 3 min at oblique angle in Intl. Vac ion mill "slow" recipe. Note that for transparent MgO substrates, piece is visibly clear when metal is fully etched through. 30 min O_2 clean to remove ion mill crosslinked resist, sonication in NMP may be necessary to remove crosslinked resist.

Deposit Ti/Au layer Same steps as Sec. D.0.2 insulating layer step, except deposit Ti(5 nm)/Au(120 nm) in e-beam evaporator at $\sim 10^{-6}$ Torr. Lift-off for the Ti/Au in heated NMP should not require sonication.

Appendix E

Supporting publications

E.1 Heusler/n-GaAs biased-detector room temperature spin injection and detection

Below the manuscript summarizing the Heusler/nGaAs spin valve measurements is reproduced with the permission of the APS, as it appears published in Physical Review B **94**, 235309 (2016). The APS retains all copyrights to the manuscript. All manuscript, analysis, and modelling files may be found at location `files.umn.edu\SPA\groups\fastspin\Publications\TPHeuslerBDSVpaper\finalsupportingfiles,pptfigures,andinfo`. The same location contains a file `raw_data_locations_guide_TP_08022016.docx` in which the location of the raw data files are indicated.

Spin injection and detection up to room temperature in Heusler alloy/*n*-GaAs spin valves

T. A. Peterson,[1] S. J. Patel,[2] C. C. Geppert,[1] K. D. Christie,[1] A. Rath,[3] D. Pennachio,[2] M. E. Flatté,[4] P. M. Voyles,[3] C. J. Palmstrøm,[2,5] and P. A. Crowell[1,*]

[1]*School of Physics and Astronomy, University of Minnesota, Minneapolis, Minnesota 55455, USA*
[2]*Materials Department, University of California, Santa Barbara, California 93106, USA*
[3]*Department of Materials Science and Engineering, University of Wisconsin-Madison, Madison, Wisconsin 53706, USA*
[4]*Department of Physics and Astronomy, University of Iowa, Iowa City, Iowa 52242, USA*
[5]*Department of Electrical & Computer Engineering, University of California, Santa Barbara, California 93106, USA*

(Received 29 July 2016; revised manuscript received 6 December 2016; published 30 December 2016)

We have measured the spin injection efficiency and spin lifetime in Co_2FeSi/*n*-GaAs lateral nonlocal spin valves from 20 to 300 K. We observe large ($\sim$40 μV) spin valve signals at room temperature and injector currents of 10^3 A/cm^2, facilitated by fabricating spin valve separations smaller than the 1 μm spin diffusion length and applying a forward bias to the detector contact. The spin transport parameters are measured by comparing the injector-detector contact separation dependence of the spin valve signal with a numerical model accounting for spin drift and diffusion. The apparent suppression of the spin injection efficiency at the lowest temperatures reflects a breakdown of the ordinary drift-diffusion model in the regime of large spin accumulation. A theoretical calculation of the D'yakonov-Perel' spin lifetime agrees well with the measured *n*-GaAs spin lifetime over the entire temperature range.

DOI: 10.1103/PhysRevB.94.235309

I. INTRODUCTION

All-electrical spin transport has been demonstrated in III-V semiconductors [1–4], group IV semiconductors [5], and in 2D materials such as graphene [6,7]. One of the most mature systems studied in the field of semiconductor spintronics is the ferromagnet (FM)/*n*-GaAs lateral spin valve (SV) structure [1–3]. GaAs-based devices have served as a test bed for several seminal semiconductor (SC) spin transport measurements, such as the Hanle effect [1,8], the spin Hall and inverse spin Hall effects [9–11], and hyperfine effects [8,12–14]. The Dresselhaus spin-orbit interaction (SOI) [15] originating from the noncentrosymmetric lattice of III-V SCs makes them attractive candidates for modulation of spin transport using the SOI [16]. At the same time, however, the Dresselhaus SOI present in III-V SCs leads to efficient spin relaxation in the diffusive transport regime.

Electron spin relaxation in *n*-GaAs at doping levels near the metal-insulator transition is governed by the D'yakonov-Perel' (DP) mechanism [17,18]. The DP spin relaxation rate in III-V semiconductors has a characteristic $\tau_s^{-1} \propto \epsilon^3$ behavior [17,19], where ϵ is the carrier energy. The spin lifetime τ_s is the inverse of the spin relaxation rate. At temperatures for which the carriers are nondegenerate ($\epsilon \sim k_bT$), the spin lifetime falls sharply as $\tau_s \propto T^{-3}$ [20]. Short spin lifetimes ($\sim$10–100 ps) have therefore challenged *n*-GaAs SV room temperature performance [4], as the short spin lifetime limits the steady-state spin accumulation.

In this article we demonstrate electrical detection of nonlocal spin accumulation in Heusler alloy FM/*n*-GaAs lateral spin valve devices up to room temperature. Clear nonlocal SV signals are measured by fabricating devices with injector-detector contact separations of less than a spin diffusion length and applying a forward bias voltage to the detector contact. We use the injector-detector contact separation dependence of the SV signal to extract the *n*-GaAs spin lifetime and FM/SC interface spin injection efficiency from 20 K up to room temperature. These data allow for a comprehensive and quantitative evaluation of the temperature-dependent performance of FM/*n*-GaAs lateral SV devices. We find that the spin lifetime in the *n*-GaAs channel is in quantitative agreement with a theoretical calculation of the DP spin lifetime over the entire temperature range. At low temperatures, we achieve a spin accumulation that is a significant fraction of the carrier density in the channel. This is accompanied by an apparent downturn in the injection efficiency which we believe is due to breakdown of the ordinary drift-diffusion model in the regime of large spin-dependent electrochemical potential splitting.

II. METHODS

A. Structure growth and device fabrication

The devices used in this study were fabricated from heterostructures grown by molecular-beam epitaxy (MBE). A 2.5 μm Si-doped ($n = 3 \times 10^{16}$ cm^{-3}) GaAs epilayer was grown following a 500 nm undoped GaAs buffer layer grown on a semi-insulating (001) GaAs substrate. To thin the naturally occurring Schottky depletion layer and provide a tunnel barrier for efficient spin injection [21–23], the doping level was increased at the FM/SC interface. A 15 nm transitional doping layer was grown ($n = 3 \times 10^{16}$ cm^{-3} $\rightarrow$ $n^+ = 5 \times 10^{18}$cm^{-3}) on top of the *n*-GaAs epilayer, followed by an 18 nm thick heavily doped ($n^+ = 5 \times 10^{18}$ cm^{-3}) layer. Following the GaAs MBE growth, the sample was cooled to $<400^\circ$ C under As_4 flux at which point the As_4 flux was turned off. This resulted in a highly ordered GaAs(001) $c(4 \times 4)$ As-rich surface reconstruction as confirmed by reflection high-energy electron diffraction (RHEED) and *in situ* scanning tunneling microscopy (STM). For the 5 nm thick epitaxial Heusler film growth, the samples were transferred to a separate growth chamber while maintaining ultrahigh vacuum (UHV). The Heusler film growth was performed at 270° C with codeposition from individual elemental sources.

*Corresponding author: crowell@umn.edu

 ©2016 American Physical Society

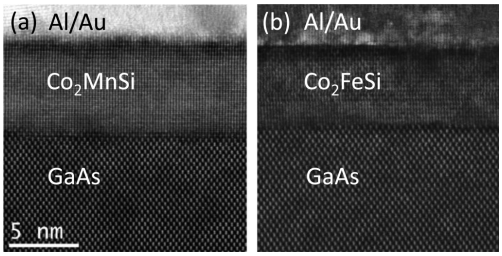

FIG. 1. Cross-sectional HAADF-STEM images of (a) the Co_2MnSi/GaAs interface and (b) the Co_2FeSi/GaAs interface. Images (a) and (b) were taken on the same heterostructures used for the Co_2MnSi and Co_2FeSi spin valve measurements presented in this paper. A 5 nm scale bar is indicated in the lower left of (a).

The Heusler compounds grow with a cube-on-cube orientation with Heusler(001)⟨110⟩|| GaAs(001)⟨110⟩ [24,25]. During Heusler growth RHEED was used to confirm layer-by-layer growth of a single crystal film. Cross-sectional high-angle annular dark field scanning transmission electron microscopy (HAADF-STEM) was performed, and example images of the interfaces are shown in Fig. 1. These images confirm the samples are single crystals with mixed $L2_1$ and B2 phases in both Co_2MnSi [Fig. 1(a)] and Co_2FeSi [Fig. 1(b)] films, and a degree of intermixing at the GaAs/Heusler interface of no more than 4–6 atomic layers. The GaAs(001)/Heusler interface resulted in a uniaxial magnetic anisotropy yielding an easy axis along the GaAs [110] direction [24,26,27] for both the Co_2FeSi and Co_2MnSi films.

The heterostructures were patterned into lateral spin valve devices using a top-down fabrication process. A combination of electron-beam lithography and photolithography was used, with Ar^+ ion milling to define the ferromagnetic contacts and wet etching to define the *n*-GaAs channel. A silicon nitride insulating layer was deposited by plasma-enhanced chemical vapor deposition (PECVD) and patterned by liftoff to electrically isolate the evaporated Ti/Au vias and bonding pads from the substrate and *n*-GaAs channel sidewalls. A micrograph of a SV device is shown in Fig. 2(a). The channel width in the GaAs [110] direction is 80 μm, the SV contact length is 50 μm, the injector width is 1 μm, and the detector width is 0.5 μm. The large aspect ratio of the SV contacts along the magnetic easy axis was chosen in order to minimize fringe magnetic fields as well as to define a two-dimensional geometry conducive to modeling (channel width $\gg$ spin diffusion length). The large-area remote contacts share the same composition as the SV contacts. The remote contacts, however, have no impact on the SV measurement, because they are placed many spin diffusion lengths away from the SV contacts. Multiple SV devices were fabricated on the same chip by wet etching through the 2.5 μm *n*-GaAs to isolate the devices electrically. SV devices on the same chip were patterned with injector-detector edge-to-edge separations ranging from 250 nm to 5 μm.

B. Charge transport

Standard multiprobe dc transport measurements were performed as a function of temperature to characterize both the

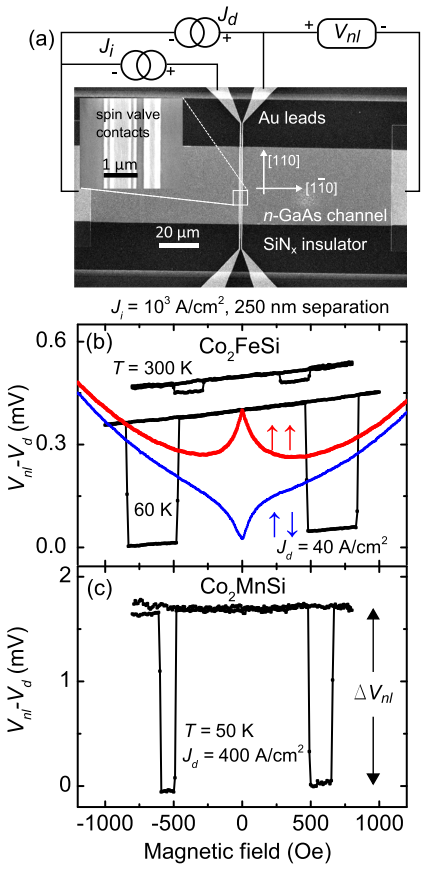

FIG. 2. (a) Scanning electron micrograph of a lateral SV device, with a schematic diagram of the measurement. The inset is a magnified image of the injector (left contact) and detector (right contact), in the device pictured with an edge-to-edge separation of 250 nm. (b), (c) Example BDSV field sweeps for devices with Co_2FeSi contacts (b) and Co_2MnSi contacts (c). The temperature and bias conditions are indicated on the figure. ΔV_{nl} is the magnitude of the parallel-antiparallel difference as indicated in (c). At the bias conditions indicated in (b) $V_d = 0.44$ V at 60 K and $V_d = 0.30$ V at 300 K. In (c) $V_d = 0.72$ V at 50 K for the bias conditions indicated. After subtracting V_d, the 60 K and 300 K data in (b) are offset for clarity. In (b), the dc NLH measurement is shown at 60 K, for both parallel (red) and antiparallel (blue) magnetization configurations.

n-GaAs channel and the Heusler alloy/*n*-GaAs interface. A companion Hall bar was fabricated from the same heterostructure used to fabricate the SV devices, and transport measurements were performed from 10 to 350 K to extract the carrier concentration and mobility of the *n*-GaAs. The Hall carrier concentration was measured to be 2.8×10^{16} cm^{-3} for the Co_2FeSi heterostructure and 3.5×10^{16} cm^{-3} for

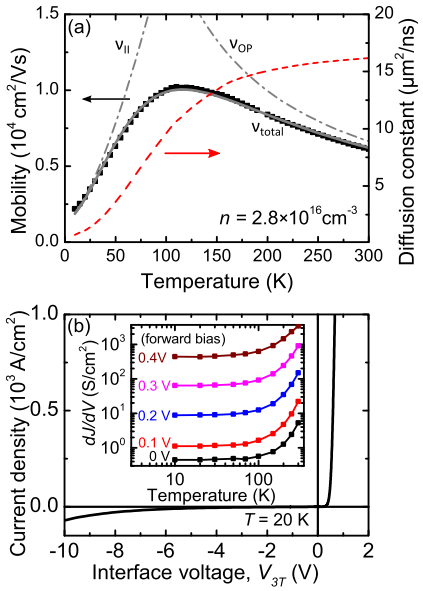

FIG. 3. (a) The n-GaAs mobility extracted from Hall measurements (left ordinate) as a function of temperature on the Co_2FeSi heterostructure. The gray solid line is a fit to the model for the mobility given by Eq. (10), with the ionized-impurity (II) and optical-phonon (OP) scattering contributions to the mobility indicated with the dash-dotted gray lines. In the fit shown, $A = 1.3 \times 10^3$ cm^2 V^{-1} s^{-1}, $B = 18$ cm^2 V^{-1} s^{-1} K$^{-3/2}$, and $C = 2.0 \times 10^6$ cm^2 V^{-1} s^{-1} K^{-1}. The red dashed line (right ordinate) is the channel diffusion constant calculated with Eq. (6). (b) Typical Co_2FeSi contact 3-terminal J-V characteristic at 20 K. The inset in (b) is the differential conductance as a function of temperature at different interface forward bias voltages. The solid curves connect data points.

the Co_2MnSi heterostructure. Figure 3(a) shows the channel electron mobility and diffusion constant as a function of temperature for the Co_2FeSi heterostructure. The Hall factor [28], which causes deviation of the Hall mobility from the electron mobility in n-GaAs, is accounted for by assuming the Hall factor is unity at 300 K [29,30] and that the carrier concentration is temperature-independent.

A typical Co_2FeSi/n-GaAs three-terminal (3T) interface current-voltage (J-V) characteristic is shown in Fig. 3(b). The inset of Fig. 3(b) shows the differential conductance per unit area (dJ/dV) as a function of temperature. Tunneling-dominated transport (field emission) is known to be necessary for spin injection in FM/GaAs Schottky contacts [31]. The existence of tunneling-dominated transport under forward bias at all temperatures is supported by two observations. First, dJ/dV increases exponentially with forward bias voltage at all temperatures, at a rate that is independent of temperature. Because of the triangular Schottky barrier [32], the forward bias voltage across a Schottky interface changes the thickness of the effective potential barrier through which tunneling occurs [33,34]. Although thermionic emission and thermionic field emission also lead to an exponential increase of dJ/dV with interface forward bias voltage, the rate for those processes is strongly temperature-dependent, ruling out those mechanisms. Second, at temperatures below the Fermi temperature of the n-GaAs (∼60 K for these samples) the forward bias differential conductance decreases weakly with decreasing temperature. Although dJ/dV at forward bias is temperature-dependent above the Fermi temperature, this does not imply thermionic emission but rather an increase in the tunneling attempt rate due to the nondegeneracy of the n-GaAs [33].

C. Spin transport

A schematic diagram of the SV measurement is shown in Fig. 2(a). A dc bias current J_i flows through the injector contact and a second bias current J_d flows through the detector contact. The injector and detector current sources share a common remote reference contact. In this article positive currents and interface voltages refer to electron extraction from the channel, i.e., forward bias of the metal/semiconductor Schottky contact. The bias current applied to the detector contact results in a voltage drop V_d over the tunnel barrier, which is the 3T interface voltage of the detector contact. In these devices, a forward bias applied at the detector contact enhances the nonlocal SV signal size compared to an unbiased detector (zero detector bias is the traditional nonlocal SV configuration pioneered by Johnson and Silsbee [35]). We will henceforth refer to the case of a bias current applied through the detector contact as the biased-detector spin valve (BDSV) measurement. The enhancement in the SV signal size with a bias applied to the detector contact has been observed in prior n-GaAs lateral SV measurements on similar heterostructures [36,37], and the possible origins will be discussed in detail later in this article.

An applied magnetic field is swept along the FM easy axis to switch the magnetizations of the injector and detector contacts from the parallel to antiparallel configuration, which allows for a definitive measurement of the nonlocal voltage due to spin accumulation. The difference in the nonlocal detector voltage V_{nl} between the parallel and antiparallel contact magnetization states is due to spin accumulation in the semiconductor [35] and is given by

$$\Delta V_{nl} = V_{NL,\uparrow\uparrow} - V_{NL,\uparrow\downarrow} = \eta(V_d)\frac{n_\uparrow - n_\downarrow}{e}\frac{\partial\mu}{\partial n}, \quad (1)$$

where $n_{\uparrow(\downarrow)}$ is the majority (minority) spin-resolved carrier density in the GaAs channel, e is the electron charge, and $\partial\mu/\partial n$ is the inverse of the thermodynamic compressibility of the semiconductor. We will refer to $n_\uparrow - n_\downarrow$ as the spin accumulation and $(n_\uparrow - n_\downarrow)/n$ as the dimensionless spin polarization throughout this article. The dimensionless detection efficiency parameter $\eta(V_d)$ characterizes the spin sensitivity of the detection contact [38] and is a function of the bias voltage. Because of the bias current applied through the detector contact, V_{nl} is not an open circuit nonlocal voltage (or "electromotive force"). The voltage drop over the detector Schottky tunnel barrier contributes an offset V_d, so that

$$V_{nl} = V_d + \frac{\Delta V_{nl}}{2}\hat{\mathbf{m}}_i \cdot \hat{\mathbf{m}}_d, \quad (2)$$

where $\hat{\mathbf{m}}_{i(d)}$ is the unit vector specifying the magnetization of the injector (detector) contact.

Example BDSV field sweeps are shown in Figs. 2(b) and 2(c) on SV devices with an injector-detector edge-to-edge separation of 250 nm at an injector bias current of $J_i = 10^3$ A/cm^2. The BDSV measurement on the device with Co_2FeSi contacts is shown in Fig. 2(b) at $J_d = 40$ A/cm^2, and for the device with Co_2MnSi contacts in Fig. 2(c) at $J_d = 400$ A/cm^2. The Co_2MnSi/*n*-GaAs contacts exhibited large voltage noise in the nonlocal SV measurements, and the signal-to-noise ratio (SNR) was not adequate for measurements at high temperatures. For this reason, the analysis presented in this article is carried out for measurements on Co_2FeSi/*n*-GaAs devices. At low temperatures, at which the SNR in Co_2MnSi/*n*-GaAs devices was adequate, the SV measurements were quantitatively similar to those on Co_2FeSi/*n*-GaAs devices. A linear background in V_{nl} can result from the Hall effect due to slight misalignment. The slope, which is a weak function of temperature, is subtracted from the data before extracting ΔV_{nl}.

Nonlocal Hanle (NLH) measurements [35,39] were also performed in the biased-detector configuration. In the NLH measurement a magnetic field applied perpendicular to the sample plane is used to apply a precessional torque, which, in combination with diffusion, dephases the spin accumulation. In all of the NLH measurements, the applied field was small enough so that the out-of-plane rotation of the contact magnetization decreased the in-plane component of the magnetization by less than 1.5%, which was considered negligible. The NLH measurement could be executed with the injector and detector contacts in either the parallel or antiparallel configuration. In the fitting of the NLH line shape discussed in Sec. III D, the difference of the parallel and antiparallel field sweeps is used.

At cryogenic temperatures, the NLH measurement in *n*-GaAs is complicated by the strong hyperfine fields due to dynamic nuclear polarization (DNP) [12,14,19]. Steady-state conditions are difficult to achieve due to long ($\sim$ seconds) nuclear depolarization time scales, and small misalignments between the applied field and the contact magnetization result in oblique Overhauser fields, which distort the NLH line shape [12,14]. To mitigate the influence of DNP effective fields on the NLH line shape, a low duty cycle ($<1\%$) pulsed current measurement was used for the NLH sweeps at temperatures below 100 K. The current was turned off for 1000 milliseconds, then pulsed on for 5 milliseconds after which the voltage was recorded and the pulse-train repeated. The current rise and fall times were much shorter than the few-millisecond current pulse duration. The pulsed measurement minimizes the nuclear polarization buildup because the current is on for a time much less than the nuclear polarization time [19]. Example NLH data obtained for the 250 nm separation Co_2FeSi device at 60 K are shown in Fig. 2(b).

III. RESULTS

A. Effect of detector bias

We now discuss the effect of detector bias on our SV measurements. First, we note that Crooker *et al.* [36] and Bruski *et al.* [37] observed similar enhancement of the spin valve signal in the presence of a detector bias current or voltage. Although several mechanisms have been proposed to explain the enhancement in the nonlocal SV signal with detector bias, the enhancement remains poorly understood. At the end of this section, we will return to discuss possible explanations in light of our measurements.

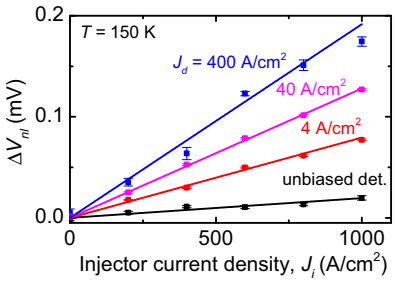

FIG. 4. Injector bias current dependence of ΔV_{nl}, for varying detector forward bias currents, on the 250 nm separation device at 150 K. The lines shown are linear fits.

We find that a sufficiently large forward bias current applied through the detector contact increases the SV signal ΔV_{nl} at all temperatures. Figure 4 shows ΔV_{nl} vs J_i for the 250 nm separation at 150 K. ΔV_{nl} increases linearly with J_i at all detector bias currents, but the slope of ΔV_{nl} vs J_i is enhanced with increasing detector forward bias current. This enhancement is particularly advantageous for measurements at high temperatures near 300 K, at which the spin valve signal becomes small in *n*-GaAs [1,4]. This effect was observed in devices with both Co_2FeSi and Co_2MnSi contacts and was observed previously for devices with Fe contacts [36].

For the case of no bias current passing through the detector (i.e., the conventional nonlocal SV measurement), ΔV_{nl} could be measured in the 250 nm separation device for temperatures less than approximately 200 K [see data points in Figs. 5(b) and 5(c) at $V_d = J_d = 0$]. For a fixed injector current, the SV measurement was then performed at different detector bias currents. The corresponding interface voltage drop V_d was measured at each bias current, and so the data may be presented as a function of either bias voltage V_d or current J_d. The results of this measurement at 60 K on the 250 nm separation are shown in Fig. 5(a) and are summarized for all temperatures in Figs. 5(b) and 5(c). At forward detector bias above interface voltages of $V_d \sim 0.2$ V, we observe significant enhancement of ΔV_{nl}. As shown in Fig. 5(a), the dependence of ΔV_{nl} on the detector bias is nonmonotonic below $\sim$200 K, and it is suppressed at small detector voltages (of either sign) and even changes sign for a narrow window of reverse bias. Although V_{nl} is sensitive to 3T signals [8] produced by *local* spin injection at the detector contact, only *nonlocally* injected spin accumulation contributes to ΔV_{nl} in a spin valve measurement, because ΔV_{nl} is the difference in nonlocal voltage between parallel and antiparallel magnetization states. Furthermore, as shown in Fig. 2(b), the NLH measurement can also be performed with the parallel-antiparallel difference at zero field matching the BDSV magnitude. The existence of the NLH effect at low temperatures demonstrates conclusively that the

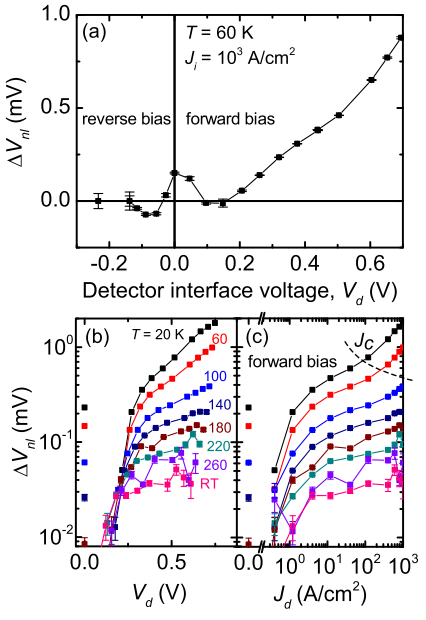

FIG. 5. (a) ΔV_{nl} as a function of detector interface voltage V_d for fixed injector bias current. (b), (c) The detector forward bias *voltage* (b) and *current* (c) dependence of ΔV_{nl} from 20 K to room temperature (RT). Only the zero detector bias and forward bias points are shown in (b) and (c) to illustrate the enhancement of ΔV_{nl} at forward detector bias. The dashed line in (c) indicates J_c, above which spin drift in the channel caused by the detector bias current enhances the spin accumulation at the detector. For clarity, the dashed line was drawn to smoothly connect J_c at each temperature. All data shown in this figure were taken with the 250 nm injector-detector separation device, and $J_i = 10^3$ A/cm^2.

biased-detector measurement in these devices is a probe of the nonlocally injected spin accumulation.

The enhancement in ΔV_{nl} under forward detector bias occurs at all temperatures measured, from 20 K to room temperature. Using the BDSV measurement a clear SV signal could be measured on the separations below 1 μm up to and above room temperature on the Co_2FeSi devices. To our knowledge, the spin signal we measure on the 250 nm separation device of $\sim$40 μV at room temperature is over an order-of-magnitude larger than that which has been achieved in FM/*n*-GaAs SVs, to date [4]. We now discuss the possible origins of the forward bias enhancement of the SV signal.

We consider first the influence of drift due to electric fields in the channel between the injector and detector contacts. Due to the relatively low carrier density in these samples, the spin drift length $l = \tau_s J/ne$ can be comparable to or larger than the spin diffusion length $\lambda = \sqrt{D\tau_s}$ [40,41]. In the case of a forward bias current applied through the detector contact (electron extraction from the channel), the electric field in the channel causes drift of electrons from the injector towards the detector contact, enhancing the nonlocal spin accumulation when compared to spin diffusion alone. To determine whether the detector bias current leads to significant drift enhancement of ΔV_{nl}, the current density in the channel between injector and detector contacts at which the spin drift length was equal to the spin diffusion length was evaluated at each temperature. Above a critical current density $J_c = ne\sqrt{D/\tau_s}$, which is the current density at which $l = \lambda$, drift enhancement of the nonlocal spin accumulation below the detector contact becomes significant. The region where this occurs is illustrated in Fig. 5(c), in which the dashed curve shows J_c. The drift enhancement is significant only at low temperatures and the highest detector bias currents. This is in contrast to the case of Si described in Ref. [41] in which the long spin lifetime at room temperature, combined with higher current densities than we apply, leads a spin drift length which can be much longer than the spin diffusion length. Because the enhancement in ΔV_{nl} occurs at all temperatures and for current densities far below J_c, it cannot be attributed solely to spin drift effects in the channel. Although variations on simple drift models have been proposed [42], it is unlikely that drift alone can play a significant role given that the enhancement is observed up to room temperature. For the purposes of discussion, we attribute the enhancement in ΔV_{nl} with detector forward bias primarily to enhancement of η, the detection efficiency, which we treat as a purely interfacial property. The detection efficiency is a function of detector bias, i.e., $\eta \rightarrow \eta(V_d)$.

Hu *et al.* [43] and Salis *et al.* [3] observed a highly nonmonotonic behavior of the sign of the injected spin polarization in similar heterostructures with Fe contacts. The sign and magnitude depended strongly on the details of the *n*-GaAs band structure in the region of n^+ doping near the interface. It is possible that the enhancement of η under forward bias is due to the enhanced participation of additional quantum well states that form on the SC side of the tunnel barrier due to the n^+ doping layer. It has been proposed that these states play a critical role in both charge and spin current in tunnel contacts using Schottky barriers through FM/SC wave-vector-matching arguments which depend on the degree of quantum confinement of the SC states [44].

Another point of view focuses on the nonlinear current-voltage characteristic of the tunnel barrier itself [45,46]. A simple analysis suggests that the ratio of the detected voltage to the spin accumulation should be modified by the ratio $(J/V)/(dJ/dV)$ of the absolute to differential conductance, although Jansen *et al.* [47] have noted that this correction factor is in fact an upper bound. In our case, however, we observe an effect that is opposite to that suggested by this argument. $(J/V)/(dJ/dV)$ is smaller at forward bias voltage than at zero bias, because J increases exponentially with V.

Because the bias current applied to the detector introduces a 3T offset V_d to V_{nl}, care must be taken to separate signals due to nonlocal spin accumulation from signals of local origin. Surface localized states in tunnel barriers have been at the center of a controversy in the semiconductor spin injection literature because of the influence these states can have on both the magnitude and line shape of the 3T Hanle measurement [48]. For example, Txoperena *et al.* [49] determined that impurity-assisted tunneling processes can lead to Lorentzian-shaped magnetoresistance effects that mimic

the Hanle effect. Also, Jansen *et al.* [50] note that in the 3T geometry the change in 3T voltage due to spin accumulation can originate from spin accumulation in interface localized states as well as bulk channel spin accumulation. Our measurement, however, probes the parallel-antiparallel difference in the nonlocal voltage, notwithstanding the bias applied to the detector contact. Although localized states may play an important role in the spin-polarized transport at our interfaces, the mechanisms discussed by Txoperena *et al.* [49] and Jansen *et al.* [50] are only relevant for 3T local spin detection where the ferromagnetic contact simultaneously serves as the injector and detector.

Another possible physical explanation for the detector bias dependence of ΔV_{nl} is that significant features exist in the spin-resolved density of states (DOS) of the Co_2FeSi/GaAs interface near the Fermi level. These features could lead to spin injection and detection efficiencies that vary with forward bias voltage, as states above the Fermi level in the FM become available for elastic tunneling from the SC. Density functional theory (DFT) calculations done for Co_2FeSi in the $L2_1$ phase [51,52] suggest strong variations in the bulk minority DOS near the Fermi level over energy ranges of ∼hundreds of meV, which are comparable to the scale of the interface voltages at the detector in our measurement. Strong bulk minority DOS variations near the Fermi level have also been predicted for Co_2MnSi which are largely insensitive to the phase ($L2_1$ vs B2) [53]. However, the bias dependence of spin detection shown in Fig. 5(a) cannot be clearly correlated with the features in the spin-resolved DOS reported by DFT calculations. Additionally, interface states, such as those which have been proposed for the Fe/GaAs(001) interface, will contribute to the tunneling current [54]. Although it is likely that the low-voltage features in $\Delta V_{nl}(V_d)$ are associated with electronic structure of the interface, we have no quantitative description of the bias dependence of the nonlocal voltage.

We now comment briefly on the sign of the spin valve signals we observe. In this article, a decrease in V_{nl} in the antiparallel magnetization state is defined as a positive ΔV_{nl}. The BDSV sweeps shown in Figs. 2(b) and 2(c) are examples of positive ΔV_{nl} values. The sign of ΔV_{nl} is determined by the relative signs of the injection and detection efficiencies. That is, same sign (opposite sign) injection and detection efficiencies correspond to a positive (negative) ΔV_{nl}. Microscopically, the individual signs of these efficiencies are determined by the difference in the spin-resolved interface conductances $g_\uparrow - g_\downarrow$, where the "up" direction is defined by the energy-integrated majority spin direction (i.e., magnetization) of the ferromagnet. Because the nonlocal voltage depends on the product of the two efficiencies, it is not possible to correlate its sign directly with the sign of the spin accumulation. At low temperatures, the influence of the electronic Knight field on the nuclear polarization in oblique Hanle geometries [12,19] can be used to determine the sign of the spin accumulation with respect to the magnetization orientation. We have determined that at high forward bias (spin extraction) the sign of the spin accumulation is minority in Co_2FeSi and majority in Co_2MnSi with respect to the magnetization of the injector contact [55].

B. Injector-detector separation dependence

We quantify device parameters at different temperatures using the injector-detector separation dependence (IDSD) of the spin valve signal size, rather than relying on NLH measurements. The NLH measurement in *n*-GaAs becomes challenging at high temperatures because of the magnetoresistance backgrounds present over the much larger magnetic field range required when the spin lifetime is small. The injector-detector separation was varied in order to extract the spatial dependence of the spin accumulation in the channel. By utilizing the enhanced signal in the BDSV configuration, clear SV signals could be measured at the smallest separations up to room temperature. For the IDSD measurement, the detector contact forward bias was fixed at a current density of 40 A/cm^2. This bias current was well into the enhancement regime shown in Fig. 5(c), but below the regime where spin drift enhancements were significant at low temperatures. ΔV_{nl} was recorded at bias conditions $J_i = 1000$ A/cm^2, $J_d = 40$ A/cm^2 for each temperature and injector-detector separation. The results of the IDSD measurement are summarized in Fig. 6. The solid lines in Fig. 6 are fits to a numerical model of the spin accumulation in the channel, which will be explained in detail later in this article.

We note that in Eq. (1), ΔV_{nl} is proportional to the spin accumulation $n_\uparrow - n_\downarrow$ and the inverse compressibility of the channel $\partial\mu/\partial n$. At temperatures above the Fermi temperature (in our samples $T_F \simeq 60$ K) at which the *n*-GaAs is no longer degenerate, $\partial\mu/\partial n$ is a function of temperature. In the nondegenerate regime ($T \gg T_F$), $\partial\mu/\partial n \propto T$. This relationship implies that as the temperature increases in the nondegenerate regime, a larger ΔV_{nl} is measured *for a given*

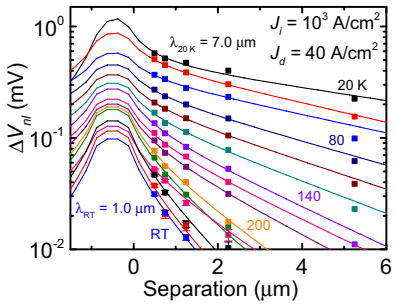

FIG. 6. The injector-detector separation dependence of ΔV_{nl} for the devices with Co_2FeSi contacts at temperatures from 20 K to 300 K, in increments of 20 K. The horizontal axis of the plot is the injector edge to detector center separation; i.e., the 1 μm wide injector extends from -1 to 0 μm on the horizontal axis. Superimposed as solid lines are the fits of a 2D numerical solution of Eq. (5) with τ_s and $\eta\alpha$ as the fitting parameters. The bias conditions are indicated on the figure as well as the spin diffusion lengths at 20 K and room temperature (RT). At low temperature, the IDSD measurement on the Co_2MnSi devices yielded comparable SV signal sizes and *n*-GaAs spin diffusion length. A complete temperature-dependence measurement, however, was not performed.

spin accumulation. For these samples,

$$\left.\frac{\partial\mu}{\partial n}\right|_{300\ \mathrm{K}} \simeq 7\left.\frac{\partial\mu}{\partial n}\right|_{20\ \mathrm{K}}. \tag{3}$$

Because of this enhancement factor, while the spin accumulation falls by two orders of magnitude from 20 K to 300 K, ΔV_{nl} at separations much smaller than a diffusion length only decreases by roughly one order of magnitude over the same temperature range.

C. Modeling of the spatial decay of spin accumulation

Here we discuss the model used to describe the spin accumulation in the channel and which is used to fit the IDSD measurement results. Typically, in systems where spin diffusion is one-dimensional, the SV signal size is interpreted with the expression [35]

$$\Delta R_{nl} = \Delta V_{nl}/I = \frac{\eta^2\rho\lambda e^{-y/\lambda}}{A}, \tag{4}$$

where ρ is the channel resistivity, A is the channel cross-sectional area, and y is injector-detector separation. Equation (4) has been used to model the SV signal size in a variety of material systems [1,6,39] in which the FM/NM barrier resistance is much larger than the channel spin resistance, so that the conductivity mismatch problem [21] may be ignored. We choose to use a more general numerical model of the spin accumulation in the channel to fit to the IDSD measurement because of several considerations. First, as discussed earlier, drift due to the bias current influences the spatial spin accumulation profile in n-GaAs at low temperatures, and the exact drift field is best captured by a numerical model. Second, at measurement temperatures near room temperature the spin diffusion length in n-GaAs is less than the channel thickness of 2.5 μm. In this regime a more general solution of the spin drift-diffusion equation is needed, because Eq. (4) is only appropriate for devices where the spin drift and diffusion are effectively one-dimensional. In two or three dimensions, the spin accumulation decays faster than $e^{-y/\lambda}$ for $y < \lambda$, in exact analogy to the two and three dimensional solutions of the screened Poisson equation.

The spatial profile of spin accumulation in the channel is modeled by solving the spin drift-diffusion equation [40] in steady state,

$$\frac{\partial\mathbf{P}}{\partial t} = 0 = -\frac{\mathbf{P}}{\tau_s} + D\nabla^2\mathbf{P} + \frac{\mathbf{J}}{ne}\cdot\nabla\mathbf{P} + \frac{\alpha\hat{\mathbf{m}}_i|\mathbf{J}_i|}{ne\Delta z}, \tag{5}$$

where $|\mathbf{P}| \equiv (n_\uparrow - n_\downarrow)/n$ is the dimensionless spin polarization of the channel, D is the spin diffusion constant (equal to the charge diffusion constant [40]), $\hat{\mathbf{m}}_i$ specifies the injector contact magnetization direction, and the last term specifies the source term, which is only nonzero at the cells of the finite element model where spin injection occurs. In the source term, the Δz factor in the denominator is the size of the injection cell in the z direction, which normalizes the injection rate in the finite-element grid properly. $\mathbf{J}$ is the current density in the channel, and the parameter α is the spin injection efficiency at the FM/SC interface (i.e., for $\alpha = 1$ the spin current at the FM/SC interface is equal to the charge current). α encompasses both the bulk polarization of the current in the FM, as well as interface effects determining the polarization of the charge current. The spin valve device geometry is cast into a finite-element grid, and Eq. (5) is solved numerically by forward iteration until steady state is reached. See Fig. 7 for a schematic diagram illustrating the model geometry. The contact length in the x direction (50 μm) is much longer than the spin diffusion length at all temperatures. The model is therefore confined to the yz plane and the spin accumulation is assumed to be uniform in the x direction. Neumann boundary conditions are enforced at the free boundary cells, i.e., the diffusive spin current $\propto \nabla\mathbf{P} = 0$ at the boundaries.

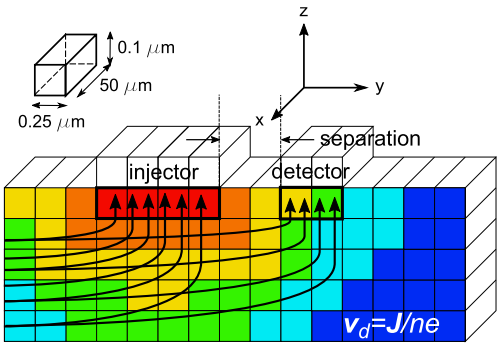

FIG. 7. Schematic illustrating the 2D finite-element model used to solve Eq. (5) numerically. The spin accumulation, which drifts and diffuses from the injector contact, is indicated for illustrative purposes in false color (red high, blue low). The channel drift velocity $\mathbf{v}_d = \mathbf{J}/ne$ is schematically shown by the field lines. The bolded black outlines the cells in which injection and detection occurs. The cell dimensions $\Delta x, \Delta y, \Delta z$ used in the simulation are shown in the upper left. The number of cells drawn is not the actual number of cells used, nor is the model drawn to scale.

The current density $\mathbf{J}$ in the channel was solved for prior to solving Eq. (5) by assuming charge neutrality throughout the channel, so that $\nabla\cdot\mathbf{E} = \nabla\cdot\mathbf{J} = 0$. Because $\nabla\cdot\mathbf{J} = 0$, there exists a scalar potential ϕ_J that satisfies $\nabla^2\phi_J = 0$. ϕ_J is solved for with a Laplace relaxation method, and finally the current density vector field is solved for by evaluating $\nabla\cdot\phi_J = \mathbf{J}$.

The diffusion constant D is calculated from the Einstein relation

$$D = \frac{n\nu}{e}\left(\frac{\partial\mu}{\partial n}\right), \tag{6}$$

where ν is the mobility. For $n = 2.8\times10^{16}$ GaAs, the Fermi temperature $T_F \simeq 60$ K, so in order to capture the transition from degenerate to nondegenerate behavior, the inverse compressibility $\partial\mu/\partial n$ is calculated using full Fermi-Dirac statistics. A parabolic conduction band density of states with GaAs effective mass $m^* = 0.067m_0$ [28] is used, and the inverse compressibility is evaluated via the expression

$$\frac{\partial\mu}{\partial n} = \frac{k_bT}{n}\frac{F_{1/2}(\zeta)}{F_{-1/2}(\zeta)}, \tag{7}$$

where $\zeta \equiv \mu/k_bT$ is the reduced chemical potential and $F_\alpha(\zeta)$ is the complete Fermi-Dirac integral. In the limits $T \ll T_F$ and

$T \gg T_F$ Eq. (7) reduces to $\partial\mu/\partial n = 2E_F/3n$ and $\partial\mu/\partial n = k_bT/n$, respectively.

To compare the solution of Eq. (5) directly with the measured ΔV_{nl}, the calculated nonlocal spin accumulation at the detector is input to Eq. (1). The overall scale of η, the detection efficiency, cannot be determined in this measurement. However, because the known injector current density constrains the spin injection rate, the product of the injection and detection efficiencies $\eta\alpha$ can be determined. We will discuss the constraints on η in more detail below.

The IDSD measurement results are fitted to the numerical solution of Eq. (5), with the spin lifetime τ_s and the dimensionless spin injection efficiency α as fitting parameters. The fits to the IDSD results are shown as solid lines in Fig. 6, and the temperature dependencies of the fitting parameters τ_s and $\eta\alpha$ are shown in Figs. 8(a) and 8(b). The product ηP_0 of the detection efficiency and the spin polarization P_0 below the injector is also shown in Fig. 8(b).

D. Hanle fitting

At low temperatures, at which the NLH measurement could be performed, the spin lifetime obtained from fits of the IDSD measurement could be compared to the spin lifetime measured by Hanle precession experiments. To fit NLH field sweeps the data were fitted to the Green's function solution of Eq. (5) in one dimension, which gives

$$V_{nl}(H) \propto \mathbf{P}(y)\cdot\hat{\mathbf{m}}_d \propto \int_{-\infty}^{t} \frac{\exp\left[-\left(\frac{y^2}{4Dt}+\frac{t}{\tau_s}\right)\right]}{\sqrt{4\pi Dt}}\cos(\gamma_e H t)dt, \quad (8)$$

where $|\gamma_e|/2\pi = 0.62$ MHz/Oe is the gyromagnetic ratio in GaAs. Equation (8) is identical to solving Eq. (5) in one dimension with an added precession term from an external transverse magnetic field H, and $\mathbf{J} = 0$. The simplification to one dimension is appropriate at low temperatures, because the spin diffusion length $\sqrt{D\tau_s}$ is larger than the channel depth of 2.5 μm.

E. Spin lifetime calculation

In order to compare the measured temperature dependence of the spin lifetime with DP theory, we used the method of Lau, Olesberg, and Flatté [56,57] to calculate the spin relaxation rate for the doping concentration $n = 2.8\times10^{16}$ cm^{-3}. The spin relaxation rate, τ_s^{-1}, can be expressed as

$$\tau_s^{-1} = \frac{1}{\tilde{n}}\int D(\epsilon)f(\epsilon)[1-f(\epsilon)]\tau_3(\epsilon)\Omega_3^2(\epsilon)d\epsilon, \quad (9)$$

where $D(\epsilon)$ is the effective-mass approximation density of states per unit volume in the GaAs, $f(\epsilon)$ is the Fermi-Dirac distribution function, τ_3 is the $l = 3$ component in the multipole expansion of the momentum scattering time, $\Omega_3(\epsilon)$ is the $l = 3$ component of the energy-dependent effective SOI magnetic field, and $\tilde{n} = \int D(\epsilon)f(\epsilon)[1-f(\epsilon)]d\epsilon$. (Although $\tilde{n}$ was not precisely defined in Ref. [56], $\tilde{n}$ corresponds to the density n that was used in Eq. (3) of Ref. [56] and for the resulting calculations and plots.) The cubic symmetry of the Dresselhaus interaction in bulk GaAs [15] results in $\Omega_l^2 = 0$ for all $l \neq 3$. Equation (9) is a generalization of the original DP expression $\tau_s^{-1} = a\langle\Omega^2\rangle\tau_p$ [17,19], where the integral over energy in Eq. (9) properly weights the spin relaxation rate to account for an arbitrary degree of degeneracy as well as energy-dependent momentum scattering mechanisms.

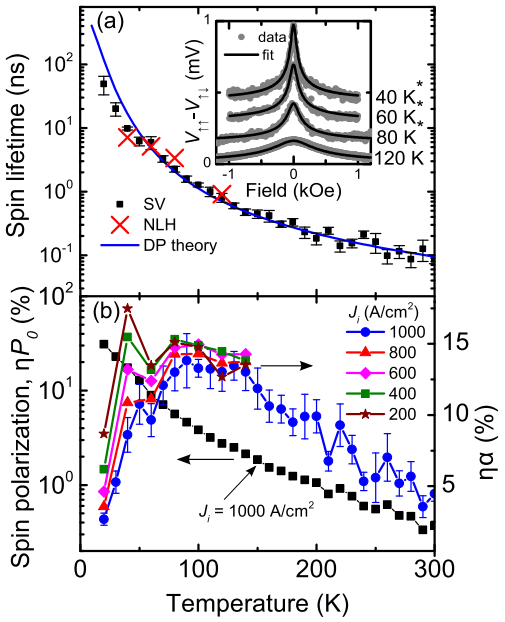

FIG. 8. (a) The temperature dependence of τ_s extracted from the fits in Fig. 6 along with the theoretical prediction based on Eq. (9), which is shown as the blue solid line. Spin lifetimes extracted from NLH measurements are shown as red crosses, with the corresponding NLH data $V_{\uparrow\uparrow} - V_{\uparrow\downarrow}$ and fits to Eq. (8) shown in the inset (artificially offset). The asterisks on the temperature labels in the inset indicate that the NLH sweeps were taken with the pulsed current measurement to mitigate DNP effects. The NLH data shown are taken at the same bias currents as used for the data of Fig. 6 on the 250 nm separation device. (b) The temperature dependence of ηP_0 (left ordinate) and $\eta\alpha$ (right ordinate). P_0 is the spin polarization directly beneath the injector from the model fits shown in Fig. 6. At temperatures below 140 K, $\eta\alpha$ is shown for different injector current densities using the symbols indicated in the legend. In (b) representative error bars are shown for the $J_i = 10^3$ A/cm^2 data only. All data in (b) were taken with $J_d = 40$ A/cm^2.

In n-GaAs, the dominant scattering mechanism changes from ionized-impurity (II) scattering at low temperatures to optical-phonon (OP) scattering at high temperatures [58], as demonstrated by the nonmonotonic temperature dependence of the mobility shown in Fig. 3(a). To determine the momentum scattering time, the experimental mobility ν is fitted to the form

$$\nu^{-1} = \underbrace{(A + BT^{3/2})^{-1}}_{\nu_{II}} + \underbrace{(CT^{-1})^{-1}}_{\nu_{OP}}, \quad (10)$$

which combines the II and OP scattering rates via Matthiessen's rule. In Eq. (10), A and B are fitting parameters for the II mechanism and C is a fitting parameter for

the OP mechanism. For II scattering, $T^{3/2}$ is the known temperature dependence of the scattering time [59] and the fitting parameter A is added to account for degeneracy at low temperatures. No universal energy exponent can be assigned to OP scattering over the experimental temperature range, due to the breakdown of the relaxation-time approximation [58,60]. We find, however, that $\nu \propto T^{-1}$ approximates the measured high-temperature mobility. This is not a rigorous relation for OP scattering, but the purpose of Eq. (10) is to provide a phenomenological scattering rate which *decreases* with temperature (II scattering) and a scattering rate which *increases* with temperature (OP scattering). The fit to Eq. (10) is shown along with the measured mobility in Fig. 3(a).

After fitting the temperature dependence of the mobility to extract the contributions due to the II and OP scattering mechanisms, each mechanism is separately fitted to the expression

$$\nu_{\mathrm{II(OP)}} = \frac{e}{m^* n} \int D(\epsilon) f(\epsilon)[1 - f(\epsilon)] \tau_{1,\mathrm{II(OP)}}(\epsilon) \frac{\epsilon}{k_b T} d\epsilon \tag{11}$$

to determine τ_1 (the momentum relaxation time) for each mechanism, at each temperature. The energy dependence of the scattering time is assumed to be $\tau_1 = a\epsilon^{\gamma}$, where $\gamma = 3/2$ and $\gamma = 1/2$ for II and OP scattering, respectively [57]. The relevant multipole component of the scattering time for DP relaxation, τ_3, can be determined from τ_1 by expressing the lth multipole component of the scattering time using the known form of the scattering cross section $\sigma(\theta,\epsilon)$

$$\tau_l^{-1}(\epsilon) = \int_0^{\pi} \sigma(\theta,\epsilon)[1 - P_l(\cos\theta)] \sin\theta d\theta, \tag{12}$$

where P_l is the Legendre polynomial of degree l. Equation (12) may be evaluated to relate τ_3 to τ_1 (for detailed evaluation of Eq. (12) see Ref. [19], resulting in $\tau_1 = \tau_3/6$ for II scattering, and $\tau_1 = 6\tau_3/41$ for OP scattering [19,57]).

After fitting the measured mobility with Eqs. (10) and (11), the $l = 3$ component of the momentum scattering rate $\tau_3^{-1} = \tau_{3,\mathrm{II}}^{-1} + \tau_{3,\mathrm{OP}}^{-1}$ is input to Eq. (9), and the DP spin relaxation rate is evaluated at all temperatures. The SOI strength used to evaluate Ω_3^2 as a function of carrier energy is taken from the $k \cdot p$ calculation with a full fourteen-band basis done by Lau *et al.* [56]. Their calculations give $\Omega = 2\beta/\hbar[\mathbf{k_x}(k_y^2 - k_z^2) + \mathbf{k_y}(k_z^2 - k_x^2) + \mathbf{k_z}(k_x^2 - k_y^2)]$ with $\beta = 25$ eV Å^3. The final result for the spin lifetime as a function of temperature from Eq. (9) is shown as the blue solid line in Fig. 8(a).

IV. DISCUSSION

As shown in Fig. 6, the spin diffusion length $\lambda = \sqrt{D\tau_s}$ falls from approximately 7 μm at 20 K to 1 μm at room temperature. Injector-detector separations less than approximately 1.0 μm are therefore ideal to detect nonlocal SV signals in n-GaAs at room temperature. We emphasize that a two-dimensional model of spin diffusion is needed to fit the separation dependence of ΔV_{nl} when the spin diffusion length is smaller than the channel depth of 2.5 μm. Fits using the 1D solution of Eq. (5) underestimate the spin lifetime and spin diffusion length when the channel thickness is greater than a spin diffusion length, because the spin accumulation in two dimensions decays faster than $e^{-y/\lambda}$ away from the injector.

As can be seen in Fig. 8(a), the temperature dependence of the spin lifetime agrees well with the DP prediction, calculated from Eq. (9), over the entire temperature range. τ_s varies from 49 ± 16 ns at 20 K to 86 ± 10 ps at 300 K. The relatively large uncertainty in the 20 K spin lifetime value results from a lack of data for injector-detector separations larger than the spin diffusion length at low temperature. Separations larger than 10 μm would be required to constrain the fit adequately. At low temperatures (40–120 K) we have also measured τ_s by the NLH measurement. The spin lifetimes obtained with NLH measurements are also shown in Fig. 8(a), with the NLH field sweeps and fits to Eq. (8) shown in the inset. The τ_s values from NLH measurements are in good agreement with the IDSD τ_s values above ~60 K. At the lowest temperatures (20–40 K), the pulsed NLH measurement technique may not be sufficient to completely remove the effects of DNP. A combined model of the electron-nuclear spin system is needed to adequately model the NLH measurement in the regime where DNP is significant, as is done in Refs. [12,14,61].

We now comment on the magnitude of ΔV_{nl} in the biased-detector SV measurement. Combining Eq. (1) and Eq. (7) allows one to determine the spin accumulation $n_\uparrow - n_\downarrow$ given ΔV_{nl}, the SV signal size. The only unknown is η, the detection efficiency. In our devices, we have demonstrated that η is a strong function of detector bias, which complicates the interpretation. Because of the detector bias dependence of η implied by the data shown in Fig. 5, we also cannot assume $\alpha = \eta$, as the injector contact is biased with a large current, while the detector bias is varied. Based on these considerations, the spin polarization of the channel and the injection efficiency may only be quantitatively evaluated up to a factor of η (i.e., ηP_0 and $\eta\alpha$, respectively), where η is the detection efficiency at the detector bias voltage at which the measurement was performed and P_0 is the spin polarization below the injector. These quantities are shown in Fig. 8(b). Although the overall scale for η cannot be determined in this experiment, it is believed to be ~50% based on spin-LED measurements on similar Fe/GaAs Schottky interfaces [62].

At the lowest temperatures, we measure ΔV_{nl} values of ~1 mV with a forward bias applied to a detector contact. This implies that the spin-resolved electrochemical potential splitting at the injector is comparable to the Fermi energy in the GaAs channel, which is ~5 meV with respect to the conduction band minimum. As the maximum possible value of η is unity, we emphasize that the ordinate scales shown in Fig. 8(b) are therefore minimum values for P_0 and α. At 20 K, we measure $\eta P_0 = 30\%$. Thus, the upper limit of 100% polarization in the GaAs puts a *lower* limit of $\eta \sim 0.3$ at 20 K. Notably, because the forward bias current (spin extraction) leads to drift *enhancement* of the spin accumulation buildup at the injector contact, ideal ferromagnetic contacts ($\alpha = 1$) are not necessary to achieve channel spin polarizations approaching 100% [40,63].

In Fig. 8(b), a downturn in the injection-detection efficiency product $\eta\alpha$ is observed at temperatures below 100 K. To address this observation, we have measured $\eta\alpha$ for different injector current biases. The results of this measurement are shown in Fig. 8(b), where it is apparent that $\eta\alpha$ is a function of

the injector current bias at low temperatures. At temperatures above ∼150 K, where the spin accumulation is small with respect to the carrier density, $\eta\alpha$ becomes independent of injector current bias.

To understand the injector bias current dependence of $\eta\alpha$, we first discuss the influence of an electric field on the spin accumulation. Electric fields at the injector necessarily accompany the bias current. In addition to the drift effects, discussed above, large electric fields in *n*-GaAs are known to enhance the spin relaxation rate. In *n*-GaAs, at low temperatures ($T \lesssim 30$ K) the itinerant electron temperature can deviate significantly from the lattice temperature due to the dominance of elastic scattering mechanisms, which hinder electron-lattice equilibration [64]. This electron heating is present above electric fields ∼10 V/cm, and leads to donor impact ionization, which prevents the electron temperature from cooling below the donor binding energy (∼6 meV for Si in GaAs [28]). At low temperatures, electric field dependence of the spin lifetime has been widely reported [9,65,66]. At the lowest temperatures in our experiment (20, 30 K), the suppression of the spin lifetime due to the applied electric field may contribute to the downturn in $\eta\alpha$ we observe. However, the injector bias dependence of $\eta\alpha$ is observed clearly up to ∼100 K in Fig. 8(b). At 100 K, all donors are thermally ionized and inelastic electron-phonon relaxation mechanisms are sufficient to prevent any electron-lattice temperature difference. Thus, we believe that electric field suppression of the spin lifetime is not the origin of the injector bias dependence of $\eta\alpha$.

We believe that the downturn in $\eta\alpha$ at low temperatures is more likely to be a consequence of the large spin polarization of the channel and consequent breakdown of the ordinary drift-diffusion model. In the presence of a spin accumulation comparable to the carrier density, Eq. (5) must be modified to prevent the spin polarization from achieving nonphysical values >100%. Physically, the model parameters themselves become functions of the spin polarization, and the assumption of linear response breaks down [67]. To be specific, it becomes necessary to specify the diffusion constants and spin relaxation rates separately for minority and majority spin carriers, i.e., $\tau_{\uparrow\downarrow}^{-1} \neq \tau_{\downarrow\uparrow}^{-1} \neq \tau_{s,0}^{-1}/2$ and $D_\uparrow \neq D_\downarrow \neq D_0$, where $\tau_{s,0}^{-1}$ and D_0 are the equilibrium spin relaxation rate and diffusion constant, respectively [68]. We note that for the DP spin relaxation mechanism ($\tau_s^{-1} \sim \epsilon^3 \tau_p$) in *n*-GaAs where II scattering is dominant ($\tau_p \sim \epsilon^{3/2}$) the spin relaxation rate is a strong function of carrier energy ϵ. The diffusion constant also increases with increasing carrier energy via the Einstein relation [Eq. (6)]. The mechanisms described above may provide feedback to limit the spin polarization in the large spin polarization regime via more efficient spin diffusion and spin relaxation processes compared to the small spin polarization linear-response limit. If this were the case, then the injector current polarization required to achieve a given spin accumulation would be larger than that calculated under the assumption of linear response.

V. CONCLUSIONS

In conclusion, we have explored several aspects of spin transport in epitaxial FM/*n*-GaAs spin valves over a wide range of temperature and bias conditions. Because these devices are based on Schottky tunnel barriers, both the injection and detection efficiencies depend on the bias. We have exploited this property to enhance the sensitivity to spin accumulation by applying a bias current to the detector in the nonlocal configuration. Although the mechanism for the enhancement is not well understood (except for the role of drift), this approach enables detection of spin accumulation up to room temperature. At injector current densities of 10^3 A/cm^2 nonlocal voltages of order ∼1 mV are detected at low temperature, which fall to ∼40 μV at room temperature. This approach has enabled measurements of the spin relaxation rate and diffusion length over the entire temperature range, and good agreement is obtained with a model based on the D'yakonov-Perel' spin relaxation mechanism. At the lowest temperatures, however, the standard drift-diffusion model appears to break down because of the large spin accumulation, which is comparable to the carrier density. At high temperatures, the devices are limited by the rapidly increasing spin relaxation rate, although the injected current polarization also decreases by a factor of three between 20 K and room temperature.

The devices discussed in this paper are based on Heusler alloys, which are predicted to have a high spin polarization and grow epitaxially on GaAs (001). There is sufficient uncertainty in the derived values of the detection efficiency and injected current polarization that it is not possible to make a statement about the polarization of the Co_2FeSi injector beyond the lower bound (30%) set by the size of the nonlocal voltage at the lowest temperature. As suggested by the bias dependence, there is likely a significant contribution to the tunneling current from interface states, a property that is shared by the epitaxial Fe/GaAs system [54]. Although these important details still need to be resolved, this work demonstrates that epitaxial FM/III-V heterostructures can be used to probe spin transport at room temperature.

ACKNOWLEDGMENTS

This work was supported by the National Science Foundation (NSF) under DMR-1104951, C-SPIN, one of the six centers of STARnet, an SRC program sponsored by MARCO and DARPA, the Materials Research Science and Engineering Centers (MRSEC) program of the NSF under DMR 08-19885 and DMR 14-20013, and the NSF NNCI program.

[1] X. Lou, C. Adelmann, S. A. Crooker, E. S. Garlid, J. Zhang, K. S. M. Reddy, S. D. Flexner, C. J. Palmstrøm, and P. A. Crowell, Nat. Phys. **3**, 197 (2007).

[2] M. Ciorga, A. Einwanger, U. Wurstbauer, D. Schuh, W. Wegscheider, and D. Weiss, Phys. Rev. B **79**, 165321 (2009).

[3] G. Salis, A. Fuhrer, R. R. Schlittler, L. Gross, and S. F. Alvarado, Phys. Rev. B **81**, 205323 (2010).

[4] T. Saito, N. Tezuka, M. Matsuura, and S. Sugimoto, Appl. Phys. Express **6**, 103006 (2013).

[5] I. Appelbaum, B. Huang, and D. J. Monsma, Nature (London) **447**, 295 (2007).

[6] N. Tombros, C. Jozsa, M. Popinciuc, H. T. Jonkman, and B. J. van Wees, Nature (London) **448**, 571 (2007).

[7] W. Han, K. Pi, K. M. McCreary, Y. Li, J. J. I. Wong, A. G. Swartz, and R. K. Kawakami, Phys. Rev. Lett. **105**, 167202 (2010).

[8] X. Lou, C. Adelmann, M. Furis, S. A. Crooker, C. J. Palmstrøm, and P. A. Crowell, Phys. Rev. Lett. **96**, 176603 (2006).

[9] Y. K. Kato, R. C. Myers, A. C. Gossard, and D. D. Awschalom, Science **306**, 1910 (2004).

[10] L. K. Werake, B. A. Ruzicka, and H. Zhao, Phys. Rev. Lett. **106**, 107205 (2011).

[11] E. S. Garlid, Q. O. Hu, M. K. Chan, C. J. Palmstrøm, and P. A. Crowell, Phys. Rev. Lett. **105**, 156602 (2010).

[12] M. K. Chan, Q. O. Hu, J. Zhang, T. Kondo, C. J. Palmstrøm, and P. A. Crowell, Phys. Rev. B **80**, 161206 (2009).

[13] C. Awo-Affouda, O. M. J. van 't Erve, G. Kioseoglou, A. T. Hanbicki, M. Holub, C. H. Li, and B. T. Jonker, Appl. Phys. Lett. **94**, 102511 (2009).

[14] G. Salis, A. Fuhrer, and S. F. Alvarado, Phys. Rev. B **80**, 115332 (2009).

[15] G. Dresselhaus, Phys. Rev. **100**, 580 (1955).

[16] S. Datta and B. Das, Appl. Phys. Lett. **56**, 665 (1990).

[17] M. I. D'yakonov and V. I. Perel', Sov. Phys. JETP **33**, 1053 (1971).

[18] R. I. Dzhioev, K. V. Kavokin, V. L. Korenev, M. V. Lazarev, B. Y. Meltser, M. N. Stepanova, B. P. Zakharchenya, D. Gammon, and D. S. Katzer, Phys. Rev. B **66**, 245204 (2002).

[19] G. E. Pikus and A. N. Titkov, in *Optical Orientation*, edited by F. Meier and B. P. Zakharchenya (North-Holland, Amsterdam, 1984), Chap. 3.

[20] J. M. Kikkawa and D. D. Awschalom, Phys. Rev. Lett. **80**, 4313 (1998).

[21] E. I. Rashba, Phys. Rev. B **62**, R16267 (2000).

[22] A. Fert and H. Jaffrès, Phys. Rev. B **64**, 184420 (2001).

[23] A. T. Hanbicki, B. T. Jonker, G. Itskos, G. Kioseoglou, and A. Petrou, Appl. Phys. Lett. **80**, 1240 (2001).

[24] M. Hashimoto, J. Herfort, H.-P. Schonherr, and K. H. Ploog, Appl. Phys. Lett. **87**, 102506 (2005).

[25] A. Hirohata, H. Kurebayashi, S. Okamura, M. Kikuchi, T. Masaki, T. Nozaki, N. Tezuka, and K. Inomata, J. Appl. Phys. **97**, 103714 (2005).

[26] C. Liu, Y. Boyko, C. C. Geppert, K. D. Christie, G. Stecklein, S. J. Patel, C. J. Palmstrøm, and P. A. Crowell, Appl. Phys. Lett. **105**, 212401 (2014).

[27] C. Liu, S. J. Patel, T. A. Peterson, C. C. Geppert, K. D. Christie, C. J. Palmstrøm, and P. A. Crowell, Nat. Commun. **7**, 10296 (2016).

[28] P. Y. Yu and M. Cardona, *Fundamentals of Semiconductors* (Springer-Verlag, Berlin, 1996).

[29] M. Benzaquen, D. Walsh, and K. Mazuruk, Phys. Rev. B **34**, 8947 (1986).

[30] B. F. Lewis and E. H. Sondheimer, Proc. R. Soc. London A **227**, 241 (1955).

[31] A. T. Hanbicki, O. M. J. van 't Erve, R. Magno, G. Kioseoglou, C. H. Li, B. T. Jonker, G. Itskos, R. Mallory, M. Yasar, and A. Petrou, Appl. Phys. Lett. **82**, 4092 (2003).

[32] A. M. Cowley and S. M. Sze, J. Appl. Phys. **36**, 3212 (1965).

[33] R. Stratton, in *Tunneling Phenomena in Solids*, edited by E. Burstein and S. Lundqvist (Plenum Press, New York, 1969), Chap. 8.

[34] W. F. Brinkman, R. C. Dynes, and J. M. Rowell, J. Appl. Phys. **41**, 1915 (1970).

[35] M. Johnson and R. H. Silsbee, Phys. Rev. Lett. **55**, 1790 (1985).

[36] S. A. Crooker, E. S. Garlid, A. N. Chantis, D. L. Smith, K. S. M. Reddy, Q. O. Hu, T. Kondo, C. J. Palmstrøm, and P. A. Crowell, Phys. Rev. B **80**, 041305 (2009).

[37] P. Bruski, Y. Manzke, R. Farshchi, O. Brandt, J. Herfort, and M. Ramsteiner, Appl. Phys. Lett. **103**, 052406 (2013).

[38] Y. Song and H. Dery, Phys. Rev. B **81**, 045321 (2010).

[39] F. J. Jedema, H. B. Heersche, A. T. Filip, J. J. A. Baselmans, and B. J. van Wees, Nature (London) **416**, 713 (2002).

[40] Z. G. Yu and M. E. Flatté, Phys. Rev. B **66**, 201202 (2002).

[41] T. Tahara, Y. Ando, M. Kameno, H. Koike, K. Tanaka, S. Miwa, Y. Suzuki, T. Sasaki, T. Oikawa, and M. Shiraishi, Phys. Rev. B **93**, 214406(R) (2016).

[42] A. N. Chantis and D. L. Smith, Phys. Rev. B **78**, 235317 (2008).

[43] Q. O. Hu, E. S. Garlid, P. A. Crowell, and C. J. Palmstrøm, Phys. Rev. B **84**, 085306 (2011).

[44] H. Dery and L. J. Sham, Phys. Rev. Lett. **98**, 046602 (2007).

[45] Y. Pu, J. Beardsley, P. M. Odenthal, A. G. Swartz, R. K. Kawakami, P. C. Hammel, E. Johnston-Halperin, J. Sinova, and J. P. Pelz, Appl. Phys. Lett. **103**, 012402 (2013).

[46] J. Shiogai, M. Ciorga, M. Utz, D. Schuh, M. Kohda, D. Bougeard, T. Nojima, J. Nitta, and D. Weiss, Phys. Rev. B **89**, 081307 (2014).

[47] R. Jansen, A. Spiesser, H. Saito, and S. Yuasa, Phys. Rev. B **92**, 075304 (2015).

[48] M. Tran, H. Jaffrès, C. Deranlot, J.-M. George, A. Fert, A. Miard, and A. Lemaître, Phys. Rev. Lett. **102**, 036601 (2009).

[49] O. Txoperena, Y. Song, L. Qing, M. Gobbi, L. E. Hueso, H. Dery, and F. Casanova, Phys. Rev. Lett. **113**, 146601 (2014).

[50] R. Jansen, A. M. Deac, H. Saito, and S. Yuasa, Phys. Rev. B **85**, 134420 (2012).

[51] S. Wurmehl, G. H. Fecher, H. C. Kandpal, V. Ksenofontov, C. Felser, H.-J. Lin, and J. Morais, Phys. Rev. B **72**, 184434 (2005).

[52] B. Balke, G. H. Fecher, H. C. Kandpal, C. Felser, K. Kobayashi, E. Ikenaga, J.-J. Kim, and S. Ueda, Phys. Rev. B **74**, 104405 (2006).

[53] S. Picozzi and A. J. Freeman, J. Phys.: Condens. Matter **19**, 315215 (2007).

[54] A. N. Chantis, K. D. Belashchenko, D. L. Smith, E. Y. Tsymbal, M. van Schilfgaarde, and R. C. Albers, Phys. Rev. Lett. **99**, 196603 (2007).

[55] K. D. Christie, Non-equilibrium spin accumulation in $Co_2Fe_xMn_{1-x}Si/n$-GaAs heterostructures, Ph.D. thesis, University of Minnesota, 2014.

[56] W. H. Lau, J. T. Olesberg, and M. E. Flatté, Phys. Rev. B **64**, 161301 (2001).

[57] W. H. Lau, J. T. Olesberg, and M. E. Flatté, arXiv:cond-mat/0406201.

[58] K. Fletcher and P. N. Butcher, J. Phys. C **5**, 212 (1972).

[59] H. Brooks, Adv. Electron. Electron Phys. **7**, 85 (1955).

[60] D. J. Howarth and E. H. Sondheimer, Proc. R. Soc. London A **219**, 53 (1953).
[61] N. J. Harmon, T. A. Peterson, C. C. Geppert, S. J. Patel, C. J. Palmstrøm, P. A. Crowell, and M. E. Flatté, Phys. Rev. B **92**, 140201 (2015).
[62] C. Adelmann, X. Lou, J. Strand, C. J. Palmstrøm, and P. A. Crowell, Phys. Rev. B **71**, 121301 (2005).
[63] A. G. Petukhov, J. Niggemann, V. N. Smelyanskiy, and V. V. Osipov, J. Phys.: Condens. Matter **19**, 315205 (2007).
[64] D. J. Oliver, Phys. Rev. **127**, 1045 (1962).
[65] M. Beck, C. Metzner, S. Malzer, and G. H. Döhler, Europhys. Lett. **75**, 597 (2005).
[66] M. Furis, D. L. Smith, J. L. Reno, and S. A. Crooker, Appl. Phys. Lett. **89**, 102102 (2006).
[67] Y. Qi, Z.-G. Yu, and M. E. Flatté, Phys. Rev. Lett. **96**, 026602 (2006).
[68] I. J. Vera-Marun, V. Ranjan, and B. J. van Wees, Nat. Phys. **8**, 313 (2011).

E.2 Heusler/Pt spin-orbit torques and the magnetic proximity effect

Below the manuscript summarizing the harmonic response spin-orbit torque measurement results on the TMC223 and TMC224 Co_2FeAl/Pt bilayers presented in Chapter 2 of this thesis is reproduced with the permission of the APS, as it appears published in Physical Review B **97**, 020403(R) (2018). The APS retains all copyrights to the manuscript. The Supplemental Material is also reproduced following the main manuscript.

E.2.1 Main text

Rapid Communications

Influence of the magnetic proximity effect on spin-orbit torque efficiencies in ferromagnet/platinum bilayers

T. A. Peterson,[1] A. P. McFadden,[2] C. J. Palmstrøm,[2] and P. A. Crowell[1,*]
[1]*School of Physics and Astronomy, University of Minnesota, Minneapolis, Minnesota 55455, USA*
[2]*Department of Electrical & Computer Engineering and Department of Materials, University of California, Santa Barbara, California 93106, USA*

(Received 28 August 2017; revised manuscript received 9 November 2017; published 10 January 2018)

Current-induced spin-orbit torques in Co_2FeAl/Pt ultrathin bilayers are studied using a magnetoresistive harmonic response technique, which distinguishes the dampinglike and fieldlike contributions. The presence of a temperature-dependent magnetic proximity effect is observed through the anomalous Hall and anisotropic magnetoresistances, which are enhanced at low temperatures for thin platinum thicknesses. The fieldlike torque efficiency decreases steadily as the temperature is lowered for all Pt thicknesses studied, which we propose is related to the influence of the magnetic proximity effect on the fieldlike torque mechanism.

DOI: 10.1103/PhysRevB.97.020403

Through the spin-orbit interaction (SOI), an electrical current $\boldsymbol{j}_e$ in a ferromagnet (F)/nonmagnetic metal (N) bilayer results in a torque on the magnetization $\boldsymbol{M}$ of F [1,2]. This spin-orbit torque (SOT) may be decomposed into two perpendicular components—a component oriented along $\hat{\boldsymbol{m}} \times (\hat{\boldsymbol{m}} \times \hat{\boldsymbol{\sigma}})$ and a component along $\hat{\boldsymbol{m}} \times \hat{\boldsymbol{\sigma}}$, where $\hat{\boldsymbol{\sigma}} \equiv \hat{\boldsymbol{j}}_e \times \hat{\boldsymbol{n}}$ denotes the orientation of the spin current created by the SOI and $\hat{\boldsymbol{n}}$ defines the unit vector normal to the plane formed by the F/N interface. These are referred to as the dampinglike (DL) and fieldlike (FL) SOTs, respectively. Although the microscopic origins of the DL and FL SOTs remain unclear, the DL contribution has been widely interpreted using the N bulk spin-Hall effect (SHE) diffusion models [2–5] and the FL contribution attributed to the F/N interfacial SOI [1,4]. Amin and Stiles [6] have recently emphasized that this interpretation is overly simplistic, showing that the interfacial SOI and the SHE in the N layer may both produce FL *and* DL torques depending on the interface details. Unfortunately, the interfacial parameters used in spin-diffusion models are not easily measured, and it remains an experimental challenge to separately identify the origins of the DL and FL torques. Also, in bilayers where interface scattering is dominant, a conventional normal-to-interface spin-diffusion length becomes difficult to define. Furthermore, magnetic proximity effects (MPEs) at F/N interfaces have been widely reported [7–10], yet how the MPE influences SOTs is unknown.

In this Rapid Communication, we report a decrease in the FL and DL torques per unit current density (hereafter referred to as SOT efficiencies) at low temperatures in Co_2FeAl/Pt bilayers. In the same bilayers, a temperature-dependent MPE is revealed through magnetoresistance (MR) measurements. The FL SOT efficiency is suppressed by nearly a factor of 4 at 20 K with respect to room temperature for all Pt thicknesses studied, which we propose is related to the increasing influence of the MPE exchange field on the F/N interface Rashba spin accumulation. Meanwhile, the DL SOT efficiency monotonically increases with decreasing Pt thickness and closely tracks the Pt resistivity as temperature is varied. Within the Pt SHE diffusion model, the latter observation may be described by either the intrinsic SHE or the spin backflow processes, between which we cannot differentiate.

The F/N bilayers used in this Rapid Communication were grown on MgO(001) substrates by molecular-beam epitaxy (MBE). Prior to F growth, an *in situ* MgO buffer was grown by electron-beam (e-beam) evaporation on prepared MgO substrates in order to bury residual carbon and improve surface morphology. The F layer is the Heusler compound Co_2FeAl (CFA) with a thickness of $t_F = 1.2$ nm, grown by MBE at a substrate temperature of 200 °C by codeposition of individual elemental sources in ultrahigh vacuum (UHV). Reflection high-energy electron diffraction (RHEED) monitored during CFA growth confirmed a 45° rotated orientation CFA⟨110⟩ ∥ MgO⟨100⟩. X-ray diffraction (XRD) measurements conducted on thicker 4- and 30-nm MgO/CFA samples confirm a single phase of (001) oriented CFA whereas the presence and relative peak area of the (002) reflection confirms at least $B2$ ordering. The samples were cooled to room temperature before capping with Pt, which was grown using e-beam evaporation in UHV. The Pt grew epitaxially and was (001) oriented with Pt⟨100⟩ ∥ CFA⟨110⟩ as confirmed by RHEED and XRD. An *in situ* shadow-mask technique was used to achieve four different Pt cap thicknesses (t_N) on the same MgO/CFA(1.2-nm) underlayer. Two growths, one with $t_N = 1, 2, 3, 4$ nm and the other with $t_N = 5, 6, 7, 8$ nm, were used in this study. After Pt capping, samples were removed from UHV and exposed to atmosphere for subsequent processing. Vibrating sample magnetometry was used to measure the CFA(1.2-nm) saturation magnetization $M_s = 800 \pm 100$ emu/cm^3 at room temperature. The saturation magnetic field of the anomalous Hall effect (AHE) at 300 K matched $4\pi M_s$ within uncertainty. Therefore, the AHE saturation field was used to infer the temperature dependence of M_s, which increased from 850 emu/cm^3 at

*Corresponding author: crowell@umn.edu

 ©2018 American Physical Society

300 K to 1050 emu/cm^3 at 10 K. Ferromagnetic resonance (FMR) measurements were performed at room temperature on a companion MgO/CFA(1.2-nm)/Pt(7-nm) bilayer for which the Kittel formula [11] fits of the FMR field for rf excitation frequencies from 4 to 20 GHz revealed a cubic in-plane anisotropy of $K_1 = -6 \times 10^3$ J/m^3 with magnetic easy axes along CFA⟨110⟩(MgO⟨100⟩).

The bilayers were patterned into Hall bars by photolithography and Ar^+-ion milling, and Ti/Au vias and bonding pads were subsequently deposited. The Hall bar width was 10 μm. A magnetoresistive second-harmonic (2ω) response technique similar to that discussed in Refs. [4,12,13] was employed to measure the SOT efficiencies. The DL and FL effective fields H_{DL} and H_{FL} result in 2ω Hall resistances due to the AHE and planar Hall effect, respectively. An applied magnetic field was rotated 360° in the sample plane, and the angular dependence of the 2ω Hall resistance was fit to extract H_{DL} and H_{FL}. Magnetothermoelectric effects [14], which can contribute to 2ω resistances, were carefully taken into account. See the Supplemental Material [15] for a detailed description of the measurement geometry and fitting procedure. The dimensionless SOT efficiency is given by [16]

$$\xi_{DL(FL)} \equiv \frac{M_s t_F H_{DL(FL)}}{(\hbar/2e) j_N^e}, \tag{1}$$

where e is the electron charge, $\hbar$ is Planck's constant, and j_N^e is the current density in the N layer.

The bilayer square resistances R_{xx} are summarized in Fig. 1(a) for all Pt thicknesses at temperatures of 300 and 20 K. The inset of Fig. 1(a) shows the Pt resistivity, which is a strong function of thickness due to diffuse surface scattering [17]. The F and N layers are treated as parallel resistances to account for the current shunted through F and determine j_N^e in the denominator of Eq. (1). See the Supplemental Material [15] for a detailed discussion of the shunting model and the method used to extract the Pt and CFA resistivities from R_{xx}. The CFA resistivity extracted from the shunting model is 130 $\mu\Omega$ cm, which is similar to resistivities we measure for thicker 5- and 10-nm CFA films capped with AlOx. For the 5- and 10-nm CFA films, resistivities are $\rho \simeq 100$ $\mu\Omega$ cm with residual resistivity ratios (RRRs) of RRR $\simeq 1.1$, and we have also measured the AHE resistivity $\rho_{\mathrm{AHE}} \simeq 0.6$ $\mu\Omega$ cm. For these CFA films we find ρ_{AHE} decreases as temperature is decreased with a trend close to $\rho_{\mathrm{AHE}} \propto \rho^2$. In contrast, for the CFA(1.2-nm)/Pt bilayers we observe an increase in the AHE resistance R_{AHE} and anisotropic MR R_{AMR} at low temperatures for thin Pt thicknesses. (R_{AHE} is defined by the expression $R_{xy} = R_{\mathrm{AHE}} m_z + R_H$ with m_z denoting the out-of-plane magnetization component, R_H denoting the ordinary Hall effect resistance, and $R_{\mathrm{AMR}} \equiv (R_{xx}^{\parallel} - R_{xx}^{\perp})/2$ with the parallel and perpendicular superscripts denoting the orientation of the current and the saturated magnetization.) Figure 2 summarizes the temperature and Pt thickness dependence of R_{AHE} and R_{AMR} by plotting these MRs vs R_{xx} in which temperature is the implicit variable. The temperature was varied between 10 K (low R_{xx}) and 300 K (high R_{xx}). (See the Supplemental Material [15] for example magnetic field sweeps used to extract R_{AHE} and R_{AMR} and for an alternative representation of the data shown in Fig. 2 in which temperature is indicated explicitly.)

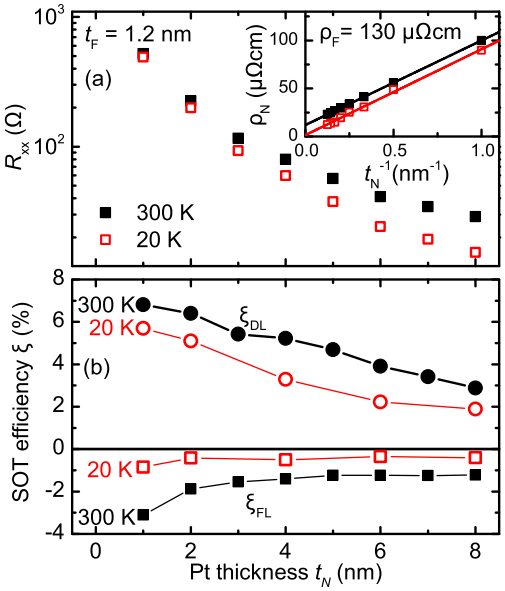

FIG. 1. (a) The bilayer square resistance for all Pt thicknesses. The solid black squares are the 300-K data, and the open red squares are the 20-K data. In the inset, the Pt resistivity is plotted vs the inverse of the Pt thickness. The intercepts of the solid lines correspond to the bulk resistivity of Pt. In (b), the SOT efficiencies ξ_{DL} (the circles) and ξ_{FL} (the squares) are shown for different Pt thicknesses at 300 K (the black solid symbols) and 20 K (the red open symbols). The lines connect the data points. For all data the CFA thickness is 1.2 nm.

The increase in the (extraordinary or anomalous [18]) MR observed at low temperatures in Fig. 2 is due to the MPE. Because of current shunting through the F in metallic F/N bilayers, MR-based studies of the MPE have typically been relegated to ferromagnet insulator/Pt bilayers [8,19–21]. However, the MR behavior shown in Fig. 2 as temperature is decreased cannot be attributed to shunting through F. Given F RRR values near unity, F shunting alone results in a measured $R_{MR} \propto R_{xx}^2$ [15]. In fact, the trends of both R_{AHE} and R_{AMR} consistently show excess MR at low temperatures compared to the $R_{MR} \propto R_{xx}^2$ trend drawn in Fig. 2, indicating an additional MPE MR contribution at low temperatures. Furthermore, for the 1- and 2-nm Pt bilayers, both AHE and AMR resistances *increase* as the temperature decreases. For the 1-nm Pt bilayer R_{AMR} increases by a factor of 3 from 300 to 10 K, in stark contrast to the F shunting prediction of a 12% decrease over the same temperature range. In fact, the bilayer $R_{\mathrm{AMR}} > 0$ is opposite in sign to that measured in 5-nm CFA films with Al capping layers, highlighting the influence of the Pt layer on the AMR.

Briefly, we discuss the relevance of the recently discovered spin-Hall MR (SMR) effect [22–25] to our MR measurements. The conventional AMR effect [18] magnitudes summarized in Fig. 2 were obtained by performing the measurement in

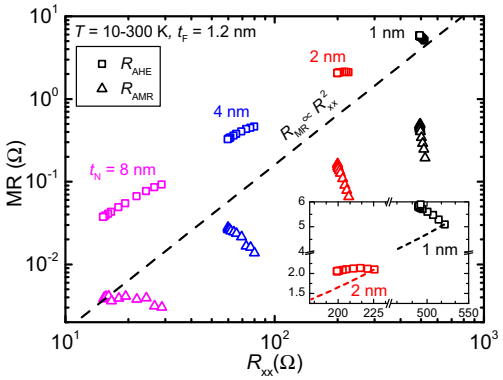

FIG. 2. Summary of R_{AHE} (the squares) and R_{AMR} (the triangles) vs R_{xx} for the different bilayers, which are labeled by the Pt thickness. Temperature is an implicit variable, and the minima and maxima of R_{xx} correspond to 10 and 300 K, respectively, for all bilayers except the 1-nm Pt bilayer in which R_{xx} shows a small upturn below 20 K. The dashed lines indicate $R_{MR} \propto R_{xx}^2$, which is expected for MR originating from F shunting alone. The inset magnifies the AHE data for the 1- and 2-nm Pt bilayers. See Fig. 5 in the Supplemental Material [15] for an alternative representation in which temperature is indicated explicitly and details on how R_{AHE} and R_{AMR} were measured.

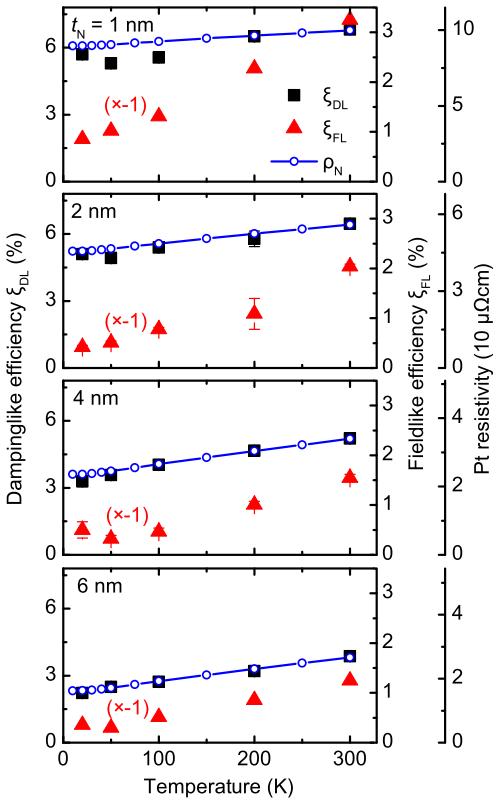

FIG. 3. The temperature dependence of the SOT efficiencies ξ_{DL} (the black squares, left ordinate) and ξ_{FL} (the red triangles, right ordinate 1) for the 1-, 2-, 4-, and 6-nm Pt bilayers as indicated in the figure. The ξ_{FL} data have been scaled by a factor of -1. The error bars represent the standard errors. The Pt resistivity is shown (right ordinate 2) as the blue open circles, and the lines connect the data points.

a geometry such that the SMR effect is absent, similar to Ref. [22]. See the Supplemental Material [15] for the details of the measurement geometry used to differentiate R_{AMR} from SMR effects. (We do observe a SMR-like MR of magnitude $\Delta R_{xx}/R_{xx} \sim 10^{-3}$, but these effects are not the focus of this Rapid Communication.) It has been reported that the SMR effect in N may give rise to an AHE-like transverse resistance (SH-AHE) [23,26,27]. In comparison to Refs. [23,26], however, in our bilayers R_{AHE} is a factor of 10–100 times larger. Furthermore, given that we observe SMR magnitudes of $\sim 10^{-3}$, we expect the SH-AHE magnitude (R_{xy}/R_{xx}) to be on the order of 10^{-4}–10^{-5} [27], much smaller than the AHE we observe.

The temperature-dependent AHE and AMR behaviors we observe are in good agreement with literature reports of a low-temperature MPE in F/Pt bilayers [8,9,20,28], although quantitative parameters, such as the magnetic moment density or MPE layer thickness, are not easily extracted from these measurements. Although few experimental papers directly discuss the influence of the MPE on SOT efficiencies, Lim *et al.* [28] have commented that the MPE at a F/Pt interface may affect spin-dependent transport significantly through enhanced transverse dephasing processes in the MPE Pt volume. The distinguishing experimental feature is expected to be the temperature dependence because the MPE is enhanced at low temperatures. To study the influence of the MPE on the SOT efficiencies, we have performed the ξ_{DL} and ξ_{FL} harmonic response measurement from 300 to 20 K, the results of which are summarized in Fig. 1(b). Both the DL and the FL components are detected for all Pt thicknesses with ξ_{FL} having an opposite sign and smaller magnitude than ξ_{DL}. The signs [29] of ξ_{DL} and ξ_{FL} are in agreement with measurements reported for CoFe/Pt bilayers [30]. In Fig. 1(b), it is clear that ξ_{FL} is strongly suppressed at low temperatures for all thicknesses, whereas ξ_{DL} shows only modest suppression. The SOT efficiencies are plotted vs temperature in Fig. 3.

In the discussion that follows below, we propose a mechanism by which the MPE may suppress ξ_{FL} at low temperatures in which we attribute the DL SOT to the Pt SHE and the FL SOT to the CFA/Pt interface Rashba effect. This causal distinction is well motivated for F/Pt bilayers [1,3–5] and is supported by the qualitatively different trends we observe in ξ_{DL} and ξ_{FL} as Pt thickness and temperature are varied. In principle, the CFA/MgO interface may also possess a Rashba interaction, however as Pt thickness is increased, a diminishing fraction of the current is shunted through the CFA layer. Because the ξ_{FL} data shown in Fig. 1(b) plateaus for large Pt thickness

when normalized by the Pt current density, the Pt and CFA/Pt interfaces give the dominant sources of SOTs. An alternative explanation of the FL SOT in F/N bilayers invokes the N SHE and a nonzero imaginary component of the interface mixing conductance Im($G_{\uparrow\downarrow}$), which has been supported by recent measurements involving light-metal spacer layers [31–33]. We will return to a discussion of our SOT measurements in the context of the SHE-Im($G_{\uparrow\downarrow}$) interpretation near the end of this Rapid Communication.

First, we discuss the ξ_{DL} measurements summarized in Fig. 1(b). DL SOT efficiencies in F/N bilayers are typically interpreted through fits to the N SHE spin-diffusion model [5,34], the hallmark of which is an increase in ξ_{DL} with increasing N thickness, saturating at a thickness set by the spin-diffusion length. Because ξ_{DL} in our samples *decreases* monotonically with increasing Pt thickness, any naive model would imply that a corresponding spin-diffusion length is less than ∼1 nm. Although the data may be interpreted by invoking a spin-diffusion length less than 1 nm, the value itself does not have real physical significance given that it is smaller than the momentum scattering length, which in this limit is set by the film thickness. In Fig. 3, the right ordinate is used to compare ξ_{DL} to Pt resistivity as the temperature is varied. We see that ξ_{DL} tracks ρ_{Pt} closely: for small thicknesses ($t_N = 1,2$ nm) where the Pt RRR is small, the temperature dependence of ξ_{DL} is weak, whereas for large thicknesses ($t_N = 6,8$ nm) where the RRR is larger, ξ_{DL} has a more pronounced temperature dependence. The observation that $\xi_{DL} \propto \rho$, if interpreted through the SHE diffusion model, is consistent with the intrinsic (or possibly side-jump) SHE scaling reported for Pt [5,35,36]. However, spin backflow could also result in a similar phenomenology as $\xi_{DL} \propto 2G_{\uparrow\downarrow}/(G_N + 2G_{\uparrow\downarrow})$ where $G_N \equiv (\rho\lambda)^{-1}$ and $G_{\uparrow\downarrow}$ is the F/N interface spin-mixing conductance [37]. Spin backflow is significant for Pt due to the relatively low resistivity and short spin-diffusion length. From a fitting point of view, we cannot constrain enough parameters to distinguish between these two explanations for the $\xi_{DL} \propto \rho$ observation. Furthermore, we caution that, when the SHE diffusion model parameters (SH ratio, spin-diffusion length, N spin resistance) vary with N resistivity, all of the models become poorly constrained.

We now turn to discussing the temperature dependence of the FL SOT efficiency, which is shown in Fig. 3. For all thicknesses, the magnitude of ξ_{FL} decreases by a factor of nearly 4 from 300 to 20 K, in contrast to ξ_{DL} for which the temperature dependence simply follows the Pt resistivity. A similar behavior of ξ_{FL} has been observed in annealed CoFe/Pt [16]. We believe that the decrease in ξ_{FL} as temperature decreases is due to the increased MPE at low temperatures. The FL component of the SOT originates from the exchange interaction between a Rashba-induced spin accumulation in N and the F magnetization [38,39]. In Fig. 4(a), the Rashba spin accumulation is drawn transverse to the magnetization to illustrate the maximal torque configuration in the absence of the MPE. However, for nonzero MPE, the Rashba spin accumulation generated at the interface transverse to $\hat{\boldsymbol{m}}$ rapidly precesses about and is dephased by the inhomogeneous MPE exchange field as is illustrated in Fig. 4(b). Perhaps counterintuitively, at low temperatures where moments in N and F are strongly coupled, ξ_{FL} decreases because the exchange interaction

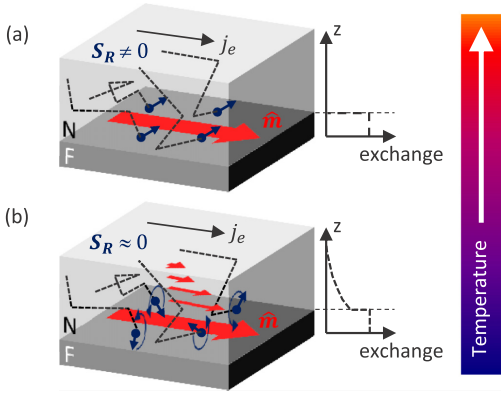

FIG. 4. Illustrations of (a) the Rashba spin accumulation S_R at high temperatures in the absence of the MPE and (b) MPE order at low temperatures which serves to precess and destroy the transverse Rashba spin accumulation. The magnetization $\hat{\boldsymbol{m}}$ and current $\boldsymbol{j}_e$ are indicated with the red and black arrows, respectively. Right-drifting carriers in N, which make up the current, are drawn as the blue arrows (denoting spin accumulation) with the black dashed trajectories implying scattering events. Plots of the exchange interaction strength vs depth coordinate z in the bilayer, which are schematic and not drawn to scale, are included.

extends into N and destroys the spin accumulation responsible for the FL SOT. We note that, in principle, the anisotropic nature of the proposed dephasing process may modify the angular dependence of the FL SOT contribution harmonic response measurement. This modification is discussed at length in the Supplemental Material [15]. Unfortunately, within the fitting uncertainty of our measurement we cannot resolve if these modifications are reflected in our data. In any case, any small modification to the angular dependence of the FL SOT harmonic response does not alter our critical observation (i.e., the suppression of the FL SOT at low temperatures). The physics of the MPE suppression of the FL SOT may not be captured by existing models, which assume an interface δ-function exchange coupling between the F and the N moments [40,41] rather than a spatially nonuniform MPE exchange interaction extending a finite thickness into N. We note that in some cases [33,42,43] the FL SOT has been observed to increase with temperature in bilayers with Ta and W as the N metal, which are not believed to support MPEs. It is not clear if the FL SOTs presented in Refs. [33,42,43] and their temperature dependencies are due to the same mechanisms as those presented in this Rapid Communication.

In the above discussion, we have attributed the FL SOT to the CFA/Pt interface Rashba effect. We briefly discuss the alternative picture in which the FL SOT arises from the Pt SHE through Im($G_{\uparrow\downarrow}$). Im($G_{\uparrow\downarrow}$) physically corresponds to incomplete absorption of transverse spin current by the F layer, which can be pictured semiclassically as the N spin current reflecting from the F layer with the spin precessed through a finite phase (rather than complete precessional dephasing). It is believed that Re($G_{\uparrow\downarrow}$) ≫ Im($G_{\uparrow\downarrow}$) with sizable Im($G_{\uparrow\downarrow}$) only

occurs for very thin (few-Å) F layers. If we interpret our data in the picture where the FL SOT arises from the Pt SHE through $\mathrm{Im}(G_{\uparrow\downarrow})$, the implication would be that $\mathrm{Im}(G_{\uparrow\downarrow})$ increases as temperature is increased. The same efficient dephasing of spin accumulation transverse to $\hat{\boldsymbol{m}}$ due to the MPE can explain this trend: At low temperatures, the extension of the magnetized volume into Pt [28,44] suppresses $\mathrm{Im}(G_{\uparrow\downarrow})$ by the increase in the effective F thickness.

We conclude by highlighting an important distinction of the MPE precessional dephasing process from interface spin-memory loss relaxation processes [45]. For spin-magnetization interactions, angular momentum conservation necessitates that the MPE suppression of the transverse interface spin accumulation represents a transverse spin current sunk into the N MPE magnetization, which should result in a DL torque (as the N magnetization is exchange coupled to the F magnetization). In the Rashba FL SOT interpretation, this would reflect a transfer of FL SOT to DL Rashba SOT, and in the SHE picture it would reflect a corresponding increase in $\mathrm{Re}(G_{\uparrow\downarrow})$ as $\mathrm{Im}(G_{\uparrow\downarrow})$ decreases. However, we observe no distinguishable increase in ξ_{DL} at low temperatures. Therefore, we conclude that the MPE suppression of the Rashba spin accumulation generates a much smaller *spin current* than is generated by the SHE, which is consistent with the discussion by Haney *et al.* [40]. In the case of the SHE spin current generated in the bulk of N away from the interface, we expect that the few-Å-thick MPE layer extends the effective F/N interface slightly into Pt but does not influence ξ_{DL}, consistent with SOT-FMR measurements by Zhang *et al.* [46] for Pt thicknesses larger than 1 nm.

In conclusion, we have demonstrated a suppression of the fieldlike SOT efficiency as the MPE increases at low temperatures in F/Pt bilayers. The fieldlike SOT is attributed to the Rashba SOT mechanism, which we propose is suppressed in the presence of a MPE exchange field. As a possible alternative, we also outline how the MPE could decrease the imaginary component of the F/N spin-mixing conductance. This identification implies engineering of the MPE may provide a technique to maximize Rashba SOT efficiencies in F/Pt bilayers.

We thank C. Liu for helpful discussions. This work was supported by C-SPIN, one of the six centers of STARnet, a SRC Program sponsored by MARCO and DARPA, the NSF through DMR-1708287, and the NSF NNCI Program.

[1] I. M. Miron, K. Garello, G. Gaudin, P.-J. Zermatten, M. V. Costache, S. Auffret, S. Bandiera, B. Rodmacq, A. Schuhl, and P. Gambardella, Nature (London) **476**, 189 (2011).
[2] L. Liu, C.-F. Pai, Y. Li, H. W. Tseng, D. C. Ralph, and R. A. Buhrman, Science **336**, 555 (2012).
[3] L. Liu, O. J. Lee, T. J. Gudmundsen, D. C. Ralph, and R. A. Buhrman, Phys. Rev. Lett. **109**, 096602 (2012).
[4] X. Fan, J. Wu, Y. Chen, M. J. Jerry, H. Zhang, and J. Q. Xiao, Nat. Commun. **4**, 1799 (2013).
[5] M.-H. Nguyen, D. C. Ralph, and R. A. Buhrman, Phys. Rev. Lett. **116**, 126601 (2016).
[6] V. P. Amin and M. D. Stiles, Phys. Rev. B **94**, 104420 (2016).
[7] L. Cheng, Z. Altounian, D. H. Ryan, J. O. Ström-Olsen, M. Sutton, and Z. Tun, Phys. Rev. B **69**, 144403 (2004).
[8] S. Y. Huang, X. Fan, D. Qu, Y. P. Chen, W. G. Wang, J. Wu, T. Y. Chen, J. Q. Xiao, and C. L. Chien, Phys. Rev. Lett. **109**, 107204 (2012).
[9] W. Zhang, M. B. Jungfleisch, W. Jiang, Y. Liu, J. E. Pearson, S. G. E. te Velthuis, A. Hoffmann, F. Freimuth, and Y. Mokrousov, Phys. Rev. B **91**, 115316 (2015).
[10] Y. Yang, B. Wu, K. Yao, S. Shannigrahi, B. Zong, and Y. Wu, J. Appl. Phys. **115**, 17C509 (2014).
[11] C. Kittel, Phys. Rev. **73**, 155 (1948).
[12] M. Kawaguchi, K. Shimamura, S. Fukami, F. Matsukura, H. Ohno, T. Moriyama, D. Chiba, and T. Ono, Appl. Phys. Express **6**, 113002 (2013).
[13] C. O. Avci, K. Garello, M. Gabureac, A. Ghosh, A. Fuhrer, S. F. Alvarado, and P. Gambardella, Phys. Rev. B **90**, 224427 (2014).
[14] G. Bauer, E. Saitoh, and B. J. Van Wees, Nat. Mater. **11**, 391 (2012).
[15] See Supplemental Material at http://link.aps.org/supplemental/10.1103/PhysRevB.97.020403 for details, which include Refs. [47–55].
[16] C.-F. Pai, Y. Ou, L. H. Vilela-Leão, D. C. Ralph, and R. A. Buhrman, Phys. Rev. B **92**, 064426 (2015).
[17] E. H. Sondheimer, Adv. Phys. **1**, 1 (1952).
[18] T. R. Mcguire and R. I. Potter, IEEE Trans. Magn. **11**, 1018 (1975).
[19] Y. M. Lu, Y. Choi, C. M. Ortega, X. M. Cheng, J. W. Cai, S. Y. Huang, L. Sun, and C. L. Chien, Phys. Rev. Lett. **110**, 147207 (2013).
[20] B. F. Miao, S. Y. Huang, D. Qu, and C. L. Chien, Phys. Rev. Lett. **112**, 236601 (2014).
[21] B. F. Miao, L. Sun, D. Wu, C. L. Chien, and H. F. Ding, Appl. Phys. Lett. **110**, 222402 (2017).
[22] H. Nakayama, M. Althammer, Y.-T. Chen, K. Uchida, Y. Kajiwara, D. Kikuchi, T. Ohtani, S. Geprägs, M. Opel, S. Takahashi, R. Gross, G. E. W. Bauer, S. T. B. Goennenwein, and E. Saitoh, Phys. Rev. Lett. **110**, 206601 (2013).
[23] M. Althammer, S. Meyer, H. Nakayama, M. Schreier, S. Altmannshofer, M. Weiler, H. Huebl, S. Geprägs, M. Opel, R. Gross, D. Meier, C. Klewe, T. Kuschel, J.-M. Schmalhorst, G. Reiss, L. Shen, A. Gupta, Y.-T. Chen, G. E. W. Bauer, E. Saitoh, and S. T. B. Goennenwein, Phys. Rev. B **87**, 224401 (2013).
[24] S. Meyer, M. Althammer, S. Geprägs, M. Opel, R. Gross, and S. T. B. Goennenwein, Appl. Phys. Lett. **104**, 242411 (2014).
[25] J. Kim, P. Sheng, S. Takahashi, S. Mitani, and M. Hayashi, Phys. Rev. Lett. **116**, 097201 (2016).
[26] S. Meyer, R. Schlitz, S. Geprägs, M. Opel, H. Huebl, R. Gross, and S. T. B. Goennenwein, Appl. Phys. Lett. **106**, 132402 (2015).
[27] Y.-T. Chen, S. Takahashi, H. Nakayama, M. Althammer, S. T. B. Goennenwein, E. Saitoh, and G. E. W. Bauer, Phys. Rev. B **87**, 144411 (2013).
[28] W. L. Lim, N. Ebrahim-Zadeh, J. C. Owens, H. G. E. Hentschel, and S. Urazhdin, Appl. Phys. Lett. **102**, 162404 (2013).
[29] With the current defining the $+x$ direction, H_{DL} along the $+z$ direction gives positive ξ_{DL} for magnetization along $+x$, and

H_{FL} along $-y$ gives negative ξ_{FL}. The signs of these efficiencies would be reversed if the order of the stack was reversed from F/N to N/F.

[30] S. Emori, U. Bauer, S.-M. Ahn, E. Martinez, and G. S. D. Beach, Nat. Mater. **12**, 611 (2013).

[31] X. Fan, H. Celik, J. Wu, C. Ni, K.-J. Lee, V. O. Lorenz, and J. Q. Xiao, Nat. Commun. **5**, 3042 (2014).

[32] T. Nan, S. Emori, C. T. Boone, X. Wang, T. M. Oxholm, J. G. Jones, B. M. Howe, G. J. Brown, and N. X. Sun, Phys. Rev. B **91**, 214416 (2015).

[33] Y. Ou, C.-F. Pai, S. Shi, D. C. Ralph, and R. A. Buhrman, Phys. Rev. B **94**, 140414 (2016).

[34] A. Ganguly, K. Kondou, H. Sukegawa, S. Mitani, S. Kasai, Y. Niimi, Y. Otani, and A. Barman, Appl. Phys. Lett. **104**, 072405 (2014).

[35] H. Nguyen, W. Pratt, and J. Bass, J. Magn. Magn. Mater. **361**, 30 (2014).

[36] E. Sagasta, Y. Omori, M. Isasa, M. Gradhand, L. E. Hueso, Y. Niimi, Y. C. Otani, and F. Casanova, Phys. Rev. B **94**, 060412(R) (2016).

[37] A. Brataas, Y. V. Nazarov, and G. E. W. Bauer, Eur. Phys. J. B **22**, 99 (2000).

[38] A. Manchon and S. Zhang, Phys. Rev. B **79**, 094422 (2009).

[39] I. M. Miron, G. Gaudin, S. Auffret, B. Rodmacq, A. Schuhl, S. Pizzini, J. Vogel, and P. Gambardella, Nat. Mater. **9**, 230 (2010).

[40] P. M. Haney, H.-W. Lee, K.-J. Lee, A. Manchon, and M. D. Stiles, Phys. Rev. B **87**, 174411 (2013).

[41] V. P. Amin and M. D. Stiles, Phys. Rev. B **94**, 104419 (2016).

[42] X. Qiu, P. Deorani, K. Narayanapillai, K.-S. Lee, K.-J. Lee, H.-W. Lee, and H. Yang, Sci. Rep. **4**, 4491 (2015).

[43] J. Kim, J. Sinha, S. Mitani, M. Hayashi, S. Takahashi, S. Maekawa, M. Yamanouchi, and H. Ohno, Phys. Rev. B **89**, 174424 (2014).

[44] C. Klewe, T. Kuschel, J.-M. Schmalhorst, F. Bertram, O. Kuschel, J. Wollschläger, J. Strempfer, M. Meinert, and G. Reiss, Phys. Rev. B **93**, 214440 (2016).

[45] W. Park, D. V. Baxter, S. Steenwyk, I. Moraru, W. P. Pratt, and J. Bass, Phys. Rev. B **62**, 1178 (2000).

[46] W. Zhang, V. Vlaminck, J. E. Pearson, R. Divan, S. D. Bader, and A. Hoffmann, Appl. Phys. Lett. **103**, 242414 (2013).

[47] U. H. Pi, K. Won Kim, J. Y. Bae, S. C. Lee, Y. J. Cho, K. S. Kim, and S. Seo, Appl. Phys. Lett. **97**, 162507 (2010).

[48] J. Kim, J. Sinha, M. Hayashi, M. Yamanouchi, S. Fukami, T. Suzuki, S. Mitani, and H. Ohno, Nat. Mater. **12**, 240 (2012).

[49] S. Y. Huang, W. G. Wang, S. F. Lee, J. Kwo, and C. L. Chien, Phys. Rev. Lett. **107**, 216604 (2011).

[50] K. Uchida, M. Ishida, T. Kikkawa, A. Kirihara, T. Murakami, and E. Saitoh, J. Phys.: Condens. Matter **26**, 343202 (2014).

[51] S. H. Wang, L. K. Zou, J. W. Cai, B. G. Shen, and J. R. Sun, Phys. Rev. B **88**, 214304 (2013).

[52] M. Johnson and R. H. Silsbee, Phys. Rev. Lett. **55**, 1790 (1985).

[53] F. J. Jedema, H. B. Heersche, A. T. Filip, J. J. A. Baselmans, and B. J. van Wees, Nature (London) **416**, 713 (2002).

[54] L. Abadlia, F. Gasser, K. Khalouk, M. Mayoufi, and J. G. Gasser, Rev. Sci. Instrum. **85**, 095121 (2014).

[55] *Handbook of Chemistry and Physics*, edited by D. R. Lide (CRC, Boca Raton, FL, 1996).

E.2.2 Supplemental material

SUPPLEMENTAL MATERIAL

Harmonic response measurement

To extract the dampinglike (DL) and fieldlike (FL) spin-orbit torque (SOT) effective magnetic fields H_{DL} and H_{FL} which appear in Eq. 1 in the main text, we used a harmonic response technique optimized for in-plane magnetized films. The technique follows closely from the original magnetoresistive (MR) harmonic response measurements of SOTs developed in References [1–3] for perpendicularly magnetized films, and the adaptation to in-plane magnetized films by Kawaguchi *et al.* [4]. Later, Avci *et al.* [5] discussed magnetothermoelectric (MTE) effects which must be accounted for in harmonic MR measurements of SOTs in the in-plane geometry. Our expressions are similar to Ref. [5], however we arrive at a more compact expression in a simplified geometry to account for MTE effects.

In the following, we describe our measurement details. Figure 1(a) shows a plan-view optical micrograph of an example Hall bar and description of the coordinate system used. The Hall bar width was 10 μm. A low-frequency ($\omega/2\pi \simeq 10$ Hz) ac excitation current $\sim \sin\omega t$ with root-mean-square (RMS) amplitude I was applied to a Hall bar, and the second harmonic Hall resistance $R_H^{2\omega} \equiv \langle V_H^+ - V_H^- \rangle^{2\omega}/I$ was measured with phase and harmonic sensitive lock-in detection, where the brackets denote the RMS amplitude of the 2ω Y-quadrature Hall voltage. The orientation ϕ of the static applied magnetic field H was rotated 360° in the bilayer plane while recording $R_H^{2\omega}$, for varied magnetic field strengths. Figure 1(b-d) shows example data for different Pt thicknesses and temperature, where H was varied between 0.6 T and 9 T. Below, we discuss the model that was used to fit the data and extract H_{DL} and H_{FL}.

The DL and FL SOTs applied at ω give rise to $R_H^{2\omega}$ angular dependencies originating from the anomalous Hall effect (AHE) and planar Hall effect (PHE), respectively. The ac current results in an effective field $\boldsymbol{H}^\omega = H_{DL}\sin\phi\sin\omega t\hat{\boldsymbol{z}} + (H_{FL} + H_{Oe})\sin\omega t\hat{\boldsymbol{y}}$, which tilts the magnetization small angles from the applied magnetic field at frequency ω. The

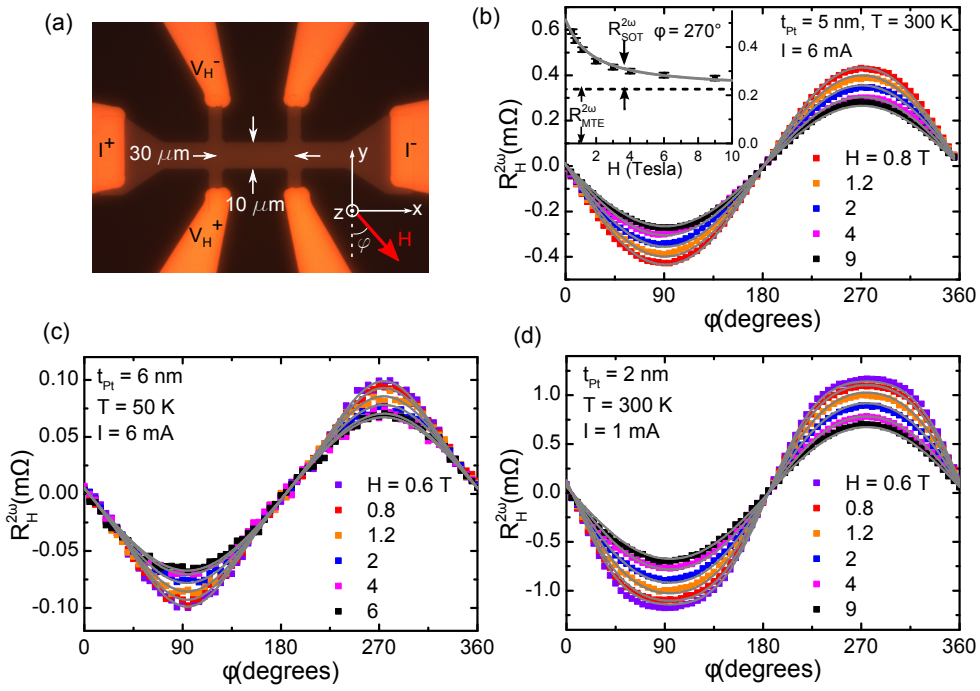

FIG. 1. (a) Plan view optical micrograph of an example Hall bar used in this study. The dimensions are indicated on the image, and the coordinate system is defined in the lower right. (b-d) Example second harmonic Hall resistance as function of in-plane angle ϕ for different applied magnetic fields, with the corresponding Pt thickness, temperature, and current indicated on the figure. The solid curves show the fit to Eq. 1. The angle-independent offset $R_0^{2\omega}$ was subtracted from the data shown. In (b), the fit values are $H_{DL} = 24$ Oe, $H_{FL} + H_{Oe} = -0.86$ Oe, and $R_{MTE}^{2\omega} = -0.22$ mΩ, in (c), $H_{DL} = 9.1$ Oe, $H_{FL} + H_{Oe} = -4.3$ Oe, and $R_{MTE}^{2\omega} = -0.059$ mΩ, and in (d), $H_{DL} = 12$ Oe, $H_{FL} + H_{Oe} = 2.9$ Oe, and $R_{MTE}^{2\omega} = -0.56$ mΩ. In the inset of (b), $R_H^{2\omega}$ at $\phi = 270°$ is plotted vs. magnetic field, with the fit to Eq. 1 shown as the solid curve. The dashed line indicates $R_{\mathrm{MTE}}^{2\omega}$.

AHE and PHE then result in a 2ω Hall resistance given by [4, 5][6]

$$\begin{aligned} R_H^{2\omega}(\phi, H) = & \\ & -\frac{1}{2}\frac{R_{AHE}H_{DL}}{(4\pi M_s + H)}\sin\phi \\ & -\frac{1}{2}\frac{R_{\mathrm{PHE}}(H_{FL} + H_{Oe})}{H}(\sin 3\phi - \sin\phi) \\ & + R_{MTE}^{2\omega}\sin\phi + R_0^{2\omega}, \end{aligned} \tag{1}$$

where R_{AHE} is the AHE resistance, R_{PHE} is the PHE resistance, and $4\pi M_s$ is the out-of-plane demagnetization field. The $R_{MTE}^{2\omega}\sin\phi$ term captures MTE emfs such as the anomalous Nernst effect (ANE) and logitudinal spin-Seebeck effect (LSSE)[7–9], which go as $\nabla T \times \hat{\boldsymbol{m}}$. ($\nabla T$ is predominantly in the z-direction due to the flow of Joule heat into the substrate.) $R_0^{2\omega}$ is an overall offset that likely originates from the Seebeck effect due to small in-plane components of ∇T. H_{Oe} is the Oersted field that results from the ac excitation current in the Pt layer, and is calculated from Ampere's law. Equation 1 is valid for $H \gg H_{DL}, H_{FL}$. The applied magnetic field is much larger than the in-plane magnetic anisotropy field ($2K_1/M_s \simeq 150$ Oe at room temperature) such that the static magnetization may be considered saturated along the applied field direction at all ϕ angles for fields larger than a few kOe. The factors of $-1/2$ in the first and second terms in Eq. 1 arise from the trigonometric identity $\sin^2\omega t = (1/2)(1 - \cos 2\omega t)$, as the 2ω lockin Y-quadrature signal is proportional to $\cos 2\omega t$. The AHE and PHE resistances were measured on the same Hall bar with low excitation current using conventional transport techniques for each Pt thickness and temperature. The sign of the SOT efficiency corresponds to the sign of the effective field (in a right-handed Cartesian coordinate system) produced by a charge current applied in the $+\hat{x}$ direction shown in Fig. 1(a). For example, the positive ξ_{DL} values reflect $\boldsymbol{H}_{DL} \parallel +\hat{z}$ for $\hat{\boldsymbol{m}} \parallel +\hat{x}$, and the negative ξ_{FL} values reflect $\boldsymbol{H}_{FL} \parallel -\hat{y}$ direction, both for current applied in $+\hat{x}$ direction. We verified that H_{DL} and H_{FL} increase linearly with excitation current, however current dependencies were not performed exhaustively as the 2ω detection method itself guarantees that $R^{2\omega} \propto I$ (i.e. $V^{2\omega} \propto I^2$).

The 360° ϕ-rotations at each Pt thickness and temperature were fit to Eq. 1 to extract H_{DL} and H_{FL}, with a single set of fitting parameters (H_{DL}, H_{FL}, $R_{MTE}^{2\omega}$, and $R_0^{2\omega}$) used for all applied magnetic field strengths. The fits are compared to the example data in Fig. 1(b-d), showing Eq. 1 captured the measured data well. The $\sin\phi$-behavior of the data shown indicate that DL SOT and MTE effects dominate the angular dependence of $R_H^{2\omega}$,

while a smaller $\sin 3\phi - \sin \phi$ signal is present due to the sum of H_{Oe} and H_{FL}. The more "triangular" shape of the Figure 1(c) data illustrate a case where $H_{FL} + H_{Oe} < 0$, and the more "square" shape of the Figure 1(d) data illustrate a case where $H_{FL} + H_{Oe} > 0$. In these bilayers, we observe MTE signals of comparable size to those due to SOT. The inset of Fig. 1(b) illustrates how the magnetic field dependence allows differentiation of the MTE signal from the DL SOT signal. We emphasize that for in-plane magnetized bilayers, the magnetic field dependence must be used to differentiate MTE 2ω resistances from those due to the DL SOT.

The SOT effective magnetic fields H_{DL} and H_{FL} obtained by fitting as described above were input to Eq. 1 of the main text for each Pt thickness and temperature, resulting in the SOT efficiency data shown in Fig. 1(b) and Fig. 3 of the main text.

Influence of transverse dephasing on the harmonic Hall measurement

It was pointed out during the review process of this article that transverse dephasing of the Rashba spin accumulation due to the magnetic proximity effect (MPE) will lead to an alteration of the angular-dependent FL SOT term in the harmonic Hall response measurement described by the second term in Eq. 1. In this section, a model is developed to account for this possibility, in which the MPE suppression of the Rashba spin accumulation is modelled with a Hanle-effect-like transverse dephasing process. However, it is shown that when fitting to our data we cannot distinguish this model from results described by Eq. 1.

The transverse dephasing of the Rashba interface spin accumulation $\boldsymbol{S}_R$ due to the MPE can be modelled as a Hanle effect[10, 11] suppression of the spin accumulation, where the MPE exchange field $\boldsymbol{H}_{MPE} = H_{MPE}\hat{\boldsymbol{m}}$ (parallel to F magnetization $\hat{\boldsymbol{m}}$) plays the role of the Hanle magnetic field. To begin, we define $\boldsymbol{S}_R$ by expressing the FL spin-orbit torque (SOT) $\boldsymbol{\tau}_{FL}$ on the magnetization through the expression

$$\boldsymbol{\tau}_{FL} = \boldsymbol{m} \times \boldsymbol{S}_R = mS_R \sin\phi \hat{\boldsymbol{z}}, \tag{2}$$

where as in Fig. 1(a) ϕ is the angle between $\boldsymbol{S}_R$ and $\boldsymbol{m}$, which lie in the xy-plane. Now, we account for the transverse dephasing of the Rashba spin accumulation through a Lorentzian expression typical of the Hanle effect

$$\boldsymbol{S}_R = \frac{S_R^0 \hat{\boldsymbol{z}}}{1 + \eta^2 \sin^2\phi}, \tag{3}$$

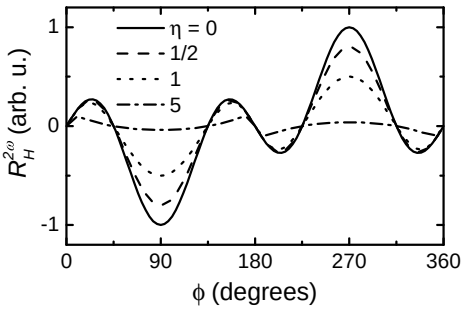

FIG. 2. Example evaluations of Eq. 5 for varied Hanle suppression η values indicated on the figure. For simplicity, the prefactors R_{PHE}, H^0_{FL}, and H of Eq. 5 are set to unity to generate these curves.

where we have defined $\eta \equiv H_{MPE}/H_c$ as a Hanle suppression factor, and H_c represents the characteristic half-width-half-maximum field of Hanle suppression for the case where $\boldsymbol{S}_R$ and $\boldsymbol{m}$ are perpendicular. Combining Eq. 2 and Eq. 3 we have

$$\boldsymbol{\tau}_{FL} = \frac{mS^0_R \hat{\boldsymbol{z}}}{\csc\phi + \eta^2 \sin\phi}. \tag{4}$$

To understand how Eq. 4 modifies the second term in Eq. 1, we must consider the angular dependence of the Hall resistance due to the PHE, $R_H = R_{PHE} \sin 2\phi$. The HR measurement is sensitive to the product of $\boldsymbol{\tau}_{FL}$ and $dR_H/d\phi$, so the second term in Eq. 1 becomes

$$R^{2\omega}_H = -\frac{1}{2}\frac{R_{\mathrm{PHE}} H^0_{FL}}{H}\frac{2\cos 2\phi}{\csc\phi + \eta^2 \sin\phi}, \tag{5}$$

where H^0_{FL} is the FL SOT effective field corresponding to S^0_R. In absence of the MPE ($\eta = 0$), the $\sin 3\phi - \sin\phi$ dependence of the second term in Eq. 1 is recovered. Figure 2 illustrates ϕ-dependencies of Eq. 5 for varied η values, in which it is apparent that for increasing η the local extrema at $\phi = 90°, 270°$ decrease in magnitude with respect to the local extrema on each side, which slightly widen in angular position with respect to the $\phi = 90°, 270°$ extrema.

What we have done for the HR measurement results presented in the main text, as described in the first section of this Supplemental material, is equivalent to setting $\eta = 0$ and fitting the temperature-dependence of the results with H_{FL} taken as a function of temperature. The results are used to calculate the FL SOT efficiency parameter ξ_{FL} presented in the

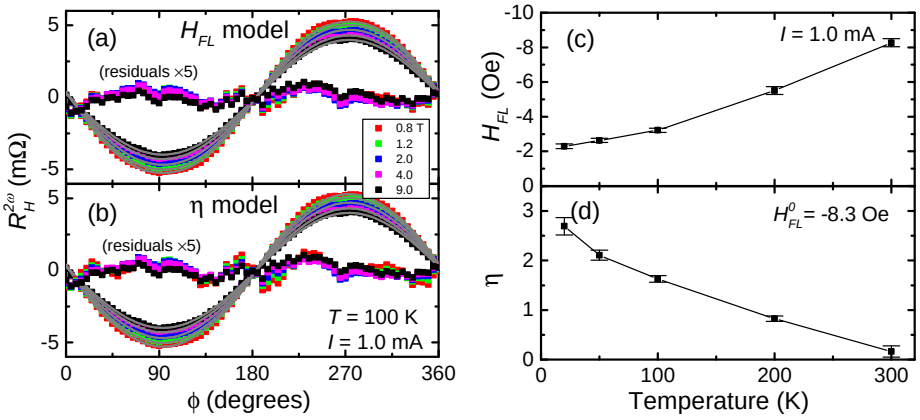

FIG. 3. Fits to the H_{FL} model (a) and the η model (b) at different magnetic field strengths for the 1.0 nm Pt bilayer at 100 K, with the fit residuals also shown and magnified by 5 for clarity. The single fit in (a) and (b) are the gray solid lines, evaluated at the magnetic field to correspond to the data. In (c), the results of the H_{FL} model fits are summarized for the 1.0 nm Pt bilayer at excitation current of 1.0 mA, and in (d) the corresponding results of the η model fits are summarized for fixed $H_{FL}^0 = -8.3$ Oe. In (c) and (d), the lines connect data points and error bars represent the standard error of the fit parameters.

main text Figures 1(b) and 3. In what follows we will refer to the orthodox FL SOT model given by Eq. 1 as the H_{FL} model, and the model developed in this section as the η model. As noted earlier, the interpretation we make on the origin of the FL SOT suppression at low temperature suggest we should describe our data through the η model with *fixed* H_{FL}^0, and allow η to vary as a function of temperature.

As an exercise, we compare the results of fits to the H_{FL} model (Eq. 1) to those of the η model (Eq. 1 with the second term replaced by Eq. 5 and fixed H_{FL}^0) for the bilayer with Pt thickness of 1.0 nm. This thickness is chosen because ξ_{FL} is largest, and the Oersted field is much smaller than H_{FL} for all temperatures except the lowest measured. (The harmonic Hall resistance created by the Oersted field does not change depending on the model and is included in the fitting as indicated in the second term of Eq. 1, with the strength of the field calculated by Ampere's Law. For excitation current of 1.0 mA on the 1.0 nm Pt

bilayer, $H_{Oe} = +0.9$ Oe and may be well approximated as temperature-independent due to the near-unity residual resistivity ratio (RRR) of that bilayer.) The results of fitting to the $H_{FL}(T)$ and $\eta(T)$ models are summarized in Fig. 3. It can be seen in Fig. 2(a) and Fig. 2(b) that the fits to the two models give nearly identical ϕ behavior, and the goodness-of-fit between the models cannot be distinguished by inspecting the fit residuals. In Fig. 2(a) and Fig. 2(b) we have chosen data collected at a temperature of 100 K, for which both the fit η is nonzero and yet the Oersted field is small with respect to the FL effective field, which are conditions for which a deviation from the H_{FL} model should be most apparent. In practice, our lack of ability to differentiate the goodness-of-fit between models is because the non-$\sin\phi$ dependence of the HR data is small, $R_H^{2\omega}$ being dominated by the DL SOT signature and MTE signatures (in these bilayers R_{PHE} is typically a factor of ten smaller than R_{AHE}).

It is to be emphasized that *either* model implies the magnitude of the FL SOT decreases strongly as temperature decreases. In Fig. 3(c) H_{FL} is decreased by a factor of 4 from 300 K to 20 K, and equivalently in Fig. 3(d) η at 20 K shows an enhancement by a factor of 10 with respect to 300 K. In the η model results shown in Fig. 3(d), we have fixed $H_{FL}^0 = -8.3$ Oe, which is the 300 K H_{FL} model result. While not rigorous (as it assumes the MPE is absent at 300 K and H_{FL}^0 is independent of temperature), this approach is sufficient for comparing models and illustrating our inability to differentiate the proper model from fits to our data. Because we cannot differentiate between models, for the results presented in the main text we have chosen to remain with the more conventional model given by Eq. 1, but note that in future studies in which the FL SOT term dominates the HR measurement and the MPE is present, the angular dependence shown in Fig. 2 may be observed.

Parallel resistances analysis used to extract resistivities

In order to obtain the Pt resistivity and account for the shunted current distribution in the bilayer, the F and N layer were treated as parallel resistances. The sheet resistances R_{xx} for each Pt thickness at 300 K and 20 K are shown in Fig. 1(a) of the main text. For ultrathin metal films the resistivity is well-approximated by the expression

$$\rho_{\mathrm{N}}(t_{\mathrm{N}}) = \rho_\infty + R_A/t_N, \tag{6}$$

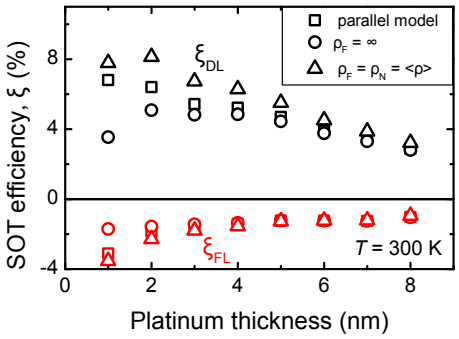

FIG. 4. Summary of the DL (black data) and FL (red data) SOT efficiencies at 300 K for various current shunting models. Shown as squares are the parallel resistance model values shown in the main text, the circles are obtained by setting $\rho_F = \infty$, and the triangles are for the uniform-resistivity model.

where ρ_∞ is the bulk ($t_N \to \infty$) resistivity, and R_A is a surface resistance-area product that accounts for the increase in resistivity for thin films due to diffuse surface scattering[12]. Diffuse surface scattering dominates over grain boundary scattering in our films, as they are epitaxial. To account for the shunting effect of the 1.2 nm CFA layer, Eq. 6 was fit to the thickness dependence of R_{xx} shown in Fig. 1(a) with a parallel-resistance model (i.e. $R_{xx}^{-1} = R_F^{-1} + R_N^{-1}$) and $R_F = \rho_F/t_F$, ρ_∞, and R_A as the fitting parameters. It was found that $\rho_F = 130$ $\mu\Omega$cm, $\rho_\infty = 12$ $\mu\Omega$cm, and $R_A = 88$ $\mu\Omega$cm nm. The results of the fit are shown in the inset of Fig. 1(a) in the main text. The value of ρ_∞ at 300 K we extract using this method is in good agreement with the 300 K resistivity reported for pure bulk Pt[13, 14]. Also $d\rho_\infty/dT = 0.038$ $\mu\Omega$cm K^{-1} in the 50-300 K temperature range, in good agreement with literature reports (0.037-0.040 $\mu\Omega$cm K^{-1})[13, 14]. The current density in N, which is the j_N^e factor in the denominator of Eq. 1 of the main text, is calculated using a standard current-divider expression

$$j_N^e = \frac{\sqrt{2}I}{t_N}\frac{R_F}{R_F + R_N} \tag{7}$$

where $R_N = \rho_N/t_N$, $R_F = \rho_F/t_F$, and the $\sqrt{2}$ in numerator converts I from an RMS amplitude to a sinusoidal amplitude.

We briefly discuss possible systematic errors introduced by our method of treating the

current shunting distribution in the bilayer. At small N thicknesses in all-metallic F/N bilayers, current shunting through the F layer represents the largest systematic error in calculating ξ. Approaches to account for current shunting in quantitative analysis vary: some have simply using a bilayer-averaged current density, and others have measured ρ_F with a companion growth[15]. For example, in Fig. 4 we show how our measured SOT efficiencies are altered by assuming different possible shunting current distributions. In addition to the parallel resistance model described previously, in Fig. 4 we show SOT efficiencies obtained by setting $\rho_F = \infty$, and also with a uniform-resistivity assumption where $\rho_F = \rho_N = \langle\rho\rangle$. The latter case may be appropriate in the regime where the carrier mean free path is comparable to the bilayer thickness and the scattering is dominated by surface scattering, as is the case in our bilayers. However, the difference between the parallel resistance model used in the main text and the uniform resistivity model can be seen to be small and does not change the results of the paper.

Measurement of AHE and AMR resistances

Here we describe the measurement details used to measure R_{AHE} and R_{AMR}, such as the values shown on Fig. 2 of the main text. Magnetic field sweeps over the range of $\pm$ 9 T were performed while recording R_{xx} and R_{xy}, with the orientation of the magnetic field H along the three coordinates x, y, and z shown in Fig. 1(a). See Fig. 5 for example magnetic field sweeps. In Fig. 5(a), we indicate how the saturated-magnetization difference between x and z H-orientations gives R_{AMR}, which must be differentiated from spin-Hall magnetoresistance (SMR)[16–19] changes in resistance that occur between the z and y H-orientations. In Fig. 5(b) the R_{xy} data are fit to the combined AHE and ordinary Hall effect (OHE) model to give R_{AHE}, which is the saturation value of the magnetization-dependent Hall resistance.

Magnetoresistance including Pt shunting

The identification of the MPE discussed in the main text relies on the differentiation of the observed magnetoresistance (MR) vs R_{xx} behavior shown in Fig. 2 of the main text from that which would be expected if the MR originated from F shunting alone. In Fig. 2 of the main text, the data is visualized with temperature as an implicit variable.

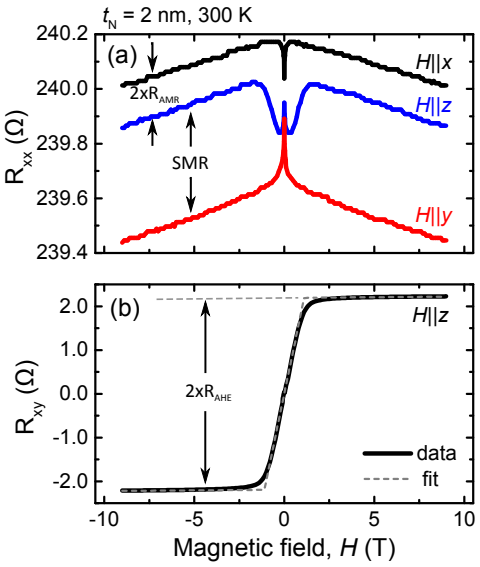

FIG. 5. Example ±9 T magnetic field sweeps for (a) R_{xx} and (b) R_{xy}, which are used to extract R_{AMR} and R_{AHE} respectively as indicated on the figure. The orientation of the field is indicated on the figure where the coordinate system is defined in 1(a). In (b) the gray line shows the fit to piecewise defined OHE plus AHE resistance, which gives $R_{AHE} = 2.19\ \Omega$, AHE saturation field of $1.11\ T$, and OHE coefficient above saturation of $+1.4\pm\ 0.4\times10^{-11}\ m^3C^{-1}$. A small H-independent offset has been subtracted from the R_{xy} data shown in (b), so that the data is odd with respect to H. All data shown in this figure was taken on the 2 nm Pt thickness at 300 K.

Here, in supplementary Fig. 6 we have included the same data plotted traditionally so that temperature is the explicit variable. To understand show the shorting effect of the N Pt layer influences the measured net MR, we first express the resistance tensors in both N and F as

$$R_F = \begin{bmatrix} R_{xx,F} & R_{xy,F} \\ -R_{xy,F} & R_{xx,F} \end{bmatrix}, R_N = \begin{bmatrix} R_{xx,N} & R_{xy,N} \\ -R_{xy,N} & R_{xx,N} \end{bmatrix}, \tag{8}$$

where we have enforced time-reversal symmetry ($R_{xy} = -R_{yx}$) and isotropic transport ($R_{xx} = R_{yy}$). The total resistance tensor R_T is given by adding R_F and R_N in parallel, i.e. $R_T^{-1} = R_F^{-1} + R_N^{-1}$. To simplify we note that $R_{xx} \gg R_{xy}$ for both N and F, and for purpose of this exercise we take $R_{xy,N} = 0$. Carrying out the algebra and simplifying for the transverse

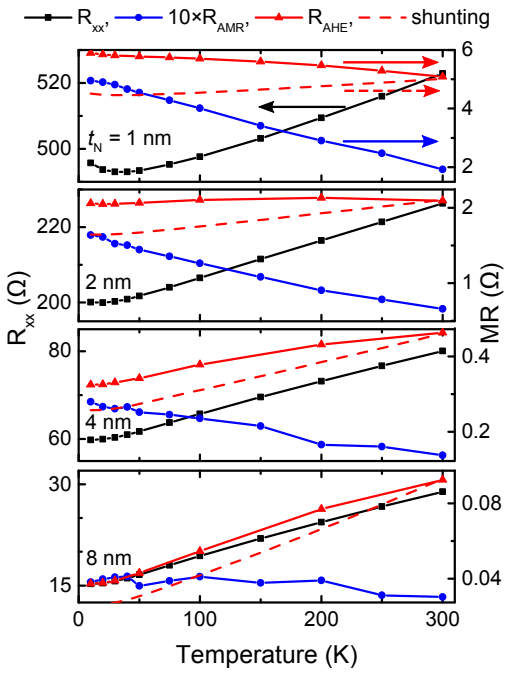

FIG. 6. The explicit temperature dependence of square resistance R_{xx} (left ordinate, black squares), and MRs R_{AHE} (right ordinate, red triangles) and R_{AMR} (right ordinate, blue circles) for the 1, 2, 4, and 8 nm Pt thicknesses. R_{AMR} has been multiplied by 10 for ease of visualization. The lines connect data points. Also shown as the dashed red line (right ordinate) is the F shunting prediction $R_{MR} \propto R_{xx}^2$, which has been scaled to match the 300 K R_{AHE} value for ease of comparison. The data shown in this figure is the same as that shown in Fig. 2 of the main text, in which the temperature dependence is implicit.

(i.e. Hall) total resistance we have

$$R_{xy,T} = \frac{R_{xx,N}^2 R_{xy,F}}{(R_{xx,F} + R_{xx,N})^2}. \tag{9}$$

In our case, $RRR_F \simeq 1$, so we may attribute all temperature dependence of $R_{xx,T}$ to temperature dependence of $R_{xx,N}$. To compare to the measured transverse resistance data,

it is most helpful to rearrange Eq. 9 by substituting $R_{xx,N}^{-1} = R_{xx,T}^{-1} - R_{xx,F}^{-1}$. We then have

$$R_{xy,T} = \frac{R_{xx,T}^2 R_{xy,F}}{R_{xx,F}}, \tag{10}$$

therefore we expect $R_{xy,T} \propto R_{xx,T}^2$, for temperature-independent $R_{xy,F}, R_{xx,F}$. It is also straightforward to show for longitudinal MR (e.g. AMR) N shunting also gives rise to $R_{AMR,T} \propto R_{xx,T}^2$. These expressions motivate the trendline drawn on Fig. 2 in the main text.

[1] U. H. Pi, K. Won Kim, J. Y. Bae, S. C. Lee, Y. J. Cho, K. S. Kim, and S. Seo, Appl. Phys. Lett. **97**, 162507 (2010).

[2] J. Kim, J. Sinha, M. Hayashi, M. Yamanouchi, S. Fukami, T. Suzuki, S. Mitani, and H. Ohno, Nat. Mater. **12**, 240 (2012).

[3] S. Emori, U. Bauer, S.-M. Ahn, E. Martinez, and G. S. D. Beach, Nat. Mater. **12**, 611 (2013).

[4] M. Kawaguchi, K. Shimamura, S. Fukami, F. Matsukura, H. Ohno, T. Moriyama, D. Chiba, and T. Ono, Appl. Phys. Express **6**, 113002 (2013).

[5] C. O. Avci, K. Garello, M. Gabureac, A. Ghosh, A. Fuhrer, S. F. Alvarado, and P. Gambardella, Phys. Rev. B **90**, 224427 (2014).

[6] The angle convention we use is shifted by 90° from that used in Refs. [4, 5]. Also, the $\sin 3\phi - \sin\phi$ term in Eq. 1 is identical to the angular dependence of the FL contribution used in Refs. [4, 5], however we have arrived at a more compact expression in the chosen geometry.

[7] S. Y. Huang, W. G. Wang, S. F. Lee, J. Kwo, and C. L. Chien, Phys. Rev. Lett. **107**, 216604 (2011).

[8] K. Uchida, M. Ishida, T. Kikkawa, A. Kirihara, T. Murakami, and E. Saitoh, J. Phys. Condens. Matter **26**, 343202 (2014).

[9] S. H. Wang, L. K. Zou, J. W. Cai, B. G. Shen, and J. R. Sun, Phys. Rev. B **88**, 214304 (2013).

[10] M. Johnson and R. H. Silsbee, Phys. Rev. Lett. **55**, 1790 (1985).

[11] F. J. Jedema, H. B. Heersche, A. T. Filip, J. J. A. Baselmans, and B. J. van Wees, Nature **416**, 713 (2002).

[12] E. H. Sondheimer, Adv. Phys. **1** (1952).

[13] L. Abadlia, F. Gasser, K. Khalouk, M. Mayoufi, and J. G. Gasser, Rev. Sci. Instrum. **85**, 095121 (2014).

[14] D. R. Lide, "Handbook of Chemistry and Physics," (1996).

[15] M.-H. Nguyen, D. C. Ralph, and R. A. Buhrman, Phys. Rev. Lett. **116**, 126601 (2016).

[16] H. Nakayama, M. Althammer, Y.-T. Chen, K. Uchida, Y. Kajiwara, D. Kikuchi, T. Ohtani, S. Geprägs, M. Opel, S. Takahashi, R. Gross, G. E. W. Bauer, S. T. B. Goennenwein, and E. Saitoh, Phys. Rev. Lett. **110**, 206601 (2013).

[17] M. Althammer, S. Meyer, H. Nakayama, M. Schreier, S. Altmannshofer, M. Weiler, H. Huebl, S. Geprägs, M. Opel, R. Gross, D. Meier, C. Klewe, T. Kuschel, J.-M. Schmalhorst, G. Reiss, L. Shen, A. Gupta, Y.-T. Chen, G. E. W. Bauer, E. Saitoh, and S. T. B. Goennenwein, Phys. Rev. B **87**, 224401 (2013).

[18] S. Meyer, M. Althammer, S. Geprägs, M. Opel, R. Gross, and S. T. B. Goennenwein, Appl. Phys. Lett. **104**, 242411 (2014).

[19] J. Kim, P. Sheng, S. Takahashi, S. Mitani, and M. Hayashi, Phys. Rev. Lett. **116**, 097201 (2016).